The Structure and Reactivity of Graphene Oxide

Helen Thomas

Thesis

Submitted to the University of Warwick

for the degree of

Doctor of Philosophy

Department of Chemistry

July 2015

To my mum,

for her infallible support.

Table of Contents

List of Figures

List of Schemes

List of Tables

Acknowledgements

I would like to thank my supervisor Dr. Jonathan Rourke for his guidance and patience throughout my studies, and for the countless hot chocolates provided over many discussions. In addition, I thank you for painstakingly going through the drafts of this thesis.

I would also like to sincerely thank all my collaborators, in particular Dr. Neil Wilson and Alex Marsden for their invaluable help and training on the microscopes. I'd like to thank Dr. Cristina Vallés, Prof. Robert Young and Prof. Ian Kinloch of Manchester University, for their insight and discussions on the fluorescence studies in this thesis. And thanks also go to Dr. Marc Walker, Steve York, Dave Hammond, Steven Hindmarsh, Dr. Ben Douglas, Phil Aston, Dr. John Hanna and Stephen Day for their help and collaboration on the various characterisation data contained in this thesis. I am grateful to the EPSRC for funding, and for their Durham-based ssNMR service.

On a more personal note, I'd like to thank the occupants of C415 for making day-to-day life enjoyable: to Paul, whose endless rants remind me that things could always be worse; to Andy 2, whose general grunts of northern disapproval brighten my day; to Andy 3, the best joke teller I have ever known; to Jess, whose drinking capabilities have never ceased to amaze me; and to Nikki who is just generally quite terrifying.

I'd also like to thank my friends outside of the lab: to Caroline, Tom and Dan for the laughs, dinners and conversation; to Claire, who was so pleased for me when I found a proper job and decided to stop being a "scrounging student"; and to Ed and Lila for being fantastic housemates and for providing me with posh gin in times of need.

I'd like to give special thanks to my family. To my Grandparents, whose unbreakable optimism and kindness has always been an inspiration to me. To my sister Claire, the biggest Harry Potter fan in the world, you once told me 'don't be a loom', and I try to live by that everyday. Thank you for being you. And to my mum, thank you for your patience and for all

the smurfy advice you've given me over the years. I would never have gotten this far without you.

Finally, I'd like to thank Matt. My partner and my best friend. The Bonniest Baby of Bromley and all round Worldie. Thank you for sticking by me all this time, for the countless dinners you've made me, and for all the ways you've helped me. I look forward to our future of sitting.

Declaration

This thesis is submitted to the University of Warwick in partial fulfilment of the requirements for the degree of Doctor of Philosophy.

I declare that this thesis contains an account of my own work, except where otherwise specifically indicated:

The fluorescence studies in Chapter 3 were carried out in collaboration with Cristina Vallés, Robert Young and Ian Kinloch, Manchester University. AFM and TEM studies were carried out in collaboration with Neil Wilson and Alex Marsden, University of Warwick. The ssNMR studies in Chapter 3 were carried out by John Hanna and Stephen Day, University of Warwick, and those in Chapters 4 and 5 by the EPSRC service at Durham University. Lastly, XPS was run in collaboration with Marc Walker, University of Warwick.

This work was performed at the University of Warwick under the supervision of Dr. Jonathan P. Rourke between October 2011 and April 2015. No part of this thesis has been submitted for examination at any other institution, although parts have been published:

Thomas, H. R.; Vallés, C.; Young, R. J.; Kinloch, I. A.; Wilson, N. R.; Rourke, J. P, Identifying the fluorescence of graphene oxide. *J. Mater. Chem. C* **2013,** 1, 338-342.

Thomas, H. R.; Day, S. P.; Woodruff, W. E.; Vallés, C.; Young, R. J.; Kinloch, I. A.; Morley, G. W.; Hanna, J. V.; Wilson, N. R.; Rourke, J. P, Deoxygenation of Graphene Oxide: Reduction or Cleaning? *Chem. Mater.* **2013,** 25, 3580-3588.

Thomas, H. R.; Marsden, A. J.; Walker, M.; Wilson, N. R.; Rourke, J. P, Sulfur-Functionalized Graphene Oxide by Epoxide Ring-Opening. *Angew. Chem. Int. Ed.* **2014,** 53, 7613-7618.

Abstract

Graphene oxide (GO) can provide a cost-effective route to a graphene-like material on an industrial scale, but produces an imperfect product. In order to improve the quality of the resultant graphene, unanswered questions regarding the structure and chemical reactivity of GO need to be addressed.

In this thesis, chapters 1 and 2 serve to introduce the field of graphene and graphene oxide research, as well as standard characterisation techniques.

Chapter 3 is concerned with investigating the validity and general applicability of a recently proposed two-component model of GO – the formation of the two components was shown to be largely independent of the oxidation protocol used in the synthesis, and additional characterisation data was presented for both base-washed graphene oxide (bwGO) and oxidation debris (OD). The removal of the OD cleans the GO, revealing its true mono-layer nature and in the process increases the C:O ratio, i.e. a deoxygenation. By contrast, treating GO with hydrazine was found to both remove the debris and reduce (cleaning and deoxygenation) the graphene-like sheets.

In chapter 4, different nucleophiles were used to explore bwGO functionalisation via epoxy ring-opening reactions. Treatment of bwGO with potassium thioacetate, followed by an aqueous work-up, was shown to yield a new thiol functionalised material (GO-SH). As far as is known, this was the first reported example of using a sulfur nucleophile to ring open epoxy groups on GO. The incorporation of malononitrile groups, and the direct grafting of polymer chains to the graphene-like sheets was also demonstrated.

The thiol groups on GO-SH are amendable to further chemistry and in chapter 5 this reactivity is exploited with alkylation, thiol-ene click and sultone ring-opening reactions. Au(I) and Pd(II) metallo-organic complexes were also prepared, and gold deposition experiments were carried out, demonstrating that GO-SH has a strong affinity for AuNPs. These CMGs have varying solubility and improved thermal stability.

Chapter 6 concludes the work covered in this thesis, and full experimental details can be found in chapter 7.

Abbreviations

at.%	*atomic percent*
AFM	*atomic force microscopy*
ATR-FTIR	*attenuated total reflection fourier transformed infrared*
BSE	*back-scattered electrons*
CA	*contact angle*
CMG	*chemically modified graphene*
CNT	*carbon nanotube*
CP	*cross polarised*
CVD	*chemical vapour deposition*
DE	*direct excitation*
DFT	*density functional theory*
DMF	*dimethylformamide*
DMSO	*dimethyl sulfoxide*
EDX	*energy dispersive x-ray spectroscopy*
ESI	*electrospray ionisation*
EWG	*electron withdrawing group*
FTIR	*fourier transformed infrared*
FWHM	*full width at half maximum*

HOPG	*highly ordered pyrolytic graphite*
HR-TEM	*high-resolution transmission electron microscopy*
MALDI-TOF	*matrix assisted laser desorption ionisation – time of flight.*
MAS	*magic angle spinning*
MS	*mass spectroscopy*
MVK	*methyl vinyl ketone*
NIPAM	*N-isopropylacrylamide*
NMR	*nuclear magnetic resonance*
NPs	*nanoparticles*
pNIPAM	*poly(N-isopropylacrylamide)*
RAFT	*reversible addition–fragmentation chain transfer*
RT	*room temperature*
SAED	*selected area electron diffraction*
SEM	*scanning electron microscope*
ssNMR	*solid-state nuclear magnetic resonance*
STM	*scanning tunnelling microscope*
SWCNT	*single-walled carbon nanotube*
TEM	*transmission electron microscopy*
TGA	*thermogravimetric analysis*
UHV	*ultra high vacuum*
wt.%	*weight percent*
XPS	*x-ray photoelectron spectroscopy*

Nomenclature

GO   *generic graphene oxide*

aGO   *as-produced graphene oxide*

bwGO   *base-washed graphene oxide*

OD   *oxidation debris*

rGO   *generic reduced graphene oxide*

raGO   *reduced as-produced graphene oxide*

rbwGO   *reduced base-washed graphene oxide*

GO-CN   *malononitrile functionalised bwGO*

GO-SH   *thiol functionalised bwGO*

GO-SPh   *thiophenol functionalised bwGO*

GO-pNIPAM$_x$ *pNIPAM functionalised bwGO, chain length x = 30; 200; 440*

GO-C$_4$ / GOS-C$_4$ *butyl chain functionalised bwGO / GO-SH*

GO-C$_{10}$ / GOS-C$_{10}$ *decyl chain functionalised bwGO / GO-SH*

GO-MVK / GOS-MVK   *MVK functionalised bwGO / GO-SH*

GO-PrSO$_3$ / GOS-PrSO$_3$ *1,3-propanesultone functionalised bwGO / GO-SH*

GOS-Au   *mono-atomic gold on GO-SH*

GOS-Pd   *mono-atomic palladium on GO-SH*

GOS-AuNPs   *gold nanoparticles on GO-SH*

Chapter 1

Introduction
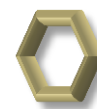
1.1 Carbon Materials

Carbon has the ability to form strong covalent bonds with a variety of different elements, yielding the versatile carbonaceous compounds which constitute organic chemistry. However, what sets carbon apart from other elements is its propensity to form strong covalent bonds with itself, resulting in an array of kinetically stable allotropes with varying dimensionality.[1] The extensive structural diversity found for carbon materials can result in vastly different properties. For example, the two best known allotropes of carbon are diamond and graphite. Diamond has a large network of sp^3 hybridised carbon involved in σ-bonding, and is a transparent, electronic insulator.[2] By comparison, graphite is an excellent electrical conductor,[3] it comprises pure sp^2 hybridised carbon forming a σ-bonded network, alongside π-bonding from p_z orbitals.

This thesis is primarily concerned with materials derived from graphene: a two-dimensional sheet of sp^2 hybridised carbon, much like a honeycomb lattice (figure 1.1).[4]
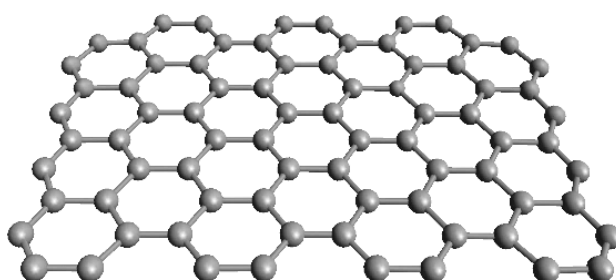
Fig. 1.1 Crystal structure of 2D graphene.

Graphene can be thought of as the building blocks for all other graphitic materials: if a graphene sheet is wrapped it forms a zero-dimensional fullerene, if rolled, a one-dimensional single wall carbon nanotube (SWCNT), and if stacked, three-dimensional

graphite.[1] All of these allotropes are thus formed from a pristine sp^2 carbon network, their structures are shown in figure 1.2.
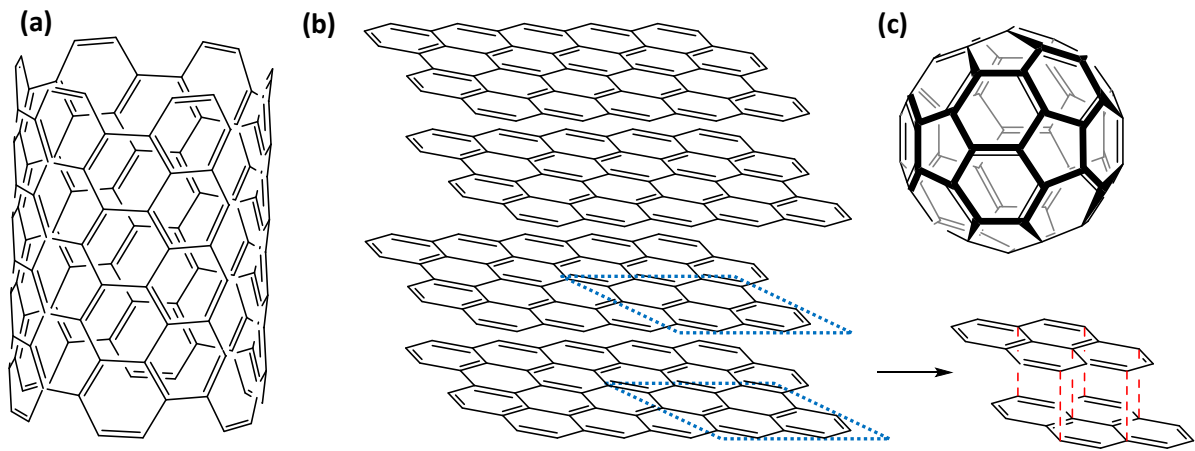
Fig. 1.2 Graphitic carbon allotrope structures: **(a)** a SWCNT (1D), **(b)** AB stacked graphite (3D) and **(c)** a fullerene (0D).

1.2 Graphene

1.2.1 Structure

As stacked layers, graphene forms the building blocks of lamellar graphite, which came into widespread use in the 1560s.[5] However individual graphene sheets were believed to be thermodynamically unstable,[6] and as a result were not isolated for 440 years.[7] In 2004, Geim and Novoselov demonstrated that a single graphene layer could be extracted from graphite by mechanical exfoliation.[3] The material has since sparked a lot of scientific interest due to its remarkable properties;[8, 9] it is exceptionally electrically[10] and thermally[11] conductive, transparent,[12] elastic,[13, 14] highly impermeable,[15, 16] extremely strong[14] and yet is the thinnest[16] 2D material ever obtained (and is ever possible to obtain).

Figure 1.3 shows the bonding orbitals of graphene: three in-plane sp^2 hybridised orbitals formed from the 2s, $2p_x$ and $2p_y$ orbitals (σ-bonding), and the out of plane $2p_z$ orbital which forms a delocalised system of electrons above and below the graphene lattice plane (π-bonding).

$2s$ $\quad$ $2p_x$ $2p_y$ $\quad$ $2p_z$ $\qquad\qquad$ sp^2 $\qquad\qquad$ $2p_z$
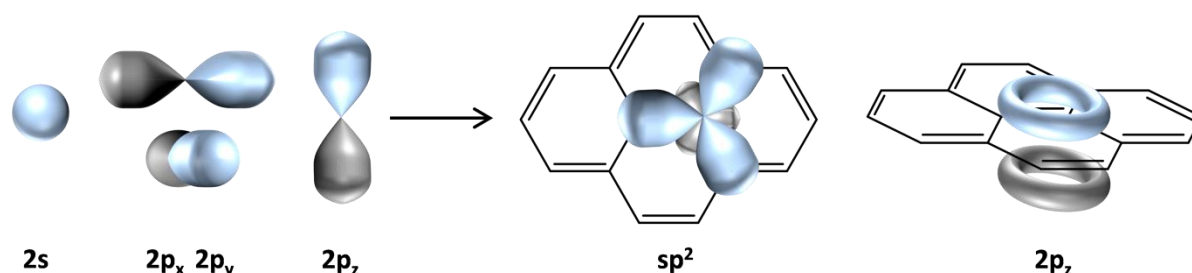
Fig. 1.3 Orbital hybridisation and bonding in graphene.

The distinctive electronic properties of 2D materials such as graphene and boron nitride arise from the confinement of excitons in the direction of sheet thickness.[17] This quantum confinement introduces relativistic effects with charge carriers behaving as Dirac fermions:[18, 19] the electrons have zero rest mass, and move across the sheet with little scattering, even at room temperature.[20]
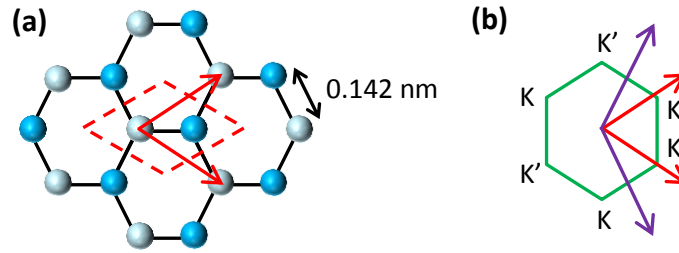
Fig. 1.4 (a) Graphene lattice where the unit cell is outlined by the dashed red area, and the primitive vectors are shown as red arrows. The nearest neighbour distance is also labelled (0.142 nm). **(b)** The first Brillouin zone of graphene (green) is shown with inequivalent Dirac points K and K' at the corners. The primitive vectors of the real lattice, and the primitive vectors of the reciprocal lattice are represented as red and purple arrows respectively.

Figure 1.4 (a) shows the diatomic unit cell of graphene, the two atoms are inequivalent due to the direction of their nearest neighbours. Graphene can thus be thought of as having two sublattices.[21] The first Brillouin zone of graphene is found using the k space of the graphene lattice, as shown in figure 1.4 (b), there are six corners to the zone, of which two are inequivalent. These corners (K and K') are referred to as Dirac points; they mark the positions at which the conduction and valence bands touch in the electronic structure of graphene, giving a Fermi surface characterised by six Dirac cones[21] (figure 1.5). Graphene thus has a zero band gap structure, and exhibits semi-metal behaviour.[22]
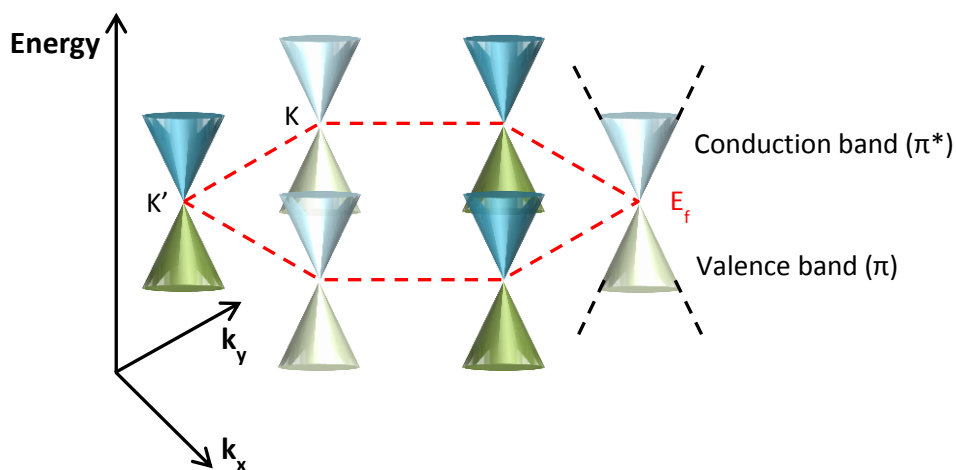
Fig. 1.5 Schematic showing the electronic band structure of graphene, respective to k space. The Fermi energy level (E_f) and Dirac points (K, K') are shown.

Graphene has vast potential in a number of different fields, boasting applications in drug delivery,[23, 24] water purification,[25] and automotive,[26] aerospace[27] and electronic engineering.[21, 28] Currently the main limitation for research stems from the difficulties with producing high quality graphene on a large scale.[29]

1.2.2 Production

Graphene can be produced by a number of different methods including mechanical exfoliation,[3] ion intercalation,[30, 31] chemical vapour deposition (CVD),[32, 33] epitaxial growth,[34, 35] liquid phase exfoliation,[36, 37] bottom-up organic synthesis,[38, 39] and the chemical modification of graphene derivatives.[40, 41] Each method has its own limitations, but mechanical cleaving, CVD, epitaxial growth, and the reduction of graphene oxide have proven to be popular approaches.[29]

Mechanical exfoliation breaks the Van der Waals and π-π stacking intermolecular forces[42] which bind graphene sheets together as graphite.[3, 43] Pristine graphene layers are thus produced from this so-called "scotch tape" method, however the yield is low making this procedure impractical and expensive to carry out on an industrial scale.[42]

CVD uses a transition metal surface, such as Cu, Ni, Pd, Pt and Ir, to grow crystalline graphene from the bottom up using a gaseous precursor such as methane.[33, 44-46] The growth of the graphene sheets is dependent on the metal substrate used.[33] Cu in particular shows promise as a low-cost catalyst for the production of large, mono- and bi-layer graphene sheets.[32] The main difficulties with CVD graphene arises from a lack of understanding and control over the atomic growth mechanism: grain size and stacking order are important considerations.[47]

Epitaxial graphene can be grown via the thermal decomposition of silicon carbide.[48] Under high temperatures (1000–1500 °C) and ultrahigh vacuum (UHV), a layer of graphene will form on the surface of SiC crystals: the Si sublimes leaving epitaxial graphene. This method allows for the direct deposition of graphene onto semi-conducting and insulating substrates, but the harsh reaction conditions and high-cost SiC material means that it is also an expensive option.[49]

Graphene oxide (GO) promises an alternative route to graphene.[40, 41] The derivative material is cheap and easy to synthesise in bulk quantities via the oxidation of graphite,[41, 50, 51] and can be manipulated chemically due to its good dispersibility in many common solvents such as water. GO sheets can be either further functionalised, or reduced back to a graphene-like material.[52]

1.3 Graphene Oxide

1.3.1 Structural Models

Graphene oxide is exfoliated from its precursor material, graphite oxide, the structure of which has been debated for over 150 years.[53] Graphite oxide was first prepared in 1859 by the chemist B. C. Brodie, who used an explosive mixture of fuming nitric acid and potassium chlorate to oxidise graphite. He calculated the elemental composition of graphite oxide to be $C_{2.19}H_{0.80}O_{1.00}$.[50]

As a derivative of graphene, graphene oxide is expected to be a mono-layer sheet of sp^2 and sp^3 hybridised carbons, where the graphene-type backbone is interrupted by various basal plane and edge site oxidative functionalities. However the relative proportions and positions of these oxidative groups is largely unknown, and it is further unclear whether or not there is any consistency between different batches of GO.[41]

The oxidative groups found on GO are essentially defects on the pristine sp^2 network. They cause perturbations, or "wrinkling" of the graphene-like sheet resulting in an increased sheet thickness and layer spacing.[54] Although the material is known to be amorphous, $C_4O(OH)$ is used as a rudimentary chemical formula.[41]

The difficulty with assigning graphite oxide – and indeed graphene oxide – an exact chemical structure comes from sample-to-sample variation, hygroscopicity and its non-stoichiometric nature.[55] Despite this, various structures have been proposed over the years.[41] Hofmann and Holst came forward in 1939, describing it as a graphite-based material with epoxy groups spread over the basal plane of the stacked sheets.[56] An amended structure was then offered in 1946 by Ruess[57] who introduced hydroxyl groups and significant sp^3 hybridisation. The 1969 Scholz-Boehm model[58] notably rejected the idea of ether and epoxy groups, instead suggesting that quinoidal species were incorporated into the graphene-like sheets. Nineteen years later, Nakajima *et al.* proposed their model of graphene oxide.[59] They reasoned that the structure was akin to $(C_2F)_n$ with the presence of carbonyl and hydroxyl groups, as well as adsorbed water which was intercalated between the graphitic sheets.

Nowadays, the most widely accepted structure of graphene oxide is the Lerf-Klinowski model, which came about from solid-state NMR (ssNMR) characterisation studies.[60] A later variation of this model,[61] shows a stoichiometric amorphous structure, containing only quaternary carbons, tertiary alcohols, epoxy (1,2-ether) groups and a mixture of alkenes (figure 1.6).
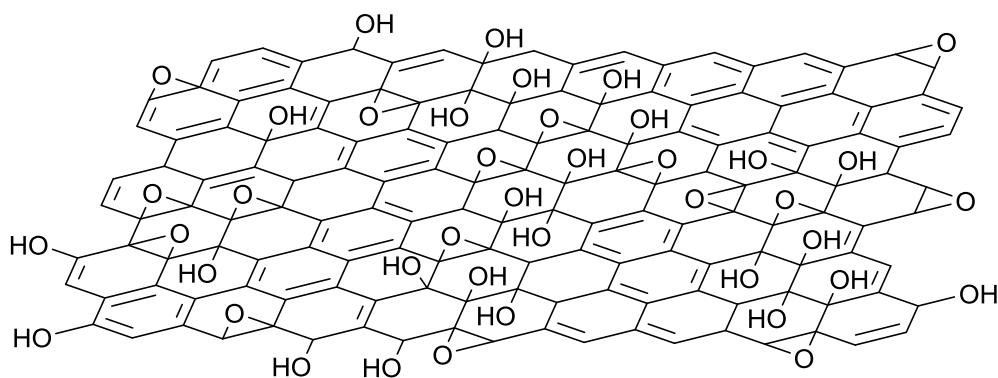
Fig. 1.6 Adapted Lerf-Klinowski structural model of graphene oxide.[41]

In order to improve the understanding behind – and manipulation of – the chemistry of GO, it is necessary to find out more about its structure. Of particular importance is the arrangement of the alkene groups since the amount of conjugation present will affect the electronic structure of the material as well as the chemical reactivity.[41]

1.3.2 Aging

One particular difficulty with studying the structure of GO is that it does not appear to be a stable material; the chemical reactivity and dispersibility of GO changes with the age of the sample. Some research has suggested that GO is in fact a meta-stable material where its structure and reactivity evolves over time.[62] Experimental and density functional theory (DFT) studies indicate that epoxide groups on the surface of the GO sheets may be being slowly hydrolysed. Due to the hygroscopic nature of GO, it has thus been postulated that surface adsorbed water is able to promote the conversion of epoxy groups to hydroxyl groups over time.[63]

1.3.3 Synthesis

While the Brodie synthesis of graphite oxide[50] – $KClO_3$ in fuming HNO_3 – remains popular with some research groups, a number of different synthetic routes have been developed over the years.

Staudenmaier was the first to adapt the Brodie synthesis in 1898, using a higher excess of $KClO_3$ and a mixture of fuming nitric acid and concentrated sulfuric acid.[51] In these two syntheses the $KClO_3$ acts as a source of the reactive species, dioxygen, as summarised by equations 1.1 and 1.2:

$$KClO_3 + 2HNO_3 \rightarrow KCl + 2O_2 + H_2O + 2NO_2 \tag{1.1}$$

$$KClO_3 + HNO_3 + H_2SO_4 \rightarrow \frac{1}{2}O_2 + KHSO_4 + H_2O + NO_2 + ClO_2 \tag{1.2}$$
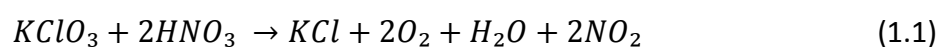
Note that a mixture of NO_2 and N_2O_4 is likely to be produced.

Sixty years after Staudenmaier's adapted procedure, Hummers and Offeman suggested an alternate oxidation protocol using a mixture of potassium permanganate, potassium nitrate and concentrated sulfuric acid followed by an aqueous work-up.[64] The Hummers synthesis is considered to be a safer route to GO, providing equivalent levels of graphite oxidation to the Brodie/Staudenmaier syntheses, but without the concerns of the explosive chlorate reactants. The active species in the Hummers synthesis is diamanganese heptoxide[65]:

$$KMnO_4 + 3H_2SO_4 \rightarrow K^+ + MnO_3^+ + H_3O^+ + 3HSO_4^- \tag{1.3}$$

$$MnO_3^+ + MnO_4^- \rightarrow Mn_2O_7 \tag{1.4}$$
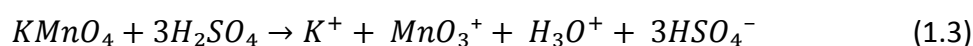
Since the Hummers synthesis was devised, there has been a variety of adapted methods reported in literature. Examples include the "improved" GO synthesis and the "pristine" GO synthesis, both devised by Tour *et al.*[66, 67]

The "improved" Hummers GO synthesis is a modification of the Hummers synthesis. The procedure excludes KNO_3 thereby preventing the liberation of toxic NO_2 and N_2O_4 gases, and the $KMnO_4$ reagent is reacted with graphite in a 9:1 mixture of H_2SO_4/H_3PO_4. The synthesis boasts a safer methodology and efficient reaction times of 12 hours.

The "pristine" GO synthesis is also a modification of the Hummers synthesis, using a mixture of concentrated sulfuric acid and potassium permanganate to oxidise graphite flakes. However the quenching and washing procedures are initially performed with only non-aqueous solvents such as methanol and ethyl acetate to give "pristine" GO.[67] At this point the GO material is washed with water, removing any sulfur-containing impurities and forming a material that resembles conventional Hummers GO. These GO materials were studied before and after exposure to water using Fourier Transform Infrared spectroscopy (FTIR), Thermal Gravimetric Analysis (TGA) and ssNMR, which suggested that aqueous conditions will promote certain chemical transformations. Tour *et al* proposed that the Hummers oxidation of graphite results in the formation of covalent sulfates on the sheet surface from epoxy ring-opening reactions via the nucleophilic attack of sulfuric acid. The subsequent reaction with water then results in sulfate hydrolysis.[67]

In each of these synthetic routes the graphite oxide material is easily exfoliated to give graphene oxide flakes via extensive washing and stirring. What is not yet clear is whether the use of different oxidation protocols has an effect on the structure or chemical properties of graphite and/or graphene oxide. With different groups favouring different protocols, consistency within GO research can be tricky.

1.3.4 Base-washed Graphene Oxide

In 2011, Rourke *et al.* demonstrated that as-produced GO (aGO), prepared via the Hummers synthesis, can be separated into two distinct entities via the simple expedient of washing with dilute NaOH.[53] They extracted a graphene-type material, termed base-washed graphene oxide (bwGO), and a white powder referred to as oxidation debris (OD) (figure 1.7). While the OD could not be separated from contaminating NaCl, the bwGO to OD mass ratio was calculated to be roughly 2:1. New results concerning this structure are given in chapter 3.
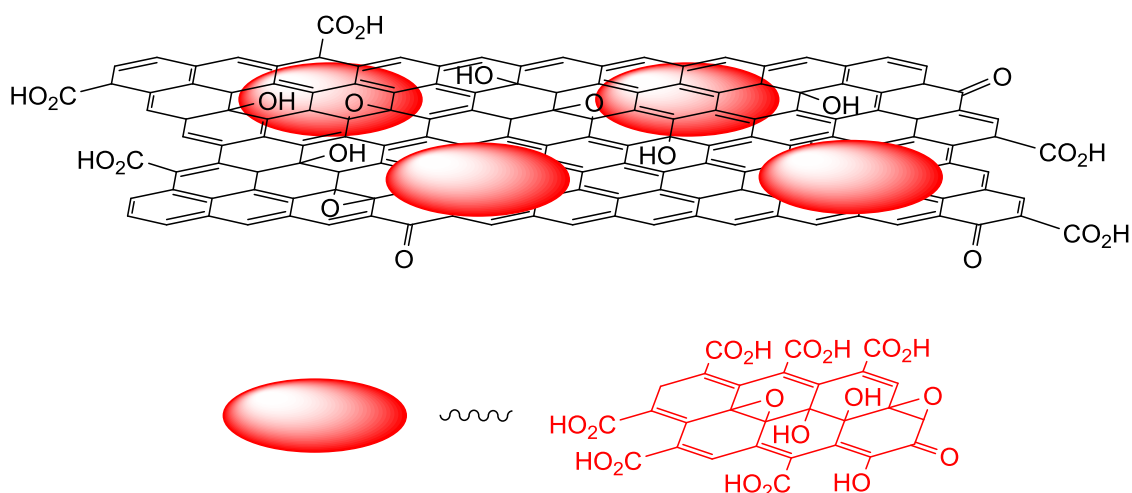
Fig. 1.7 Two component structure of aGO: the oxidation debris (red) is surface adsorbed to base-washed GO (black). The structures are for illustrative purposes only. Figure adapted from ref 62.

Introducing defects to a pristine sp^2 network will affect the electronic structure, creating a tuneable band gap. Thus when graphite is oxidised to GO, the new sp^3 hybridisation results in a loss of conductivity: aGO is an insulator.[68] Curiously though, bwGO is reported to show conductive behaviour, with conductivity measured at 10^0–10^1 S m^{-1}.[53]

Rourke *et al* also found that treatment of aGO with NaOH significantly reduces its dispersibility in most common solvents. A possible mechanism for this interaction is shown in scheme 1.1.

- - - - π-π stacking

|||||||| Hydrogen bond

- - - π-cation interaction
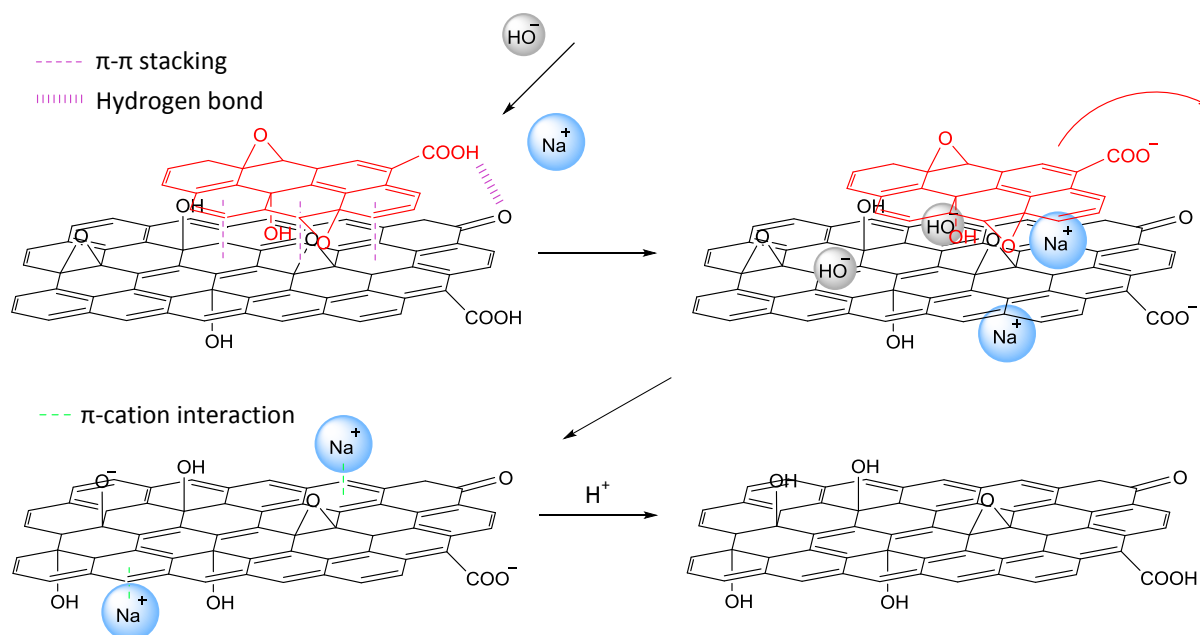
Scheme 1.1 Interaction of aGO with aqueous NaOH.

When aqueous NaOH is mixed with aGO the ions are expected to intercalate between the GO sheets and the OD, disrupting the hydrogen bonding and π-π stacking interactions. The sodium cations may occupy sites on the graphene sheets via π-cation interactions and the hydroxide anions may encourage ring opening of the epoxides. Without the hydrophilic OD, the hydrophobic graphene-like sheet regions are exposed and thus dispersibility is reduced.

These initial studies strongly suggest that aGO actually comprises conductive, graphene-like sheets (bwGO) interspersed with low molecular weight, highly oxidised, fragments (OD). This study was found to be analogous with previous work on oxidised SWCNTs by Green *et al*.[69]

This two component model of aGO has been recently contested in literature by Dimiev *et al*.,[70] but is gaining popularity with other research groups.[71-75] Dimiev *et al*. argue that, as the only carbon source in the synthesis, the graphite must be responsible for the OD. They propose that the basic wash alters the chemical structure of aGO, with basal plane hydroxyl groups being converted into edge site keto groups, breaking up the GO sheets into small pieces thereby forming the OD.[70] This mechanism would result in an increase in keto group functionalities on the GO sheets, which is not apparent from ssNMR studies.[53] Instead, as others have suggested,[75] it is likely that the OD is formed as a result of the oxidative protocol in the synthesis of aGO. In the Hummers synthesis, the sulfuric acid and nitric acid

are expected to intercalate between the graphene sheets, acting as chemical scissors to chop up some of the sheets forming humic-like OD.[75] Any small fulvic-like fractions are expected to be lost during the washing process.

1.3.5 Applications

Whilst GO may hold the key to large scale, high quality graphene production, it also has important uses in its own right. The solution processability, amphiphilicity and high surface area of GO makes it ideal for sensors,[76, 77] energy storage,[78, 79] electronic[80, 81] and biomedical[82] applications.

The zero band gap of graphene limits its potential for opto-electronic applications, but band gaps of varying sizes can be introduced by surface functionalisation of the graphene sheets, allowing for carbonaceous materials with unique optical properties to be prepared:[83] GO is an example of a chemically modified graphene (CMG) material which exhibits such versatile chemistry and tuneable fluorescence. GO emission is dependent on factors such as the degree of oxidation and sheet size, but it is generally a low energy emission of around 550–600 nm.[84]

The practical applications of fluorescent materials are vast and in recent years the interest in carbon-based fluorescent materials has increased. Compared to conventional materials, carbon-based ones often show greater stability, biocompatibility and lower cytoxicity; properties which are of great advantage in biological applications.[84] The photo-luminescence of GO has already been used for various applications including sensors,[85] drug delivery,[86] catalysis[87] and low-cost opto-electronic devices.[88, 89]

1.4 Chemically Modified Graphene

Graphene sheets can be chemically modified, introducing different functional groups onto a graphene backbone. By manipulating the size of the graphene sheets,[90, 91] or by adapting the type and density of the functional groups present,[92] the chemical, physical, optical and electronic properties of graphene-based materials can be altered. This allows researchers to develop CMGs tuned for use in specific applications including transistors,[93] supercapacitors,[94, 95] memory[96, 97] and photovoltaic devices,[98] intracellular imaging,[99] energy storage[36] and a variety of sensors.[85, 100]

1.4.1 Non-covalent Interactions

The non-covalent functionalisation of graphene (or graphene-type materials) occurs via π interactions, providing a means of introducing different functional groups without altering the electronic structure of graphene.[92] The π system can act as a lewis base, forming H-π interactions,[101] and can bind to gaseous molecules such as H_2, CO_2, NH_3 and N_2 via electrostatic and dispersion (Van der Waals) interactions.[102]

For example, CO_2 adsorption on graphene could be used to regulate car emissions, with adsorption capacities of 12 mmol g^{-1} observed at 100 °C.[103] DFT studies predict that the CO_2 molecule lies in plane with the graphene sheet, with the oxygen atoms centred above two neighbouring rings.[104]
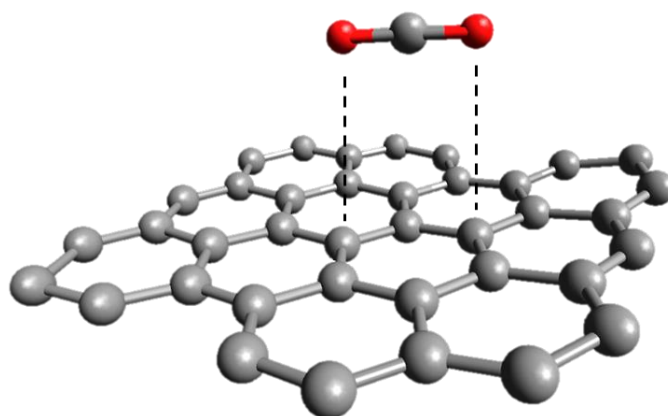
Fig. 1.8 Adsorption of a CO_2 molecule onto graphene via Van der Waals interactions.

π-π stacking interactions occur between the sheets of graphite, and in a similar fashion, can bind aromatic systems to the basal plane and edge sites of graphene (face-to-face and edge-to-face interactions).[105, 106]

The interaction of cations (both metal and organic) with the graphene π system is dominated by electrostatic and induction interactions.[107] These interactions have been extensively studied in literature. They have been used to control the self-assembly of organic nanostructures, and are present in a variety of sensors.[92]

1.4.2 Covalent Interactions

The covalent functionalisation of graphene sheets will disrupt the sp^2 hybridised system allowing control over the material properties. Due to the difficulty with obtaining large quantities of processable graphene sheets, GO is often used as a convenient route to other CMGs: the oxygen functional groups present on GO make it a reactive material which is easy to manipulate chemically.[55] According to the bwGO-OD model of GO,[53] aGO has carboxylic acid and ketone edge groups, as well as epoxy and hydroxyl groups on the basal plane.

aGO has proven itself to be a good platform for many chemical modifications: the edge site carboxyl groups and basal plane OH groups have been widely exploited for amidation,[108-110] (scheme 1.2) esterification[111-113] (scheme 1.3) and carbamation[114-116] (scheme 1.4) reactions.
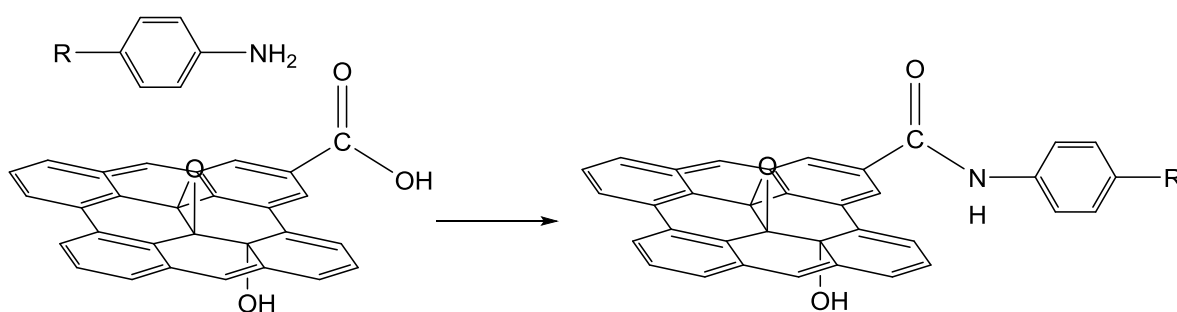
Scheme 1.2 Example amidation of the carboxyl groups on GO.
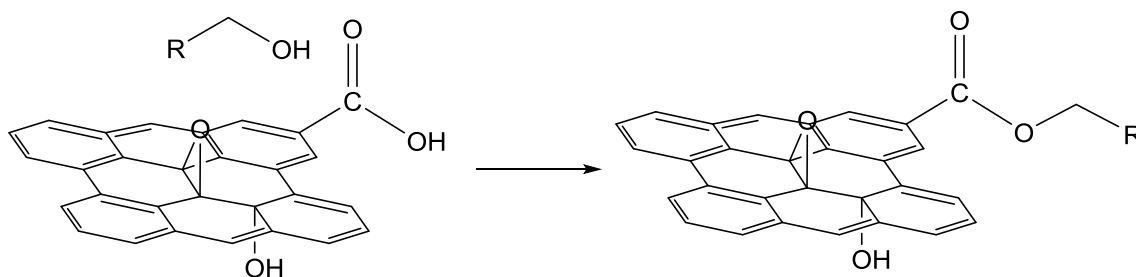
Scheme 1.3 Example esterification of the carboxyl groups on GO.
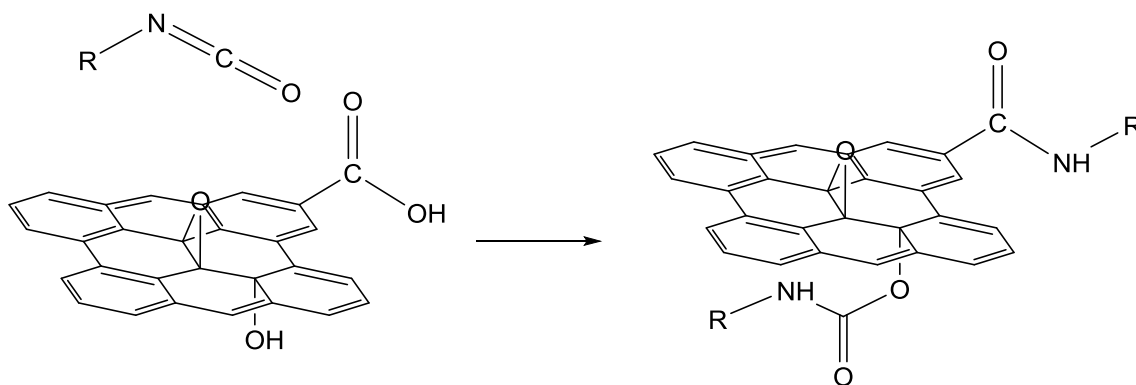
Scheme 1.4 Example carbamation of the hydroxyl groups on GO.

Amination of graphene oxide using nitrogen nucleophiles to ring open surface epoxides has also been explored (scheme 1.5).[117]
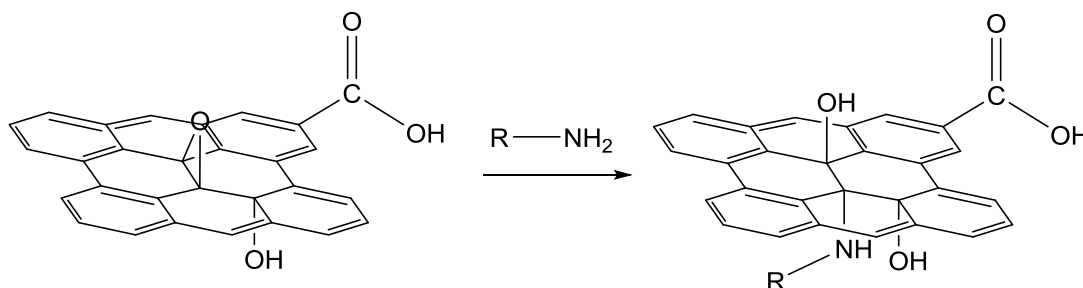
Scheme 1.5 Example amination of the epoxy groups on GO.

However, while nitrogen functionalised CMGs are prevalent in graphene oxide chemistry, sulfur functionalised CMG, until very recently, were not. Scheme 1.6 shows an example thiolation reaction, which was only published in early 2015.[118]
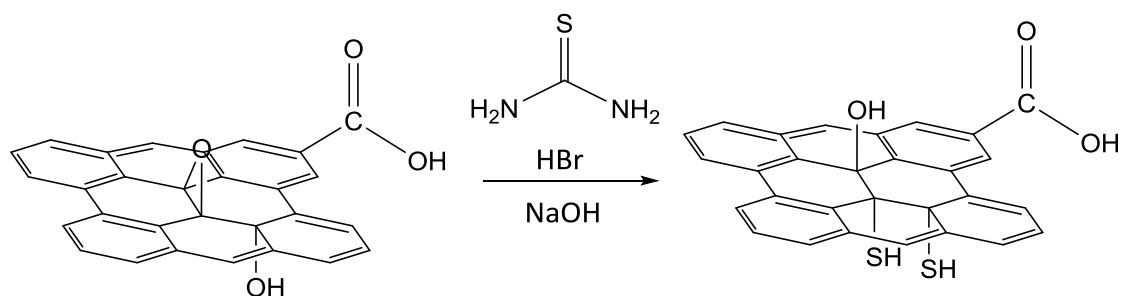
Scheme 1.6 Example thiolation of the epoxy and hydroxyl groups on GO.

Covalently modifying the surface of graphene oxide can yield functionalised CMGs with specially tuned properties. Thus new – and more importantly, selective – routes to functionalisation are still a topic of great interest. A better understanding of the structure of GO would give researchers more control for chemical modification.

1.4.3 Reduction

The oxygen groups on GO can be largely removed using reductive techniques, providing a convenient route to functionalised graphene materials.[119] There are many different ways of reducing GO: it can be done electrochemically,[120] thermally[121] or by a variety of chemicals[122] such as hydrazine,[123] NaBH$_4$,[124] and hydriodic acid.[125] In all cases, a general material known as reduced graphene oxide (rGO) is produced. Various mechanisms of hydrazine reduction have been proposed,[126-129] scheme 1.7 shows a possible route to epoxy group reduction.
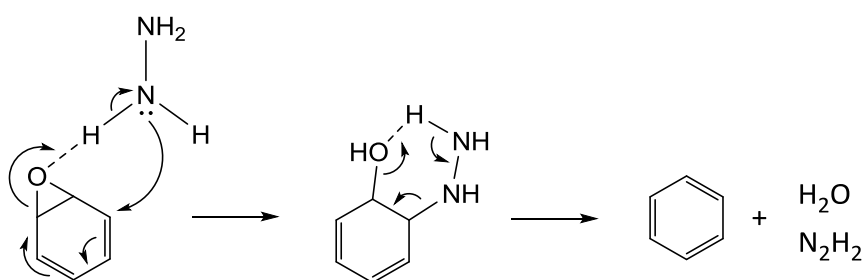
Scheme 1.7 Potential hydrazine reduction mechanism of the epoxy groups on GO.[126]

While rGO cannot be referred to as pristine graphene, it is possible to achieve a reasonable likeness – many of the physical properties of graphene are, at least partially, restored. For example, on reduction of GO the sp^2 hybridised structure of graphene is somewhat

reformed resulting in a once more conductive material.[80, 125, 130, 131] The C:O ratio has also been seen to increase from 2:1 to 10:1 on the reduction of GO.[52] Note that in order to truly reduce GO, electrons must be donated to the GO system and oxygen must be removed.[132]

1.4.4 Polymer Composites

There is currently much interest in combining the superlative physical properties of graphene with the tuneable properties of polymers to form multifunctional composites.[133, 134] Graphene-based nanofillers can be dispersed into a polymer matrix via solution mixing, melt blending or *in situ* polymerisation[135] resulting in many different examples of rGO and GO polymer composites in literature.[136-138] However, the manufacture of these materials is challenging due to phase separation and aggregation issues.[139-141]

1.4.5 Metal Interactions

A different way of tuning the sensitivity of graphene is to develop metallo-organic CMGs by means of nanoparticle deposition through cation-π interactions (figure 1.9), or metal coordination through ligands on a graphene-type surface.[142] Indeed, such metallo-organic CMGs have shown promise as energy storage,[143, 144] sensor,[130, 145] and supercapacitor[146, 147] materials, and have also demonstrated good antimicrobial activity.[148, 149]
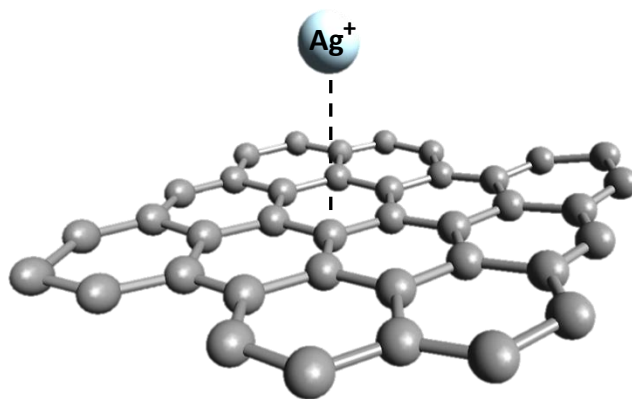
Fig. 1.9 Example of cation-π interactions: the cation is bound to the graphene-type sheet through electrostatic interactions with the ring-central δ^- dipole.

Transition metals such as Au, Pt, Pd and Ag have been successfully deposited on both graphene and carbon nanotubes,[150-153] forming hybrid structures which are commonly used

as sensors. When such metals are deposited by chemical means; reacting the metal precursor directly with a graphene-type material, the shape, size and distribution is dependent on the reaction conditions rather than the graphene-metal interactions.[154]

Au, Pt, Pd and Ag can be considered as soft lewis acids, and are thus likely to react with soft lewis bases. Hence a CMG functionalised with thiolate, phosphine or thiocyanate groups would provide potential ligands for these heavy metals.

1.5   Outline of Thesis

The focus of this thesis is the structure and reactivity of graphene oxide, a material which has progressed from a chemical curiosity to one of global interest over the last 150 years. Understanding its structure, and its interactions with other molecules and metals, is key to developing CMGs with tuned functionality.

A lot of questions remain in the study of GO materials, and thus a large number of different characterisation techniques are required. Chapter 2 gives an overview of the main analytical methods used in this thesis.

Chapter 3 is an in depth study on the structure of GO, providing further characterisation and investigation into the 2011 bwGO-OD model, while chapters 4 and 5 probe its chemical reactivity. Chapter 4 focuses on the surface functionalisation of GO via epoxy opening, describing the synthesis of a novel thiol-functionalised CMG. Chapter 5 exploits this CMG for functionalisation with different organic groups and transition metals. Lastly, concluding remarks are found in chapter 6, and full experimental data in chapter 7.

1.   Srinivasan, C. *Curr. Sci.* **2007,** 92, (10), 1338-1339.
2.   Bobrov, K.; Mayne, A. J.; Dujardin, G. *Nature* **2001,** 413, (6856), 616-619.
3.   Novoselov, K. S.; Geim, A. K.; Morozov, S. V.; Jiang, D.; Zhang, Y.; Dubonos, S. V.; Grigorieva, I. V.; Firsov, A. A. *Science* **2004,** 306, (5696), 666-669.
4.   Huang, X.; Yin, Z.; Wu, S.; Qi, X.; He, Q.; Zhang, Q.; Yan, Q.; Boey, F.; Zhang, H. *Small* **2011,** 7, (14), 1876-1902.
5.   Petroski, H., *The Pencil: A History of Design and Circumstance*. Knopf: New York, 1989.
6.   Geim, A. K.; Novoselov, K. S. *Nat Mater* **2007,** 6, (3), 183-191.
7.   Allen, M. J.; Tung, V. C.; Kaner, R. B. *Chem. Rev.* **2009,** 110, (1), 132-145.
8.   Novoselov, K. S. *Angew. Chem., Int. Ed.* **2011,** 50, (31), 6986-7002.
9.   Palermo, V. *Chem. Commun.* **2013,** 49, (28), 2848-2857.
10.   Meric, I.; Han, M., Y.; Young, A. F.; Ozyilmaz, B.; Kim, P.; Shepard, K. L. *Nat. Nanotechnol.* **2008,** 3, (11), 654-659.
11.   Balandin, A. A.; Ghosh, S.; Bao, W.; Calizo, I.; Teweldebrhan, D.; Miao, F.; Lau, C. N. *Nano Lett.* **2008,** 8, (3), 902-907.
12.   Loh, K. P.; Bao, Q.; Eda, G.; Chhowalla, M. *Nat. Chem.* **2010,** 2, (12), 1015-1024.
13.   Sakhaee-Pour, A. *Solid State Commun.* **2009,** 149, (1–2), 91-95.
14.   Lee, C.; Wei, X.; Kysar, J. W.; Hone, J. *Science* **2008,** 321, (5887), 385-388.
15.   Bunch, J. S.; Verbridge, S. S.; Alden, J. S.; van der Zande, A. M.; Parpia, J. M.; Craighead, H. G.; McEuen, P. L. *Nano Lett.* **2008,** 8, (8), 2458-2462.
16.   Berry, V. *Carbon* **2013,** 62, (0), 1-10.
17.   Goerbig, M. O. *Rev. Mod. Phys.* **2011,** 83, (4), 1193-1243.
18.   Novoselov, K. S.; Geim, A. K.; Morozov, S. V.; Jiang, D.; Katsnelson, M. I.; Grigorieva, I. V.; Dubonos, S. V.; Firsov, A. A. *Nature* **2005,** 438, (7065), 197-200.
19.   Castro Neto, A. H.; Guinea, F.; Peres, N. M. R.; Novoselov, K. S.; Geim, A. K. *Rev. Mod. Phys.* **2009,** 81, (1), 109-162.
20.   Novoselov, K. S.; Jiang, Z.; Zhang, Y.; Morozov, S. V.; Stormer, H. L.; Zeitler, U.; Maan, J. C.; Boebinger, G. S.; Kim, P.; Geim, A. K. *Science* **2007,** 315, (5817), 1379-1379.
21.   Zhang, X.; Rajaraman, B. R. S.; Liu, H.; Ramakrishna, S. *RSC Adv.* **2014,** 4, (55), 28987-29011.
22.   Yao, J.; Sun, Y.; Yang, M.; Duan, Y. *J. Mater. Chem.* **2012,** 22, (29), 14313-14329.
23.   Liu, J.; Cui, L.; Losic, D. *Acta Biomater.* **2013,** 9, (12), 9243-9257.
24.   Goenka, S.; Sant, V.; Sant, S. *J. Control. Release* **2014,** 173, (0), 75-88.
25.   Cohen-Tanugi, D.; Grossman, J. C. *Nano Lett.* **2012,** 12, (7), 3602-3608.
26.   Bohm, S. *Nat. Nano.* **2014,** 9, (10), 741-742.
27.   Siochi, E. J. *Nat. Nano.* **2014,** 9, (10), 745-747.
28.   Ahn, J.-H.; Hong, B. H. *Nat. Nano.* **2014,** 9, (10), 737-738.
29.   Bonaccorso, F.; Lombardo, A.; Hasan, T.; Sun, Z.; Colombo, L.; Ferrari, A. C. *Materials Today* **2012,** 15, (12), 564-589.
30.   Viculis, L. M.; Mack, J. J.; Kaner, R. B. *Science* **2003,** 299, (5611), 1361.
31.   Abdelkader, A. M.; Kinloch, I. A.; Dryfe, R. A. W. *ACS Appl. Mater. Interfaces* **2014,** 6, (3), 1632-1639.
32.   Li, X.; Cai, W.; An, J.; Kim, S.; Nah, J.; Yang, D.; Piner, R.; Velamakanni, A.; Jung, I.; Tutuc, E.; Banerjee, S. K.; Colombo, L.; Ruoff, R. S. *Science* **2009,** 324, (5932), 1312-1314.
33.   Zhang, Y.; Zhang, L.; Zhou, C. *Acc. Chem. Res.* **2013,** 46, (10), 2329-2339.
34.   Berger, C.; Song, Z.; Li, X.; Wu, X.; Brown, N.; Naud, C.; Mayou, D.; Li, T.; Hass, J.; Marchenkov, A. N.; Conrad, E. H.; First, P. N.; de Heer, W. A. *Science* **2006,** 312, (5777), 1191-1196.
35.   Berger, C.; Song, Z.; Li, T.; Li, X.; Ogbazghi, A. Y.; Feng, R.; Dai, Z.; Marchenkov, A. N.; Conrad, E. H.; First, P. N.; de Heer, W. A. *J. Phys. Chem. B* **2004,** 108, (52), 19912-19916.
36.   Coleman, J. N.; Lotya, M.; O'Neill, A.; Bergin, S. D.; King, P. J.; Khan, U.; Young, K.; Gaucher, A.; De, S.; Smith, R. J.; Shvets, I. V.; Arora, S. K.; Stanton, G.; Kim, H.-Y.; Lee, K.; Kim, G. T.; Duesberg, G. S.; Hallam, T.; Boland, J. J.; Wang, J. J.; Donegan, J. F.; Grunlan, J. C.; Moriarty, G.; Shmeliov, A.;

Nicholls, R. J.; Perkins, J. M.; Grieveson, E. M.; Theuwissen, K.; McComb, D. W.; Nellist, P. D.; Nicolosi, V. *Science* **2011,** 331, (6017), 568-571.

37. Hernandez, Y.; Nicolosi, V.; Lotya, M.; Blighe, F. M.; Sun, Z.; De, S.; McGovern, I. T.; Holland, B.; Byrne, M.; Gun'Ko, Y. K.; Boland, J. J.; Niraj, P.; Duesberg, G.; Krishnamurthy, S.; Goodhue, R.; Hutchison, J.; Scardaci, V.; Ferrari, A. C.; Coleman, J. N. *Nat. Nano.* **2008,** 3, (9), 563-568.

38. Jiang, L.; Niu, T.; Lu, X.; Dong, H.; Chen, W.; Liu, Y.; Hu, W.; Zhu, D. *J. Am. Chem. Soc.* **2013,** 135, (24), 9050-9054.

39. Cai, J.; Ruffieux, P.; Jaafar, R.; Bieri, M.; Braun, T.; Blankenburg, S.; Muoth, M.; Seitsonen, A. P.; Saleh, M.; Feng, X.; Mullen, K.; Fasel, R. *Nature* **2010,** 466, (7305), 470-473.

40. Park, S.; Ruoff, R. S. *Nat. Nano.* **2009,** 4, (4), 217-224.

41. Dreyer, D. R.; Park, S.; Bielawski, C. W.; Ruoff, R. S. *Chem. Soc. Rev.* **2010,** 39, (1), 228-240.

42. Li, D.; Kaner, R. B. *Science* **2008,** 320, (5880), 1170-1171.

43. Novoselov, K. S.; Jiang, D.; Schedin, F.; Booth, T. J.; Khotkevich, V. V.; Morozov, S. V.; Geim, A. K. *Proc. Natl. Acad. Sci. U.S.A.* **2005,** 102, (30), 10451-10453.

44. Wintterlin, J.; Bocquet, M. L. *Surf. Sci.* **2009,** 603, (10–12), 1841-1852.

45. Coraux, J.; N'Diaye, A.; Engler, M.; Busse, C.; Wall, D.; Buckanie, N.; Heringdorf, F.; Gastel, R.; Poelsema, B.; Michely, T. *New J. Phys.* **2009,** 11, (2), 023006.

46. Niu, T.; Zhou, M.; Zhang, J.; Feng, Y.; Chen, W. *J. Am. Chem. Soc.* **2013,** 135, (22), 8409-8414.

47. Yan, Z.; Peng, Z.; Tour, J. M. *Acc. Chem. Res.* **2014,** 47, (4), 1327-1337.

48. Heer, W. A. d.; Berger, C.; Ruan, M.; Sprinkle, M.; Li, X.; Hu, Y.; Zhang, B.; Hankinson, J.; Conrad, E. *Proc. Nat. Acad. Sci. USA* **2011,** 108, (41), 16900-16905.

49. Norimatsu, W.; Kusunoki, M. *Physical Chemistry Chemical Physics* **2014,** 16, (8), 3501-3511.

50. Brodie, B. C. *Philos.Trans. R. Soc. London* **1859,** 149, 249-259.

51. Staudenmaier, L. *Ber. Dtsch. Chem. Ges.* **1898,** 31, (2), 1481-1487.

52. Pei, S.; Cheng, H.-M. *Carbon* **2012,** 50, (9), 3210-3228.

53. Rourke, J. P.; Pandey, P. A.; Moore, J. J.; Bates, M.; Kinloch, I. A.; Young, R. J.; Wilson, N. R. *Angew. Chem., Int. Ed.* **2011,** 50, (14), 3173-3177.

54. Shen, X.; Lin, X.; Yousefi, N.; Jia, J.; Kim, J.-K. *Carbon* **2014,** 66, (0), 84-92.

55. Dreyer, D. R.; Todd, A. D.; Bielawski, C. W. *Chem. Soc. Rev.* **2014,** 43, (15), 5288-5301.

56. Hofmann, U.; Holst, R. *Ber. Dtsch. Chem. Ges. B.* **1939,** 72, (4), 754-771.

57. Ruess, G. *Monatsh. Chem.* **1947,** 76, (3-5), 381-417.

58. Scholz, W.; Boehm, H. P. *Z. Anorg. Allg. Chem.* **1969,** 369, (3-6), 327-340.

59. Nakajima, T.; Mabuchi, A.; Hagiwara, R. *Carbon* **1988,** 26, (3), 357-361.

60. He, H.; Riedl, T.; Lerf, A.; Klinowski, J. *J. Phys. Chem.* **1996,** 100, (51), 19954-19958.

61. He, H.; Klinowski, J.; Forster, M.; Lerf, A. *Chem. Phys. Lett.* **1998,** 287, (1–2), 53-56.

62. Kim, S.; Zhou, S.; Hu, Y.; Acik, M.; Chabal, Y. J.; Berger, C.; de Heer, W.; Bongiorno, A.; Riedo, E. *Nat. Mater.* **2012,** 11, (6), 544-549.

63. Stankovich, S.; Dikin, D. A.; Dommett, G. H. B.; Kohlhaas, K. M.; Zimney, E. J.; Stach, E. A.; Piner, R. D.; Nguyen, S. T.; Ruoff, R. S. *Nature* **2006,** 442, (7100), 282-286.

64. Hummers, W. S.; Offeman, R. E. *J. Am. Chem. Soc.* **1958,** 80, (6), 1339-1339.

65. Zhong, Y. L.; Tian, Z.; Simon, G. P.; Li, D. *Materials Today* **2015,** 18, (2), 73-78.

66. Marcano, D. C.; Kosynkin, D. V.; Berlin, J. M.; Sinitskii, A.; Sun, Z.; Slesarev, A.; Alemany, L. B.; Lu, W.; Tour, J. M. *ACS Nano* **2010,** 4, (8), 4806-4814.

67. Dimiev, A.; Kosynkin, D. V.; Alemany, L. B.; Chaguine, P.; Tour, J. M. *J. Am. Chem. Soc.* **2012,** 134, (5), 2815-2822.

68. Shen, Y.; Yang, S.; Zhou, P.; Sun, Q.; Wang, P.; Wan, L.; Li, J.; Chen, L.; Wang, X.; Ding, S.; Zhang, D. W. *Carbon* **2013,** 62, (0), 157-164.

69. Salzmann, C. G.; Llewellyn, S. A.; Tobias, G.; Ward, M. A. H.; Huh, Y.; Green, M. L. H. *Adv. Mater.* **2007,** 19, (6), 883-887.

70. Dimiev, A. M.; Polson, T. A. *Carbon* **2015,** 93, (0), 544-554.

71. Guo, Z.; Wang, S.; Wang, G.; Niu, Z.; Yang, J.; Wu, W. *Carbon* **2014,** 76, (0), 203-211.

72.   Faria, A. F.; Martinez, D. S. T.; Moraes, A. C. M.; Maia da Costa, M. E. H.; Barros, E. B.; Souza Filho, A. G.; Paula, A. J.; Alves, O. L. *Chem. Mater.* **2012,** 24, (21), 4080-4087.

73.   Taniguchi, T.; Kurihara, S.; Tateishi, H.; Hatakeyama, K.; Koinuma, M.; Yokoi, H.; Hara, M.; Ishikawa, H.; Matsumoto, Y. *Carbon* **2015,** 84, (0), 560-566.

74.   Bonanni, A.; Ambrosi, A.; Chua, C. K.; Pumera, M. *ACS Nano* **2014,** 8, (5), 4197-4204.

75.   Rodriguez-Pastor, I.; Ramos-Fernandez, G.; Varela-Rizo, H.; Terrones, M.; Martin-Gullon, I. *Carbon* **2015,** 84, (0), 299-309.

76.   Borini, S.; White, R.; Wei, D.; Astley, M.; Haque, S.; Spigone, E.; Harris, N.; Kivioja, J.; Ryhänen, T. *ACS Nano* **2013,** 7, (12), 11166-11173.

77.   Basu, S.; Bhattacharyya, P. *Sensor. Actuat. B: Chem.* **2012,** 173, (0), 1-21.

78.   Yang, S.; Feng, X.; Ivanovici, S.; Müllen, K. *Angew. Chem., Int. Ed.* **2010,** 49, (45), 8408-8411.

79.   Zhu, Y.; Murali, S.; Stoller, M. D.; Velamakanni, A.; Piner, R. D.; Ruoff, R. S. *Carbon* **2010,** 48, (7), 2118-2122.

80.   Becerril, H. A.; Mao, J.; Liu, Z.; Stoltenberg, R. M.; Bao, Z.; Chen, Y. *ACS Nano* **2008,** 2, (3), 463-470.

81.   Matyba, P.; Yamaguchi, H.; Eda, G.; Chhowalla, M.; Edman, L.; Robinson, N. D. *ACS Nano* **2010,** 4, (2), 637-642.

82.   Chung, C.; Kim, Y.-K.; Shin, D.; Ryoo, S.-R.; Hong, B. H.; Min, D.-H. *Acc. Chem. Res.* **2013,** 46, (10), 2211-2224.

83.   Lu, Y.; Jiang, Y.; Wei, W.; Wu, H.; Liu, M.; Niu, L.; Chen, W. *J. Mater. Chem.* **2012,** 22, (7), 2929-2934.

84.   Zhu, S.; Tang, S.; Zhang, J.; Yang, B. *Chem. Commun.* **2012,** 48, (38), 4527-4539.

85.   Zhang, M.; Ye, B.-C. *Chem. Commun.* **2012,** 48, (30), 3647-3649.

86.   Sun, X.; Liu, Z.; Welsher, K.; Robinson, J.; Goodwin, A.; Zaric, S.; Dai, H. *Nano Res.* **2008,** 1, (3), 203-212.

87.   Zhang, X.-Y.; Li, H.-P.; Cui, X.-L.; Lin, Y. *J. Mater. Chem.* **2010,** 20, (14), 2801-2806.

88.   Shen, J.; Zhu, Y.; Yang, X.; Li, C. *Chem. Commun.* **2012,** 48, (31), 3686-3699.

89.   Sheats, J. R.; Antoniadis, H.; Hueschen, M.; Leonard, W.; Miller, J.; Moon, R.; Roitman, D.; Stocking, A. *Science* **1996,** 273, (5277), 884-888.

90.   Luo, Z.; Vora, P. M.; Mele, E. J.; Johnson, A. T. C.; Kikkawa, J. M. *Appl. Phys. Lett.* **2009,** 94, (11), 111909-3.

91.   Sarkar, S.; Niyogi, S.; Bekyarova, E.; Haddon, R. C. *Chem. Sci.* **2011,** 2, (7), 1326-1333.

92.   Georgakilas, V.; Otyepka, M.; Bourlinos, A. B.; Chandra, V.; Kim, N.; Kemp, K. C.; Hobza, P.; Zboril, R.; Kim, K. S. *Chem. Rev.* **2012,** 112, (11), 6156-6214.

93.   Hertel, S.; Waldmann, D.; Jobst, J.; Albert, A.; Albrecht, M.; Reshanov, S.; Schöner, A.; Krieger, M.; Weber, H. B. *Nat. Commun.* **2012,** 3, 957.

94.   Yu, D.; Dai, L. *J. Phys. Chem. Lett.* **2009,** 1, (2), 467-470.

95.   Fan, Z.; Yan, J.; Zhi, L.; Zhang, Q.; Wei, T.; Feng, J.; Zhang, M.; Qian, W.; Wei, F. *Adv. Mater.* **2010,** 22, (33), 3723-3728.

96.   Gunlycke, D.; Areshkin, D. A.; Li, J.; Mintmire, J. W.; White, C. T. *Nano. Lett.* **2007,** 7, (12), 3608-3611.

97.   He, C. L.; Zhuge, F.; Zhou, X. F.; Li, M.; Zhou, G. C.; Liu, Y. W.; Wang, J. Z.; Chen, B.; Su, W. J.; Liu, Z. P.; Wu, Y. H.; Cui, P.; Li, R.-W. *Appl. Phys. Lett.* **2009,** 95, (23), 232101-3.

98.   Eda, G.; Lin, Y.-Y.; Miller, S.; Chen, C.-W.; Su, W.-F.; Chhowalla, M. *Appl. Phys. Lett.* **2008,** 92, (23), 233305-3.

99.   Peng, C.; Hu, W.; Zhou, Y.; Fan, C.; Huang, Q. *Small* **2010,** 6, (15), 1686-1692.

100.   Schedin, F.; Geim, A. K.; Morozov, S. V.; Hill, E. W.; Blake, P.; Katsnelson, M. I.; Novoselov, K. S. *Nat. Mater.* **2007,** 6, (9), 652-655.

101.   Grabowski, S. J. *J. Phys. Chem. A* **2007,** 111, (51), 13537-13543.

102.   Gadipelli, S.; Guo, Z. X. *Prog. Mater. Sci.* **2015,** 69, (0), 1-60.

103.   Mishra, A. K.; Ramaprabhu, S. *AIP Adv.* **2011,** 1, (3), 032152.

104.   Wood, B. C.; Bhide, S. Y.; Dutta, D.; Kandagal, V. S.; Pathak, A. D.; Punnathanam, S. N.; Ayappa, K. G.; Narasimhan, S. *J. Chem. Phys.* **2012,** 137, 054702.
105.   Björk, J.; Hanke, F.; Palma, C.-A.; Samori, P.; Cecchini, M.; Persson, M. *J. Phys. Chem. Lett.* **2010,** 1, (23), 3407-3412.
106.   Hsun Su, Y.; Kai Wu, Y.; Tu, S. L.; Chang, S.-J. *Appl. Phys. Lett.* **2011,** 99, (16), 163102.
107.   Kim, D.; Hu, S.; Tarakeshwar, P.; Kim, K. S.; Lisy, J. M. *J. Phys. Chem. A* **2003,** 107, (8), 1228-1238.
108.   Shen, J.; Shi, M.; Yan, B.; Ma, H.; Li, N.; Hu, Y.; Ye, M. *Colloids Surf., B* **2010,** 81, (2), 434-438.
109.   Shen, J.; Yan, B.; Shi, M.; Ma, H.; Li, N.; Ye, M. *J. Colloid Interf. Sci.* **2011,** 356, (2), 543-549.
110.   Xu, Y.; Liu, Z.; Zhang, X.; Wang, Y.; Tian, J.; Huang, Y.; Ma, Y.; Zhang, X.; Chen, Y. *Adv. Mater.* **2009,** 21, (12), 1275-1279.
111.   Jia, Z.; Wang, Y. *J. Mater. Chem. A* **2015,** 3, (8), 4405-4412.
112.   Yu, D.; Yang, Y.; Durstock, M.; Baek, J.-B.; Dai, L. *ACS Nano* **2010,** 4, (10), 5633-5640.
113.   Pham, T. A.; Kumar, N. A.; Jeong, Y. T. *Synth. Met.* **2010,** 160, (17–18), 2028-2036.
114.   Stankovich, S.; Piner, R. D.; Nguyen, S. T.; Ruoff, R. S. *Carbon* **2006,** 44, (15), 3342-3347.
115.   Saha, U.; Jaiswal, R.; Singh, J.; Goswami, T. *J. Nanopart. Res.* **2014,** 16, (5), 1-21.
116.   Zhao, H.; Wu, L.; Zhou, Z.; Zhang, L.; Chen, H. *Phys. Chem. Chem. Phys.* **2013,** 15, (23), 9084-9092.
117.   Compton, O. C.; Dikin, D. A.; Putz, K. W.; Brinson, L. C.; Nguyen, S. T. *Adv. Mater.* **2010,** 22, (8), 892-896.
118.   Chua, C. K.; Pumera, M. *ACS Nano* **2015**.
119.   Lü, P.; Feng, Y.; Zhang, X.; Li, Y.; Feng, W. *Sci. China Technol. Sci.* **2010,** 53, (9), 2311-2319.
120.   Shao, Y.; Wang, J.; Engelhard, M.; Wang, C.; Lin, Y. *J. Mater. Chem.* **2010,** 20, (4), 743-748.
121.   Larciprete, R.; Fabris, S.; Sun, T.; Lacovig, P.; Baraldi, A.; Lizzit, S. *J. Am. Chem. Soc.* **2011,** 133, (43), 17315-17321.
122.   Cui, P.; Lee, J.; Hwang, E.; Lee, H. *Chem. Commun.* **2011,** 47, (45), 12370-12372.
123.   Qi, X.; Pu, K.-Y.; Li, H.; Zhou, X.; Wu, S.; Fan, Q.-L.; Liu, B.; Boey, F.; Huang, W.; Zhang, H. *Angew. Chem. Int. Ed.* **2010,** 49, (49), 9426-9429.
124.   Shin, H.-J.; Kim, K. K.; Benayad, A.; Yoon, S.-M.; Park, H. K.; Jung, I.-S.; Jin, M. H.; Jeong, H.-K.; Kim, J. M.; Choi, J.-Y.; Lee, Y. H. *Adv. Funct. Mater.* **2009,** 19, (12), 1987-1992.
125.   Pei, S.; Zhao, J.; Du, J.; Ren, W.; Cheng, H.-M. *Carbon* **2010,** 48, (15), 4466-4474.
126.   Gao, X.; Jang, J.; Nagase, S. *J. Phys. Chem. C* **2009,** 114, (2), 832-842.
127.   Park, S.; Hu, Y.; Hwang, J. O.; Lee, E.-S.; Casabianca, L. B.; Cai, W.; Potts, J. R.; Ha, H.-W.; Chen, S.; Oh, J.; Kim, S. O.; Kim, Y.-H.; Ishii, Y.; Ruoff, R. S. *Nat Commun* **2012,** 3, 638.
128.   Peng-Gang, R.; Ding-Xiang, Y.; Xu, J.; Tao, C.; Zhong-Ming, L. *Nanotechnology* **2011,** 22, (5), 055705.
129.   Wang, R.; Wang, Y.; Xu, C.; Sun, J.; Gao, L. *RSC Advances* **2013,** 3, (4), 1194-1200.
130.   Gómez-Navarro, C.; Meyer, J. C.; Sundaram, R. S.; Chuvilin, A.; Kurasch, S.; Burghard, M.; Kern, K.; Kaiser, U. *Nano. Lett.* **2010,** 10, (4), 1144-1148.
131.   Wu, J.; Becerril, H. A.; Bao, Z.; Liu, Z.; Chen, Y.; Peumans, P. *Appl. Phys. Lett.* **2008,** 92, (26), 263302-263303.
132.   Wilson, N. R.; Pandey, P. A.; Beanland, R.; Rourke, J. P.; Lupo, U.; Rowlands, G.; Römer, R. A. *New J. Phys.* **2010,** 12, (12), 125010.
133.   Das, T. K.; Prusty, S. *Polym. Plast. Technol. Eng.* **2013,** 52, (4), 319-331.
134.   Kuilla, T.; Bhadra, S.; Yao, D.; Kim, N. H.; Bose, S.; Lee, J. H. *Prog. Polym. Sci.* **2010,** 35, (11), 1350-1375.
135.   Du, J.; Cheng, H.-M. *Macromol. Chem. Phys.* **2012,** 213, (10-11), 1060-1077.
136.   Yoo, B. M.; Shin, H. J.; Yoon, H. W.; Park, H. B. *J. Appl. Polym. Sci.* **2014,** 131, (1), n/a-n/a.
137.   McGrail, B. T.; Rodier, B. J.; Pentzer, E. *Chem. Mater.* **2014,** 26, (19), 5806-5811.
138.   Ye, Y.-S.; Chen, Y.-N.; Wang, J.-S.; Rick, J.; Huang, Y.-J.; Chang, F.-C.; Hwang, B.-J. *Chem. Mater.* **2012,** 24, (15), 2987-2997.

139.   Zhao, X.; Xu, Z.; Zheng, B.; Gao, C. *Sci. Rep.* **2013,** 3.

140.   Potts, J. R.; Dreyer, D. R.; Bielawski, C. W.; Ruoff, R. S. *Polymer* **2011,** 52, (1), 5-25.

141.   Naveen, M. H.; Noh, H.-B.; Hossain, M. S. A.; Kim, J. H.; Shim, Y.-B. *J. Mater. Chem. A* **2015,** 3, (10), 5426-5433.

142.   Ding, M.; Tang, Y.; Star, A. *J. Phys. Chem. Lett.* **2013,** 4, (1), 147-160.

143.   Chidembo, A.; Aboutalebi, S. H.; Konstantinov, K.; Salari, M.; Winton, B.; Yamini, S. A.; Nevirkovets, I. P.; Liu, H. K. *Energy Environ. Sci.* **2012,** 5, (1), 5236-5240.

144.   Zhou, D.; Cui, Y.; Han, B. *Chin. Sci. Bull.* **2012,** 57, (23), 2983-2994.

145.   Sreeprasad, T. S.; Maliyekkal, S. M.; Lisha, K. P.; Pradeep, T. *J. Hazard. Mater.* **2011,** 186, (1), 921-931.

146.   Lake, J. R.; Cheng, A.; Selverston, S.; Tanaka, Z.; Koehne, J.; Meyyappan, M.; Chen, B. *J. Vac. Sci. Technol. B* **2012,** 30, (3), 03D118.

147.   Sun, G.; Liu, J.; Zhang, X.; Wang, X.; Li, H.; Yu, Y.; Huang, W.; Zhang, H.; Chen, P. *Angew. Chem., Int. Ed.* **2014,** 53, (46), 12576-12580.

148.   Das, M. R.; Sarma, R. K.; Saikia, R.; Kale, V. S.; Shelke, M. V.; Sengupta, P. *Colloid. Surf. B: Biointerf.* **2011,** 83, (1), 16-22.

149.   Haldorai, Y.; Kim, B.-K.; Jo, Y.-L.; Shim, J.-J. *Mater. Chem. Phys.* **2014,** 143, (3), 1452-1461.

150.   Du, N.; Zhang, H.; Ma, X.; Yang, D. *Chem. Commun.* **2008**, (46), 6182-6184.

151.   Cui, S.; Mao, S.; Wen, Z.; Chang, J.; Zhang, Y.; Chen, J. *Analyst* **2013,** 138, (10), 2877-2882.

152.   Xu, C.; Wang, X.; Zhu, J. *J. Phys. Chem. C* **2008,** 112, (50), 19841-19845.

153.   Yoo, E.; Okata, T.; Akita, T.; Kohyama, M.; Nakamura, J.; Honma, I. *Nano Lett.* **2009,** 9, (6), 2255-2259.

154.   Pandey, P. A.; Bell, G. R.; Rourke, J. P.; Sanchez, A. M.; Elkin, M. D.; Hickey, B. J.; Wilson, N. R. *Small* **2011,** 7, (22), 3202-10.

Chapter 2

Experimental Techniques
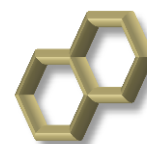
The results discussed in this thesis revolve around a variety of different microscopic and spectroscopic studies. This chapter serves to discuss the advantages and limitations of each of these techniques.

2.1 Topography Studies

2.1.1 Atomic Force Microscopy (AFM)

AFM is a useful technique for graphene-based materials as it provides a three-dimensional surface profile: the lateral sheet size, sheet thickness and layer spacing of the sample can be measured.[1, 2] The technique was developed in the 1980s by Binnig, Quate and Gerber,[3] using the basic principles of a scanning tunnelling microscope (STM) to provide atomic scale investigations of insulating materials with little or no sample preparation.[4]

AFM uses a flexible cantilever with a sharp tip (shown in figure 2.1) to interact with the sample surface. The tip itself is typically etched from silicon or silicon nitride, and at its apex has a radius of curvature of 5-15 nm.[5] This cantilever replaces the tunnelling probe of STM, and is used to detect short and long range tip-sample forces.[6]
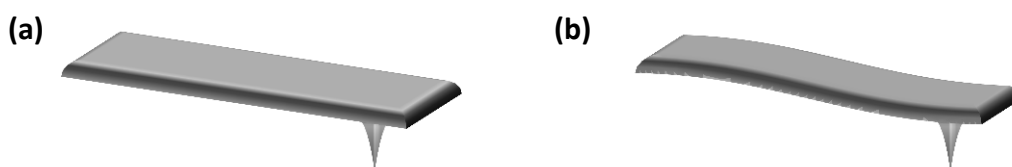
Fig. 2.1 AFM cantilever and sharp probe at **(a)** equilibrium position, and **(b)** when deflected by tip-sample forces.

Under ambient conditions, AFM can detect both attractive and repulsive interactions between the tip and the sample which can be plotted as a function of tip-sample separation according to Hooke's law[7]:

$$F = -kx \tag{2.1}$$

where k is the spring constant of the cantilever and x is the displacement of the cantilever from its equilibrium position. The spring constant of a rectangular cantilever is dependent on its length (l), width (w), thickness (t) and the stiffness of the material (E),[8] it can be estimated using:

$$k = \frac{Ewt^3}{4l^3} \tag{2.2}$$

A typical AFM schematic is shown in figure 2.2. The laser is focused on the cantilever, above the tip, and is reflected onto a photodiode. As the tip moves across the sample surface any displacement from its equilibrium position is detected via a change in the optical path of the laser via the four quadrant photodetector.
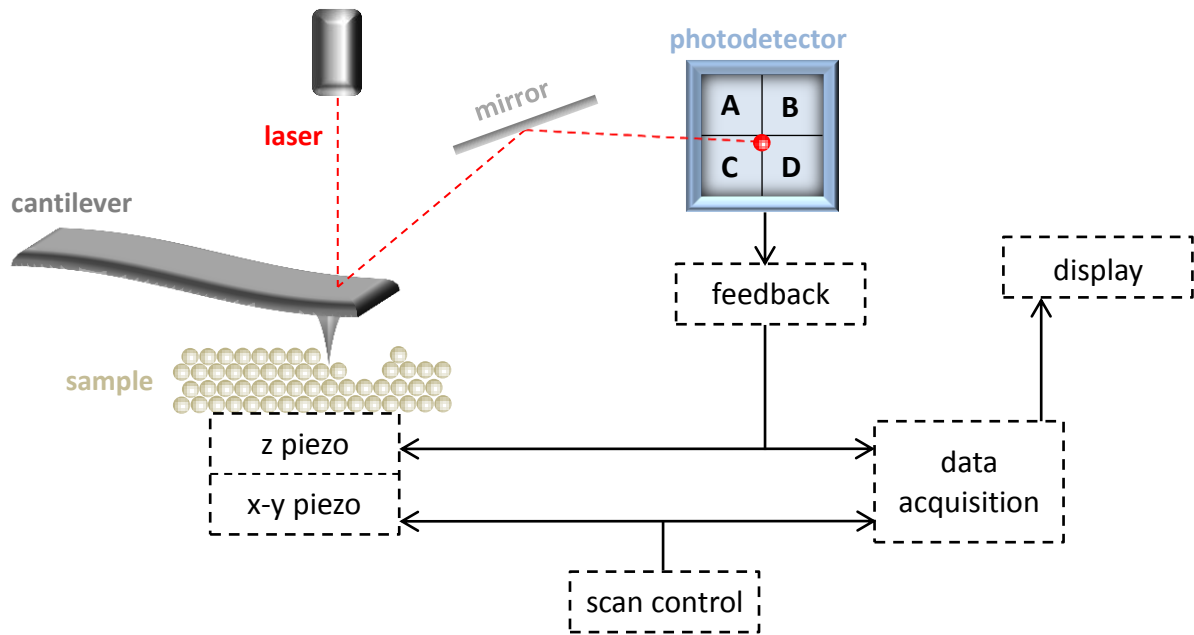
Fig. 2.2 Schematic showing the general components of an AFM system.

Frictional forces between the tip and the sample can cause the cantilever to twist, resulting in a lateral displacement of the laser beam from the central point of the photodetector. Meanwhile attractive and repulsive tip-sample forces cause the cantilever to bend, resulting

in a vertical displacement. These changes in the optical path are monitored and used to adjust the tip-sample separation by means of a feedback loop.[6]

When the tip is in close contact with the sample (within a few tens of nanometres) repulsive interactions are at play due to the overlap of atomic orbitals. Further away from the surface, attractive Van der Waals forces operate at short range, alongside long range (up to 100 nm) electrostatic and magnetic forces.[4, 6] This is summarised by the force curve shown in figure 2.3.
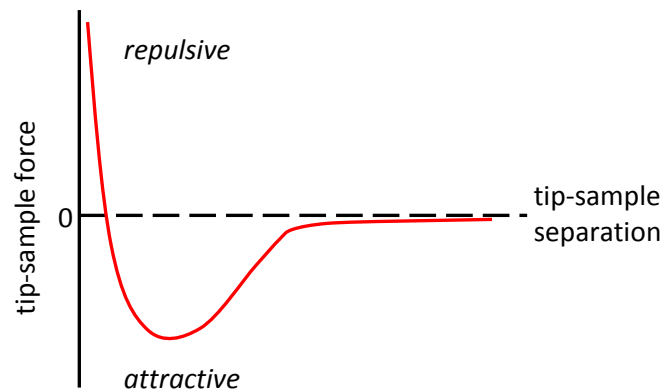
Fig. 2.3 Force curve illustrating the sample-tip interactions in AFM.

There are two main methods of AFM operation: contact mode and tapping mode.[2] In contact mode AFM the tip is in direct contact with the sample as it is scanned across the surface. The cantilever bends on contact with the surface and this level of deflection is maintained via a constant feedback loop: the sample is moved up and down to ensure the force on the cantilever, and thus the optical path is constant. The major drawback of contact mode AFM is that the large contact and lateral forces can cause damage to both the tip and the sample.[2]

To avoid such damage, the alternative tapping (or dynamic) mode was developed.[9] In tapping mode AFM, the cantilever is raised above the sample and oscillates freely at a known amplitude. The sample is then raised up until it comes into contact with the tip, and the oscillation of the cantilever is damped resulting in a decreased amplitude of oscillation (figure 2.4).
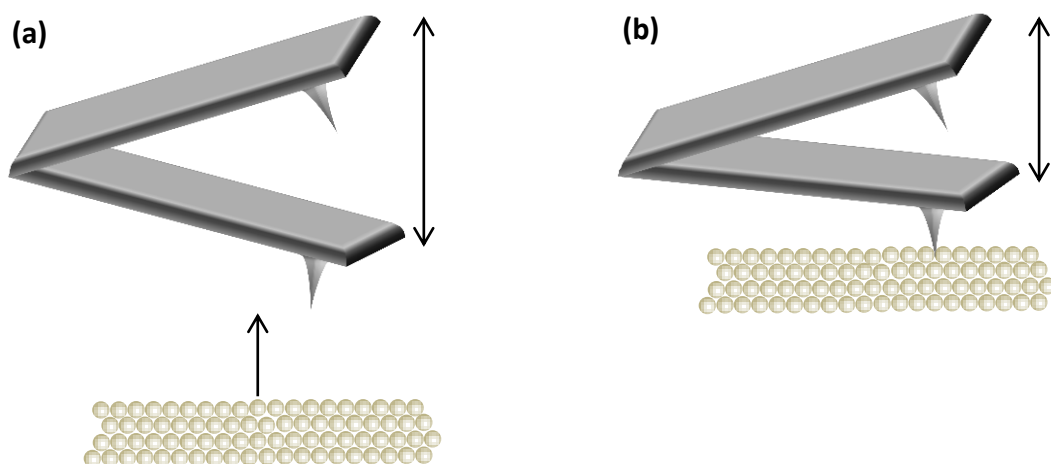
Fig. 2.4 Schematic showing **(a)** free and **(b)** damped oscillations of the AFM cantilever.

The photodetector monitors the oscillation of the cantilever in tapping mode, using the feedback loop to maintain a constant amplitude of oscillation, which will be less than the amplitude of free oscillation. Since the sample is only 'tapped' by the sharp probe the contact and lateral forces are minimised.[9] This tapping mode was used for all of the AFM studies detailed in this thesis.

AFM has many advantages over other microscopy techniques, including the ability to record data under ambient conditions and ease of sample preparation. However, it is limited by its lateral resolution, scanning speed[10] and environmental factors such as humidity.[11]

The lateral resolution of AFM (typically on the nm scale) depends on the sharpness of the tip: as it blunts with use, artefacts may be introduced and the results become less reliable.[6] Figure 2.5 shows examples where the rounded end of a cantilever tip can result in surface profiles which are not wholly representative of the sample.
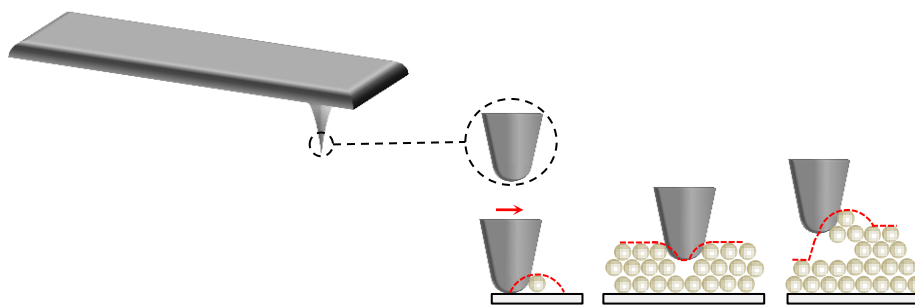
Fig. 2.5 AFM schematic showing how the scanning accuracy of AFM is dependent on the tip radius of curvature.

In the context of GO samples, AFM can determine the sheet size and whether or not the material is fully exfoliated to monolayers. The effects on the sheet size and layer spacing as a result of different processing conditions can also be probed. For example, chemically reducing GO should decrease the sheet perturbations, detectable by a decreased layer spacing.

GO is also known to be highly hygrophilic. Without UHV conditions GO samples are thus expected to be coated with surface water, causing a meniscus to form between the tip and the sample. This meniscus provides a strong adhesive force, making high resolution imaging of a GO surface difficult.[12]

For AFM studies, samples were prepared by spin coating onto silicon oxide substrates, which were cleaned in an oxygen plasma prior to deposition (100 W, 2 minutes, Emitech K1050X). AFM characterisation thus relies on the dispersibility of the GO material: a stable suspension of approximately 1 mg ml^{-1} is required, with H_2O, DMF or DMSO solvents being typically used. Figure 2.6 shows an example AFM topography image for a graphene-based material. Individual sheets, which vary from 1-4 μm in lateral size, can be seen. They lie flat on the silicon oxide substrate, with some overlapping sheets.
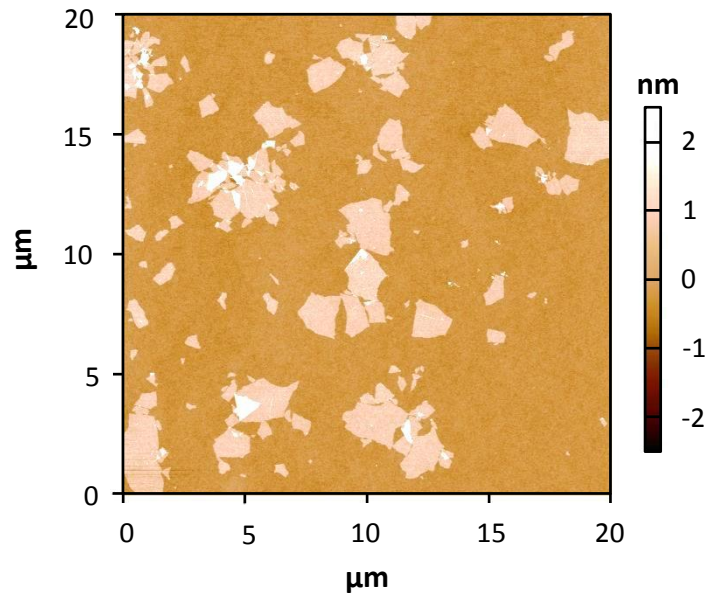
Fig. 2.6 Representative AFM topography image of a graphene-type material.

2.1.2 Transmission Electron Microscopy (TEM)

The first functioning TEM was built in 1931 by Knoll and Ruska,[13] which led to a flurry of interest in electron microscope design by many other researchers. In principle, TEM is very similar to an optical microscope, using a series of lenses to magnify a real image. However, instead of a beam of light, an electron microscope uses a high energy beam of electrons under UHV.[14] Due to the small de Broglie wavelength of electrons, much higher resolutions (sub-nanometer) can be achieved. Figure 2.7 shows the basic structure of a TEM.

Electron gun

Electron beam

Condenser lenses

Sample

Objective lens

Objective aperture

Intermediate lenses

Projector lens

Fluorescent screen
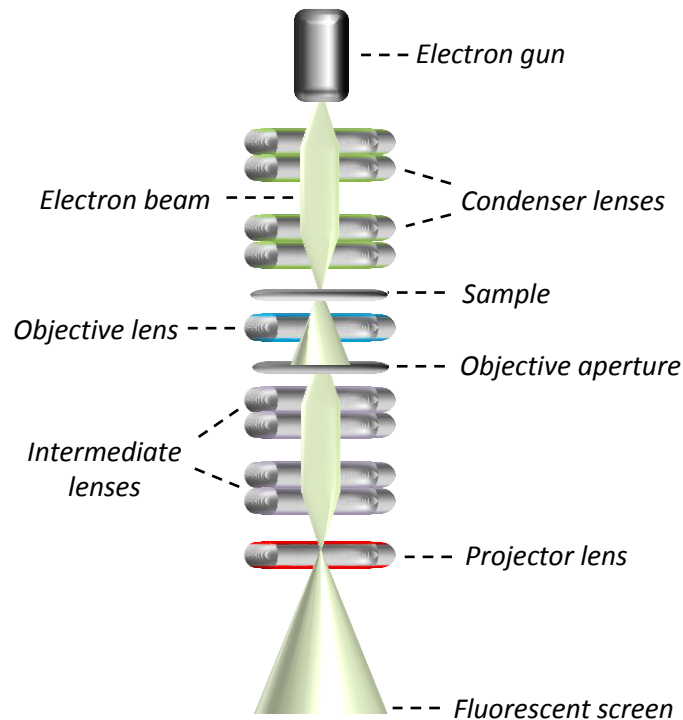
Fig. 2.7 TEM schematic: a high voltage electron beam is used to project a sample image onto a fluorescent screen.

The electron gun typically uses a tungsten filament as the electron source. When connected to a high voltage (100–300 kV), the electrons are emitted and accelerated using an anode. A series of electromagnetic lenses is then used to manipulate the electrons.[15] The condenser lenses are firstly used to form a narrow, coherent beam of electrons which is converged and transmitted through a thin sample specimen. An image is formed via the interaction of the electrons with the sample: some electrons will be absorbed by the sample, and those that are able to pass through may be scattered by the electrostatic potential of the atoms in the sample. The scattered beam is refocused using the objective lens to form an intermediate image. The remaining intermediate and projector lenses are responsible for magnifying the image onto a fluorescent screen, which emits light where struck.

Alternatively, TEM can be used to study diffraction patterns: at the focal plane of the objective lens, the Bragg scattered electrons form a diffraction pattern. If the intermediate lens is focused on the focal plane, instead of the intermediate sample image, this diffraction pattern will be magnified and shown on the fluorescent screen by the projector lens. To obtain a selected area electron diffraction pattern (SAED), an aperture can be placed in the

plane of the first intermediate image. These electron beam pathways for image and diffraction pattern projection are summarised in figure 2.8.
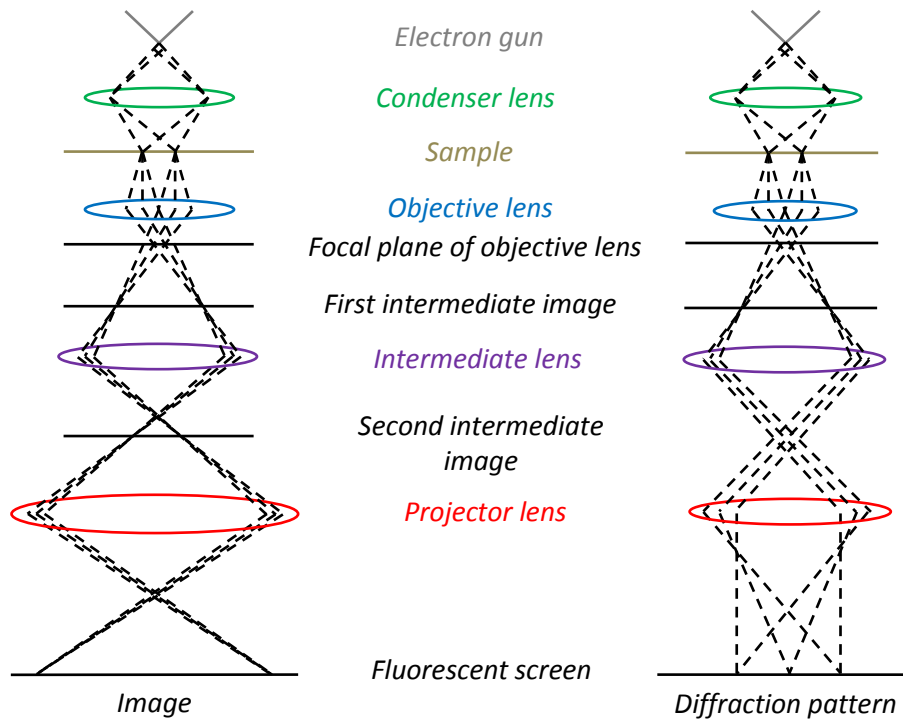
Fig. 2.8 The electron beam pathways for imaging and diffraction TEM.

When obtaining a 2D projection of a sample, an objective aperture may be placed at the focal plane of the objective lens, allowing only the non-diffracted electron beam to pass through. Hence only the direct electron beam is used to create the sample projection, this is known as a bright field image. The contrast of a bright field image shows light areas where the electrons were able to pass unobstructed through the sample, and dark areas where the electrons have been absorbed or scattered. Note that heavy elements will scatter electrons more strongly, and so will appear as a darker contrast compared to lighter elements. If the aperture is not centralised on the optical axis it will allow only a diffracted electron beam to pass through: the resultant projection in this case is known as a dark field image.

TEM analysis is an important tool for graphene-based investigations. A SAED pattern can confirm whether or not a sample is graphene-based, and furthermore whether or not it is fully exfoliated to monolayers. For a monolayer graphene-type material, a hexagonal diffraction pattern is expected, with a single set of hk = 10 type spots and a roughly equally intense set of outlying hk = 11 type spots, as indexed using Miller-Bravais indices (figure

2.9). If the hk = 11 type spots are more intense than the hk = 10 type spots, then the sample has multiple layers of AB stacked graphene (i.e it is graphite-like).[16]
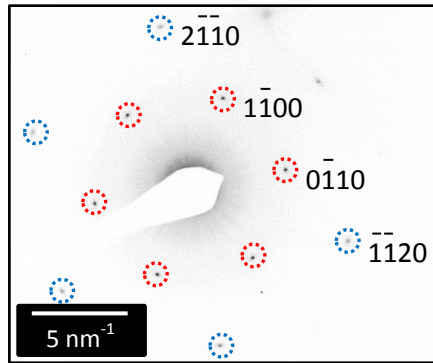
Fig. 2.9 Selected area electron diffraction (SAED) pattern of graphene oxide with the hk = 10 type spots circled in red and the hk = 11 type spots circled in blue.

Graphene sheets are almost electron transparent, and so hardly any contrast can be seen in their bright field TEM images. Although such studies can still give an idea of the overall structural integrity, as any substantial holes or sheet aggregation will be apparent. High resolution TEM (HR-TEM) however, can produce images with atomic resolution: for graphene-based materials, the hexagonal sheet structure can be identified, as can the presence of defect sites (figure 2.10). Unfortunately though, the high voltage electron beam is damaging to the samples – holes are seen to initiate and grow in a matter of seconds after the start of exposure, even at an 80 kV accelerating voltage.
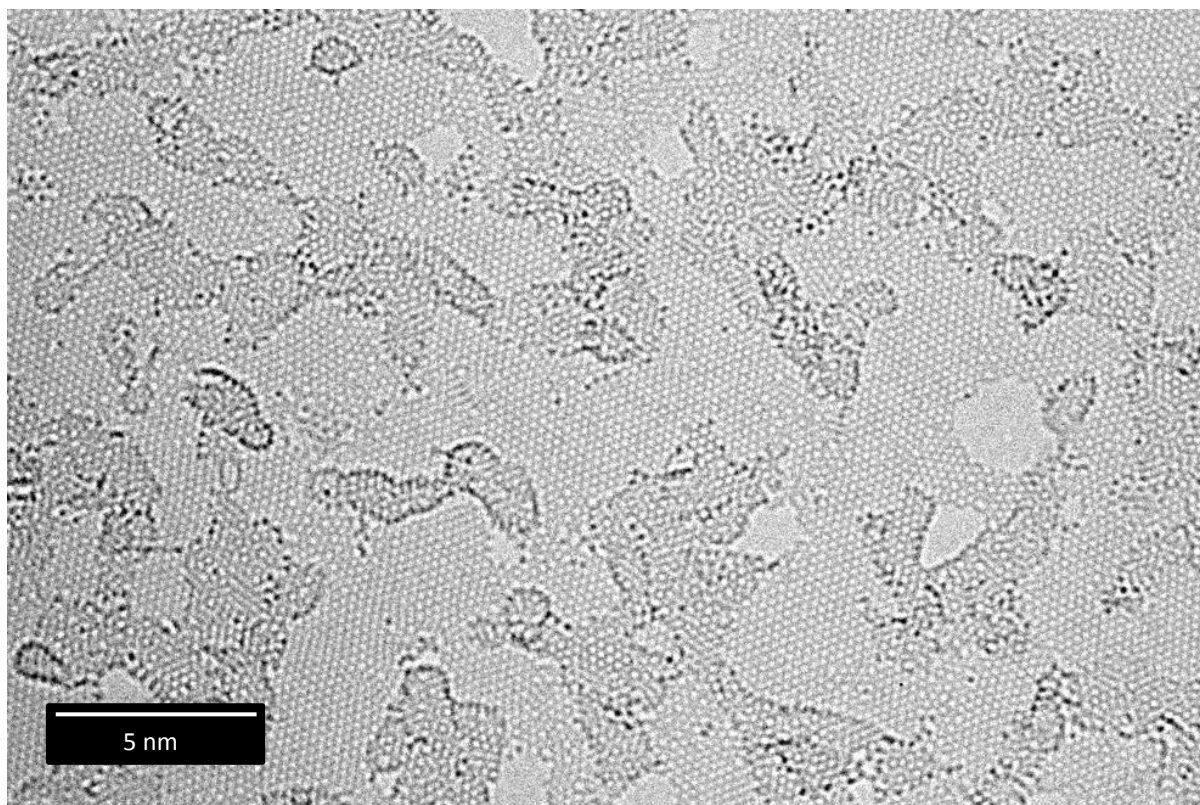
Fig. 2.10 Example HR-TEM image of a GO-type material. Hexagonal graphene-like regions can be seen, alongside holes in the lattice, amorphous regions, and dark contrast atoms which are likely to be metal impurities.

TEM samples must be thin enough to allow a sufficient number of electrons to pass through – the samples studied in this thesis were prepared by drop casting dispersions onto a lacey carbon support grid. The grids were left to dry in air and were then used with no further processing. Thus, as with AFM, TEM relies on being able to prepare stable dispersions (~0.2 mg ml^{-1}) of the graphene-like samples.

2.1.3 Scanning Electron Microscopy (SEM)

SEM is a second form of electron microscopy. Like TEM, a tight beam of electrons is formed and is fired at the sample surface. Unlike TEM, the beam is focused to a small point that can be scanned across the sample. When the electrons in the beam hit the sample they can scatter inelastically, ejecting electrons from atoms within the sample. These secondary electrons have a low energy and so have a short inelastic mean free path, which means that only those near the sample surface can escape. Once detected, their speed and scattering

angle gives information about the topography of the sample.[17] Some electrons from the electron beam will be elastically scattered, their scattering angle gives information on the topography and composition of the sample: a greater degree of scattering implies that heavy elements are present. These electrons are detected as they bounce off the sample and are known as backscattered electrons (BSE). This process is illustrated in figure 2.11.
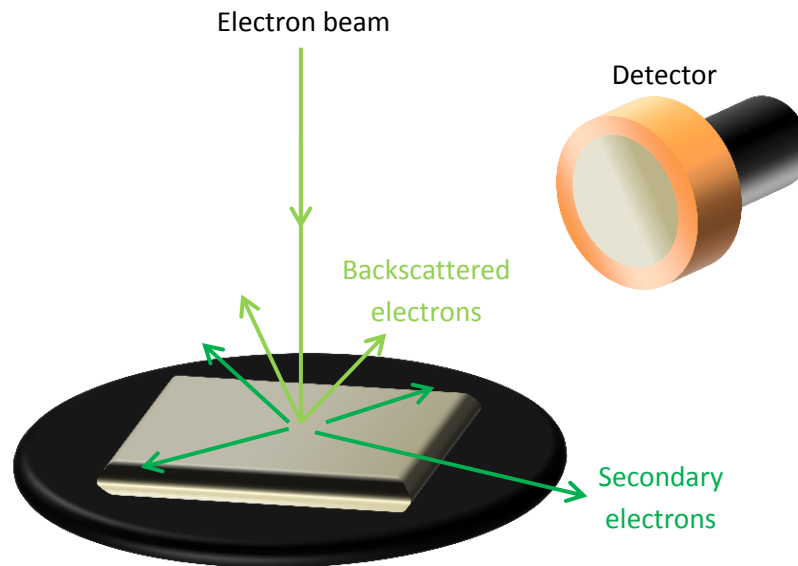
Fig. 2.11 SEM schematic showing the incident electrons hitting the sample surface, and a detector for the secondary electrons.

Only electrons close to the sample surface will be emitted as secondary electrons in SEM since the mean free path of a secondary electron is in the order of 1 nm, dependent on the imaging conditions.[18] This shallow penetration depth makes SEM ideal for studying sample topography, with a typical resolution of 5 nm. In comparison, BSE can escape from a sample depth of several tens of nm, depending on the atomic nuclei present. The spatial resolution from BSE is thus poorer than from secondary electrons, but usefully provides a contrast image with brighter regions corresponding to atoms with larger nuclei. The actual interaction volume of the incident electrons extends further than the both secondary and backscattered electrons, with X-ray emissions (see section 2.2.1) detected from a sample depth of up to several μm (figure 2.12).[19]
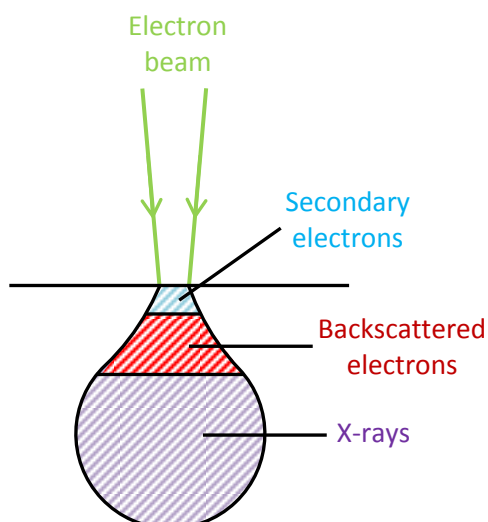
Fig. 2.12 Schematic showing the interaction volume of the incident electrons in SEM. The secondary electron emission depth is typically 1 nm. BSEs are emitted from the top 10 nm of sample, and X-rays from several μm.

The interaction volume depends on the voltage of the incident electrons and the sample: a higher accelerating voltage will provide a greater depth of penetration, as will samples with lower atomic number elements.

SEM provides a quick and easy route to analysis with good resolution, fast scan rates, and easy sample preparation.[19] The technique is also much less damaging to the sample than TEM. In terms of GO, SEM provides a useful imaging alternative to AFM and TEM as it enables the study of solid-state samples which are deposited onto a sticky carbon tab. Figure 2.13 shows a low resolution SEM image of a powdered GO-based material.
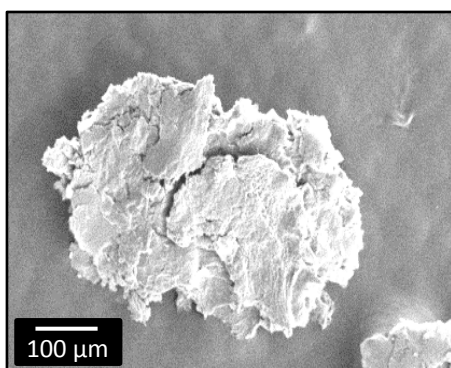
Fig. 2.13 Example secondary electron SEM image of a GO-based material on a carbon tab.

2.2   Composition studies

2.2.1 Energy Dispersive X-ray Spectroscopy (EDX)

EDX has become a useful tool for measuring the elemental composition of solid-state GO based materials. Generally an EDX system is attached to an SEM: the high energy beam of electrons is generated and fired at the sample in the same manner as SEM. However, for EDX, instead of looking to the secondary and backscattered electrons, interest lies with the emitted X-rays.

In EDX analysis, high energy incident electrons are used to eject core electrons, leaving behind an electron vacancy. An electron from an outer shell then falls down to this lower energy orbital, filling the vacancy. In doing so, the electron will release radiation equivalent to the energy difference between the orbitals (figure 2.14). The emitted radiation is detected and measured.
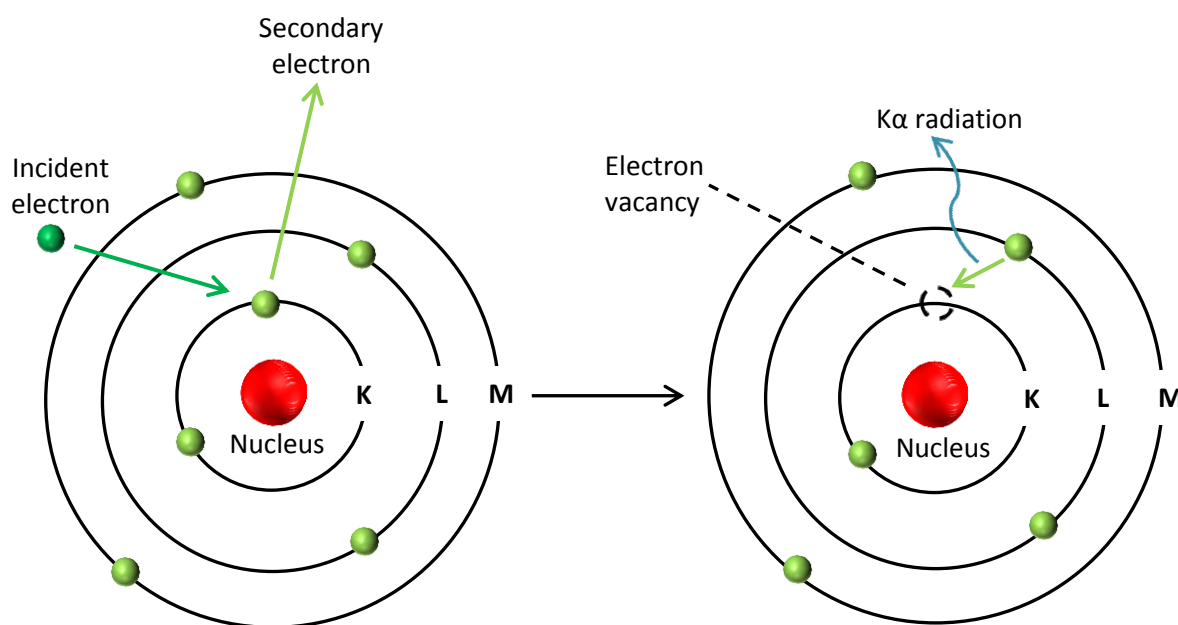
Fig. 2.14 Diagram showing the interaction of an incident electron with an atom in EDX analysis.

EDX works on the principle that every element has a unique atomic structure, and thus the energy of the X-rays detected will be characteristic of a specific element.[20] Since the emission depth of X-rays can be several µm, dependent on imaging conditions,

measurements are generally representative of the bulk sample rather than surface topography.

While EDX is useful for identifying the elements present in a sample, no information on the chemical environment of the elements is given. As a result, measurements may be skewed by sample contamination. For example, as a hygroscopic material GO is prone to water contamination, thus the percentage of oxygen incorporation as measured by EDX may come from a mixture of adsorbed water and oxidative functionalities on the GO sheet. To improve the reliability of EDX, measurements are taken from at least four different areas of the same sample to give an averaged result with quoted standard deviation values. EDX requires next to no sample preparation for GO-based materials, using powdered samples deposited onto a sticky carbon tab. EDX measurements give the elemental composition to an accuracy of approximately ±1 at.%, and to ensure accuracy they should be calibrated against samples of known (and similar) composition.

2.2.2 X-ray Photoelectron Spectroscopy (XPS)

XPS is an alternative means of calculating the elemental composition, empirical formula, chemical state and electronic state of elements within a sample. The samples are irradiated with X-ray radiation of a known energy, which excites the core electrons in the samples, enabling them to escape (figure 2.15).
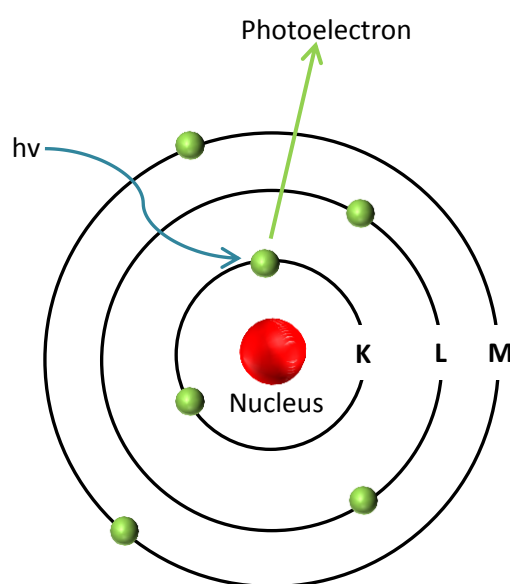
Fig. 2.15 Diagram showing the interaction of X-ray radiation with an atom in XPS.

The emitted photoelectrons are detected, and their kinetic energies are measured. Since the radiation energy (E), and the kinetic energy (E_{Kin}) of the photoelectrons is known, the binding energy (ɸ) of the material can be calculated from:

$$E = \phi + E_{Kin} \tag{2.3}$$

Due to their individual structure, every atomic orbital has a characteristic binding energy. Hence XPS uses the kinetic energy of emitted photoelectrons to quantitatively analyse the elemental composition of a sample.[21] While the X-rays have good penetration, the depth of photoelectron emission is limited: only photoelectrons in the top 1–10 nm of the sample will have enough energy to escape from the material and thus be detected. XPS is therefore a surface sensitive technique and can suffer from contamination effects such as surface adsorbed water and adventitious carbon.

XPS can work with powdered samples and so the preparation for GO-based materials is minimal. XPS analysis can be used to produce survey scans which directly show the percentage composition of a material (figure 2.16). The accuracy of such measurements is typically quoted as within 10% of the atomic percent,[22, 23] although more accurate quantification is possible by taking the scattering cross section of the elements into consideration.
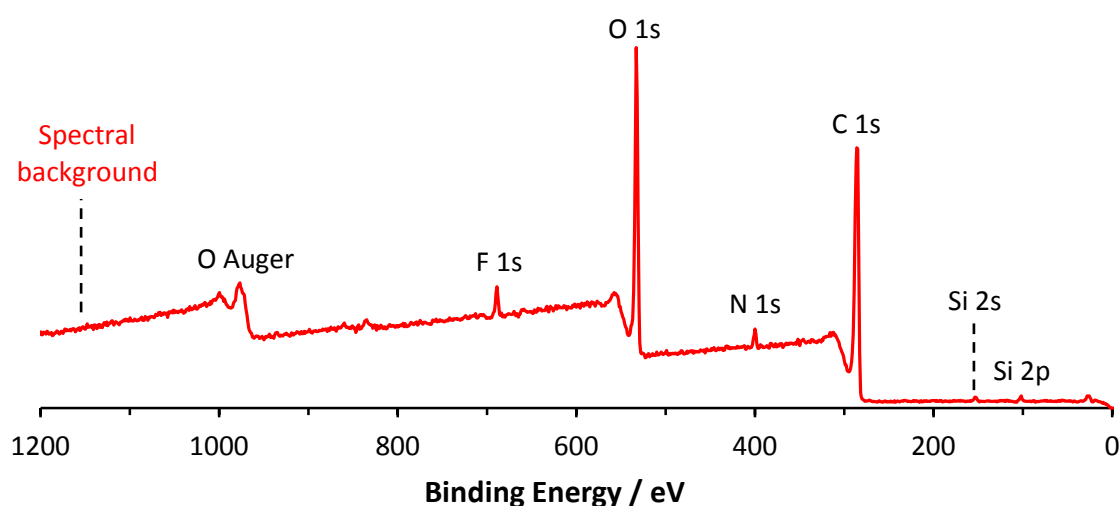
Fig. 2.16 Example XPS survey scan showing photoelectric and Auger lines.

Not all peaks in an XPS spectrum are due to the incident electrons. As seen in figure 2.16, alongside photoelectric lines, the survey scan shows Auger peaks. These lines are caused

when a higher energy electron falls to fill the vacancy left by a photoelectron, and a second electron, with energy characteristic of the energy difference between the orbital shells, is emitted. This process is demonstrated schematically in figure 2.17.
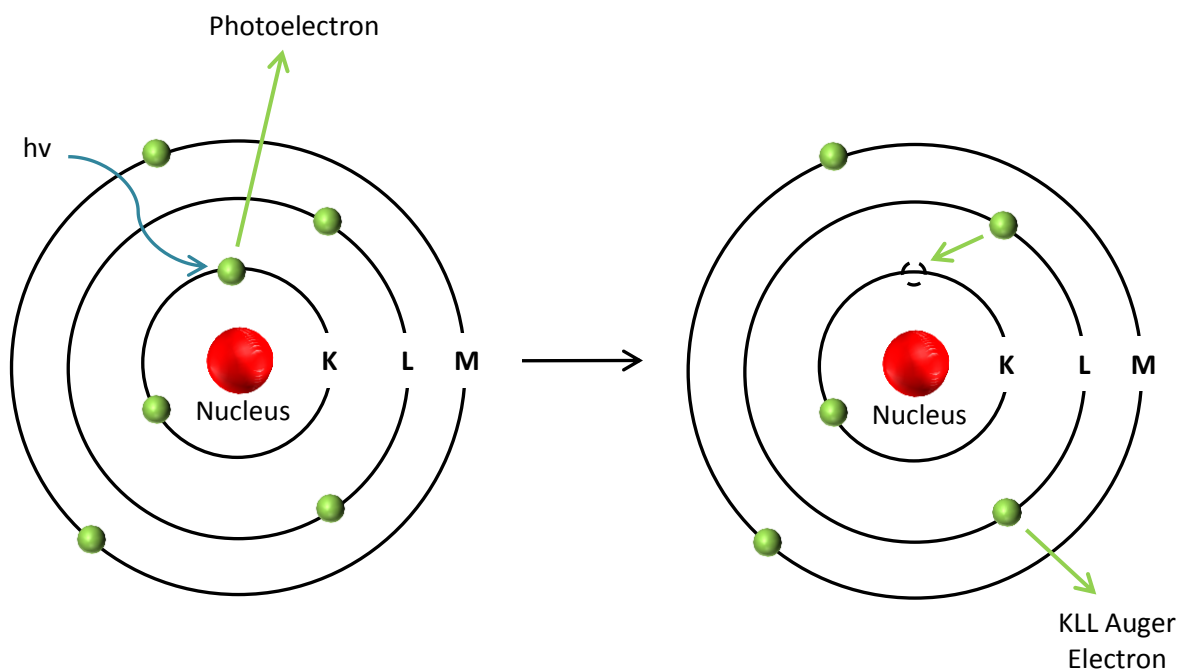
Fig. 2.17 Diagram showing the emission of an Auger electron in XPS.

While the Auger electrons are responsible for some peaks in the survey scan, in XPS it is the line intensity and position of the photoelectric signals which are used to gather information on the sample. Core level spectra provide a more in depth study of the elements in a sample, revealing the chemical environment of an element based on chemical shifts. This information is used to study chemical modifications of GO-based materials, disclosing, for example, the proportion of carbon involved in C-O and C=O bonding. This provides a big advantage over EDX analysis.
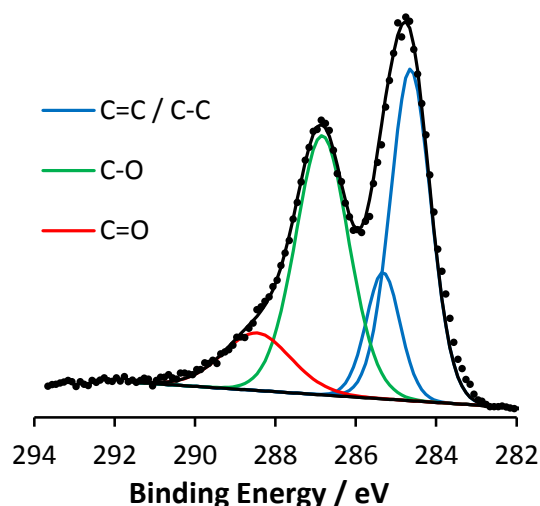
Fig. 2.18 Example C 1s core level spectrum of a GO-based material.

Figure 2.18 shows a representative C 1s core level spectrum of a GO-based material. The spectrum can be split into individual contributions from C=C / C-C, C-O and C=O binding environments, assigned according to chemical shift measurements via a peak fitting process using mixed Gaussian-Lorentzian (Voigt) lineshapes. For GO-type materials, it is generally accepted that the peak around 284.8 eV is a combination of sp^2 and sp^3 hybridised carbon-carbon bonds, although often the contributions cannot be definitively separated with confidence due to their clashing chemical shifts.[24]

Often a π-π* satellite can also be seen in C 1s spectra – satellites occur when the incident radiation promotes an electron to a higher energy level (a bonding to anti-bonding transition in this case) before photoionisation takes place.[25] As a result the emitted electron has less kinetic energy, which is thus observed in the spectrum as a satellite peak with an apparently higher binding energy.

XPS has been used to characterise a variety of samples in this thesis, using the survey scans to determine changes in the elemental composition, and C 1s, S 2p, N 1s, Au 4f and Pd 3d core level spectra to gain information on the specific chemical environments. CasaXPS software was used for the XPS peak fitting, with mixed Gaussian-Lorentzian lineshapes and a Shirley background. The line widths and peak intensities were restricted to ensure that the peak fitting was reasonable, allowing quantitative analysis of the sample composition.

2.3   Spectroscopic Studies

2.3.1 Raman Spectroscopy

Raman spectroscopy is a sensitive light scattering technique, complementary to FTIR, and provides a spectral fingerprint for samples.

When monochromatic radiation hits a molecule, most of the light will be elastically scattered (Rayleigh scattering). In this case, the radiation excites the molecule to a virtual energy state. The molecule then relaxes back down, almost instantly, to its original energy state by releasing a photon with equal energy to the incident photon.

Raman spectroscopy is concerned with the less common Stokes, and anti-Stokes, inelastic light scattering phenomenon. In this case, incoming electromagnetic radiation polarises the electron cloud of a molecule, distorting its shape, size, or orientation. The incident photon excites a virtual electron-hole pair, which is then scattered by a phonon mode.[26] At room temperature, a molecule will normally be in its ground vibrational state. Thus when Raman scattering occurs and an incident photon promotes a molecule to a virtual energy state, a lower energy photon will be emitted when the lattice relaxes; this is Stokes scattering. For anti-Stokes scattering, the lattice must already be in an excited vibrational state on interaction with electromagnetic radiation. As a result, the lattice can relax from its virtual energy state to a lower energy vibrational state than before, emitting a blue-shifted photon in the process.

These three light scattering events – Rayleigh, Stokes and anti-Stokes – are illustrated in figure 2.19.
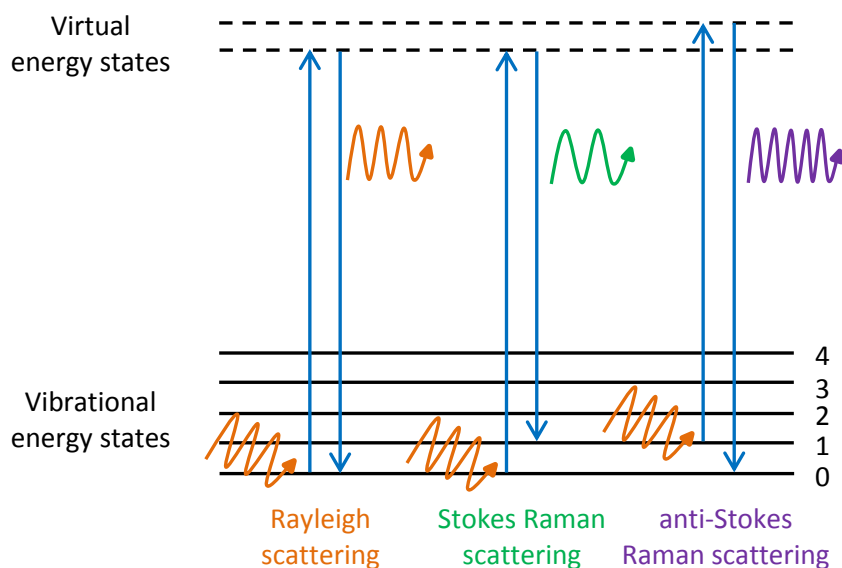
Fig. 2.19 Jablonski diagram showing the energy state transitions for elastic and inelastic light scattering.

This change in the wavelength of the incident photon to give the emitted photon in Raman scattering is known as the Raman shift. As vibrational energy levels are highly specific, Raman shifts are characteristic of particular bonds, and can thus be used to provide structural information.

Only a small proportion of incident light will be Raman scattered (approximately 0.0001% of photons for conventional, non-resonant Raman scattering), thus the signal is often weak; large sample volumes, high intensity lasers, and sensitive detectors are required. If the signal is still not sufficient, or is obscured by fluorescent transitions, surface enhanced Raman spectroscopy (SERS) can be employed.

Raman can be a very useful analytical tool for graphene-based materials as the system of delocalised electrons is easily polarisable,[27] providing a large photon scattering cross-section and thus strong Raman signals. Graphene has three optical phonon modes – two of which are in-plane, and one of which is out-of-plane[28] – which give rise to the primary signals seen in Raman spectra of graphene-type materials.

Graphene-type materials will exhibit a dominant band at ~1580 cm^{-1}, known as the G band. The G band arises from a first order excitation process from the doubly degenerate sp^2

stretching modes shown in figure 2.20 (a), the band is thus characteristic of graphitic materials.
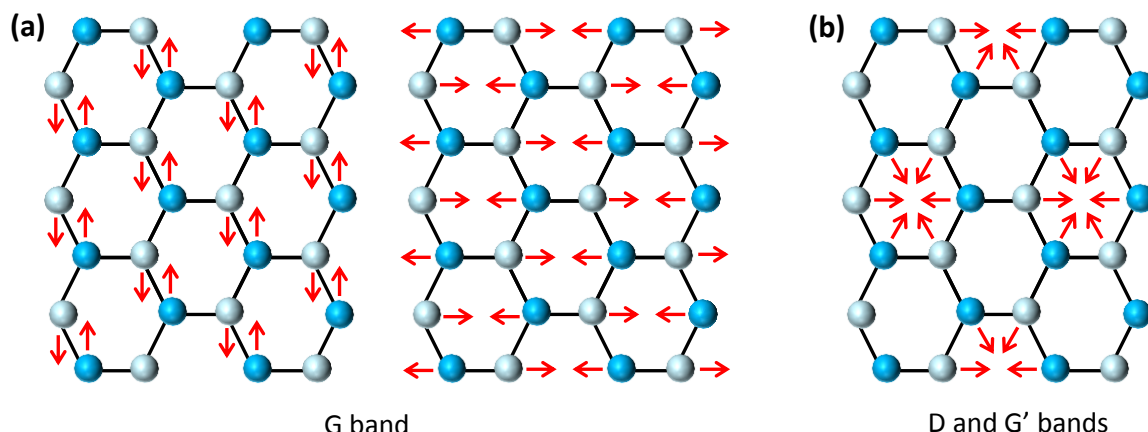
Fig. 2.20 Schematic showing the optical phonon vibrations of graphene, with the sp^2 C-C stretching modes which correspond to **(a)** the G band, and **(b)** the D and G' bands in Raman.

The G' (or 2D) band seen around 2700 cm^{-1} is also characteristic of sp^2 systems, arising from a second-order excitation process:[29] an electron near the K point (Dirac point) at the corner of the Brillouin zone is excited to the conduction band of graphene, and itself (or the corresponding hole) is further scattered, by the phonon vibration shown in figure 2.20 (b), to the inequivalent K' point.[30] In order to conserve energy and momentum, the electron (or hole) is scattered by a second phonon vibration, back to the K point where the electron-hole recombines, emitting a photon in the process. These G and G' bands can be seen in the Raman spectrum of highly ordered pyrolytic graphite (HOPG), as shown in figure 2.21.

D band ~ 1340 cm⁻¹   **G band** ~ 1600 cm⁻¹   **G' band** ~ 2700 cm⁻¹
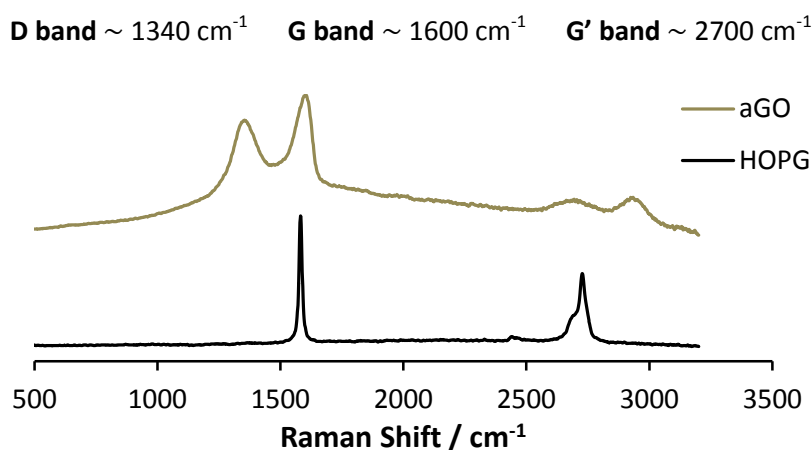
Fig. 2.21 Example Raman spectra of as-produced GO, showing the D (1340 cm⁻¹), G (1600 cm⁻¹) and G' (2700 cm⁻¹) bands, and of HOPG, showing the sp² characteristic G and G' bands.

The shape, intensity and position of the G and G' bands in graphitic samples reveal the extent of exfoliation in graphene-type materials: significant differences between the respective peaks of monolayer aGO and HOPG can be seen in figure 2.20.

The third band of interest for graphene-type materials is the D band which, as shown in the Raman spectrum of aGO in figure 2.21, occurs around 1340 cm⁻¹. Although characteristic of graphitic materials, in pristine sp² hybridised samples this band is Raman inactive. Like the G' Raman scattering, an electron (or hole) is excited by an incident photon, and is further scattered by the phonon breathing mode shown in figure 2.20 (b). The D band is a one phonon process and thus requires an atomic defect which breaks the symmetry of the sp² lattice to scatter the electron (or hole) back to the K point making the process Raman active.[31] As a result the D band is known as the disorder band, with the relative areas of the D and G bands being used as a measure of defect density in a graphene-type structure.[32] Although, it is worth noting that the D/G ratio of defective graphene-type materials does not tend to change significantly in response to further surface functionalisation – the D/G ratio is dominated by the structural defects (holes) of a sheet rather than the level of oxidation, for example, which has comparatively little effect on the D/G ratio.

Raman can be a very convenient method of characterisation: the analysis is quick, non-destructive and uses solid-state samples. Raman thus provides an alternative method of

structural characterisation for samples which are unsuitable for AFM and TEM studies due to poor dispersibility.

2.3.2 Solid-state Nuclear Magnetic Resonance (ssNMR)

In an external magnetic field, B_0, the nuclear spins of a molecule will align, orienting themselves either in line with (low energy) or against (high energy) the applied magnetic field. This results in an induced magnetic field which serves to shield or de-shield the nucleus from the applied magnetic field,[33] dependent on the bonding environment. This shielding (or de-shielding) effect produces characteristic chemical shifts (ppm), generating an NMR spectrum.

Both solution and solid-state NMR produces results which are reflective of the average composition of the samples. However, solution NMR is only appropriate for low molecular weight molecules: in solution, small molecules and proteins of up to 10 kDa tumble at such a speed that their NMR spectrum represents an isotropic average of spin interactions, resulting in narrow line widths. Graphitic materials do not have the same translational freedom as small molecules; even in solution the large sheets cannot rotate quickly enough to negate spin interactions. Solution NMR is thus unsuitable for the materials studied throughout this thesis, and ssNMR was deferred to instead.

The spin interactions in ssNMR are orientation dependent, and unless steps are taken to minimise these effects aromatic carbon systems can exhibit large anisotropies of up to 200 ppm.[34] The anisotropic interactions in ssNMR are dependent on the sample angle of rotation (θ), as determined by the equation:

$$3(\cos^2 \theta) - 1 \tag{2.4}$$

By setting this equation as equal to zero, it can be solved for θ, thereby finding the angle of rotation which will eliminate any anisotropic effects. This value of θ = 54.7° is known as the magic-angle. Introducing artificial motion to a sample by rotating the sample rotor on a magic-angle axis relative to the applied field (figure 2.22) will remove anisotropic effects and improve the quality of spectra, provided that the rate of spinning exceeds the magnitude of the anisotropic interaction.[35]
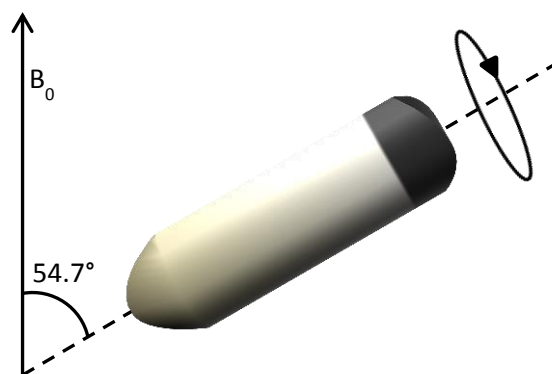
Fig. 2.22 Schematic of a ssNMR sample rotor spinning at the magic angle relative to B_0.

Two types of ^{13}C MAS ssNMR experiments were employed for the studies on graphene-type materials covered in this thesis: direct excitation (DE) ^{13}C MAS NMR, which excites all nuclei equally, providing a semi-quantitative survey of all carbon species in the sample; and cross polarised (CP) ^{13}C MAS NMR which provides different structural information. MAS was used with a typical spin rate of 15 kHz, yielding line widths of ~20 ppm for all amorphous GO samples.

An example DE ^{13}C MAS NMR spectrum of GO is shown in figure 2.23. The spectrum has been peak fitted using broadened Gaussian-Lorentzian lineshapes, with the individual peaks assigned as labelled. The predominant signals arise from sp^2 C-C, C-OH and C-O-C carbons as expected.
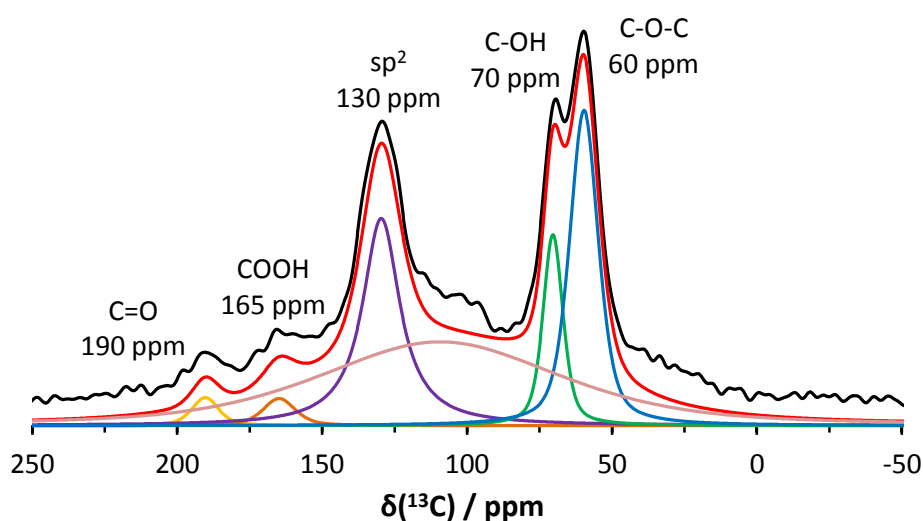
Fig. 2.23 Direct excitation ^{13}C MAS NMR spectrum of GO, showing contributions from C=O, COOH, C-OH, C-O-C and sp^2 C-C functional groups.

The ^{1}H-^{13}C CP MAS NMR experiments give enhanced signals for carbon species in close proximity to protons.[36] The cross polarisation process is a through space phenomenon, implying that both intermolecular and intramolecular proton interactions can play a role in signal enhancement.[37, 38] Under ^{1}H-^{13}C CP MAS NMR experiment conditions, the intensity of the hydroxyl carbon signal, and any CH groups, is expected to increase relative to the sp^2 and epoxy carbon signals. Hence CP MAS NMR experiments are useful for identifying functionalisation when the groups introduced to the graphene-type material contain aliphatic carbons.

Figure 2.24 shows an example of the DE and CP spectra of a CMG material. As in figure 2.23, the sp^2 C-C, C-OH and C-O-C signals can be clearly identified in both spectra, alongside a new aliphatic signal around 30 ppm. The intensity of the C-OH carbon signal at 70 ppm has been significantly enhanced in the CP spectrum.
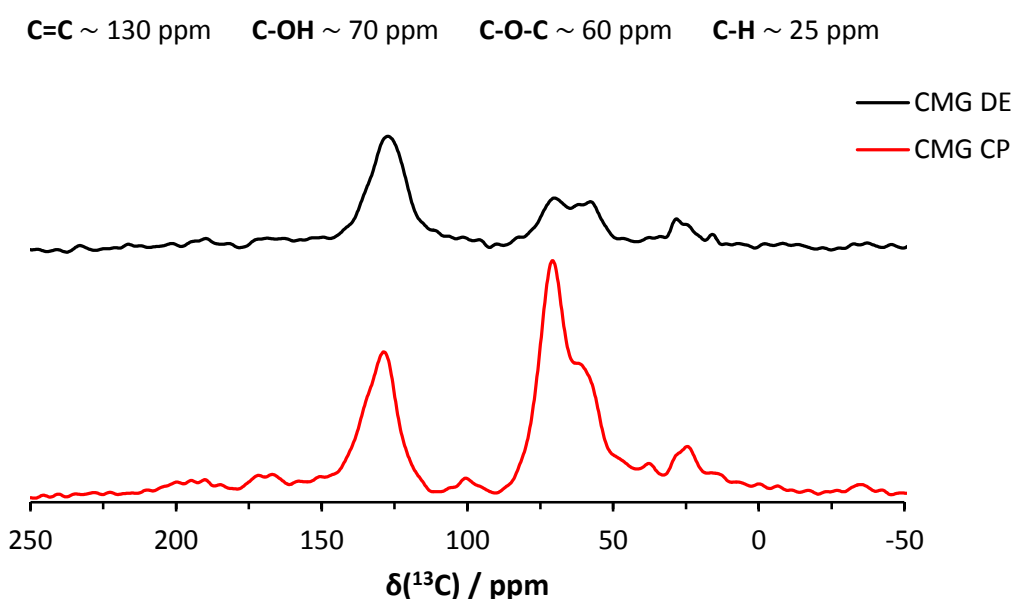
Fig. 2.24 ^{13}C MAS NMR spectra of a CMG, showing both the DE (black) and the CP (red) experiments.

ssNMR uses powdered samples, and so the preparation for GO-based materials is trivial. However, the quantities required are 50 times that needed for AFM, TEM, SEM, EDX, XPS and Raman analysis, making ssNMR unsuitable for CMGs which have expensive reagents or a low yield.

2.4   Physical Property Measurements

2.4.1 Thermal Gravimetric Analysis (TGA)

For TGA analysis, samples are placed on a highly sensitive mass balance, which measures the mass loss as a function of temperature.[39] TGA provides information on the thermal stability and decomposition pattern of a material, thus changes in a TGA profile can be indicative of a change in the physical and chemical properties of a material.

The thermal analysis of GO shows that mass loss occurs at three distinct temperatures (figure 2.25), which can be rationalised as the loss of water below 100 °C, the loss of OD at around 200 °C, and the decomposition of the graphitic-like sheets above 500 °C.[40]
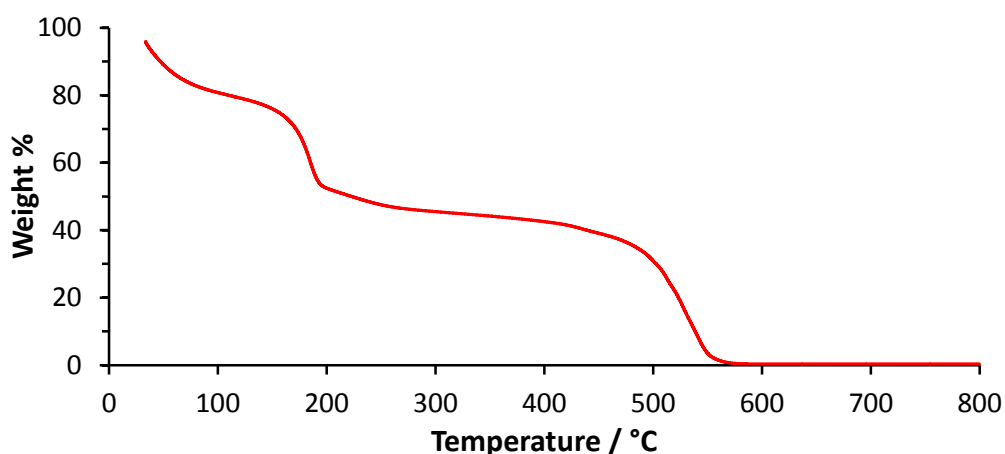
Fig. 2.25 Example TGA profile of aGO, showing mass loss as a function of increasing temperature.

TGA uses a few mg of solid state samples making it a convenient method of characterisation. TGA was used throughout this thesis to investigate changes in the physical properties of graphene-based materials as a result of chemical functionalisation.

2.4.2 Contact Angle (CA) Measurements

Drop shape analysis can be used to measure the contact angle (CA) of water on a sample surface. This provides a means of quantifying the hydrophilicity of different samples.[41] As shown in figure 2.26, the contact angle of graphitic materials can vary substantially as a result of chemical modification: figure 2.26 (a) shows a very hydrophilic GO-based material

with a contact angle of 22°, whereas figure 2.26 (b) shows a more graphene-like rGO material with a contact angle of 80°.
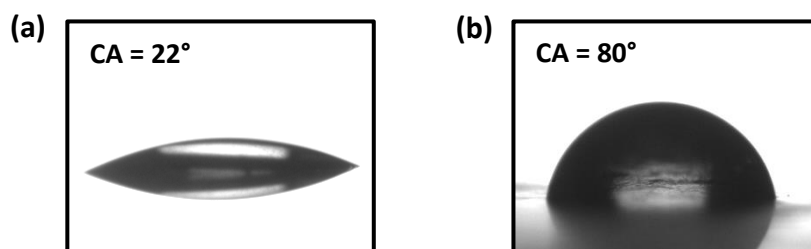
Fig. 2.26 Contact angle measurements of **(a)** GO-based and **(b)** rGO materials.

The sample surfaces were prepared by drop-casting an aqueous dispersion onto a clean glass slide, and allowing to air dry: this method of characterisation is thus reliant on the dispersibility of the sample. Contact angle measurements are susceptible to surface contamination, but serve as a convenient way of identifying any trends in hydrophilicity as a result of functionalisation in this thesis.

1.   Jalili, N.; Laxminarayana, K. *Mechatronics* **2004,** 14, (8), 907-945.
2.   Meyer, E.; Hug, H. J.; Bennewitz, R., *Scanning Probe Microscopy: The Lab on a Tip*. Springer-Verlag.
3.   Binnig, G.; Quate, C. F.; Gerber, C. *Phys. Rev. Lett.* **1986,** 56, (9), 930-933.
4.   Giessibl, F. J. *Rev. Mod. Phys.* **2003,** 75, (3), 949-983.
5.   Li, J.-d.; Xie, J.; Xue, W.; Wu, D.-m. *Microsyst. Technol.* **2013,** 19, (2), 285-290.
6.   Yongho, S.; Wonho, J. *Rep. Prog. Phys.* **2008,** 71, (1), 016101.
7.   Cappella, B.; Dietler, G. *Surface Science Reports* **1999,** 34, (1–3), 1-104.
8.   Poggi, M. A.; McFarland, A. W.; Colton, J. S.; Bottomley, L. A. *Anal. Chem.* **2005,** 77, (4), 1192-1195.
9.   Zhong, Q.; Inniss, D.; Kjoller, K.; Elings, V. B. *Surface Science Letters* **1993,** 290, (1–2), L688-L692.
10.   Frederix, P. L. T. M.; Bosshart, P. D.; Engel, A. *Biophys. J.* **2009,** 96, (2), 329-338.
11.   Zitzler, L.; Herminghaus, S.; Mugele, F. *Phys. Rev. B* **2002,** 66, (15), 155436.
12.   Dufrêne, Y. F. *J. Bacteriol.* **2002,** 184, (19), 5205-5213.
13.   Knoll, M.; Ruska, E. *Ann. Phys.* **1932,** 12, 607-640.
14.   Egerton, R., *Physical Principles of Electron Microscopy*. 1st ed.; Springer US: 2005.
15.   Williams, D.; Carter, C., *Transmission Electron Microscopy*. 2nd ed.; Springer: 2009.
16.   Wilson, N. R.; Pandey, P. A.; Beanland, R.; Rourke, J. P.; Lupo, U.; Rowlands, G.; Römer, R. A. *New J. Phys.* **2010,** 12, (12), 125010.
17.   Apkarian, R.; Joy, D., *Scanning Microscopy for Nanotechnology*. Springer: 2006.
18.   Sastry, M. *Journal of Electron Spectroscopy and Related Phenomena* **2000,** 106, (1), 93-99.
19.   Vernon-Parry, K. D. *III-Vs Review* **2000,** 13, (4), 40-44.
20.   Goldstein, J., *Scanning Electron Microscopy and X-ray Microanalysis*. Springer: 2003.
21.   Hüfner, S., *Photoelectron Spectroscopy: Principles and Applications*. Springer Verlag: 1995.
22.   CasaXPS, XPS Spectra. 2013; pp 1-77.
23.   Hesse, R.; Streubel, P.; Szargan, R. *Surf. Interface Anal.* **2005,** 37, (7), 589-607.
24.   Sydlik, S. A.; Swager, T. M. *Adv. Funct. Mater.* **2013,** 23, (15), 1873-1882.
25.   CasaXPS, Introduction to XPS. In *The Nature of X-ray Photoelectron Spectra*, CasaXPS, 2005.
26.   Ferrari, A. C.; Basko, D. M. *Nat. Nano.* **2013,** 8, (4), 235-246.
27.   Marshall, C. P.; Edwards, H. G. M.; Jehlicka, J. *Astrobiology* **2010,** 10, (2), 229-243.
28.   Ryan, B.; Luiz Gustavo, C.; Lukas, N. *J. Phys.: Condens. Matter* **2015,** 27, (8), 083002.
29.   Ferrari, A. C. *Solid State Commun.* **2007,** 143, (1–2), 47-57.
30.   Casiraghi, C. *Phys. Status Solidi B* **2011,** 248, (11), 2593-2597.
31.   Dresselhaus, M. S.; Jorio, A.; Saito, R. *Annu. Rev. Condens. Mater. Phys.* **2010,** 1, (1), 89-108.
32.   Eckmann, A.; Felten, A.; Verzhbitskiy, I.; Davey, R.; Casiraghi, C. *Phys. Rev. B* **2013,** 88, (3), 035426.
33.   Pranitha, D.; Parthiban, N.; Kumar, D.; Ghosh, S.; Banji, D.; Jana, S. *Asian J. Pharm. Clin. Res.* **2011,** 4, (4), 9-14.
34.   Schmidt-Rohr, K.; Wolfgang, H., *Multidimensional Solid-State NMR and Polymers*. Elsevier: 1994.
35.   Hennel, J.; Klinowski, J., *New Techniques in solid-state NMR*. Springer-Verlag: 2005.
36.   Thomas, H. R.; Day, S. P.; Woodruff, W. E.; Vallés, C.; Young, R. J.; Kinloch, I. A.; Morley, G. W.; Hanna, J. V.; Wilson, N. R.; Rourke, J. P. *Chem. Mater.* **2013,** 25, (18), 3580-3588.
37.   Hanna, J. V.; Wilson, M. A. *J. Phys. Chem.* **1992,** 96, (16), 6518-6523.
38.   Cizmeciyan, D.; Sonnichsen, L. B.; Garcia-Garibay, M. A. *J. Am. Chem. Soc.* **1997,** 119, (1), 184-188.
39.   Coats, A. W.; Redfern, J. P. *Analyst* **1963,** 88, (1053), 906-924.
40.   Rourke, J. P.; Pandey, P. A.; Moore, J. J.; Bates, M.; Kinloch, I. A.; Young, R. J.; Wilson, N. R. *Angew. Chem., Int. Ed.* **2011,** 50, (14), 3173-3177.
41.   Mazzola, L.; Bemporad, E.; Carassiti, F. *Measurement* **2012,** 45, (3), 317-324.

Chapter 3

Refining the Structure of Graphene Oxide

The structure of GO has been a topic of debate for over 150 years, and during that time numerous models have been proposed (see section 1.3.1). A relatively new two component model was proposed by Rourke *et al*. in 2011,[1] but at the time a lot of unanswered questions remained. A basic NaOH wash was found to separate as-produced Hummers graphene oxide into two components – mass balance, TGA, FTIR, and mass spectrometry results indicated that low molecular weight carbonaceous fragments were left in solution after the basic wash. This chapter explores and advances the understanding behind the two component model. GO from different synthetic routes are studied to identify whether or not the two component model is specific to Hummers GO. In addition a different base washing process is investigated to identify any dependence on the presence of NaOH. Numerous characterisation techniques aid the study, providing insight on the structure, optical properties and deoxygenation versus reduction mechanisms of GO.

3.1   The Two Component Structure of Graphene Oxide

There is significant evidence to suggest that the structure of as-produced graphene oxide (aGO) prepared via the Hummers synthesis is in fact a two-component mixture of highly oxidised carbonaceous debris complexed to oxygen functionalised graphene sheets.[1, 2] This debris is akin to the debris seen for oxidised carbon nanotubes (CNTs),[3, 4] but is present in greater proportions: mass balance measurements suggest that the oxidation debris (OD) contributes roughly one third of the mass of aGO,[1] compared to one quarter for oxidised CNTs.[5] These small organic fragments are bound to the graphene-like sheets of aGO via intermolecular forces such as π-π stacking and hydrogen bonding, but it has been shown that these intermolecular forces can be broken by refluxing in a basic solution such as NaOH for approximately 30 minutes.[1] The two components of aGO can thus be separated via the simple expedient of washing with dilute aqueous base, followed by centrifugation and neutralisation with HCl. The removal of the OD reveals the 'true' GO material, referred to as base-washed GO (bwGO).
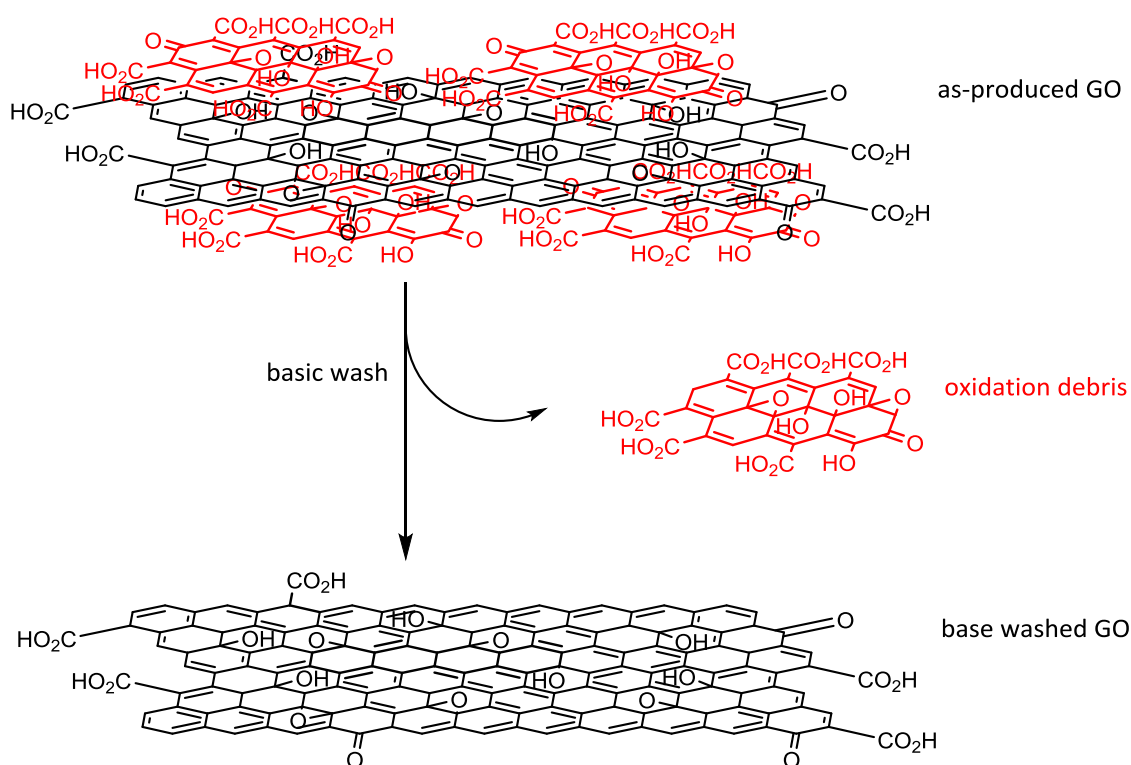
Scheme 3.1 The separation of aGO into OD and bwGO. The structures shown are used for illustrative purposes only.

Preliminary spectroscopic studies by the Rourke group show the OD to be highly oxygenated.[1] With this in mind, certain changes can be expected to occur on the removal of the OD. Without the presence of the highly oxygenated OD, the less oxygenated bwGO sheets should have a higher C/O ratio compared to aGO. This change in the chemical composition is a result of deoxygenation. Other effects such as changes in dispersibility, conductivity and colour are also of note: bwGO materials are significantly darker in colour than the golden brown of aGO. Similar colour changes as a result of adding base to GO have been well documented in the past, and others have also attributed it to a deoxygenation effect.[6] Rourke *et al*. also found that the bwGO material had significantly reduced dispersibility, as discussed later, and increased conductivity.[1]

3.1.1 Base-washed Graphene Oxide

A wide variety of spectroscopic techniques were employed in order to better the understanding behind these individual bwGO and OD components. Furthermore, attempts were made to try to establish whether or not this picture is a general feature of GO – rather than one specific to Hummers GO – by investigating a number of different oxidation protocols.

Figure 3.1 shows the solid-state NMR (ssNMR) spectra of the Hummers aGO and bwGO materials, from which deductions can be made about the effect of the basic wash used to extract bwGO.

C=C ~ 130 ppm   C-OH ~ 70 ppm   C-O-C ~ 60 ppm
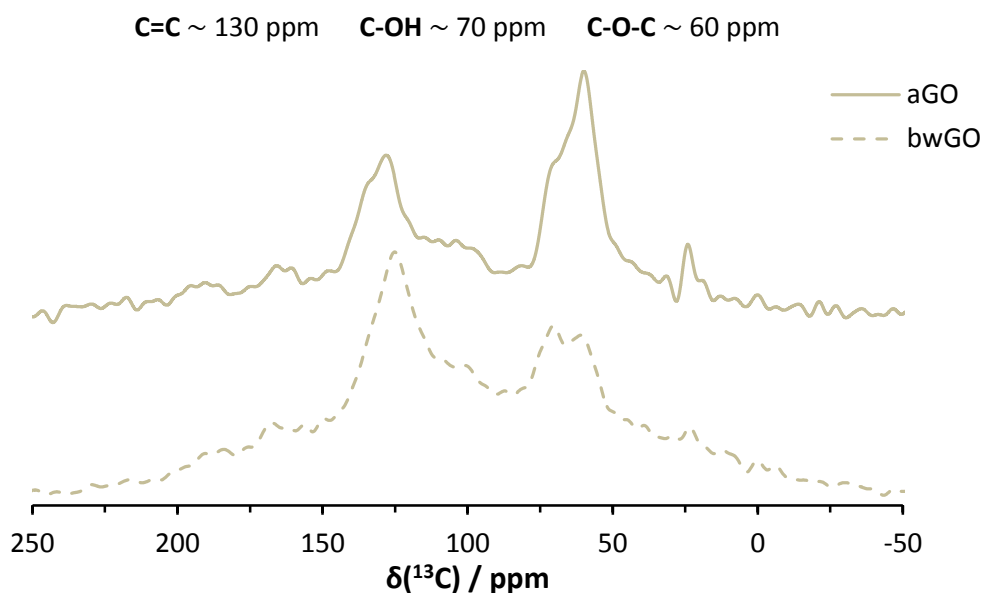
Fig. 3.1 Direct excitation ^{13}C MAS ssNMR spectra of aGO (top) and bwGO (bottom).

There are clear structural similarities between the two samples shown in figure 3.1. The sp^{2} carbon signal is seen at roughly 130 ppm, while the hydroxide and epoxide carbon functionalities are seen at 70 and 60 ppm respectively.[7] However, the C-O and C-O-C peaks are significantly less intense for bwGO than for aGO, which suggests that the base-washing process decreases the amount of oxidative functionalities relative to the sp^{2} carbon structure.

A more subtle change is that the ratio of epoxides to hydroxides is lower in bwGO than in aGO. This could be the result of the OD containing a greater proportion of epoxides than are present on the graphene-like sheets of bwGO, or it might be that the base washing procedure itself is ring-opening epoxides to generate hydroxyls. At this point in time it is not possible to distinguish which is behind the decreased epoxy concentration, but it is pertinent to note that the inherent instability of epoxides in GO has been observed spectroscopically and rationalised theoretically.[8] Some researchers even suggest that the ring-opening process of epoxides to hydroxyl groups on GO is reversible and dependent on changes in pH.[9]

This loss of oxygen is also apparent in the C/O ratio of the GO materials as measured via energy dispersive X-ray analysis (EDX) and X-ray photoelectron spectroscopy (XPS). Using

these techniques, the C/O ratio of aGO was determined to be 2:1, whereas the C/O ratio for bwGO was determined to be 4:1. This increase in the C/O ratio is expected and is not necessarily indicative of a chemical change resulting from the basic wash, as it can be explained by the loss of the highly oxygenated OD.

The FTIR spectra of aGO and bwGO (figure 3.2) show absorbance bands for O-H stretching (3200 cm^{-1}), O-H bending (1400 cm^{-1}), C=O stretching (1720 cm^{-1}), C=C stretching (1620 cm^{-1}), and C-O stretching (epoxy 1250 cm^{-1}; alkoxy 1050 cm^{-1}). Although it is worth noting that the absorbance around 1600 cm^{-1} has also been attributed to the deformation vibrations (scissor mode) of intercalated water,[10] and it is thus likely to be a combination of C=C stretching and H-O-H deformations.
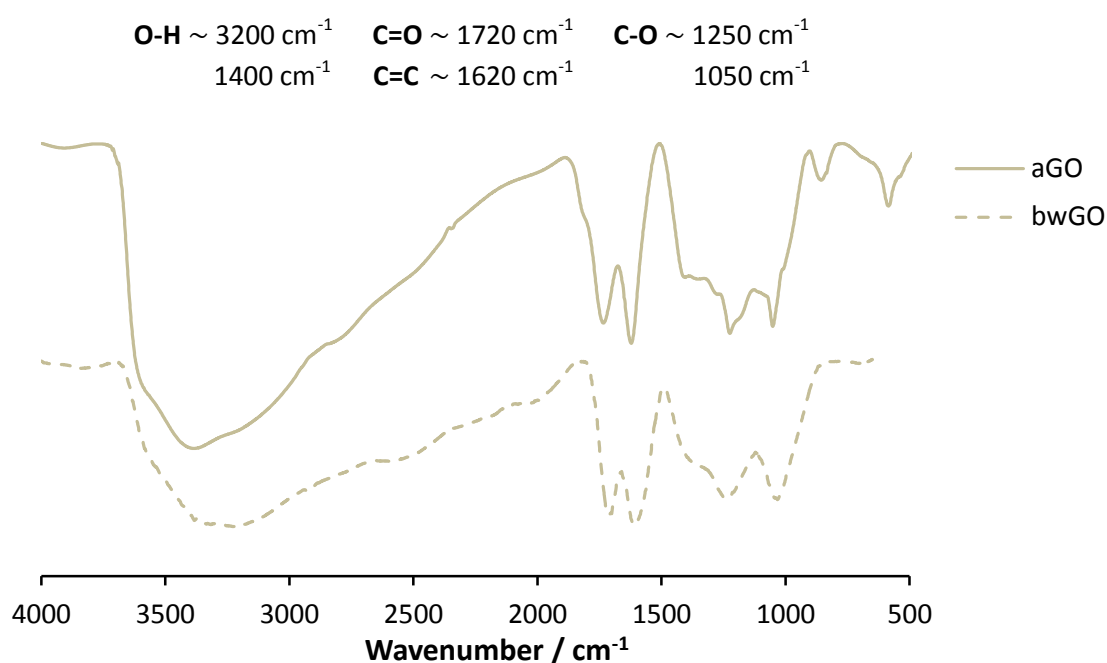
Fig. 3.2 ATR-FTIR spectra of aGO (top) and bwGO (bottom).

While the FTIR spectra of the aGO and bwGO materials show signals corresponding to the same functional groups, bwGO shows a notable decrease in intensity for C-OH and C-O-C, relative to the C=O and C=C bands, which is again symptomatic of a deoxygenation.

From a stable dispersion, bwGO can be controllably deposited on a range of substrates enabling further structural characterisation. Atomic Force Microscopy (AFM), Transmission

Electron Microscopy (TEM) and Raman spectroscopy were all used to determine whether or not the graphene-like structure of aGO remains intact for bwGO.

For AFM, aqueous dispersions of aGO and bwGO were prepared at 0.25 mg ml^{-1} before being spin coated onto silicon oxide substrates. The AFM images are shown in figure 3.3.
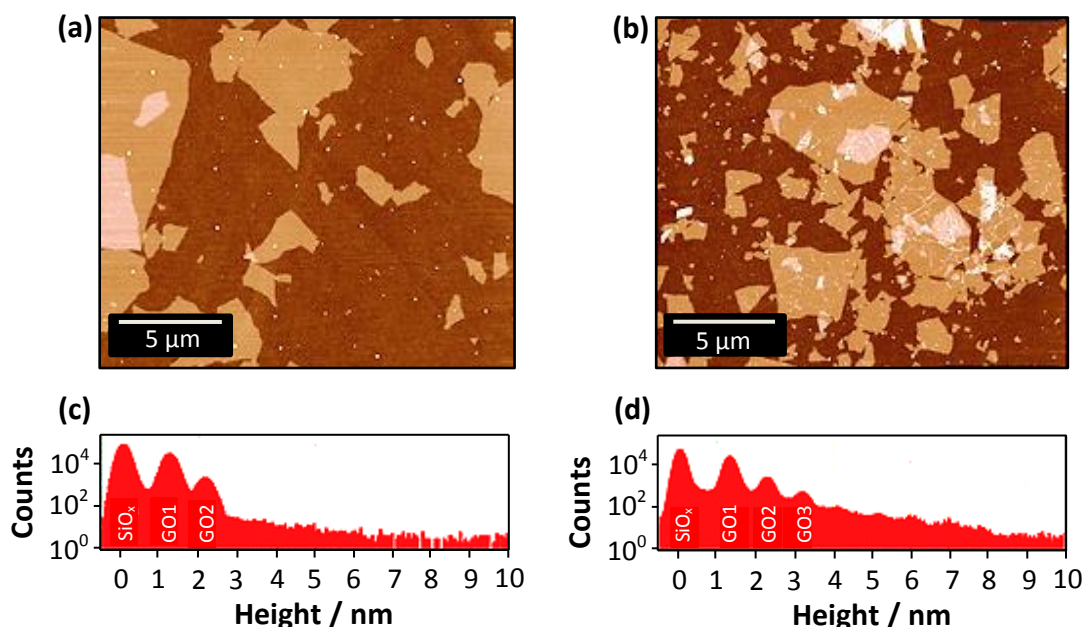
Fig. 3.3 (a-b) AFM topography images of aGO and bwGO samples respectively, the full height scale in both images is 5 nm. **(c-d)** height profile histograms for the aGO and bwGO samples respectively. The contributions from the silicon oxide substrate (SiOx), and the first (GO1), second (GO2) and third (GO3) graphene oxide layers to the histogram are labelled.

Figure 3.3 (a-b) shows that both of the GO materials can be deposited as flat monolayer sheets without coagulation. Other researchers have shown that the sheet size is dependent on the starting material and the way it is processed,[11] for example, extensive sonication is known to break up graphene oxide sheets.[12] bwGO is notably less dispersible than aGO and thus requires significant sonication to achieve the stable dispersions used for AFM, this is reflected by a slightly reduced average lateral sheet size of the bwGO sample compared to aGO. However, the average sheet size of bwGO is still more than 1 μm across and the images suggest no significant chemical changes: the monolayer sheet structure of aGO remains intact for bwGO.

The layer spacing in ordered graphite is 3.35 Å[13] and the length of a C-O bond is less than 0.15 nm,[14] thus the layer spacing expansion to >1 nm seen for GO-based materials cannot be simply explained by the presence of oxidative functionalities. The functionalisation of a graphene sheet results in sp^3 hybridised carbons which disrupt the flat structure of the sp^2 graphene causing nanoscale distortions.[15, 16] These ripples account for the increased layer spacing of graphene oxide compared to graphene itself. The height distribution histograms (c-d) of images (a-b) represent the "population" of heights in the respective images – the pixel count is measured and plotted against the height. Both histograms show distinct peaks due separately to the silicon oxide substrate, the first layer of aGO/bwGO, and the multiple overlapping layers. From these histograms, the thickness of single aGO and bwGO sheets on the substrate can be determined, as can their effective layer spacing. For aGO, a first layer thickness of 1.2 nm is extracted, with a layer spacing of 1.0 nm. For bwGO, the first layer is 1.3 nm, with subsequent layers showing a spacing of 1.0 nm. The thickness of the aGO is consistent with previous reports of monolayer aGO, and is known to vary substantially depending, for example, on humidity.[17] An increased effective thickness is observed for the first layer of the GO materials, which is in agreement with previous reports.[16, 18]

Within the accuracy of these measurements, there is no evidence for a difference between the effective thickness of aGO/bwGO on silicon oxide, nor is there evidence for a difference between the layer spacing of aGO/bwGO. This is consistent with the idea that the layer spacing of GO materials is determined by the sheet undulations caused by sp^3 bonds. As small organic fragments, unable to be distinguished by AFM, the oxidative debris is able to slot in between the aGO sheets without affecting the layer spacing.

TEM was another useful tool for confirming the graphene-like structure of bwGO. A dispersion of bwGO was prepared in an acetonitrile/water mixture, which was then drop cast onto a lacey carbon support film. Figure 3.4 shows the bright field TEM image of bwGO with the corresponding electron diffraction pattern.
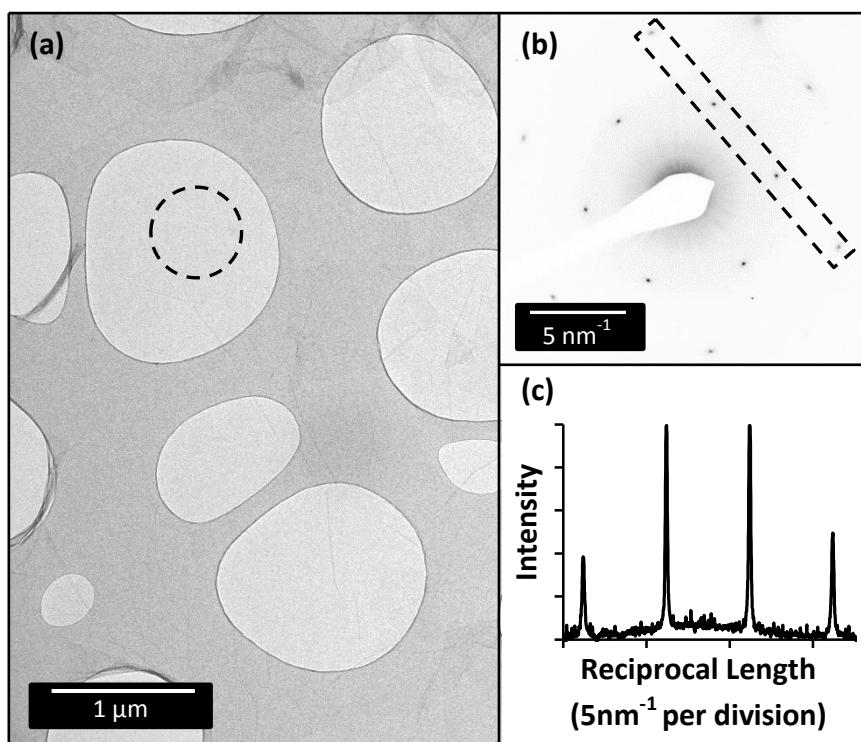
Fig. 3.4 (a) Bright field TEM image of bwGO on a lacey carbon support. The dashed black circle indicates the area from which the electron diffraction pattern **(b)** was taken (note that the contrast has been inverted for clarity). **(c)** Intensity profile taken from within the dashed black area in part **(b)**.

Graphene oxide is almost electron transparent, but the sheets can be discerned in figure 3.4 (a) by the occasional crease and fold, or overlapping sheet. The image shows that the structural integrity of the sheet is retained with no evidence of any significant structural changes. The diffraction pattern shown in figure 3.4 (b) shows the presence of a single set of hexagonal diffraction spots, which is characteristic of graphene-based materials. As seen in figure 3.4 (c), the inner hk = 10 type spots are more intense than the outer hk = 11 spots. This confirms that the material is fully exfoliated as a monolayer material.[15] TEM of bwGO at this resolution is thus indistinguishable from TEM of aGO.[19]

High resolution TEM (HR-TEM) was used to capture images with atomic resolution. Figure 3.5 shows a HR-TEM image of bwGO, where the hexagonal structure of the atoms in graphene oxide can be easily observed. These graphene-like areas (circled in black) are

broken up by defect holes (blue); dark contrast atoms (white); and amorphous regions (red), which are likely to be adventitious carbon adsorbed to the surface.
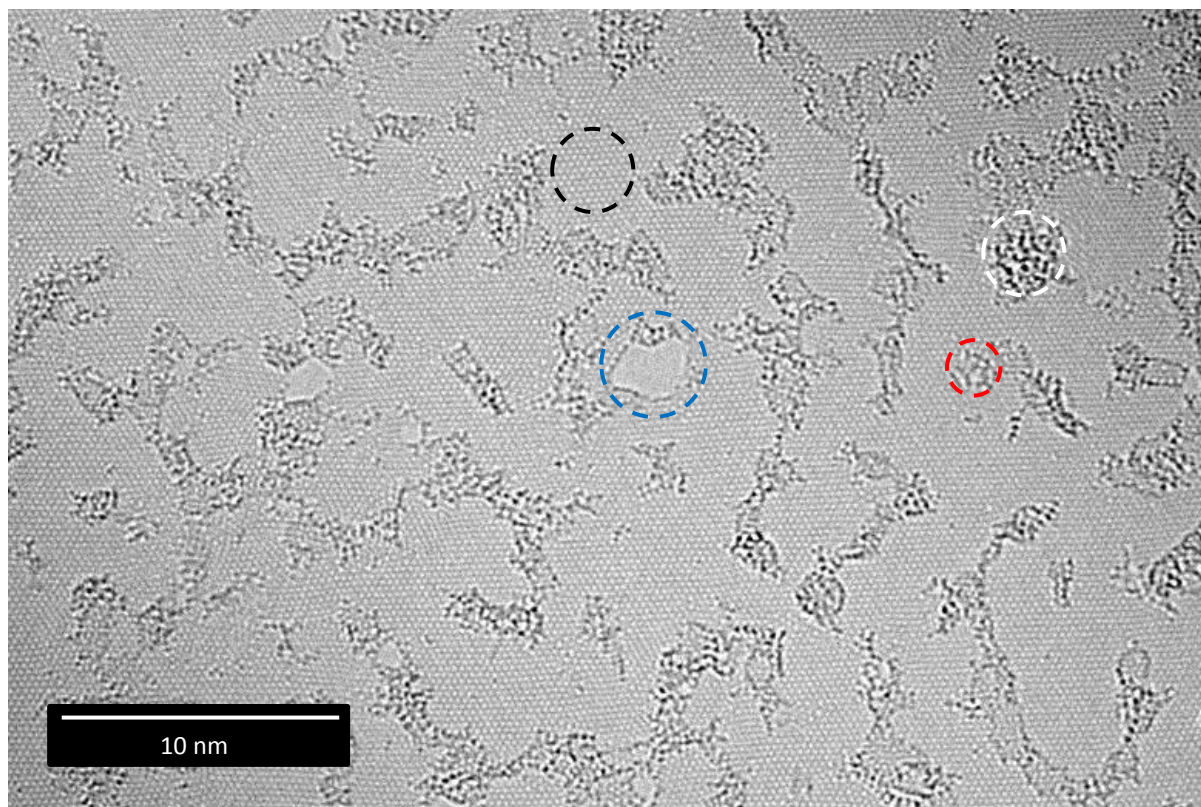
Fig. 3.5 HR-TEM image of bwGO with graphene-like segments, holes, dark contrast atoms and amorphous regions circled in black, blue, white and red respectively.

The darker contrast atoms seen in figure 3.5, circled in white, are likely to be metal impurities such as Mn and Na. They preferentially deposit on amorphous regions of the sheet and can be seen to move under the electron beam, indicating that they are unlikely to be covalently bound to the sample. The lighter contrast atoms are due to elements of lower atomic weight such as carbon and oxygen, although it is not possible to distinguish between the two.

Raman spectroscopy of aGO and bwGO show the characteristic D and G bands expected for disordered graphene-type materials (figure 3.6). The underlying broadness seen for aGO is due to the fluorescent nature of the material distorting the spectrum (see section 3.5). This was not observed for the bwGO sample.

D band ~ 1340 cm^{-1} **G band** ~ 1600 cm^{-1} **G' band** ~ 2700 cm^{-1}
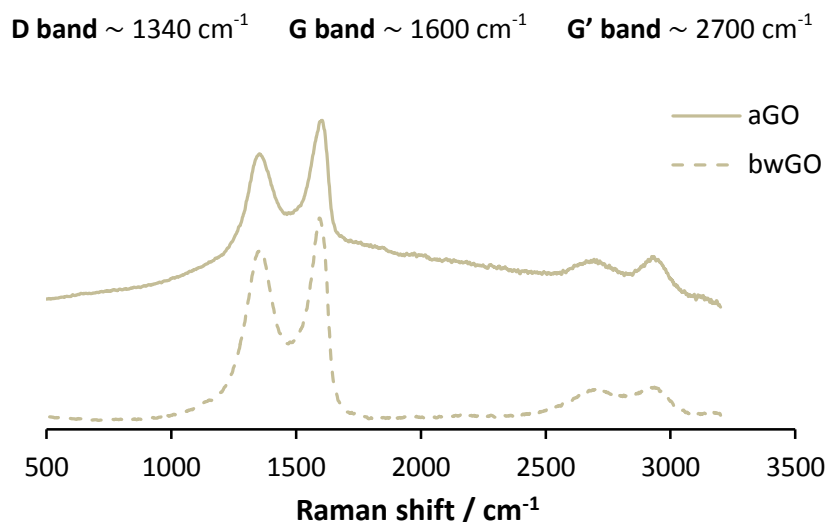
Fig. 3.6 Raman spectra of aGO (top) and bwGO (bottom); excitation wavelength 514 nm.

Other than the fluorescence, the Raman spectra of aGO and bwGO are very similar, indicating that no major changes occur to the graphene-like structure upon base-washing.

AFM, TEM and Raman studies are consistent with the OD being initially complexed to the surface of the aGO and (considering the total mass of the OD) are not consistent with the OD being formed by excision of large regions from within the graphene sheet.

The results thus far strongly suggest that both aGO and bwGO are graphene-based materials. Their monolayer sheets are decorated by various oxidative functionalities which interrupt the aromaticity. Removal of the oxidation debris in aGO, cleans the GO, revealing its true monolayer nature and in the process increases the C/O ratio by a deoxygenation process. See section 3.4 for more details on the structure and properties of OD.

3.2   Base-washing Protocols

In the initial work presented here, and in the original report[1] of the removal of OD, the base-washing procedure was performed with aqueous NaOH. In order to see whether the bwGO material was independent of the base used, aGO samples were washed with aqueous ammonia (0.45 M) via a 30 minute reflux. The starting Hummers aGO material was the same for both the NaOH and the NH_3 wash. The collected characterisation data is summarised below.
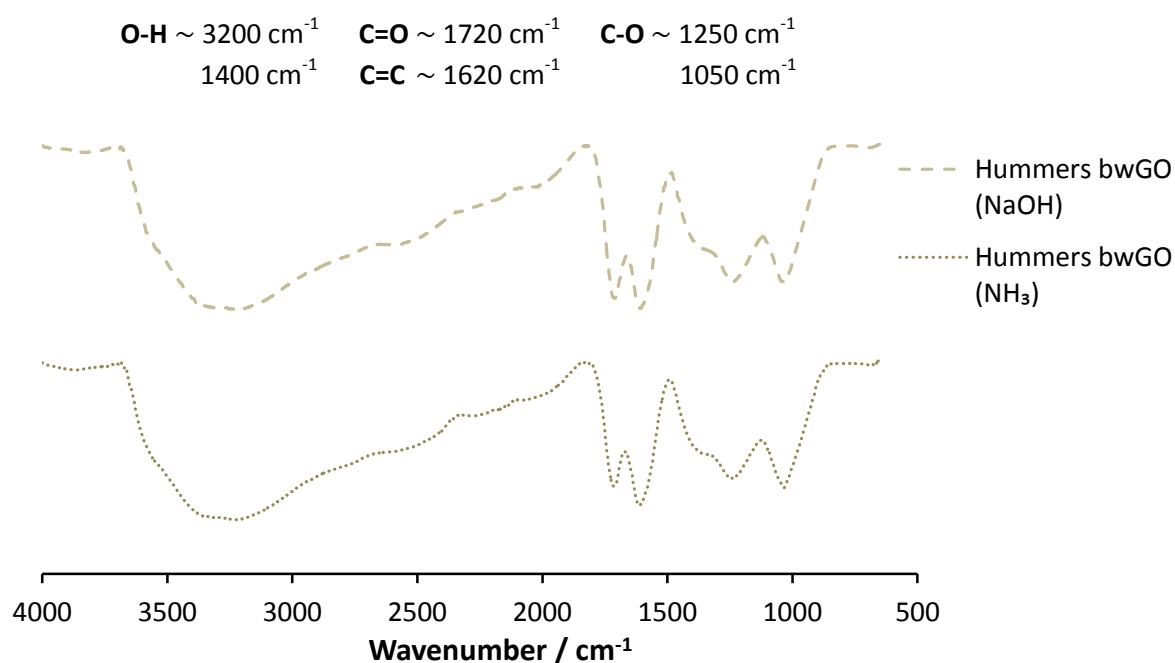
Fig. 3.7 ATR-FTIR spectra of bwGO extracted with NaOH (top) and bwGO extracted with ammonia solution (bottom). Both bwGO samples were obtained from Hummers aGO.

The FTIR spectra shown in figure 3.7 show no dependence on the base used: the same functional groups, in similar quantities, are apparent for both bwGO synthetic routes. Further characterisation was sought from ^{13}C ssNMR.

C=C ~ 130 ppm   C-OH ~ 70 ppm   C-O-C ~ 60 ppm

δ(^{13}C) / ppm
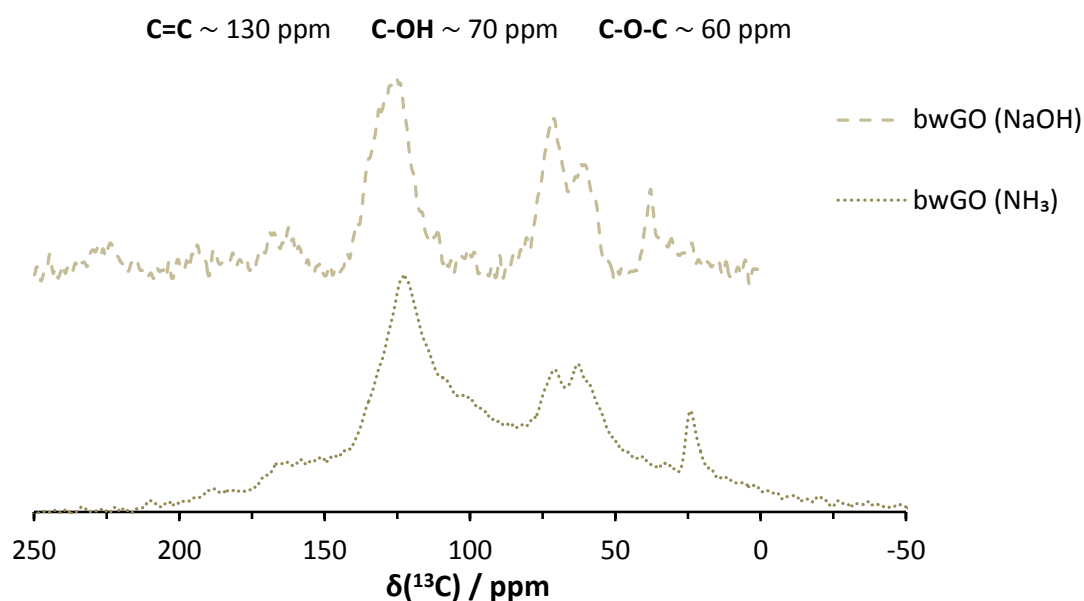
Fig. 3.8 Direct excitation ^{13}C MAS ssNMR spectra of bwGO extracted with NaOH (top) and bwGO extracted with ammonia solution (bottom).

Aside from the signal to noise ratio, the ^{13}C ssNMR spectra of NaOH and NH$_3$ bwGO (figure 3.8) are also very similar. Both show deoxygenation relative to the aGO counterpart. The NH$_3$ bwGO seems to show a greater decrease in the proportion of hydroxide carbons; possibly the ammonia solution is slightly more effective at removing the OD.

D band ~ 1340 cm^{-1} **G band** ~ 1600 cm^{-1} **G' band** ~ 2700 cm^{-1}

Raman shift / cm^{-1}
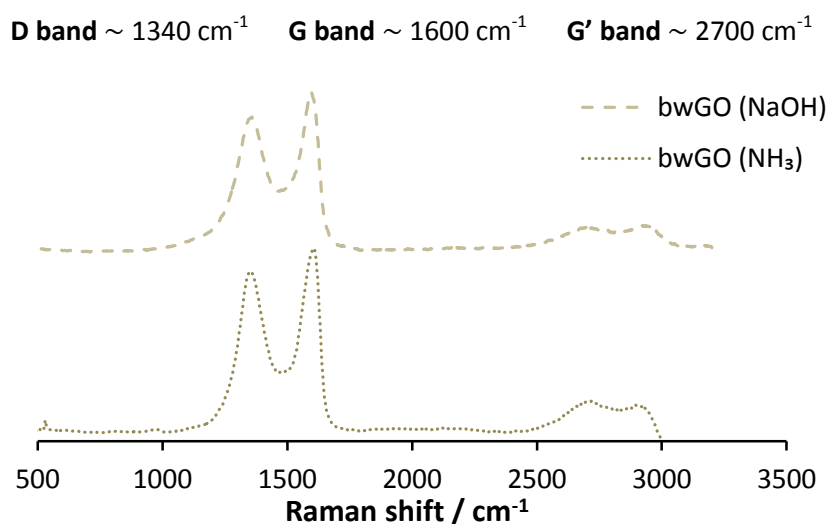
Fig. 3.9 Raman spectra of bwGO washed with NaOH (top) and bwGO washed with ammonia solution (bottom); excitation wavelength 633 nm.

There is no discernible difference between the Raman spectra of the bwGO samples (figure 3.9). Both washes are seen to remove the fluorescence found for aGO, and have the expected D, G and G' bands.

Thus ammonia solutions (0.45 M) were found to work equally as well as NaOH (1 M) at removing the OD that is complexed to the GO sheets. With equivalent preparation times, no significant differences were detected between the bwGO sheets prepared this way, compared with those washed with NaOH. This strongly suggests that bwGO is independent of the base used in the washing procedure.

3.2.1 Dispersibility

One of the physical properties affected by the base washing process is dispersibility. aGO is a hydrophilic material with good dispersibility in a lot of common solvents, including pyridine, methanol and THF. The bwGO materials demonstrate significantly reduced dispersibility in most solvents, however, stable suspensions can still be prepared in DMF, DMSO and a water/acetonitrile mixture.

The photograph below in figure 3.10 shows the difference in dispersibility between aGO (left hand of each pair) and bwGO (right hand of each pair) in three solvents: pyridine, ethanol and a 1:1 water/acetonitrile mixture.
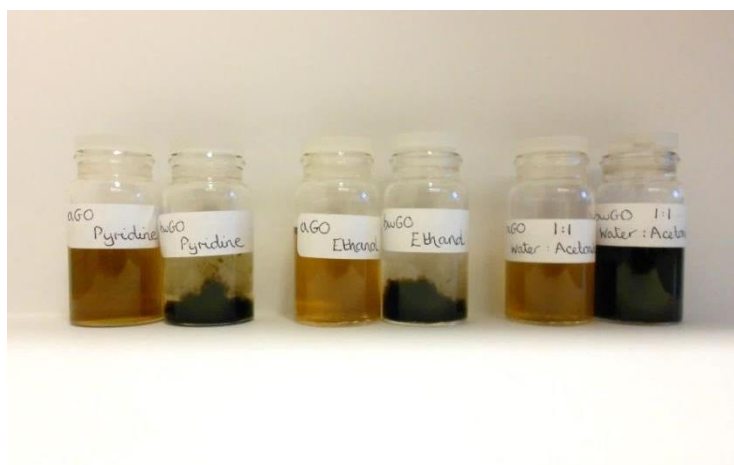
Fig. 3.10 Photograph documenting the reduced dispersibility of bwGO (black) compared to aGO (brown) in a variety of common solvents.

Hansen solubility studies[20] and contact angle (CA) measurements were carried out as a way to quantify the change in dispersibility upon base-washing.

Solvent	aGO	bwGO	δ_d	δ_p	δ_h	$\delta_p + \delta_h$
Water	✓	✓	15.5	16.0	42.3	58.3
DMSO	✓	✓	18.4	16.4	10.2	26.6
1:1 water:CH_3CN	✓	✓	15.4	17.0	24.2	41.2
DMF	✓	✓	17.4	13.7	11.3	25.0
IPA	✓	✗	15.8	6.1	16.4	22.5
Ethanol	✓	✗	15.8	8.8	19.4	28.2
Pyridine	✓	✗	19.0	8.8	19.4	28.2
THF	✓	✗	16.8	5.7	8.0	13.7
Methanol	✓	✗	15.1	12.3	22.3	34.6
Acetone	✓	✗	15.5	10.4	7.0	17.4
Acetic acid	✗	✗	14.5	8.0	13.5	21.5
Acetonitrile	✗	✗	15.3	18.0	6.1	24.1
Petroleum ether	✗	*	17.9	0.7	1.8	2.5
Toluene	✗	*	18.0	1.4	2.0	3.4
Benzene	✗	*	18.4	0.0	2.0	2.0
Diethyl ether	✗	*	14.5	2.9	5.1	8.0
Chloroform	✗	*	17.8	3.1	5.7	8.8

Table 3.1 Hansen solubility study, documenting the dispersibility of aGO and bwGO in a variety of different solvents. ✓ soluble; ✗ insoluble; *Immiscible.

aGO and bwGO dispersions were prepared in a roughly 2:1 water:acetonitrile mixture at 1 mg ml^{-1}. 9 ml of solvent was added to 1 ml of the 1 mg ml^{-1} dispersions and the mixtures were vigorously shaken. Dispersibility was assessed immediately and then again after being allowed to settle for 24 hours, no differences were observed with time, and thus these dispersions are considered to be stable. The results can be seen above in table 3.1. In terms of Hansen solubility parameters[20] – δ_d, dispersion; δ_p, polarisation; and δ_h, hydrogen bonding – generally it seems that acceptable dispersibility is found in solvents with a δ_p greater than 13 for bwGO, and a δ_p greater than 8 for aGO.[21]

The solubility measurements indicate that aGO is more hydrophilic than bwGO, and this is also supported by the CA measurements taken from the drop shape analysis shown in figure 3.11.
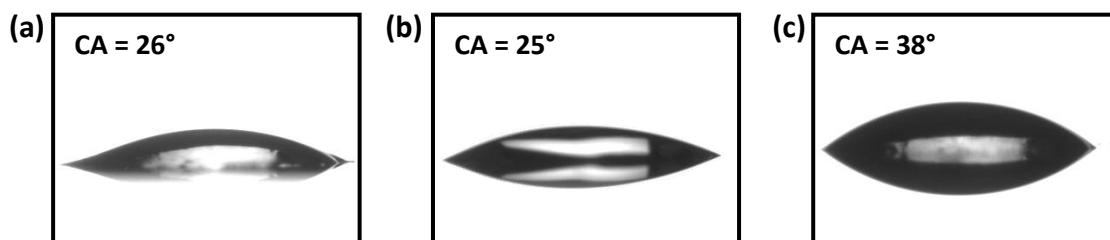
Fig. 3.11 Drop shape analysis of **(a)** Hummers aGO, **(b)** Hummers OD (extracted with NH$_3$), and **(c)** Hummers bwGO.

Figure 3.11 shows that aGO and OD have a similar contact angle with water, indicative of highly hydrophilic materials. The 26° contact angle for aGO is comparative with literature values,[22] however removing the OD was found to significantly increase the contact angle (38°). This ties in with the reduced dispersibility and higher C/O ratio of bwGO.

To conclude, the OD acts as a surfactant to stabilise GO in solution, making aGO a very versatile material which is easy to manipulate chemically. However, in order to disregard concerns over competing reactions and altered properties, the OD should be removed as completely as possible before any further chemistry takes place.

3.3   Oxidation Protocols

Graphene oxide can be synthesised using a number of different oxidation protocols. Namely by the Brodie/Staudenmaier routes[23, 24] which use potassium chlorate in a mixture of fuming nitric acid and concentrated sulfuric acid, or by the Hummers method[25] which uses a potassium nitrate and potassium permanganate mixture in concentrated sulfuric acid. Recently, different refinements of the methodologies have also been reported: the "improved" Hummers synthesis[26] which uses a mixture of phosphoric and sulfuric acid with a greatly reduced oxidation time, as published by the Tour research group; and the "pristine" GO synthesis[27] which uses a permanganate oxidation and an anhydrous workup. The "pristine" GO can then be hydrolysed by treatment with water to give a more conventional aGO. The authors believe that this hydrolysis step is very important for the controlled synthesis of their GO material, and refer to the step as quenching. From this point on, these two modified GO materials are referred to as "Tour GO" and "Quenched GO" respectively.

Whilst the Hummers synthesis provides a convenient route to GO, due to the popularity of other protocols, it was prudent to investigate those also. The different GO materials were investigated to see whether there were any substantial differences between them, and in particular whether or not the presence of OD was specific to Hummers aGO.

Aqueous dispersions of the aGO formed via the chlorate oxidation (Brodie) and those from the permanganate oxidations (Hummers, Tour and Quenched) look similar: all four are golden brown. On evaporation, the materials are more easily distinguished: the chlorate material is noticeably lighter in colour. Following a wash with aqueous NaOH, all four materials darken substantially becoming dark brown/black, and it was possible to collect roughly one third of the original mass as very lightly coloured OD from all samples.

O-H ~ 3200 cm^{-1} C=O ~ 1720 cm^{-1} C-O ~ 1250 cm^{-1}
1400 cm^{-1} C=C ~ 1620 cm^{-1} 1050 cm^{-1}
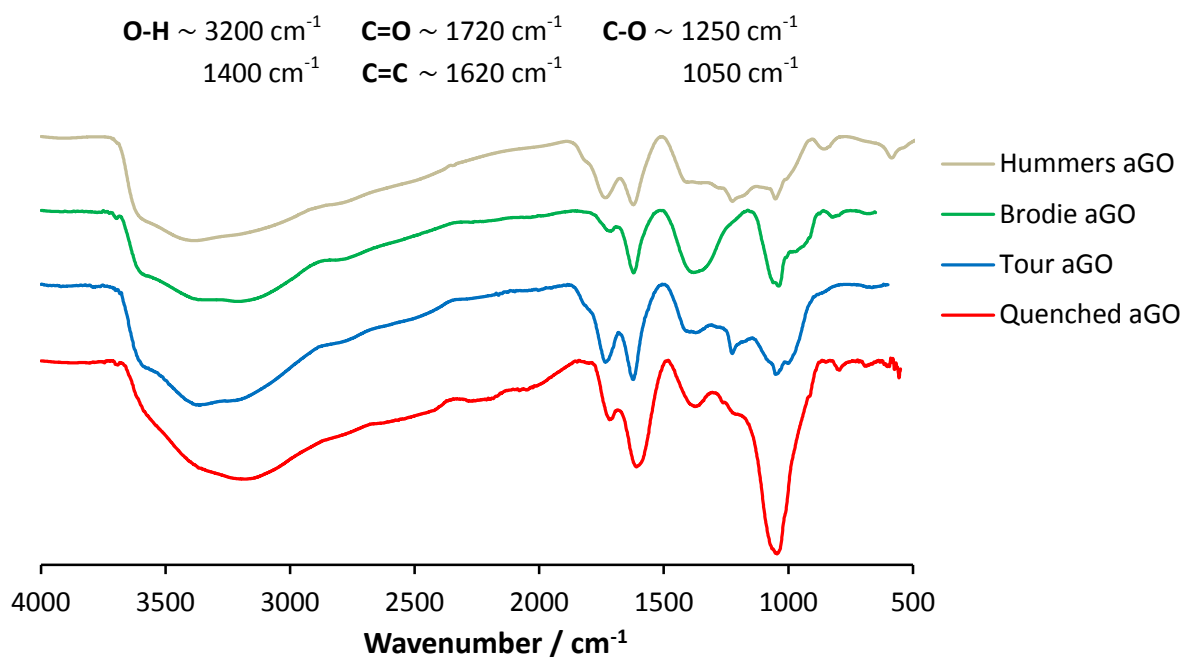
Fig. 3.12 ATR-FTIR spectra comparing aGO from four different synthetic routes: Hummers, Brodie, Tour, and Quenched.

The FTIR spectra shown in figure 3.12 show the same functional groups for all four aGO materials, with some variation. The main differences can be seen for Quenched aGO, which appears to have a higher proportion of C-O alkoxy groups; and for Brodie aGO which shows little contribution from carboxylic acid and ketone groups.
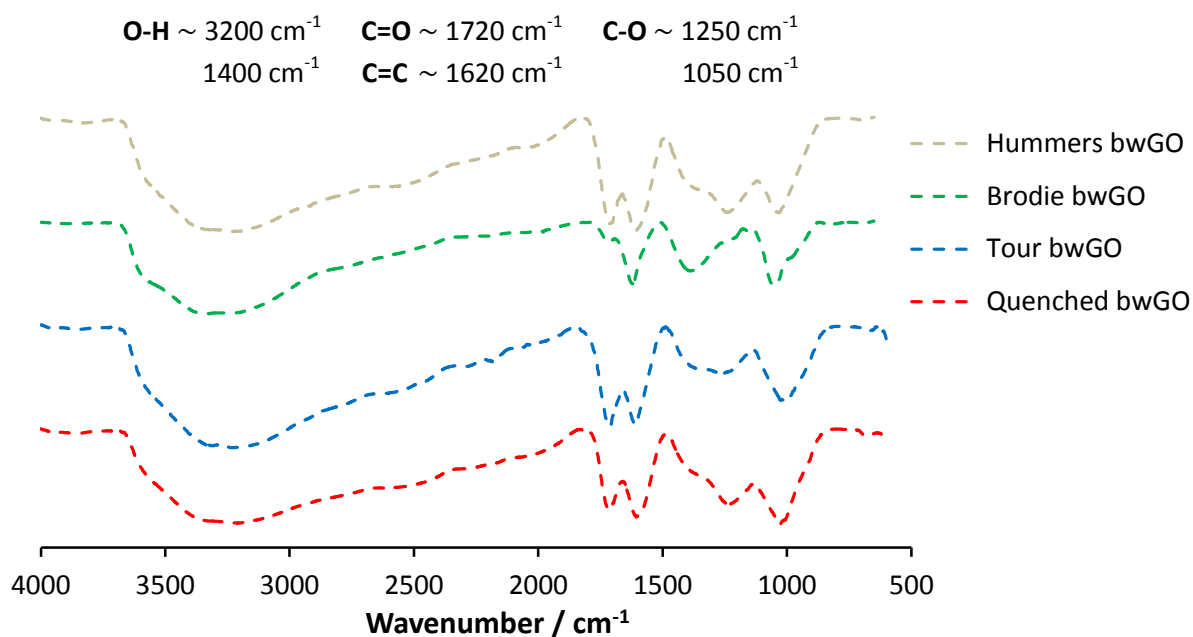
Fig. 3.13 ATR-FTIR spectra comparing bwGO from four different synthetic routes: Hummers, Brodie, Tour, and Quenched.

After the basic wash, the FTIR spectra of the permanganate bwGO materials (Hummers, Tour and Quenched GO) are very similar (figure 3.13). This suggests that the differences seen in figure 3.12 arise primarily from the presence of OD. The FTIR spectrum of the chlorate bwGO material (Brodie GO), however, still suggests fewer carboxylic acid and ketone groups. This is thus likely to be a symptom of the original oxidation protocol.
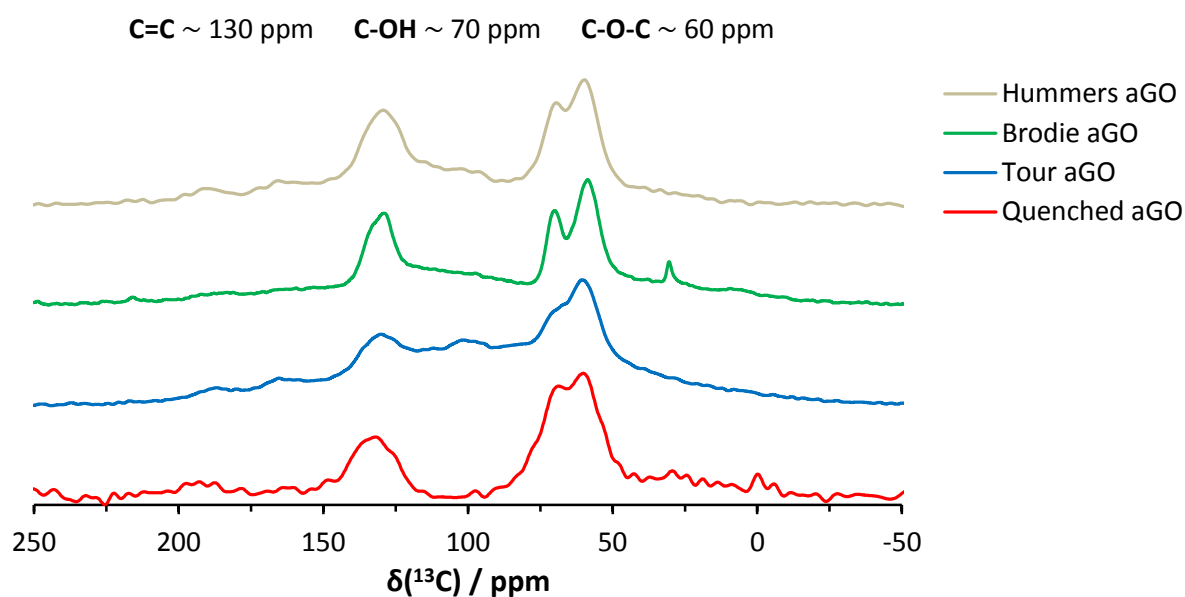
Fig. 3.14 Direct excitation ^{13}C MAS ssNMR spectra of Hummers (brown), Brodie (green), Tour (blue) and Quenched (red) aGO.

The ssNMR spectra for the different aGO materials, shown in figure 3.14, show clear similarities: The sp^2 carbon signal is clearly observable in each spectrum, as are the epoxide and hydroxide carbons. The Brodie spectrum correlates with its FTIR, showing little signal intensity arising from the COOH and C=O groups. The peak at roughly 100 ppm seen weakly for Hummers and strongly for Tour aGO is likely to be due to the presence of 5 and 6 membered ring lactols.[28]
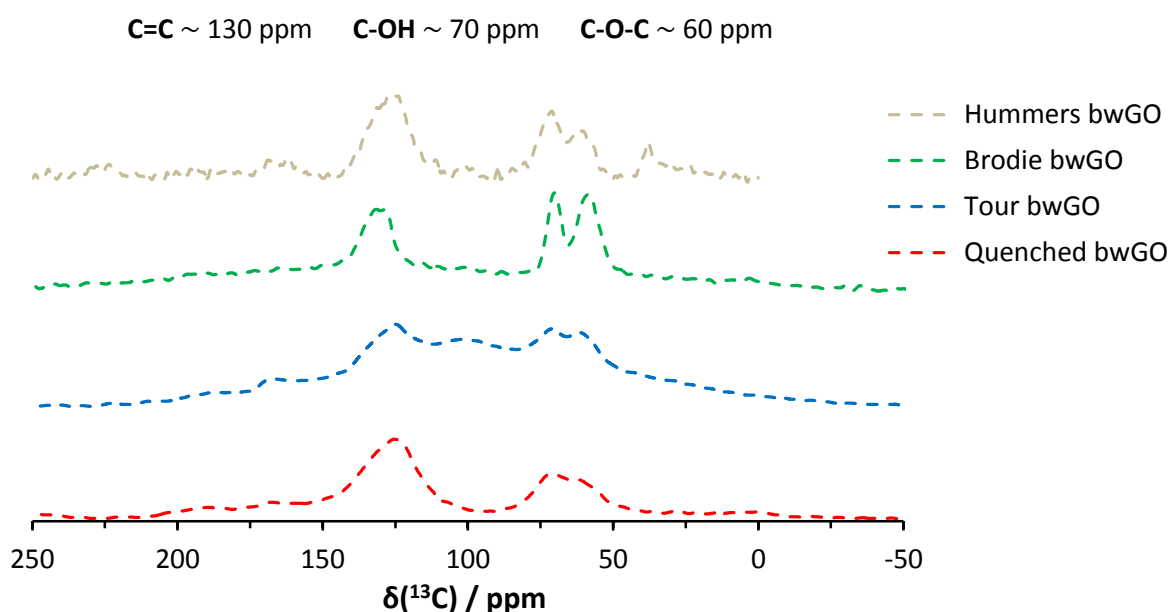
Fig. 3.15 Direct excitation ^{13}C MAS ssNMR spectra of Hummers (brown), Brodie (green), Tour (blue) and Quenched (red) bwGO.

The ssNMR spectra of the bwGO samples (figure 3.15) help to identify which functional groups belong to the bwGO sheets, and which belong to the OD. All four samples show a decrease in hydroxide and epoxide carbons relative to the graphitic carbons; correlating with the FTIR results previously discussed. The intensity of the lactol signals at 100 ppm however, do not noticeably decrease upon base washing, suggesting that the lactols are part of the GO sheets themselves.

EDX measurements (table 3.2) show that all four of the aGO materials tested are similarly affected by the base-washing procedure: an increased C/O ratio is seen for the respective bwGO materials.

	aGO atomic % (standard deviation)				bwGO atomic % (standard deviation)				
	C	**O**	**S**	**C/O**	**C**	**O**	**Na**	**Cl**	**C/O**
Hummers	58 (1)	40 (2)	-	**3:2**	76 (1)	21 (1)	1.9 (0.4)	1.0 (0.1)	**7:2**
Brodie	51 (2)	45 (1)	1.9 (1)	**9:8**	77 (1)	22 (1)	-	0.4 (0.2)	**7:2**
Tour	58 (2)	38 (1)	2.8 (0.5)	**3:2**	76 (1)	22 (1)	0.7 (0.3)	0.4 (0.1)	**7:2**
Quenched	72 (1)	27 (1)	-	**8:3**	77 (2)	18 (1)	1.1 (0.2)	1.2 (0.4)	**4:1**
Average	60 (2)	38 (1)	1.2 (0.4)	**2:1**	77 (1)	21 (1)	0.9 (0.2)	0.8 (0.2)	**4:1**

Table 3.2 Atomic composition and C/O ratios for all aGO and bwGO materials as measured by EDX.

Raman spectroscopy was then used to measure any changes in the structural integrity of the GO materials.
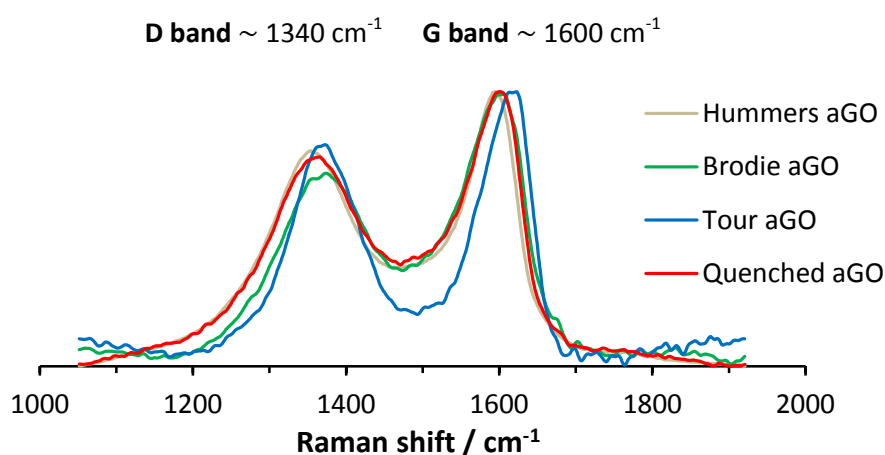
Fig. 3.16 Raman spectra showing D and G bands for all four aGO materials; excitation wavelength 514 nm.

D band ~ 1340 cm^{-1} **G band** ~ 1600 cm^{-1}
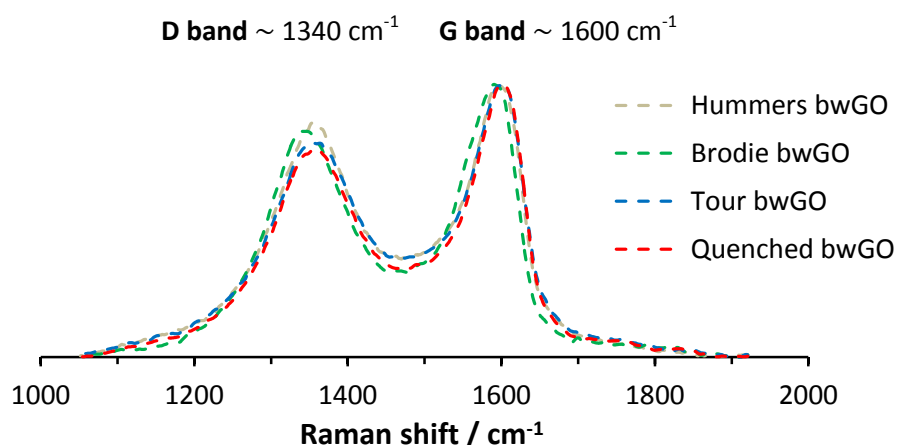
Fig. 3.17 Raman spectra showing D and G bands for all four bwGO materials; excitation wavelength 514 nm.

The Raman spectra can be peak fitted to give separate D and G bands, which can then integrated to calculate the relative areas, and hence the D/G ratio. A change in the D/G ratio is indicative of a structural change of the graphene-like sheets.

	aGO			bwGO		
	D_{area}	G_{area}	**D/G** ($\pm$ 0.1)	D_{area}	G_{area}	**D/G** ($\pm$ 0.1)
Hummers	172.2	137.1	**1.3**	182.2	109.4	**1.3**
Brodie	129.6	121.5	**1.1**	157.9	139.8	**1.1**
Tour	138.4	111.4	**1.2**	178.7	140.5	**1.3**
Quenched	170.8	139.7	**1.2**	165.4	135.6	**1.2**

Table 3.3 Peak areas and D/G ratios for all aGO and bwGO materials.

The Raman studies (figures 3.16 and 3.17) show no notable differences between any of the aGO materials, and there is no significant change in the D/G ratio upon the removal of the OD (table 3.3). This D/G ratio of roughly 1.2 for all samples matches the findings of other researchers.[29]
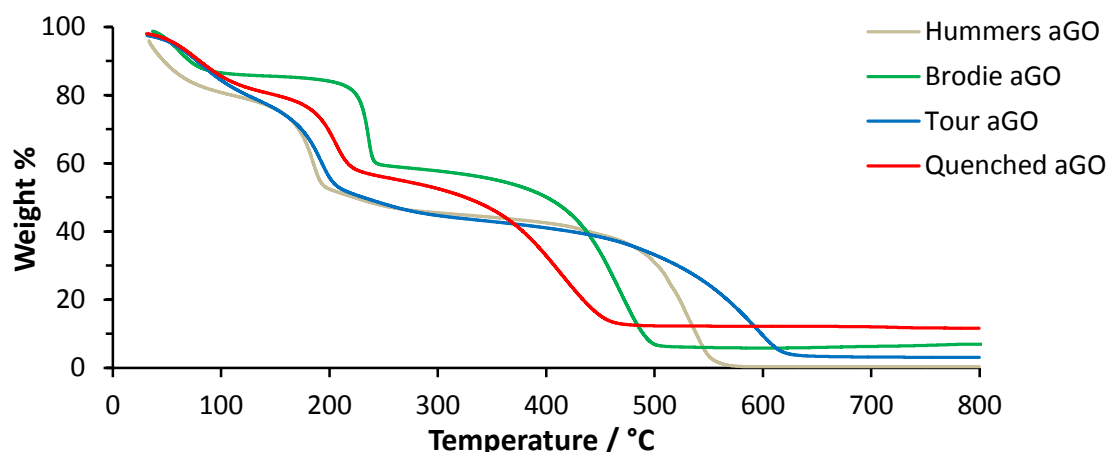
Fig. 3.18 TGA profiles of Hummers, Brodie, Tour and Quenched aGO.

Shown in figure 3.18 are the TGA profiles of the four different aGO materials. For each sample there appears to be mass loss at three distinct temperatures: the mass loss which occurs below 100 °C is believed to be due to the loss of adsorbed water; the mass loss seen at around 200 °C, which consitutes roughly one third of the total mass loss, is believed to be due to the loss of OD; and lastly, the high temperature mass loss is due to the decomposition of the graphene-like sheets.

To maintain good dispersibility for further reactions, the OD was only partially removed with a short base wash. However, the results are already obvious from a change in the TGA profiles for bwGO, seen in figure 3.19.
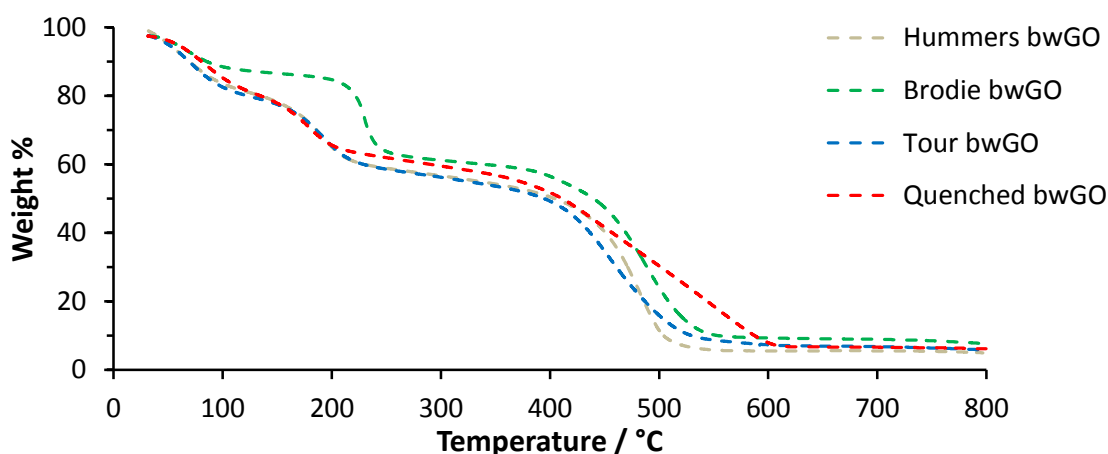
Fig. 3.19 TGA profiles of Hummers, Brodie, Tour and Quenched bwGO.

Comparing the TGA of figures 3.18 and 3.19, it can be seen that the thermal stability of the Quenched GO in particular increases significantly on base washing. This ties in with the FTIR

studies which showed Quenched aGO to have a high level of hydroxyl incorporation. Hydroxyl and epoxy sites are believed to initiate the thermal decomposition pathway of GO,[30] which could theoretically result in a lower thermal decomposition temperature. Once the OD is removed (figure 3.19), the samples show similar TGA profiles with similar thermal stability.

Further to the discussion in section 3.2, drop shape analysis was carried out on all of the GO samples in order to monitor the degree of hydrophilicity. Contact angles of between 22° and 30° were measured for the samples of aGO (figure 3.20).
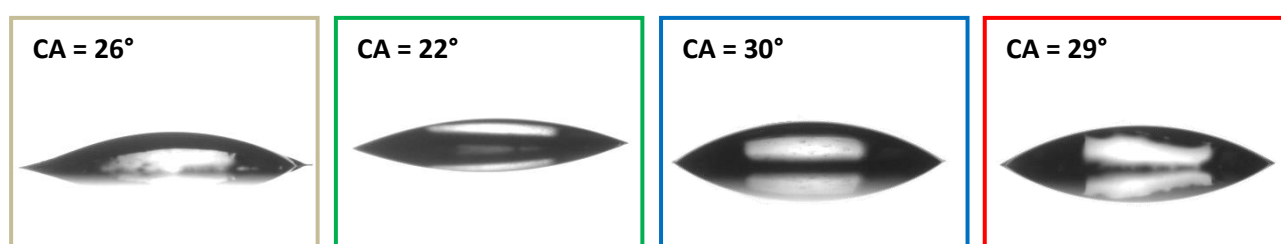
Fig. 3.20 Drop shape analysis of Hummers (brown outline), Brodie (green), Tour (blue) and Quenched (red) aGO.
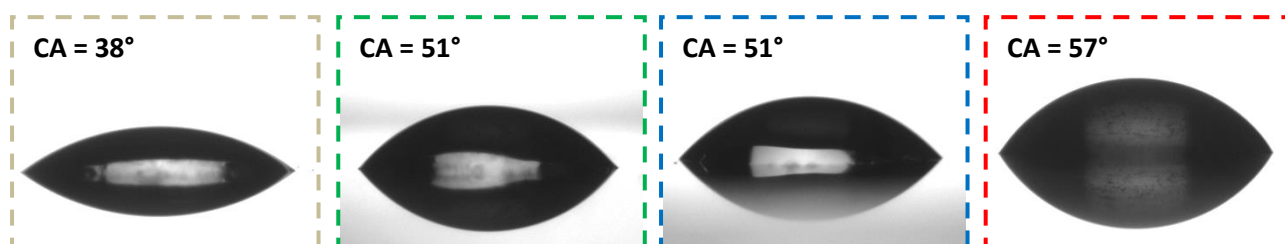
Fig. 3.21 Drop shape analysis of Hummers (brown outline), Brodie (green), Tour (blue) and Quenched (red) bwGO.

For the bwGO materials, contact angles of between 38° and 57° were measured (figure 3.21). As expected, a clear decrease in hydrophilicity is seen as a result of the base washing.

All the characterisation data collected suggests that there are no significant differences in the four GO materials formed from the different oxidation protocols. The only minor variance found was that aGO prepared via the chlorate oxidation route showed little evidence for the presence of carboxylic acid and ketone groups.

3.4 Oxidative Debris

The OD collected via an ammonia wash needs no subsequent neutralisation because any excess ammonia is removed when the solvent is evaporated and dried under vacuum, although it is likely that any carboxylic acids would then be present as the ammonium salt. By contrast, a significant quantity of NaOH (typically 90% of the sample by mass) remains after a NaOH wash. To simplify the handling of these samples, they are normally neutralised with aqueous HCl; consequently, OD samples collected via NaOH washing contain significant quantities of NaCl (>95% by mass). When a measured quantity of NaOH is used, it is possible to calculate the quantity of NaCl present in the final sample. The OD collected via a NaOH wash is normally slightly off-white, while that from an ammonia wash is pale yellow.

The low molecular weight nature of OD has been established previously,[1] and repeated TEM and AFM investigations again confirmed this analysis: neither technique showed the presence of any sheet-like material in the OD. The fact that AFM does not resolve the presence or absence of OD on the graphene-like sheets is unsurprising: the expected lateral dimensions of the OD (likely to be <1 nm) are small, and the coverage is high. Since the bwGO sheets contribute roughly twice the mass (to aGO) than OD, roughly one-quarter of a bwGO sheet surface is expected to have OD complexed to it. This suggests that the separation between the OD fragments would be ~1 nm: significantly less than the AFM tip diameter and thus lower than the lateral resolution of the AFM. At the same time, the expected thickness of the OD (~0.5 nm) is less than the roughness of the GO, again meaning that it is extremely unlikely to be resolved.

A variety of spectroscopic data was collected for OD in an attempt to gather more concrete structural characterisation.

O-H ~ 3200 cm^{-1} NH$_4^+$ ~ 3000 cm^{-1} C=O ~ 1720 cm^{-1} C-O ~ 1250 cm^{-1}
1400 cm^{-1} C=C ~ 1620 cm^{-1} 1050 cm^{-1}
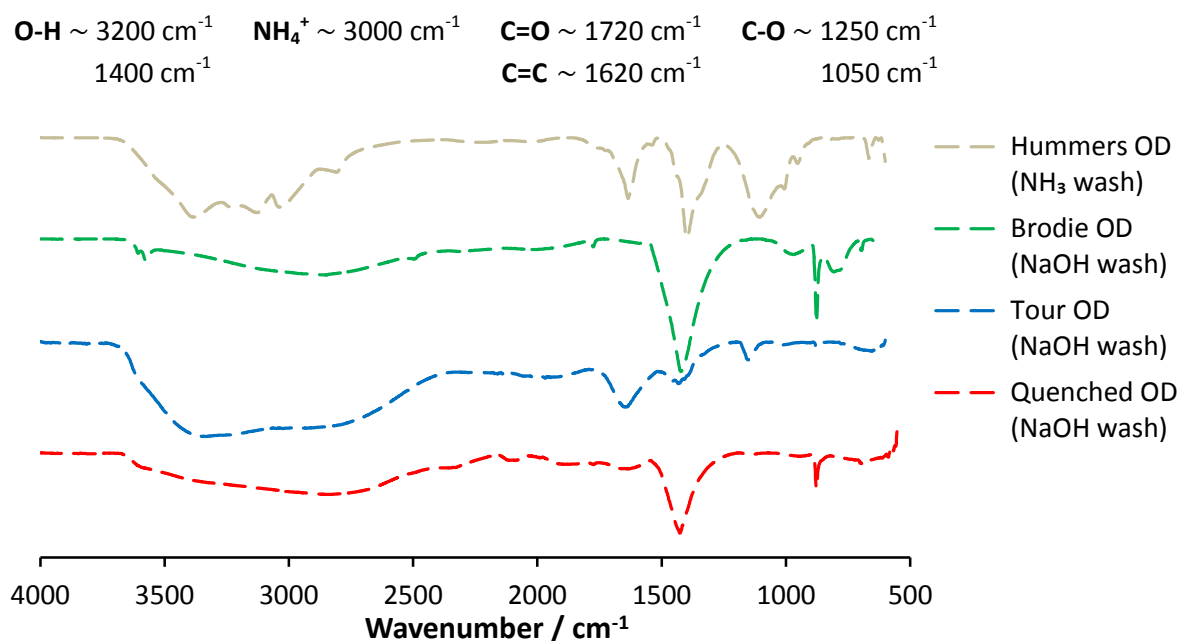
Fig. 3.22 ATR-FTIR spectra of OD extracted from four different aGO materials: Hummers, Brodie, Tour and Quenched.

The FTIR spectra of the OD materials (figure 3.22) contain similar functional groups to the bwGO materials, with main contributions from O-H, C=C and aromatic C-H. The sample of Hummers OD for figure 3.22 was extracted with NH$_3$, whereas the Brodie, Tour and Quenched OD were extracted with NaOH. The presence of ammonium salts is evident in the FTIR of Hummers OD by the bands around 3000 cm^{-1}. The broad OH stretch extending to 2500 cm^{-1} in the other three samples is characteristic of COOH groups.

Further characterisation on the OD was sought, and hence further spectroscopic studies were carried out on the OD derived from our preferred GO synthesis: Hummers. The Raman spectrum of OD (figure 3.23) shows no evidence of D or G bands, implying that the organic fragments contain no large graphitic regions. This is in contrast to the aGO and bwGO materials. The OD is highly fluorescent, which obscures any other low intensity signals which might contain information on the structure.
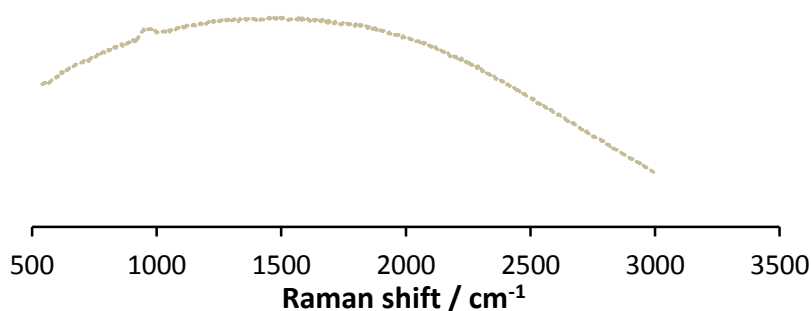
Fig. 3.23 Raman spectrum of OD; excitation wavelength 633 nm.

To learn more from the Raman spectrum of OD, Surface Enhanced Raman Spectroscopy (SERS) was used. A substrate was prepared by creating a rough Ag surface on silicon,[31] and a solution of OD in water was then drop cast onto the surface.

Si ~ 500 cm^{-1} **C-O-C** ~ 1000 cm^{-1} **C-H** ~ 1400 cm^{-1} **C=C** ~ 1600 cm^{-1}
3100 cm^{-1}
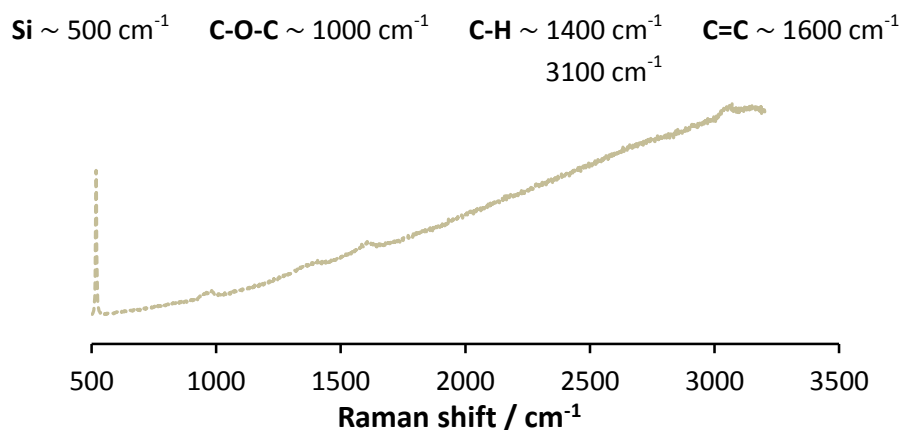
Fig. 3.24 SERS spectrum of OD; excitation wavelength 514 nm.

Using SERS (figure 3.24) has reduced the distortion in the spectrum of OD, caused by its fluorescence. Small assignable peaks have been revealed, but it is clear that prominent D and G bands are still absent.
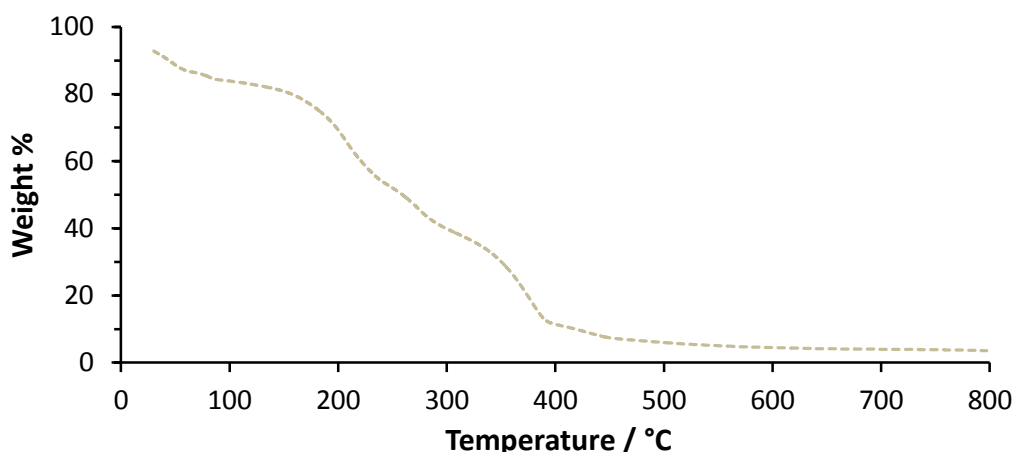
Fig. 3.25 TGA profile of Hummers OD (washed with NH_3).

The TGA profile of OD (figure 3.25) shows certain similarities to the aGO and bwGO materials: mass loss is seen below 100 °C due to the loss of adsorbed water, as well as a fairly sharp mass loss at around 200 °C. However, the OD shows complete mass loss before 400 °C, it is thus less thermally stable than the aGO and bwGO samples by more than 100 °C. This spectrum supports the idea that the mass loss seen at 200 °C for the aGO samples (and less so for the bwGO samples) is due to the presence of the OD.

As low molecular weight molecules, the OD is suitable for solution NMR studies. The ^{1}H and ^{13}C spectra are shown in figures 3.26 and 3.27 respectively.
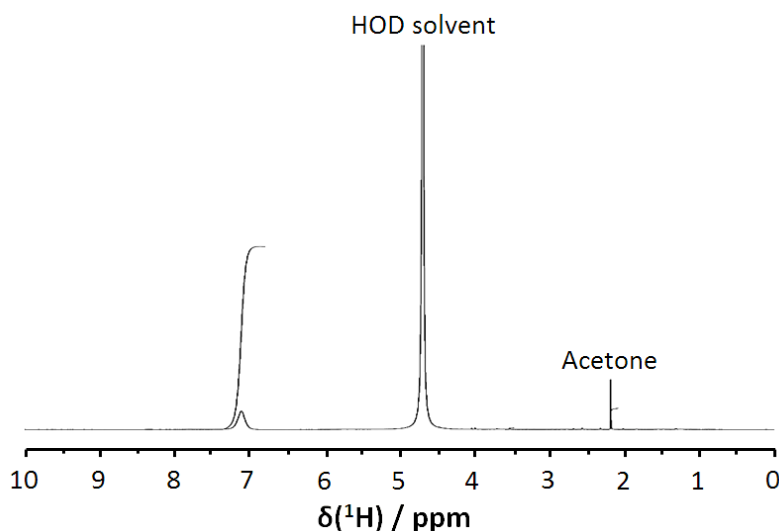
Fig. 3.26 Directly observed ^{1}H solution NMR of Hummers OD, referenced to external tetramethylsilane.
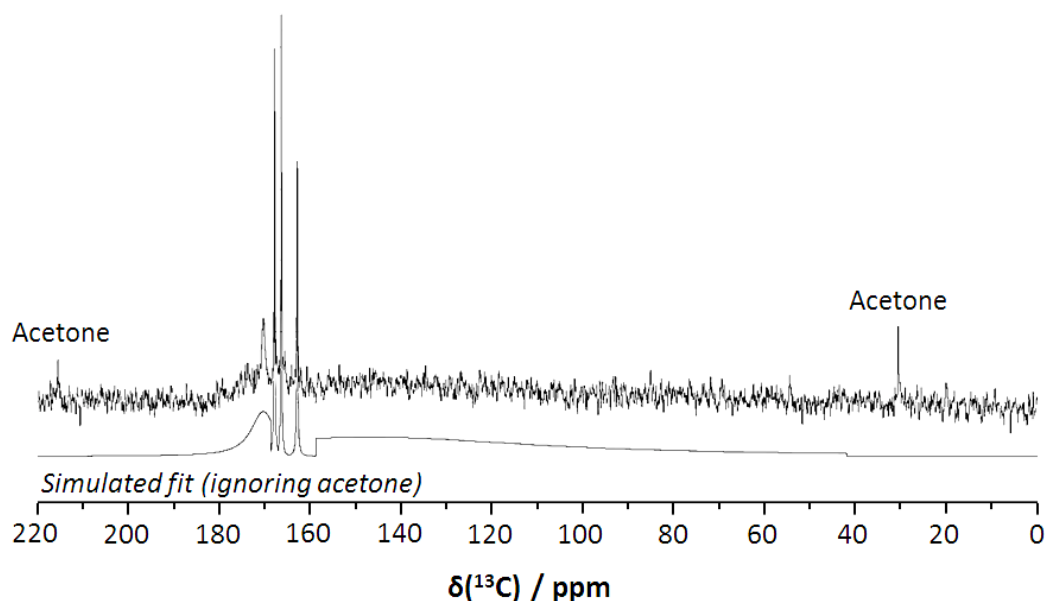
Fig. 3.27 Directly observed with gated decoupling ^{13}C solution NMR of Hummers OD, referenced to external tetramethylsilane.

The ^{1}H solution NMR spectrum of Hummers OD (extracted with NH_3) in D_2O solvent reveals little: a broad resonance between 7.0 and 7.2 ppm is indicative of a large number of aromatic environments for the hydrogens. Carboxylic acid and alcohol protons would not be expected to show up in such a spectrum as these protons are readily exchanged for the NMR silent deuterium present in the solvent. The ^{13}C NMR spectrum is more revealing: as well as sharp peaks at 162.8, 166.4, and 167.9, there is a broad peak at 170.3 ppm and a large underlying, very broad, peak between 180 and 160 ppm; a further very broad peak exists between 110 and 160 ppm. The broad peak between 160 and 180 ppm can be ascribed to multiple carboxyl carbon (esters, lactones and acids) resonances and the presence of ketones and aldehydes (expected chemical shift 190–210 ppm) can be ruled out in significant quantities. The broad peak between 110 and 160 ppm presumably arises from a large number of signals from aromatic type carbons (for example, a simple benzene ring resonance is expected at 128 ppm, a benzene ring with a carboxyl group at 131 ppm, and one with an OH at 155 ppm). Thus, the solution NMR spectra are consistent with OD being a large number of different compounds with the same type of functional groups as aGO. The insolubility of the OD in solvents other than water is consistent with these observations: highly carboxylated materials would not be expected to be soluble in organic solvents.

81

While solution NMR will show the average composition, mass spectra will be dominated by compounds that readily ionize and fly. Thus, a mass spectrum might show strong peaks that are actually only present in low proportions. With that caveat, mass spectra were recorded using two different ionization techniques: Electrospray Ionisation (ESI) and Matrix Assisted Laser Desorption Ionisation (MALDI). Each technique gives a different result, but both techniques show ranges of signals between 200 and 900 m/z. Accurate mass analysis allowed a formula to be assigned to some signals; identifying a range of small, highly oxidised organic fragments.

The assignable peaks from ESI are given below alongside their calculated formulas and expected masses in parentheses. Note that since all measured peaks have a single positive charge from protonation, the formula of the neutral species has one less hydrogen; also note that it was not possible to identify the relative proportions of these materials present.

209.1168 ($C_{12}H_{17}O_3$ 209.1172)

213.1479 ($C_{12}H_{21}O_3$ 213.1485)

227.1275 ($C_{12}H_{19}O_4$ 227.1278)

305.2774 ($C_{20}H_{33}O_2$ 305.2475)

309.2050 ($C_{18}H_{29}O_4$ 309.2060)

319.2283 ($C_{20}H_{31}O_3$ 319.2268)

337.2376 ($C_{20}H_{33}O_4$ 337.2373)

353.2680 ($C_{21}H_{37}O_4$ 353.2686)

359.2428 ($C_{19}H_{35}O_6$ 359.2428)

393.2122 ($C_{18}H_{33}O_9$ 393.2119)

481.2654 ($C_{22}H_{41}O_{11}$ 481.2643)

657.2775 ($C_{31}H_{45}O_{15}$ 657.2753)

MALDI-TOF gave the following ions using 2,5-dihydroxybenzoic acid (DHB) and α-cyano-4-hydroxycinnamic acid (CHCA) as matrices:

294.070 ($C_{17}H_{12}O_4N$ 294.07665) DHB

335.103 ($C_{19}H_{15}O_4N_2$ 335.1032) DHB

656.060 ($C_{34}H_{17}O_{13}Na$ 656.0567) CHCA + NaI

877.089 ($C_{41}H_{23}O_{20}N_3$ 877.0876) DHB

The C=C bonds in graphene are known to be 0.140 nm, thus using basic trigonometry we can calculate the width and diameter of a carbon ring of graphene. Whilst these dimensions will not be exact for GO, they can be used as a basic estimate. The structure in figure 3.28 shows an example structure of $C_{34}H_{17}O_{13}Na$, which was a peak identified using MALDI spectroscopy. This representative structure shows a lactol group, hydroxides, epoxides and carboxylic acids which are all believed to be present on OD from solution NMR and FTIR studies. This molecule is expected to be around 1 nm in size.
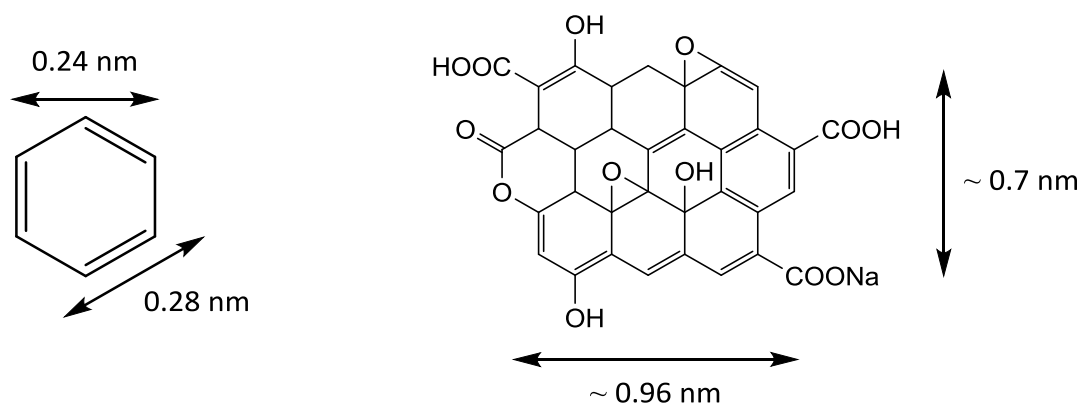
Fig. 3.28 Representative structure of an OD molecule as identified by MALDI spectroscopy – $C_{34}H_{17}O_{13}Na$. Note that the Na is a result of the sample-matrix mixture used.

3.5   Fluorescence

In recent years, interest in carbon-based fluorescent materials has increased. Compared to conventional materials, carbon-based ones often show greater stability, biocompatibility and lower cytotoxicity; properties which are of great advantage in biological applications.[32] Examples of such luminescent materials include graphene oxide (GO) and its derivatives:[33] carbon nanoparticles[34] and quantum dots;[35] carbon nanotubes;[3, 36] nanodiamonds;[37] and fullerenes.[38]

aGO is well known to be a fluorescent material,[39] but what is not clear, is whether the fluorescence is truly a function of the graphene-like sheets, or whether it stems from the presence of the OD.

During Raman studies, the OD exhibited strong fluorescence. This prompted an investigation into the optical properties of the GO materials. A sample of aGO was initially base-washed using aqueous ammonia. The obtained bwGO (neutralised) and OD materials were both dried under vacuum, as was a sample of the original aGO.
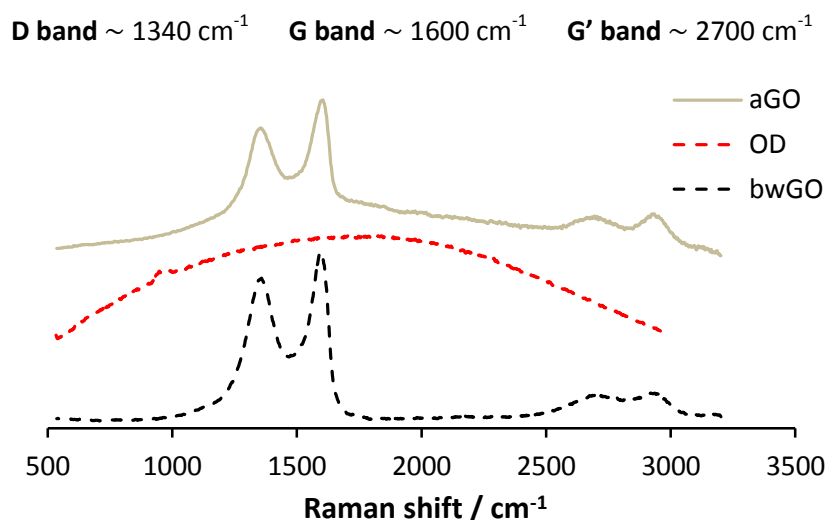
Fig. 3.29 Raman spectra of aGO (brown), bwGO (black) and OD (red); excitation wavelength 633 nm.

Figure 3.29 shows the Raman spectra of these three aGO, bwGO and OD samples. Both bwGO and aGO show strong, and broad, D and G peaks characteristic of defective functionalised graphene. The D and G peaks are almost indistinguishable between aGO and

bwGO, however bwGO shows substantially reduced fluorescence compared with aGO. Meanwhile, the OD shows just fluorescence, with no evidence for any graphitic fragments (i.e. no D or G bands). A similar result has been seen previously for SWCNTs, where a simple NaOH treatment removed carboxylated carbonaceous fragments that were shown to be fluorescent.[3]

In order to establish the photoluminescent properties of aGO and its constituent parts, dispersions of the samples used in Raman (figure 3.28) were prepared. The original aGO and the obtained OD were dispersed in water, while the obtained bwGO was dispersed in acetonitrile.

Figure 3.30 compares the fluorescence spectra of these aGO, OD, and bwGO dispersions, acquired under excitation at a wavelength of 400 nm. The dispersions were made up at 0.75 mg ml^{-1} for aGO and 0.5 mg ml^{-1} for both bwGO and OD. The spectra were scaled to the concentration expected in aGO (aGO is roughly composed of ⅔ bwGO and ⅓ OD by weight).
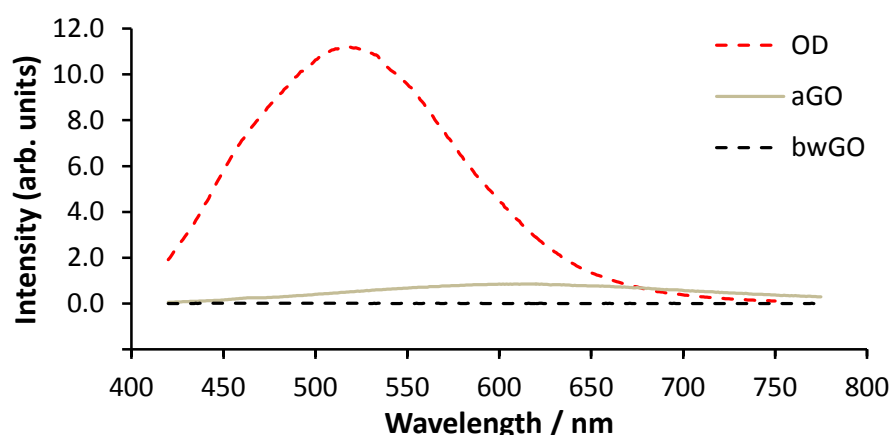
Fig. 3.30 Fluorescence spectra of OD (0.5 mg ml^{-1} in water), aGO (0.75 mg ml^{-1} in water) and bwGO (0.5 mg ml^{-1} in acetonitrile). The spectra were taken under identical conditions (room temperature; excitation wavelength 400 nm) but the intensity of the OD spectra has been reduced by a factor of 2 to mimic its expected concentration in aGO.

The aGO spectrum shows a broadband emission peaking at around 610 nm, similar to previous reports in literature.[32, 40-42] The emission peak is well fit by a lognormal distribution and has a full width half maximum (FWHM) of 230 nm. The isolated OD fluoresces more strongly than the aGO, with a sharper blue-shifted emission. The emission peak is again well

fit by a lognormal distribution with a maximum intensity at around 520 nm and a narrower FWHM of 140 nm. By weight, the observed fluorescence here is >20 times more intense for the OD than for the aGO. No luminescence is observed for bwGO. There is thus a striking evolution in the optical properties of graphene oxide upon washing with base; the graphene oxide itself no longer fluoresces whilst strong blue-shifted fluorescence is observed in the fragmentary oxidation debris.

In order to try and understand how the change in the fluorescence of the GO evolves, an aqueous dispersion of aGO in a spectrometer cuvette was treated with aqueous NaOH. Even at low concentrations of NaOH, the dispersion of GO darkens instantly, but if added at sufficient concentration, the graphene oxide begins to separate into a black/brown coagulant and a colourless solution, as shown by the image in figure 3.31.
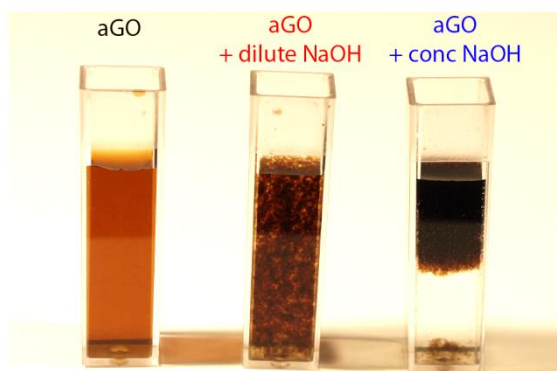
Fig. 3.31 Photograph of graphene oxide dispersions in water: (left) 0.75 mg ml^{-1} aGO; (centre) after the addition of dilute NaOH; and (right) after the addition of concentrated NaOH.

As mentioned in section 3.2.1, the OD acts as a surfactant to stabilise bwGO dispersions. The OD itself is water soluble due to the high proportion of oxygenated groups, and in aGO may conceal hydrophobic graphene-like regions of the bwGO sheets through π-π stacking interactions. When NaOH or NH$_3$ is added to aGO the π-π stacking interactions and hydrogen bonds are disrupted, splitting apart the bwGO sheets and the OD. Similar to the salting out effect, the exposed hydrophobic regions of the bwGO sheets cause them to precipitate out of solution. This separation of the bwGO and OD was found to be irreversible – it is likely that after sufficient removal of the OD, the bwGO sheets crumple up to minimise hydrophobic interactions.

Agitating the sample of aGO with *in situ* dilute NaOH encouraged separation of the mixture, allowing the fluorescence spectra to be recorded separately through the colourless fraction and through the coagulated material. The colourless fraction, from the separated aGO + dilute NaOH sample, showed the intense blue-shifted fluorescence of the OD, whilst the coagulated material showed essentially no fluorescence – the thick black coagulant likely absorbs the excitation energy and any emission. Figure 3.32 shows an increase in absorbance for the coagulated fraction (compared to aGO) across the excitation and emission wavelengths, this makes it difficult to disentangle changes in emission from changes in absorption. Meanwhile the OD is almost transparent across the visible range.
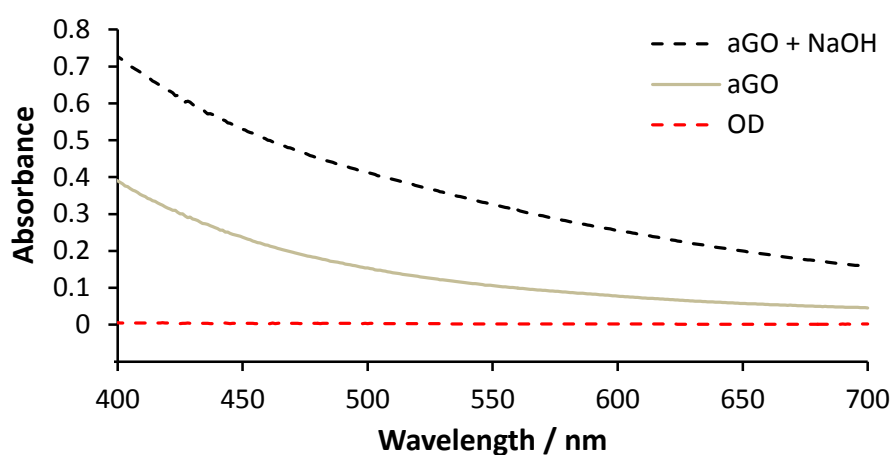
Fig. 3.32 UV-visible absorption spectra from 1 mg ml^{-1} oxidation debris (red), and 0.1 mg ml^{-1} aGO before (brown) and after (black) the addition of dilute NaOH.

Greater insight into the material properties can be gained by studying the dependence of the fluorescence on excitation wavelength. In figure 3.33 the fluorescence intensity is plotted in colour as a function of excitation and emission wavelengths, with the excitation wavelength increased in 10 nm intervals from 350–550 nm. aGO shows a single broad emission, with the emission wavelength peaking at around 620 nm, with maximum intensity centred around an excitation wavelength of 425 nm. There is no apparent dispersion, i.e. the peak emission is independent of the excitation wavelength.

By contrast, the emission of OD is strongly wavelength dependent, figure 3.34. The emission is blue-shifted relative to aGO, with the maximum emission intensity shifting to 450 nm at 350 nm excitation, to 530 nm at 450 nm excitation, and to 600 nm at 550 nm excitation. The width of the emission peak is independent of the excitation wavelength.
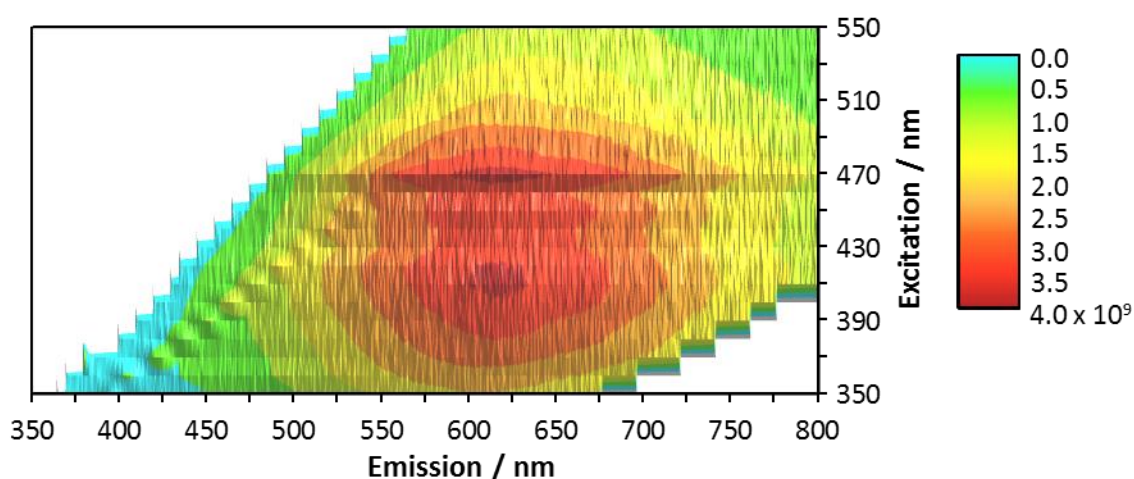
Fig. 3.33 Fluorescence map of aGO showing the intensity of the emitted fluorescence as a function of the excitation and emission wavelengths.
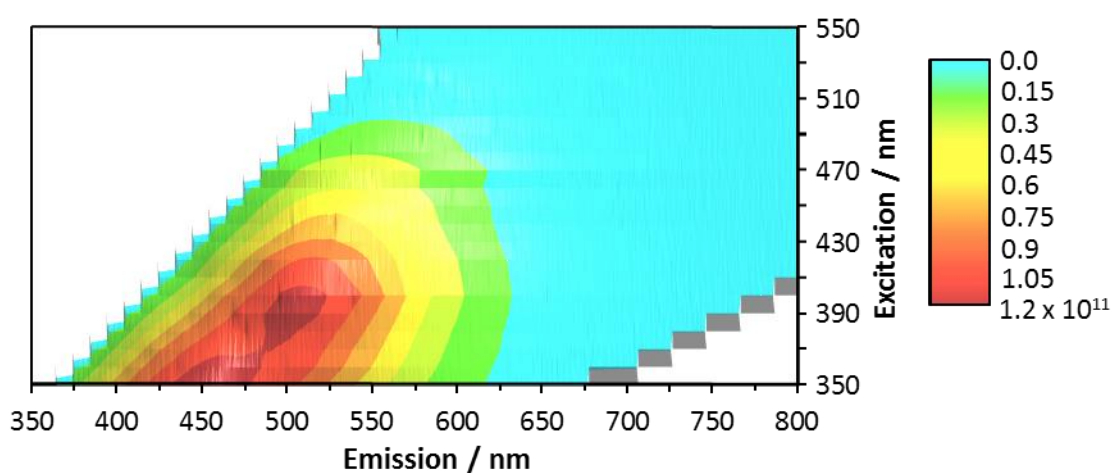
Fig. 3.34 Fluorescence map of OD showing the intensity of the emitted fluorescence as a function of the excitation and emission wavelengths.

The observed evolution in fluorescence and absorption upon the addition of dilute NaOH to aGO is consistent with the dominant change being an increase in absorption, which previous work shows is also associated with an increase in conductivity.[1] The luminescence profile remains similar, suggesting that the OD stays loosely bound to the graphene-like sheets. Graphitic carbon and graphene oxide are known to effectively quench fluorescence,[43-45] which explains the lack of fluorescence from the OD whilst still in close proximity to the functionalised graphene. Upon the addition of more concentrated NaOH there is an

apparently instantaneous darkening through the coagulation of the now highly absorbing graphene-like sheets. The luminescence from the clear solution (once the coagulated fraction has separated) was measured, and showed a distinctly blue-shifted photo-luminescence spectrum, suggesting that the OD is also instantaneously isolated from the bwGO.

The changes induced upon the addition of dilute NaOH (which would still correspond to pH ~12) were observed to be reversible, whilst the changes after the coagulation induced by concentrated NaOH were not. Previous reports have studied the pH dependence of the luminescence of graphene or graphite oxide,[46, 47] and have found changes in the intensity and the profile of the emission as a function of pH. This suggests that caution should be taken in identifying whether the as-produced GO is being studied, or whether the basic solution causes its separation into bwGO and OD.

The clear difference between the excitation wavelength dependence of the luminescence from OD, aGO and bwGO points to important differences in their physical properties. For example, carbon-based quantum dots are known to exhibit excitation wavelength dependent properties,[48-50] and this has been attributed to the unavoidable distribution of sizes leading to an ensemble of energetically different molecules. The fluorescence of OD is thus consistent with it being composed of highly oxidised fragments of graphene.

Importantly, the clear differences in absorption and luminescence between aGO, bwGO and OD indicate that the OD cannot be thought of just as small sheets of graphene oxide. For example, the transparency of OD in the visible region and the Raman spectra distinguish OD from aGO and from the graphene oxide quantum dots that are formed by cutting GO sheets down to approximately 10 nm in diameter.[51] Instead, OD encompasses a family of molecules with similar chemical functionalisations.

In light of the optical properties of OD and bwGO, the luminescence from graphene oxide needs to be reassessed. The broad non-dispersive emission of aGO is consistent with previous reports, in which various mechanisms for the luminescence have been proposed: a range of optical gaps due to the heterogeneous nature of the material;[52] quantum dots confined to sp^2 domains within the graphene sheet;[33, 53] quasi-molecular fluorophores due

to reversible protonation of carbene-like zig-zag edges,[51] or formed by the electronic coupling of carboxylic acid groups with nearby carbon atoms of graphene.[54] Gokus *et al.*[55] recently analysed the photo-luminescence from graphene after oxidation by an oxygen plasma and found a broad emission similar to that reported here for aGO. They showed that the observed luminescence was not consistent with quantum confinement in quantum dots within the graphene sheet but could be attributed to the broadening of a single emission species. The results presented here are entirely consistent with such a single emission, indicating that in this case the species absorbs around 420 nm (2.9 eV) and emits around 620 nm (2.0 eV). The lack of any obvious feature around 420 nm in the absorption spectrum of aGO confirms that the emission is due to a very small fraction of the aGO.

Clearly it is tempting to attribute the source of this aGO luminescence to the OD, due to its relatively intense fluorescence when separated from the GO. The excitation wavelength dependence of OD would be expected to be removed by energy transfer through the graphene sheet in aGO, resulting in only the lowest energy emission remaining.[56] The OD could act as the chromophore, absorbing light and transferring energy to an emission site on the oxidised graphene sheet, or as the fluorophore, red-shifted due to interaction with the GO. However, these results do not resolve whether or not these mechanisms are involved and it is possible that the weak luminescence of aGO does indeed come from a quasi-molecular fluorophore as suggested in previous reports.[51, 54] What is certain is that the removal of the OD changes the optical properties of the graphene oxide such that luminescence is no longer observed.

3.6   Cleaning versus Reduction

One of the classic methods of reducing GO is with the use of hydrazine.[57] Since the use of NaOH can result in a deoxygenation it is possible, as others have speculated,[6] that one of the roles of the basic hydrazine is equivalent to the base-washing step.

Treatment of GO with hydrazine monohydrate solutions (0.5 M) at room temperature for 3 hours results in changed samples, with both aGO and bwGO producing very similar looking materials. The quantity of the rGO material produced is significantly different as ~150 mg of aGO produces ~100 mg of rGO, whereas only ~110 mg of bwGO is needed to produce ~100 mg of rGO; this is consistent with the hydrazine having a cleaning role and removing the OD. A variety of different reaction conditions and characterisation techniques were used to investigate whether hydrazine merely cleans the GO surface of OD, or whether it truly reduces the graphene-like sheets.
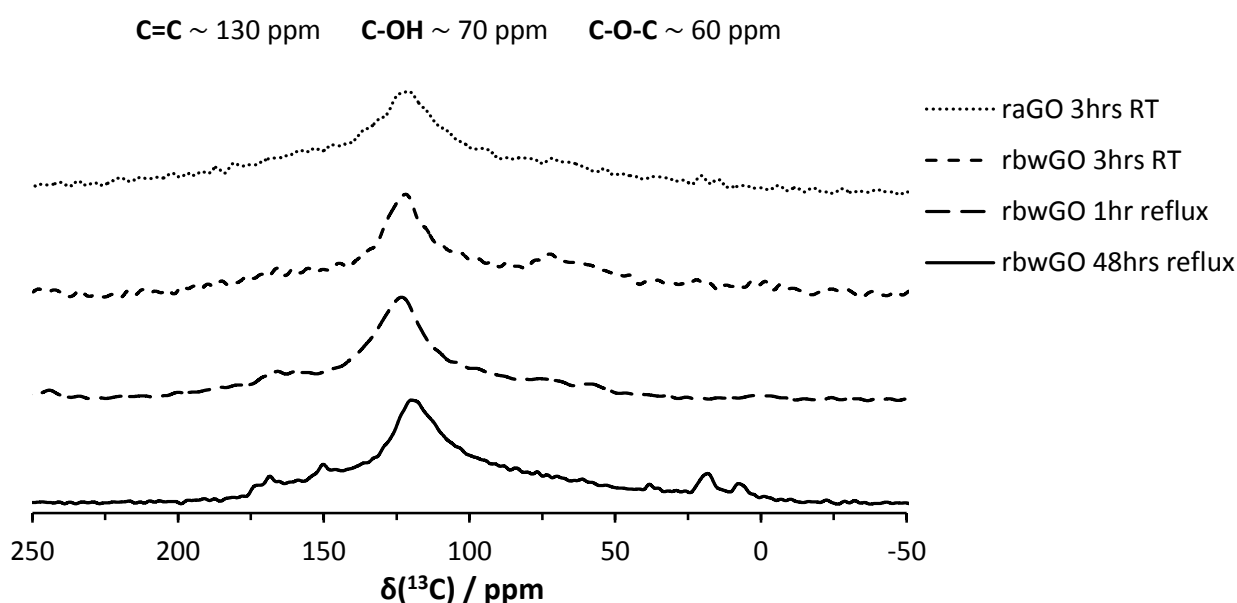
Fig. 3.35 Direct excitation ^{13}C MAS ssNMR spectra of four GO materials reduced with hydrazine under different reaction conditions.

Treating aGO and bwGO with hydrazine for 3 hrs at RT gave, spectroscopically, very similar results: there is a very substantial decrease in the intensity of the directly detected ^{13}C ssNMR signals of the epoxide, hydroxide, and carboxyl groups, relative to those of the sp^2 carbons (figure 3.35). For the aGO sample these oxygenated carbon signals disappear into

the noise of the spectrum, for the bwGO sample they can still just about be seen. Two further experiments were thus preformed on bwGO: a 1 hr reflux and a 48 hr reflux. After the 48 hours, there was no sign of any oxygenated carbons by ssNMR.

Treatment with hydrazine reduces the intensity of the epoxide and hydroxide signals to a considerably greater extent than base washing alone (compare with figure 3.1). This is mirrored by a change in the C/O ratio as seen by EDX: table 3.4 shows the EDX values for rGO samples treated sequentially from the same Hummers aGO starting material.

Sample	atomic % (standard deviation)		
	C	**O**	**C/O**
aGO	58 (1)	41 (1)	**3:2**
raGO (3 hrs RT)	70 (1)	30 (1)	**7:3**
bwGO	64 (1)	32 (2)	**2:1**
rbwGO (3 hrs RT)	71 (1)	27 (2)	**3:1**
rbwGO (1 hr 80 °C)	77 (1)	23 (1)	**3:1**
rbwGO (24 hrs 80 °C)	85 (0.4)	15 (0.4)	**6:1**
rbwGO (48 hrs 80 °C)	91 (2)	8 (2)	**11:1**

Table 3.4 EDX derived atomic % of rGO materials with the standard deviation given in parentheses.

From the EDX values it can see that more vigorous reaction conditions with hydrazine will increase the C/O, suggesting that as well as removing the OD, the hydrazine is genuinely reducing the GO sheets. The 48 hour reflux results in almost complete removal of the oxygenated groups. Once again of note, is the propensity of EDX to show O levels greater than expected, and if the inaccuracies are considered to be dominated by the hygroscopic nature of the material, then the inaccuracies are expected to become less significant as the reduction proceeds. Definitively though, nitrogen was not observed by EDX in any of the

hydrazine treated samples, consistent with DFT studies of hydrazine de-epoxidation mechanisms that indicate that the only stable hydrazino alcohol intermediate are those that form from epoxide groups at the edges of the aromatic regions.[57]
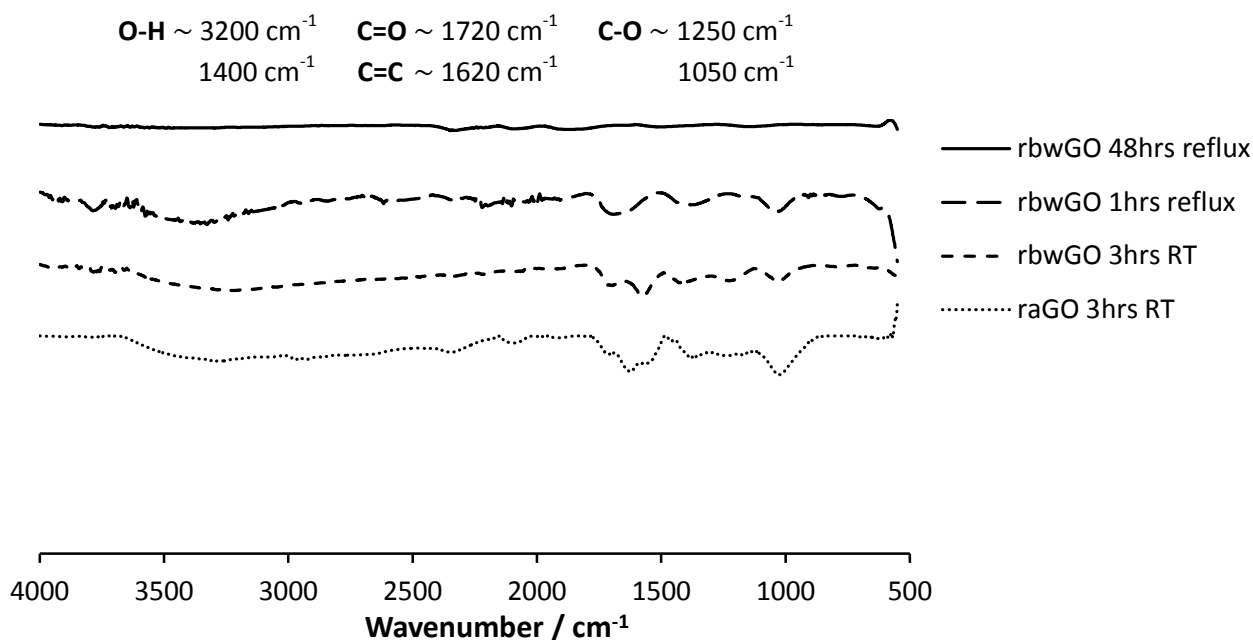
Fig. 3.36 ATR-FTIR spectra of four GO materials reduced with hydrazine under different reaction conditions.

The FTIR spectra (figure 3.36) mirror the ssNMR and EDX results, showing a decrease in oxygenated functionalities for all hydrazine reduced materials, although the 48 hour reflux is required to completely reduce the GO sheets.

D band ~ 1340 cm^{-1} **G band** ~ 1600 cm^{-1} **G' band** ~ 2700 cm^{-1}
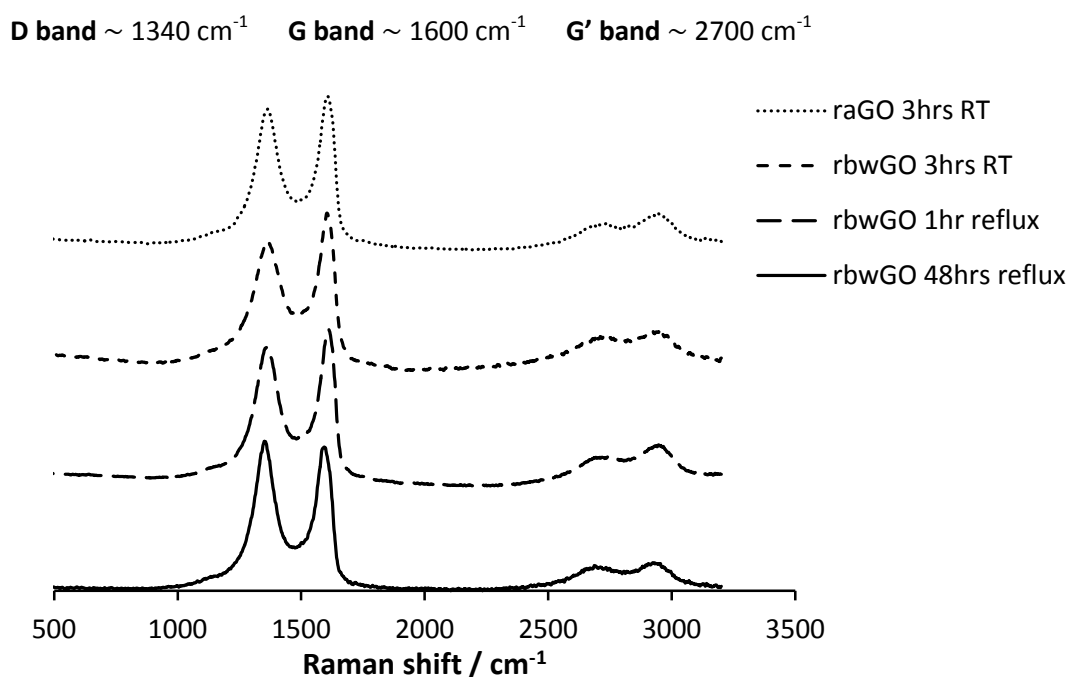
Fig. 3.37 Raman spectra of various rGO materials; excitation wavelength 514 nm.

The Raman spectra for the reduced GO materials are very similar (figure 3.37), although the D/G ratios shown in Table 3.5 do suggest a trend: longer reaction times appear to yield materials with higher D/G ratios. Possibly the harsher reduction conditions are introducing sheet defects in the graphene-type materials, resulting in a more intense D band.

Samples	D/G Ratio Calculation		
	D_{area}	G_{area}	D/G (±0.1)
raGO 3 hrs RT	155.5	95.3	**1.6**
rbwGO 3 hrs RT	157.9	93.6	**1.7**
rbwGO 1 hr reflux	177.6	107.4	**1.7**
rbwGO 48 hrs reflux	174.5	99.4	**1.8**

Table 3.5 Peak areas and D/G ratios for the rGO materials.

TGA analysis (figure 3.38) mirrors both the ssNMR and EDX findings, with decreasing quantities of material lost around 200 °C as the extent of reduction is increased; the most reduced material shows no mass loss below 600 °C. The TGA also confirms that the more reduced materials are less hygroscopic, with the 48 hr reduced rbwGO material showing no

mass loss due to adsorbed water. The fact that the 48 hr rGO material has the highest decomposition temperature suggests that the decomposition of GO sheets begins at functional groups, rather than defect holes.
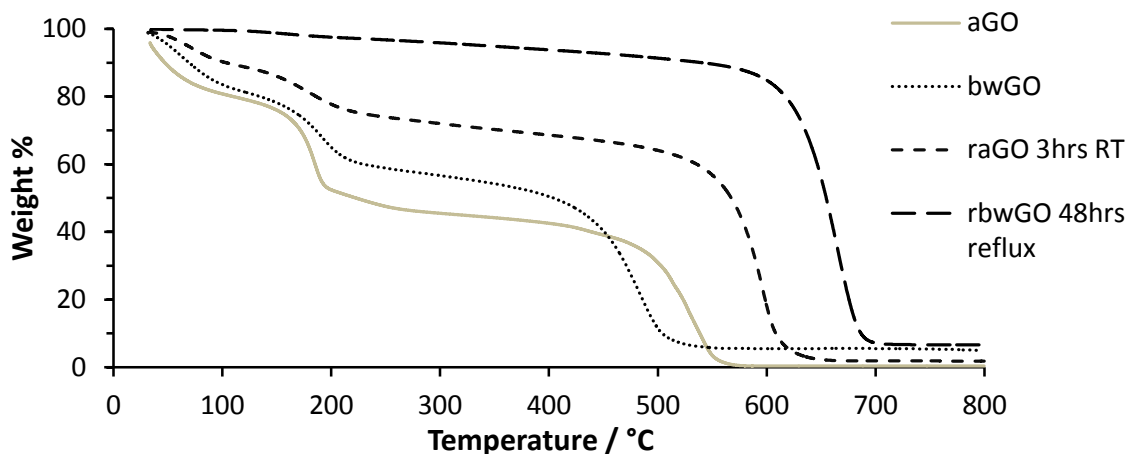
Fig. 3.38 TGA of aGO, bwGO and rGO materials.
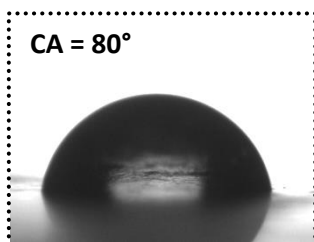
Fig. 3.39 Drop shape analysis of raGO (3 hrs, RT).

Treatment with hydrazine dramatically affects the dispersibility of the GO materials, as shown by drop shape analysis (figure 3.39). Even the least reduced material (raGO 3hrs, RT) has an increased contact angle of 80° – significantly changed from the 26° seen for Hummers aGO (figure 3.11). This change is unlikely to simply be a result of removing the OD.

3.7 Conclusions

The presence of oxidation debris in as-produced graphene oxide is not a function of oxidation method: aGO synthetic protocols with the widely used chlorate and permanganate oxidants both give materials that contain roughly one third highly oxidised low molecular weight material. The removal of this highly oxygenated OD from the aGO with base (NaOH or NH_3) gives graphene-like sheets with a reduced oxygen content compared with aGO. This cleaned version of GO is shown by TEM to be a genuinely single sheet material, and AFM shows that it can be processed in much the same way as aGO, but without concerns about the presence of OD.

An investigation into the photo-luminescence of GO showed that the fluorescence of bwGO is considerably different to that of aGO. The OD was found to be highly fluorescent, behaving as an ensemble of nanometre-sized carbon based fluorophores. By contrast, the aGO showed a single non-dispersive peak, consistent with a broadening of the emission from a single species rather than from an ensemble of quantum dots within the graphene sheet. These results have important implications for the development of chemically modified graphenes for optical applications.

When revisiting the literature, it becomes apparent that many researchers in the past have inadvertently removed the OD from their samples via washing or thermal treatments. Reacting aGO with hydrazine was found to both clean the OD from the graphene-like sheets and reduce them.
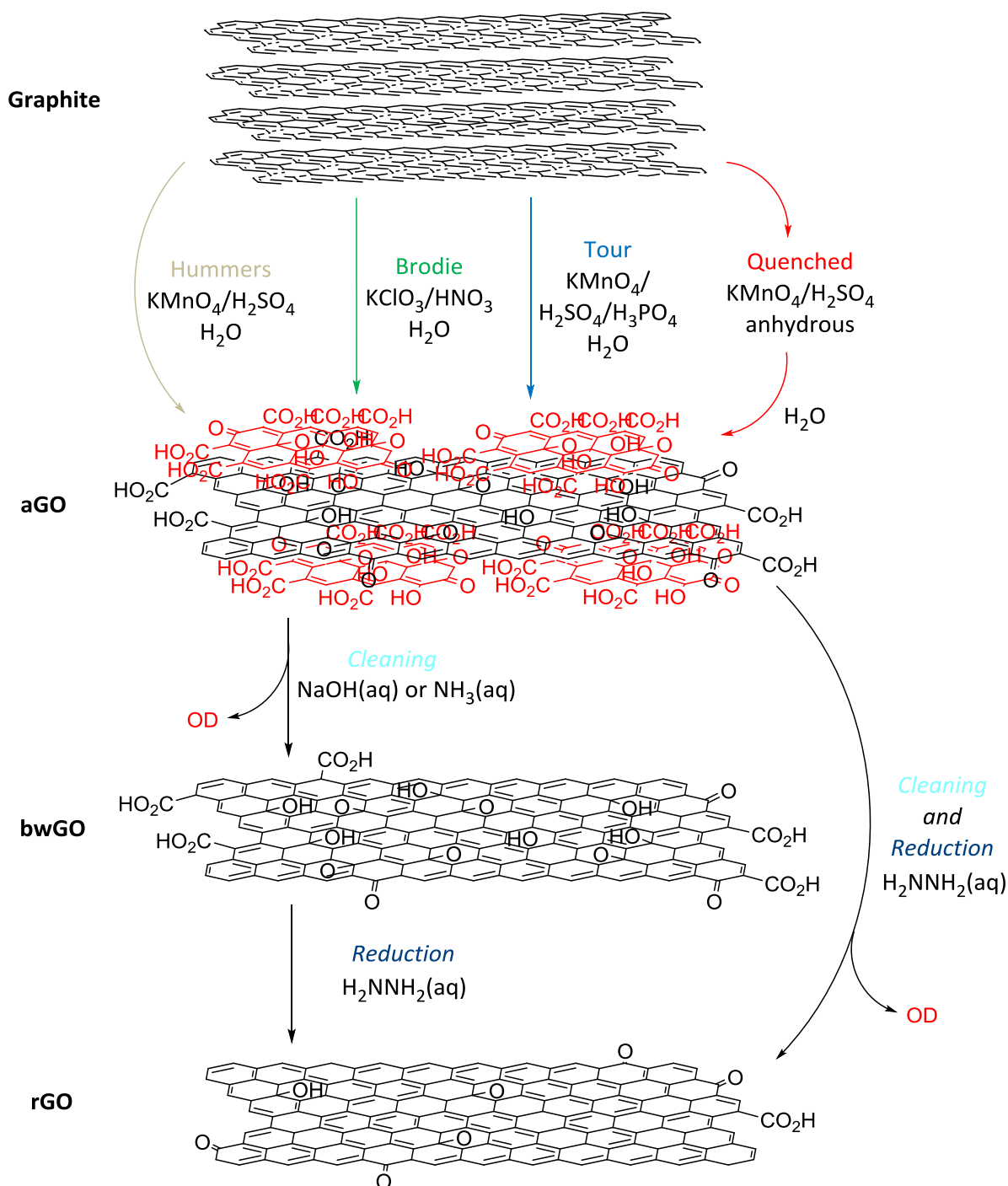
Scheme 3.2 Summary of the oxidising, cleaning and deoxygenating processes involving graphite and GO.

Two important processes that can occur during the treatment of graphene oxide are thus identified: reduction and "cleaning". The separation of the highly oxidised material (the OD) from the bulk sample of aGO to give graphene-like sheets is "cleaning"; it reveals more of the true nature of graphene oxide. The graphene-like sheets are unchanged by this process,

but the resultant material, bwGO, has a lower level of oxygenation than aGO (an increase in the C/O ratio), and hence, deoxygenation has occurred. Since the graphene-like sheets are unaltered by the cleaning process, they have not themselves been reduced. True reduction of GO requires reagents that add electrons to the graphene-like sheets, removing the directly bonded oxygen groups. A standard reducing reagent such as hydrazine cleans and reduces the graphene oxide, and this deoxygenation is thus the result of two separate processes, which, as has been demonstrated, can be performed sequentially. Correctly identifying and characterising these deoxygenation processes will allow for the improvement of functional properties in chemically modified graphenes.[58]

1.   Rourke, J. P.; Pandey, P. A.; Moore, J. J.; Bates, M.; Kinloch, I. A.; Young, R. J.; Wilson, N. R. *Angew. Chem., Int. Ed.* **2011,** 50, (14), 3173-3177.

2.   Thomas, H. R.; Day, S. P.; Woodruff, W. E.; Vallés, C.; Young, R. J.; Kinloch, I. A.; Morley, G. W.; Hanna, J. V.; Wilson, N. R.; Rourke, J. P. *Chem. Mater.* **2013,** 25, (18), 3580-3588.

3.   Salzmann, C. G.; Llewellyn, S. A.; Tobias, G.; Ward, M. A. H.; Huh, Y.; Green, M. L. H. *Adv. Mater.* **2007,** 19, (6), 883-887.

4.   Wang, Z.; Shirley, M. D.; Meikle, S. T.; Whitby, R. L. D.; Mikhalovsky, S. V. *Carbon* **2009,** 47, (1), 73-79.

5.   Verdejo, R.; Lamoriniere, S.; Cottam, B.; Bismarck, A.; Shaffer, M. *Chem. Commun.* **2007,** (5), 513-515.

6.   Fan, X.; Peng, W.; Li, Y.; Li, X.; Wang, S.; Zhang, G.; Zhang, F. *Adv. Mater.* **2008,** 20, (23), 4490-4493.

7.   Casabianca, L. B.; Shaibat, M. A.; Cai, W. W.; Park, S.; Piner, R.; Ruoff, R. S.; Ishii, Y. *Journal of the American Chemical Society* **2010,** 132, (16), 5672-5676.

8.   Larciprete, R.; Fabris, S.; Sun, T.; Lacovig, P.; Baraldi, A.; Lizzit, S. *J. Am. Chem. Soc.* **2011,** 133, (43), 17315-17321.

9.   Taniguchi, T.; Kurihara, S.; Tateishi, H.; Hatakeyama, K.; Koinuma, M.; Yokoi, H.; Hara, M.; Ishikawa, H.; Matsumoto, Y. *Carbon* **2015,** 84, (0), 560-566.

10.   Kumar, P. V.; Bardhan, N. M.; Tongay, S.; Wu, J.; Belcher, A. M.; Grossman, J. C. *Nat Chem* **2014,** 6, (2), 151-158.

11.   Zhang, L.; Liang, J.; Huang, Y.; Ma, Y.; Wang, Y.; Chen, Y. *Carbon* **2009,** 47, (14), 3365-3368.

12.   Pan, S.; Aksay, I. A. *ACS Nano* **2011,** 5, (5), 4073-4083.

13.   Bacon, G. E. *Acta Crystallogr.* **1951,** 4, (6), 558-561.

14.   Glockler, G. *J. Phys. Chem.* **1958,** 62, (9), 1049-1054.

15.   Wilson, N. R.; Pandey, P. A.; Beanland, R.; Rourke, J. P.; Lupo, U.; Rowlands, G.; Römer, R. A. *New J. Phys.* **2010,** 12, (12), 125010.

16.   Mkhoyan, K. A.; Contryman, A. W.; Silcox, J.; Stewart, D. A.; Eda, G.; Mattevi, C.; Miller, S.; Chhowalla, M. *Nano Lett.* **2009,** 9, (3), 1058-1063.

17.   Dreyer, D. R.; Park, S.; Bielawski, C. W.; Ruoff, R. S. *Chem. Soc. Rev.* **2010,** 39, (1), 228-240.

18.   Jung, I.; Pelton, M.; Piner, R.; Dikin, D. A.; Stankovich, S.; Watcharotone, S.; Hausner, M.; Ruoff, R. S. *Nano Lett.* **2007,** 7, (12), 3569-3575.

19.   Wilson, N. R.; Pandey, P. A.; Beanland, R.; Young, R. J.; Kinloch, I. A.; Gong, L.; Liu, Z.; Suenaga, K.; Rourke, J. P.; York, S. J.; Sloan, J. *ACS Nano* **2009,** 3, (9), 2547-2556.

20.   Hansen, C. M., *Hansen Solubility Parameters: A User's Handbook*. 2nd ed.; CRC Press: 2007.

21.   Park, S.; An, J.; Jung, I.; Piner, R. D.; An, S. J.; Li, X.; Velamakanni, A.; Ruoff, R. S. *Nano Lett.* **2009,** 9, (4), 1593-1597.

22.   Patterson, J. P.; Sanchez, A. M.; Petzetakis, N.; Smart, T. P.; Epps, I. I. I. T. H.; Portman, I.; Wilson, N. R.; O'Reilly, R. K. *Soft Matter* **2012,** 8, (12), 3322-3328.

23.   Staudenmaier, L. *Ber. Dtsch. Chem. Ges.* **1898,** 31, (2), 1481-1487.

24.   Brodie, B. C. *Philos.Trans. R. Soc. London* **1859,** 149, 249-259.

25.   Hummers, W. S.; Offeman, R. E. *J. Am. Chem. Soc.* **1958,** 80, (6), 1339-1339.

26.   Marcano, D. C.; Kosynkin, D. V.; Berlin, J. M.; Sinitskii, A.; Sun, Z.; Slesarev, A.; Alemany, L. B.; Lu, W.; Tour, J. M. *ACS Nano* **2010,** 4, (8), 4806-4814.

27.   Dimiev, A.; Kosynkin, D. V.; Alemany, L. B.; Chaguine, P.; Tour, J. M. *J. Am. Chem. Soc.* **2012,** 134, (5), 2815-2822.

28.   Gao, W.; Alemany, L. B.; Ci, L. J.; Ajayan, P. M. *Nat. Chem.* **2009,** 1, (5), 403-408.

29.   Eigler, S.; Dotzer, C.; Hirsch, A. *Carbon* **2012,** 50, (10), 3666-3673.

30.   Zhou, S.; Bongiorno, A. *Sci. Rep.* **2013,** 3, 2484.

31.   Shrestha, L. K.; Wi, J. S.; Williams, J.; Akada, M.; Ariga, K. *J. Nanosci. Nanotechno.* **2014,** 14, (3), 2245-2251.

32. Zhu, S.; Tang, S.; Zhang, J.; Yang, B. *Chem. Commun.* **2012,** 48, (38), 4527-4539.

33. Eda, G.; Lin, Y.-Y.; Mattevi, C.; Yamaguchi, H.; Chen, H.-A.; Chen, I. S.; Chen, C.-W.; Chhowalla, M. *Adv. Mater.* **2010,** 22, (4), 505-509.

34. Shen, J.; Zhu, Y.; Yang, X.; Li, C. *Chem. Commun.* **2012,** 48, (31), 3686-3699.

35. Chen, S.; Liu, J.-W.; Chen, M.-L.; Chen, X.-W.; Wang, J.-H. *Chem. Commun.* **2012,** 48, (61), 7637-7639.

36. Lin, Y.; Zhou, B.; Martin, R. B.; Henbest, K. B.; Harruff, B. A.; Riggs, J. E.; Guo, Z.-X.; Allard, L. F.; Sun, Y.-P. *J. Phys. Chem. B* **2005,** 109, (31), 14779-14782.

37. Jang, D. M.; Myung, Y.; Im, H. S.; Seo, Y. S.; Cho, Y. J.; Lee, C. W.; Park, J.; Jee, A.-Y.; Lee, M. *Chem. Commun.* **2012,** 48, (5), 696-698.

38. Li, H.; Zhang, Y.; Luo, Y.; Sun, X. *Small* **2011,** 7, (11), 1562-1568.

39. Shang, J.; Ma, L.; Li, J.; Ai, W.; Yu, T.; Gurzadyan, G. G. *Sci. Rep.* **2012,** 2.

40. Jung, J. H.; Cheon, D. S.; Liu, F.; Lee, K. B.; Seo, T. S. *Angew. Chem., Int. Ed.* **2010,** 49, (33), 5708-5711.

41. Liu, F.; Choi, J. Y.; Seo, T. S. *Biosens. Bioelectron.* **2010,** 25, (10), 2361-2365.

42. Piao, Y.; Liu, F.; Seo, T. S. *Chem. Commun.* **2011,** 47, (44), 12149-12151.

43. Kagan, M. R.; McCreery, R. L. *Anal. Chem.* **1994,** 66, (23), 4159-4165.

44. Treossi, E.; Melucci, M.; Liscio, A.; Gazzano, M.; Samorì, P.; Palermo, V. *J Am. Chem. Soc.* **2009,** 131, (43), 15576-15577.

45. Wang, Y.; Kurunthu, D.; Scott, G. W.; Bardeen, C. J. *J. Phys. Chem. C* **2010,** 114, (9), 4153-4159.

46. Kochmann, S.; Hirsch, T.; Wolfbeis, O. *J Fluoresc* **2012,** 22, (3), 849-855.

47. Chen, J.-L.; Yan, X.-P. *Chem. Commun.* **2011,** 47, (11), 3135-3137.

48. Tang, L.; Ji, R.; Cao, X.; Lin, J.; Jiang, H.; Li, X.; Teng, K. S.; Luk, C. M.; Zeng, S.; Hao, J.; Lau, S. P. *ACS Nano* **2012,** 6, (6), 5102-5110.

49. Zhang, H.; Xu, X.; Ji, H.-F. *Chem. Commun.* **2010,** 46, (11), 1917-1919.

50. Sun, Y.-P.; Zhou, B.; Lin, Y.; Wang, W.; Fernando, K. A. S.; Pathak, P.; Meziani, M. J.; Harruff, B. A.; Wang, X.; Wang, H.; Luo, P. G.; Yang, H.; Kose, M. E.; Chen, B.; Veca, L. M.; Xie, S.-Y. *J Am. Chem. Soc.* **2006,** 128, (24), 7756-7757.

51. Pan, D.; Zhang, J.; Li, Z.; Wu, M. *Adv. Mater.* **2010,** 22, (6), 734-738.

52. Luo, Z.; Vora, P. M.; Mele, E. J.; Johnson, A. T. C.; Kikkawa, J. M. *Appl. Phys. Lett.* **2009,** 94, (11), 111909-3.

53. Sun, X.; Liu, Z.; Welsher, K.; Robinson, J.; Goodwin, A.; Zaric, S.; Dai, H. *Nano Res.* **2008,** 1, (3), 203-212.

54. Galande, C.; Mohite, A. D.; Naumov, A. V.; Gao, W.; Ci, L.; Ajayan, A.; Gao, H.; Srivastava, A.; Weisman, R. B.; Ajayan, P. M. *Sci. Rep.* **2011,** 1.

55. Gokus, T.; Nair, R. R.; Bonetti, A.; Böhmler, M.; Lombardo, A.; Novoselov, K. S.; Geim, A. K.; Ferrari, A. C.; Hartschuh, A. *ACS Nano* **2009,** 3, (12), 3963-3968.

56. Mandal, P. K.; Paul, A.; Samanta, A. *J. Photochem. Photobiol., A* **2006,** 182, (2), 113-120.

57. Gao, X.; Jang, J.; Nagase, S. *J. Phys. Chem. C* **2009,** 114, (2), 832-842.

58. Radich, J. G.; Kamat, P. V. *ACS Nano* **2013,** 7, (6), 5546-5557.

Chapter 4

Ring-opening Surface Epoxides on bwGO
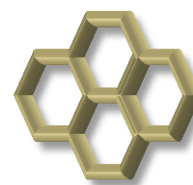
Having established that the two component structure of GO is a generic feature, and that the base washing procedure does not appear to chemically modify the GO sheets. In this chapter the clean bwGO sheets were used as a convenient precursor to chemically modified graphene materials. Initially, reaction with a carbon nucleophile was investigated. Carbanions readily react with water becoming hydrolysed,[1] which can pose a problem for reactions with GO, as even under careful anhydrous conditions some intercalated water is thought to remain.[2-4] A carbon nucleophile with a pKa of less than water should be water-compatible, and thus the malononitrile anion was deemed as an appropriate choice. Later on in this chapter, three different sulfur nucleophiles are investigated. Potassium thioacetate was chosen as a reactant due to its easy conversion to a thiol by cleaving the acetate group. Thiophenol was chosen as a convenient route to surface thioethers, and with a significant level of functionalisation, the phenyl group could also serve as a way to increase the surface area of the GO. The last nucleophile studied was a NIPAM polymer with a thiolate anion end group, it was hoped that the composite GO-polymer material would have desirable properties from both components. At the time, the functionalisation of GO sheets via epoxy opening reactions with a sulfur nucleophile was unexplored, and thus this chapter demonstrates a novel approach to the study of GO reactivity.

4.1   Reaction of bwGO with Nitrogen Nucleophiles

In order to prepare CMGs free from the concerns of OD, it was necessary to explore the functionalisation of clean GO, namely bwGO. Functionalisation is, in theory, possible through each of the four groups known to be present on the surface of GO: carboxylic acids, ketone/aldehyde groups, hydroxyl groups and epoxides.[5, 6] The carboxylic acid groups in particular have been extensively exploited for chemical modification in the development of CMGs.[7-12] Edge site ketones[13, 14] and surface hydroxyl[15-18] groups have also been studied, but work on surface epoxide functionalisation is less extensive. Nucleophilic attack on the epoxide groups of GO has been previously demonstrated with nitrogen nucleophiles,[19-23] and more recently with carbon nucleophiles.[1] These ring-opening reactions leave reactive groups on the GO surface, which can then be utilised for further chemistry. The selective reduction of epoxides has also been recently studied.[24] Given the results from chapter 3, in which around one third of the mass of GO was identified as highly oxidised, low molecular weight, oxidative debris (OD) with the same functional groups as GO itself, it is entirely possible that some of these nucleophiles functionalised the OD, rather than the graphene-like sheets.

Initially the reaction of GO with malononitrile – studied first of all by the Swager group[1] – was considered. Swager *et al*. reacted the malononitrile anion with their aGO material, using the carbon nucleophile to ring open the epoxides. However, it is unclear whether the functionalisation was limited to the GO sheets or whether the OD was indirectly functionalised. Hence it was of interest to see whether the same level of nitrogen incorporation could be achieved with bwGO. GO materials are hygroscopic and thus have surface adsorbed water[2] which will hydrolyse highly basic carbanions. Malononitrile is fairly acidic due to its ability to form different resonance structures on deprotonation; its anion is thus compatible with the use of aqueous solutions.

A mixture of malononitrile and NaH, in acetonitrile, was prepared and added to a suspension of bwGO in acetonitrile. The mixture was worked up after an overnight reflux under N_2.
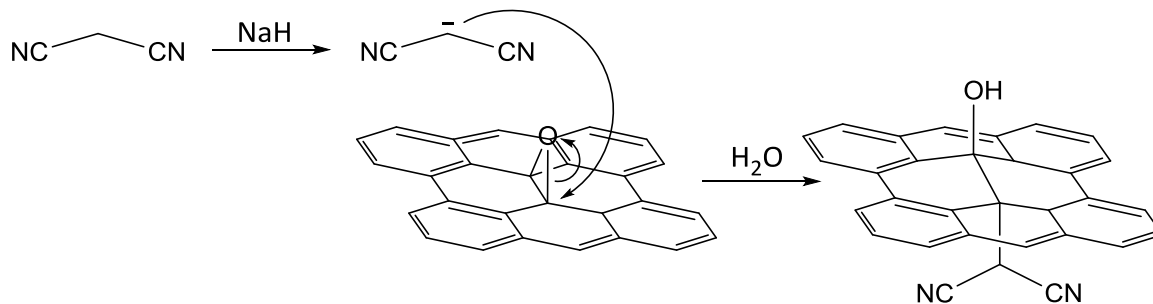
Scheme 4.1 Mechanism for the reaction of malononitrile with epoxide groups on the bwGO sheet surface.

Scheme 4.1 shows the expected reaction between surface epoxides and the malononitrile anion, to give the functionalised bwGO material (GO-CN). However it is important to note that nucleophilic attack may occur at the electrophilic carbon atoms of an epoxide, or at a carbon double bond adjacent to the epoxy group. Both reaction pathways will cause ring-opening of an epoxide, relieving strain. While the direct S_N2 opening of the epoxide requires the incoming nucleophile to approach from the opposite face of the epoxide, attack at a double bond (an S_N2' reaction) allows for the nucleophile to attack at either the same face as the epoxide or at the opposite one (scheme 4.2).
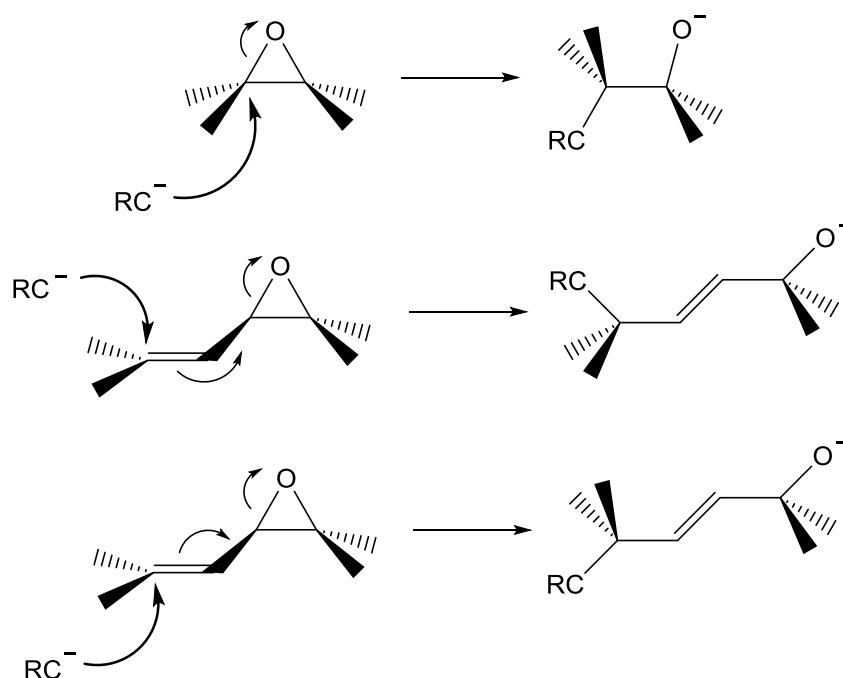
Scheme 4.2 Possible reaction pathways for nucleophilic attack at an epoxide.

bwGO will have epoxides on both sides of the graphene-like sheet, so ultimately it does not matter which reaction pathway is followed; malononitrile and hydroxyl groups are expected

to end up on both sides of the sheet. The relative rates of the S_N2 and S_N2' reactions on GO are not known, but it is entirely feasible that the S_N2' reaction dominates.[25, 26] GO-CN was studied with a variety of spectroscopic techniques, where any evidence of nitrile groups was looked for in order to determine whether or not the reaction had been successful.

O-H ~ 3200 cm^{-1} C-N ~ 2200 cm^{-1} C=O ~ 1720 cm^{-1} C-O ~ 1250 cm^{-1}
1400 cm^{-1} C=C ~ 1620 cm^{-1} 1050 cm^{-1}
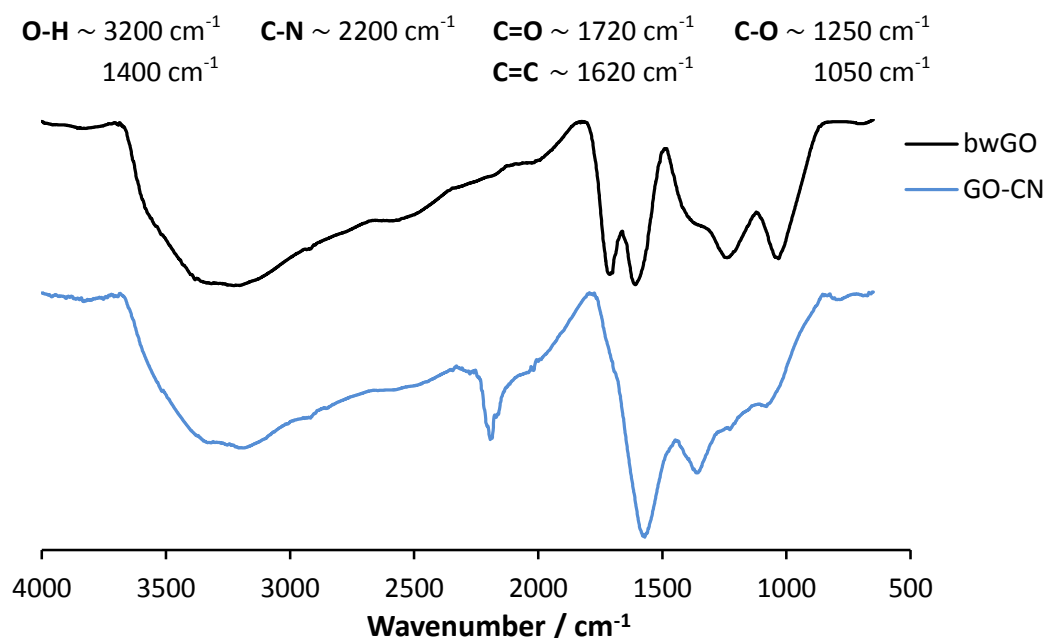
Fig. 4.1 ATR-FTIR spectra of bwGO (black) and malononitrile functionalised bwGO (blue).

Figure 4.1 shows the FTIR spectra of bwGO and GO-CN. The GO-CN spectrum shows a decrease in intensity for C-OH, C-O-C, and C=O bands relative to the C=C band (1590 cm^{-1}). The C=O band is hard to distinguish; it is likely that the carboxyl groups are present as the sodium salt, in which case the characteristic asymmetric COO stretch (expected at around 1560 cm^{-1})[27] would be overlapped by the C=C band in the GO-CN spectrum. The hydroxyl groups remain largely present in GO-CN, but the number of epoxy groups has decreased significantly. The most important FTIR band of the GO-CN material occurs sharply at 2200 cm^{-1}, and corresponds to nitrile groups. The CN peak appears to be made up of two overlapping peaks, suggesting that both S_N2 and S_N2' reaction pathways are occurring. As seen in scheme 4.2, in S_N2 the incoming malononitrile anion directly ring-opens the surface epoxides, meaning that the nitrile groups will be in close proximity to a hydroxyl group. Alternatively in S_N2', the malononitrile anion will attack a double bond adjacent to the

epoxide group, and as such will not necessarily be in close proximity to a hydroxyl group, resulting in two slightly different chemical environments.

Any unreacted malononitrile is expected to be removed from the GO-CN material via extensive water, acetone and methanol washes during the workup, thus the FTIR suggests that the malononitrile is covalently attached to the bwGO sheets, and is preferentially attacking the epoxide groups.

C=C ~ 130 ppm   **C-N** ~ 108 ppm   **C-OH** ~ 70 ppm   **C-C** ~ 45 ppm
                                          C-O-C ~ 60 ppm   **C-H** ~ 30 ppm
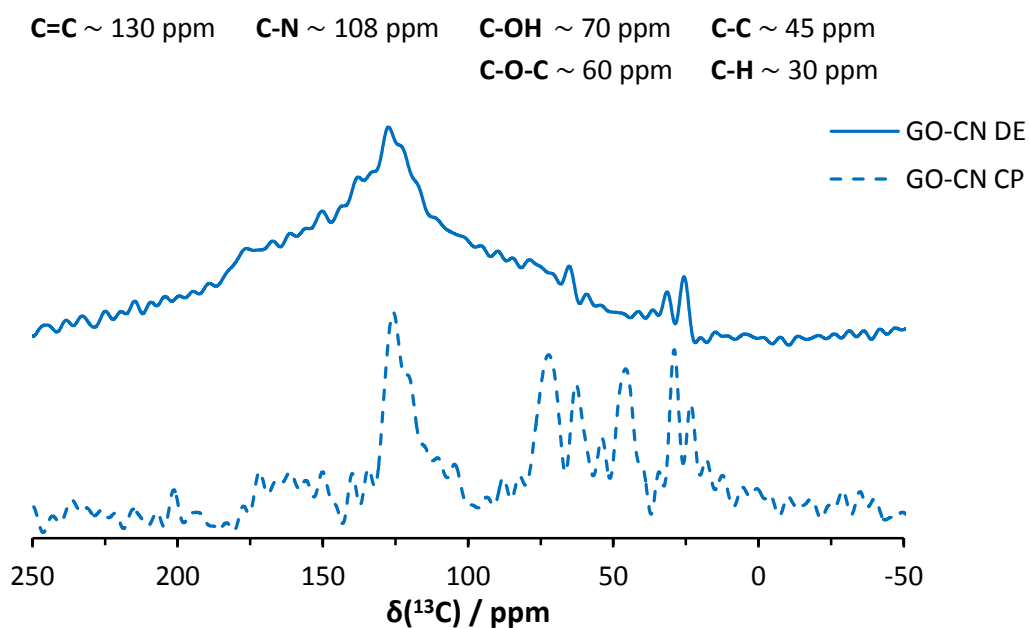
Fig. 4.2 ^{13}C MAS ssNMR spectra of GO-CN, both the direct excitation (DE) spectrum (solid) and the cross polarised (CP) spectrum (dashed) are shown.

^{13}C MAS ssNMR was looked to for further characterisation of GO-CN. Figure 4.2 shows the DE and CP spectra for GO-CN, clearly indicating that a chemical change has occurred on reaction with malononitrile: even with the line broadening (DE spectrum) it is clear that the hydroxyl and epoxy carbon signals have decreased in intensity when compared to bwGO, and new low chemical shift peaks are apparent. The sp^2 carbon signal at 127 ppm remains strong for GO-CN, indicating that the graphene-like base structure remains intact.

105
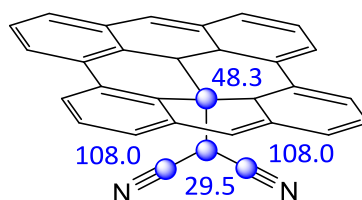
Fig. 4.3 ^{13}C ssNMR chemical shift predictions for the new signals in GO-CN. The blue spheres indicate carbons of interest, with predicted chemical shifts as labelled.

An exact prediction of the chemical shifts expected for GO-based materials is not possible as the environment is not one that can be modelled accurately. However from basic estimates (figure 4.3), and literature values (the hydroxyl and epoxy chemical shifts are well established) some assignments for the new GO-CN peaks can be made. The peak at 47 ppm in the CP spectrum is likely to be due to the basal plane carbon directly bonded to the malononitrile group. The remaining low chemical shift peaks can be assigned to the CH carbon of the malononitrile group, and other sp^3 hybridised carbons found in the basal plane: introducing surface functionalisation disrupts the sp^2 carbon system and it is plausible that some sp^3 hybridisation occurs around the malononitrile groups as a result. The nitrile carbon should be observable in the ^{13}C ssNMR spectrum at around 108 ppm; looking at the GO-CN CP spectrum in figure 4.2, a small peak can be seen at this chemical shift as a shoulder to the sp^2 carbon signal.

D band ~ 1340 cm^{-1}   **G band** ~ 1600 cm^{-1}   **C-N** ~ 2220 cm^{-1}   **G' band** ~ 2700 cm^{-1}
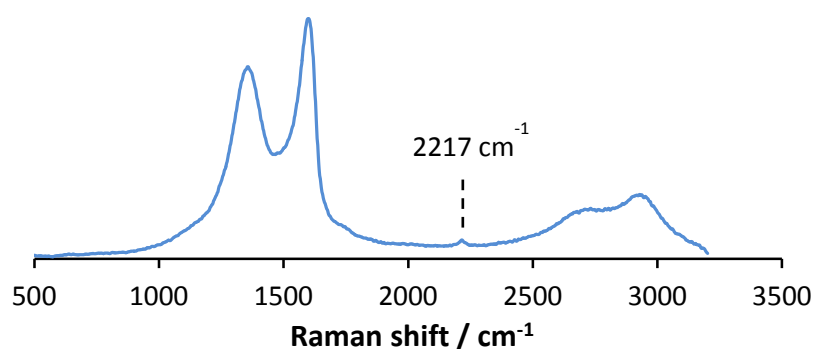
Fig. 4.4 Raman spectrum of GO-CN; excitation wavelength 514 nm.

The Raman spectrum of GO-CN (figure 4.4) gives complementary structural information to FTIR. The D, G and G' bands are clearly observable, confirming that the graphene-type structure remains intact. With a D/G ratio of 1.3, it seems that treatment with malononitrile

has not largely reduced the GO sheets, making the CMG available for further chemical modification. A small peak at 2217 cm^{-1} can also be seen, this band corresponds to the nitrile group.

EDX shows the percentage composition of GO-CN (with standard deviation values shown in parenthesis) to be: C 75 (2); N 1.5 (0.5); O 19 (2); Na 5 (2). The CMG thus has 1.5 at.% nitrogen with negligible change to the C/O ratio when compared to bwGO.
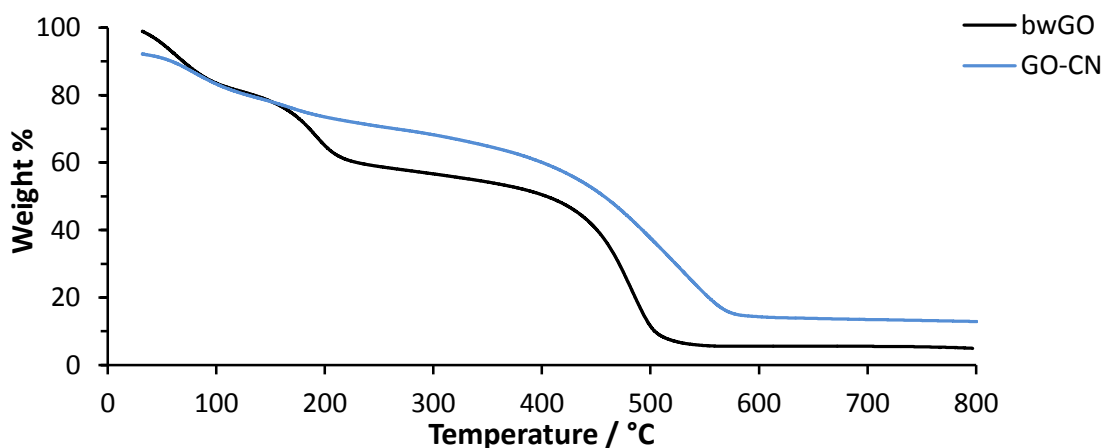
Fig. 4.5 TGA profiles of bwGO (black) and GO-CN (blue).

The TGA profile of GO-CN (figure 4.5) reveals an increased thermal stability for GO-CN: the decomposition temperature has increased by 50 °C compared to bwGO. A second important observation is that there is no sign of any mass loss at 200 °C for GO-CN, suggesting that the functionalisation has occurred on the bwGO sheets, rather than on any residual OD.

The unchanged D/G and C/O ratios as measured by Raman and EDX respectively, are reflected in drop shape analysis (figure 4.6), which shows no apparent change in hydrophilicity when compared to the average contact angle (CA) of bwGO (49°; see section 2.3).
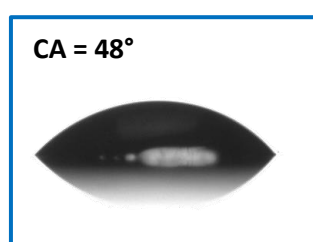
Fig. 4.6 Drop shape analysis of GO-CN.

Reaction with malononitrile thus produces a nitrogen functionalised CMG material with increased thermal stability and no loss in dispersibility. The Swager group reported a nitrogen incorporation of 4.4 at.%,[1] using the same synthetic protocol with bwGO yielded only 1.5 at.% N, it is thus likely that previous attempts to functionalise GO sheets with malononitrile have not given a true picture, as inadvertent functionalisation of the OD has occurred.

4.2   Reaction of bwGO with Sulfur Nucleophiles

4.2.1 Reaction with Potassium Thioacetate

After confirming the attachment of malononitrile to bwGO, attention was focused on targeting the epoxide functionalities on GO with sulfur nucleophiles; something which, at the time, was unexplored. Potassium thioacetate is a convenient source of nucleophilic sulfur[6, 28] and introduces a group that can be subsequently elaborated to reveal a thiol group. As with the reaction with malononitrile, to avoid the possibility of side reactions, the OD was removed prior to reaction.

When applied to bwGO, the thioacetate anion is expected to selectively attack the epoxide groups, as shown in scheme 4.3. The reaction work-up included an aqueous step, which is expected to result in the hydrolysis of the thioacetate to leave just surface-bound thiol groups. Extensive washing of the material after work-up should remove all unreacted reagents.
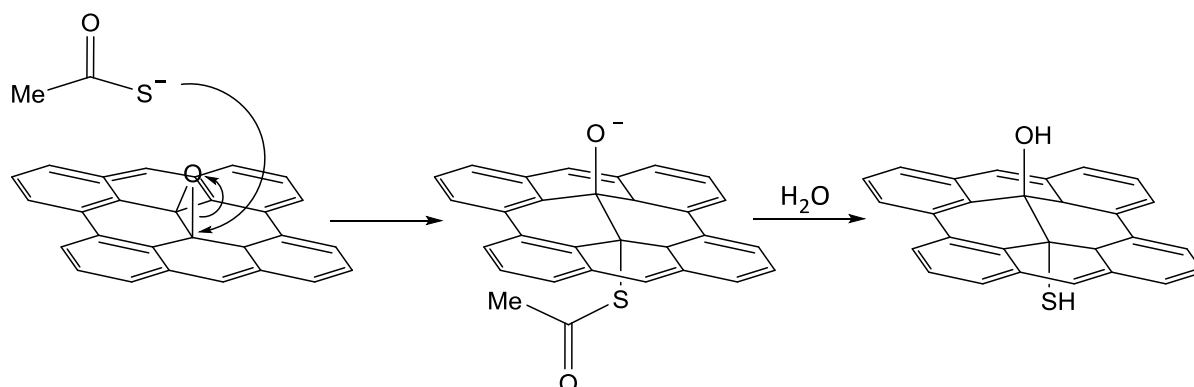
Scheme 4.3 Nucleophilic attack of thioacetate at an epoxide to form a thiol group.

As for the reaction with malononitrile in section 4.1, hydroxyl and thiol groups are expected to end up on both sides of the GO sheet. The FTIR spectrum of this thiol functionalised bwGO material (GO-SH) is shown in figure 4.7.
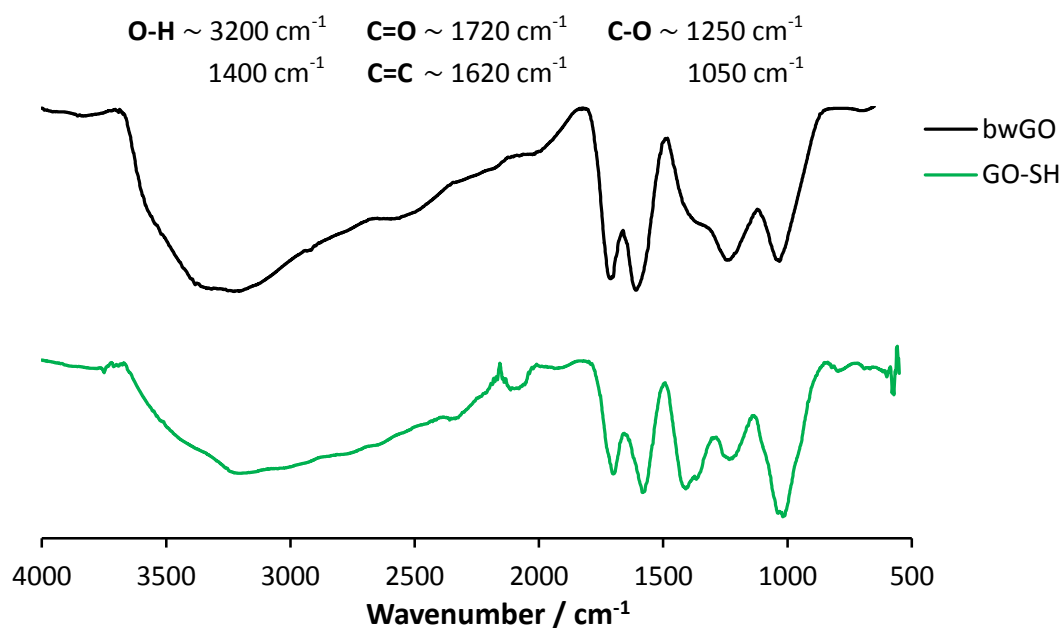
Fig. 4.7 ATR-FTIR spectra of bwGO (black) and thiol functionalised bwGO (green).

The FTIR spectrum of GO-SH (figure 4.7) shows a significant reduction in the C-O epoxy groups (1250 cm^{-1}) compared to bwGO, however no evidence of S-H stretching was detected: the weak S-H band is expected between 2600 and 2550 cm^{-1}, and so is presumably obscured by the broad OH absorbance.
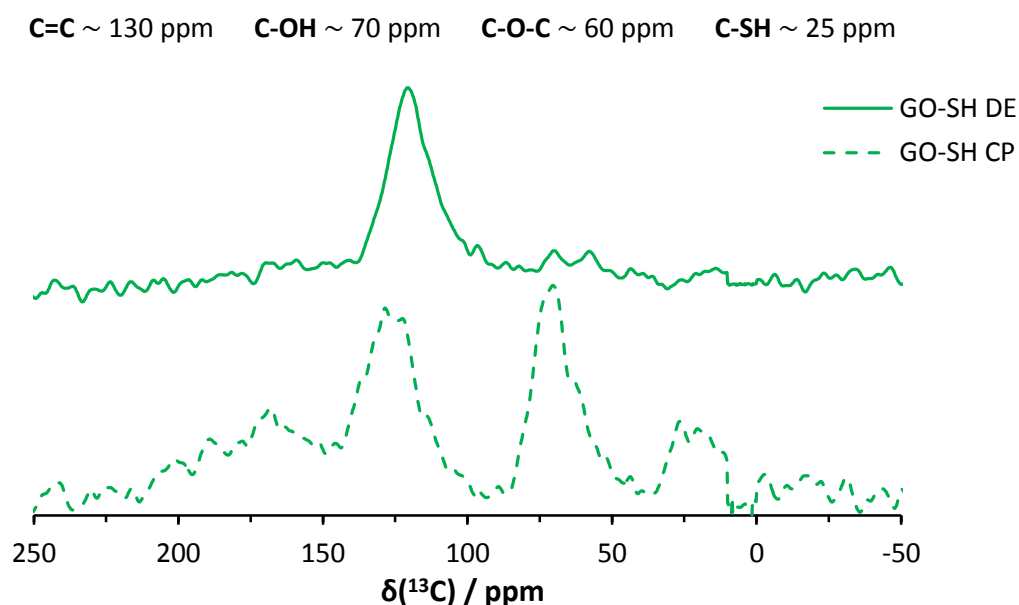
Fig. 4.8 ^{13}C MAS ssNMR spectra of GO-SH, both the direct excitation (DE) spectrum (solid) and the cross polarised (CP) spectrum (dashed) are shown.

Figure 4.8 shows the ^{13}C ssNMR spectra of GO-SH. The dominant peak in the directly observed spectrum is the characteristic sp^2 C-C peak at 122 ppm, together with much weaker peaks at 72 ppm (C-OH) and 61 ppm (C-O-C). A carbon with a thiol group would be expected to exhibit a resonance 30–40 ppm lower than one with an oxygen atom attached. The small peak at around 26 ppm is likely to be caused by these carbon atoms as this peak is substantially enhanced in the cross polarised spectrum.

The intensity of the signal for the carbon atoms with hydroxide and epoxide groups attached is greatly reduced for GO-SH. This loss of OH groups may be the result of a reduction: while thioacetates are not an obvious reducing agent, their reducing properties do have synthetic utility in certain areas of organic chemistry.[29-31] Thus this loss of hydroxide and epoxide functionality is likely attributable to a combination of epoxide-opening reactions and chemical reduction.

EDX was used to measure the elemental composition of GO-SH as a function of reaction time (i.e. the length of time it was exposed to potassium thioacetate). An increase in the proportion of sulfur is seen up to 5.5 hours, before it starts to decrease. At the same time a steady decrease in the proportion of oxygen is seen; after 60 hours reaction time, the material produced has essentially no sulfur and has a C/O ratio similar to that obtained after a 24 hour hydrazine reduction (Table 4.1). Others have surmised that the deoxygenation process of GO aging occurs via the dissociation of H_2O at room temperature.[32] Therefore, it is possible that an analogous process is occurring under the elevated reaction temperature with the dissociation of H_2S or thioacetate. Alternatively elimination of disulphides could be occurring with the driving force being the reformation of the aromatic system.

Sample	Reaction time / hours	atomic % (standard deviation)			
		C	O	S	C/O
GO-SH	3	79 (1)	19 (1)	2.3 (0.4)	4:1
	5.5	80 (1)	16 (1)	3.7 (0.8)	5:1
	17	81 (2)	18 (1)	1.2 (0.8)	5:1
	60	86 (1)	13 (1)	0.1 (0.1)	7:1
rbwGO	24	85 (1)	15 (1)	-	6:1
	48	91 (2)	8 (2)	-	11:1

Table 4.1 EDX derived atomic % of GO-SH and rGO materials with the standard deviation given in parentheses.

A reaction time of 5.5 hours was found to yield a material with optimum sulfur incorporation. Hence all characterisation data (including the FTIR and ^{13}C ssNMR shown above) were collected from the GO-SH material prepared via a 5.5 hour reaction.

D band ~ 1340 cm^{-1} **G band** ~ 1600 cm^{-1} **G' band** ~ 2700 cm^{-1}
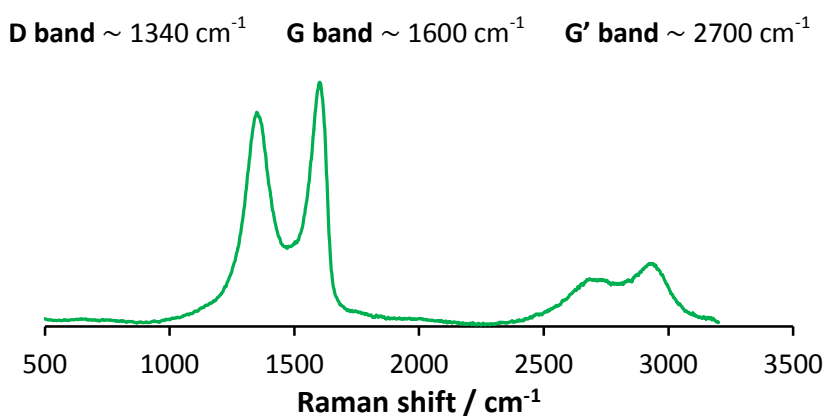
Fig. 4.9 Raman spectrum of GO-SH; excitation wavelength 514 nm.

The Raman spectrum shown in figure 4.9 confirms that the GO-SH material is still graphene-based, however the D/G ratio has increased to 1.7, again indicating a degree of reduction when compared to bwGO (D/G = 1.2). As with FTIR, the S-H band is not observed – presumably it lies under the G' band at 2600 cm^{-1}.

XPS data on the GO-SH material was gathered in order to determine the bonding environment of the sulfur, the results are shown in figure 4.10.
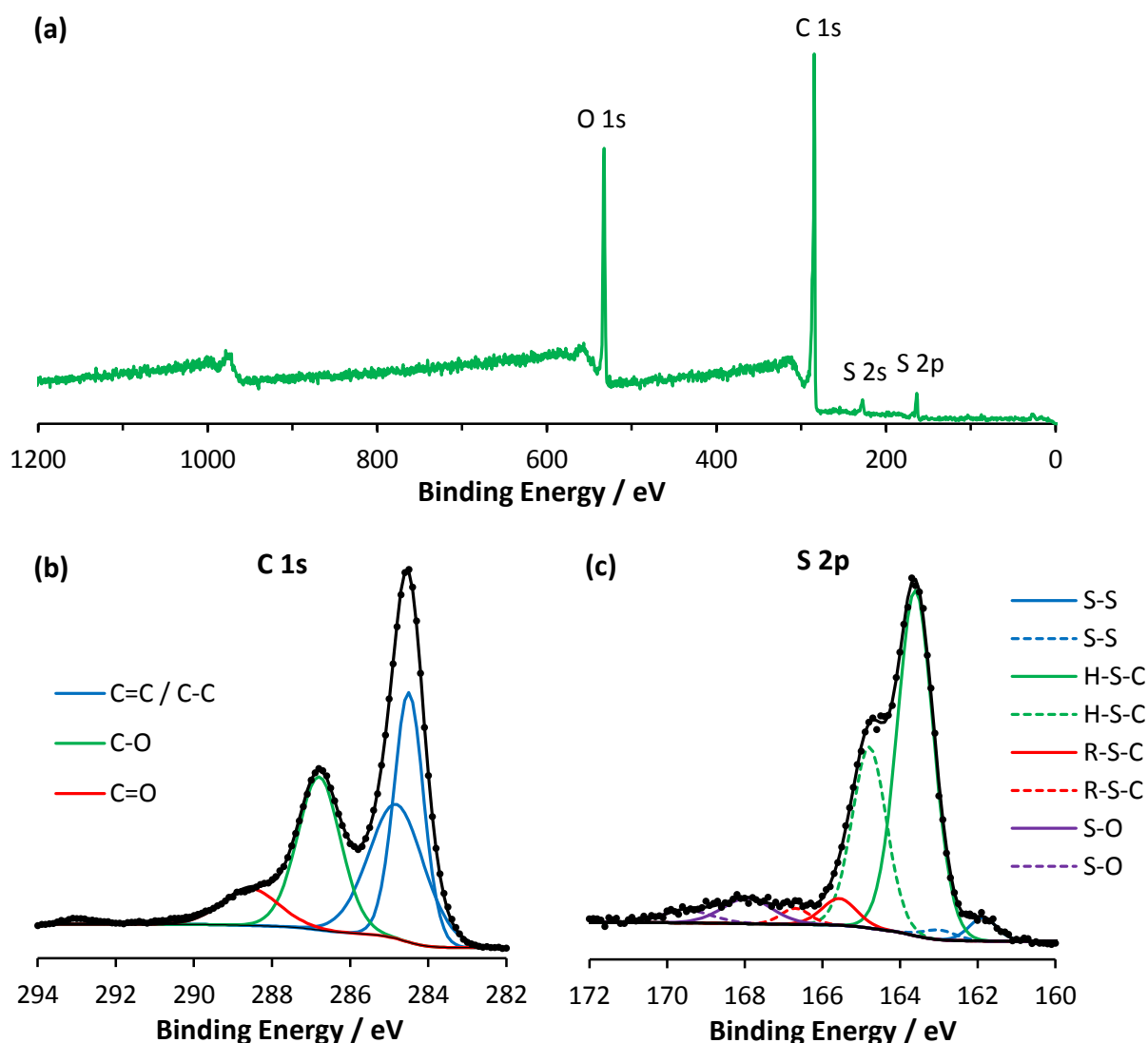
Fig. 4.10 XPS analysis of GO-SH, complete with survey scan **(a)**, and core level spectra C 1s **(b)** and S 2p **(c)**. The experimental data is shown as points with the underlying lines showing the fitted peaks (assignments as labelled). Note that for **(c)** the $2p_{3/2}$ orbital assignments are represented by solid lines while the corresponding dashed lines refer to the $2p_{1/2}$ orbitals.

The atomic percentages derivated from the XPS survey scan in figure 4.10 (a) are as follows: C 77.0; O 19.0; S 4.1. They are thus in close agreement with the EDX measurements; both techniques indicate a sulfur incorporation of around 4 at.%. This equates to an attached sulfur for every 19 carbon atoms, or for every 9 or 10 graphitic rings within a graphene-type sheet.

This 4 at.% sulfur incorporation seen for GO-SH can be compared to the 1.5 at.% nitrogen incorporation seen for GO-CN in section 4.1. The higher percentage of sulfur incorporation can be explained in terms of reactivity – it can be seen from the ssNMR spectra (figures 4.2 and 4.8) that some epoxy groups remain on the malononitrile functionalised GO whereas none are seen for GO-SH. Carbon and sulfur are similarly electronegative (C 2.55 and S 2.58 on the Pauling scale) but sulfur has a larger atomic radius (C 0.07 nm *vs* S 0.104 nm) and thus sulfur is expected to be more nucleophilic than carbon. The Ritchie equation provides a way of quantifying nucleophilicity and indeed thiolates are found to be more nucleophilic than most carbanions.[33] The smaller atomic radius of the carbanion also means that its reactivity is likely to be reduced to a greater extent in a protic solvent like water – other groups have discussed the inherent surface water of GO which is present even under careful anhydrous conditions,[1, 3, 4] this might play a role in the observed lower reactivity of malononitrile.

The binding energy of a carbon with a C-S bond is very similar to that of a carbon with a C-C bond, and thus it is not possible to use the C 1s core level spectrum in figure 4.10 (b) to prove the presence of a sulfur bound species at such low S atomic %. Instead it demonstrates a typical GO-based C 1s XPS profile. The S 2p spectrum, figure 4.10 (c), was used to study the sulfur environment. The S 2p spectrum is fitted with $2p_{3/2}$ (the lower binding energy component of the spin-orbit split doublet) components at 161.8, 163.6, 165.5 and 168.0 eV. These can be assigned as S-S, H-S-C, R-S-C and S-O bonds respectively, with the dominant contribution from the H-S-C bonds. Thus the majority of sulfur (78%) is covalently attached to carbon and hydroylsed to a thiol group. A small amount of sulfur (10%) is present as R-S-C, which is presumably due to a number of unhydrolysed MeCOS-C groups. An inert atmosphere was used to prevent unwanted oxidation impurities,[34] however the spectrum indicates that a small proportion (12%) of the sulfur is present in the form of S-S and S-O bonds.
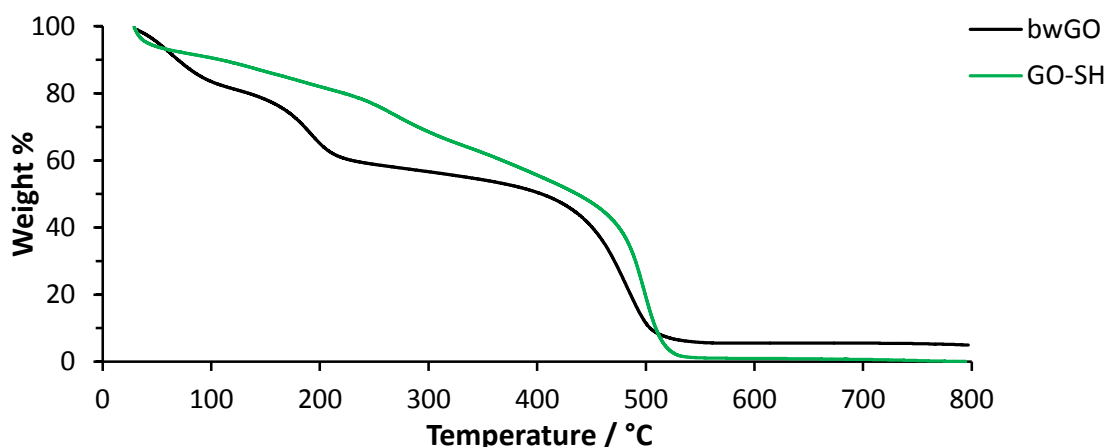
Fig. 4.11 TGA profile of bwGO (black) and GO-SH (green).

TGA (figure 4.11) shows that functionalisation of bwGO has significantly decreased the amount of surface adsorbed water (indicated by the low mass loss around 100 °C), suggesting that the CMG has a less hygroscopic nature. Similarly to chemically reduced GO samples, there is little mass loss below 500 °C with the major mass loss coming from the decomposition of the graphene-like sheets. This single mass loss for GO-SH also provides further evidence of the covalent functionalisation: if the thioacetate reactant had simply been adsorbed to the surface of the GO material, a mass loss corresponding to its desorption would be expected at a temperature lower than 500 °C.

Despite the reductive effects of thioacetate, GO-SH retains appreciable dispersibility in DMSO (unlike hydrazine-reduced GO). Drop shape analysis (figure 4.12) demonstrates that GO-SH retains similar levels of hydrophilicity to bwGO.
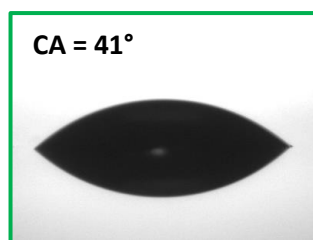
Fig. 4.12 Drop shape analysis of GO-SH.

Finally, TEM analysis confirms the monolayer graphene-like structure of GO-SH (figure 4.13). The sheets have flatly deposited, without coagulation, and are visible in the bright-field TEM image, figure 4.13 (a), stretched across holes in the lacey carbon support. Although the sheets are almost electron-transparent, they can be discerned in images due to the

occasional crease or fold, for example, to the right of the dashed circle in figure 4.13 (a). Electron diffraction patterns from individual GO-SH sheets show a hexagonal array of diffraction spots – the SAED pattern in figure 4.13 (b) was taken from the area in figure 4.13 (a) marked by the dashed circle. The inner hexagon of spots are more intense than the outer ones, as shown by the line profile given in figure 4.13 (c). The diffraction pattern is thus characteristic of a material with a monolayer graphene-like backbone, indistinguishable from those of graphene oxide.
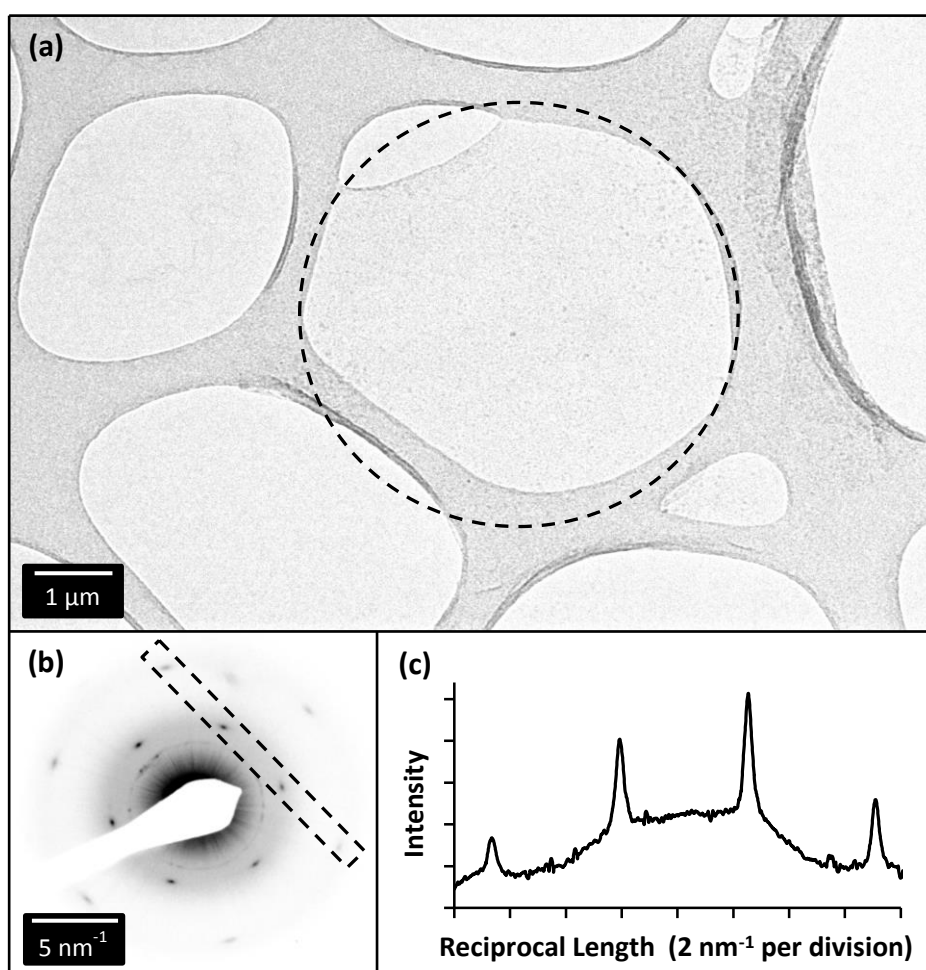
Fig. 4.13 TEM analysis of GO-SH. **(a)** Bright-field TEM image showing a sheet of GO-SH suspended across a hole in a lacey carbon support grid. **(b)** A selected area electron diffraction pattern from the dashed region in **(a)**. **(c)** Line profile as marked on the diffraction pattern showing that the outer diffraction peaks are less intense than the inner ones.

All the characterisation data gathered provides evidence for surface functionalisation via epoxide-opening using a sulfur nucleophile. Subsequent hydrolysis yields a clean graphene-like material with surface thiol groups (GO-SH). These surface thiols should be nucleophilic in their own right and thus amenable to further reaction with electrophiles (see chapter 5). A reaction time of 5.5 hours was found to give a good balance of SH functionalisation with acceptable levels of reduction.

4.2.2 Reaction with Thiophenol

Attaching different functional groups to the surface of GO provides a way of tweaking certain properties. Having shown that the surface epoxides are a good route to functionalisation, the use of different sulfur nucleophiles to modify the GO surface was looked at. The large surface area of graphene-based materials is an attractive property for energy storage applications: hydrogen adsorption[35, 36] and electrode materials.[37] Attaching a group such as thiophenol could increase the surface area without dramatically affecting the hydrophilicity of the material. In order to ring-open surface epoxides in this manner, the thiophenol solution was deprotonated with LiOH and subsequently reacted with a dispersion of bwGO in acetonitrile. The mixture was left stirring at room temperature for 6 hours before being extracted with CH_2Cl_2 and washed with water. This GO material is referred to as GO-SPh.
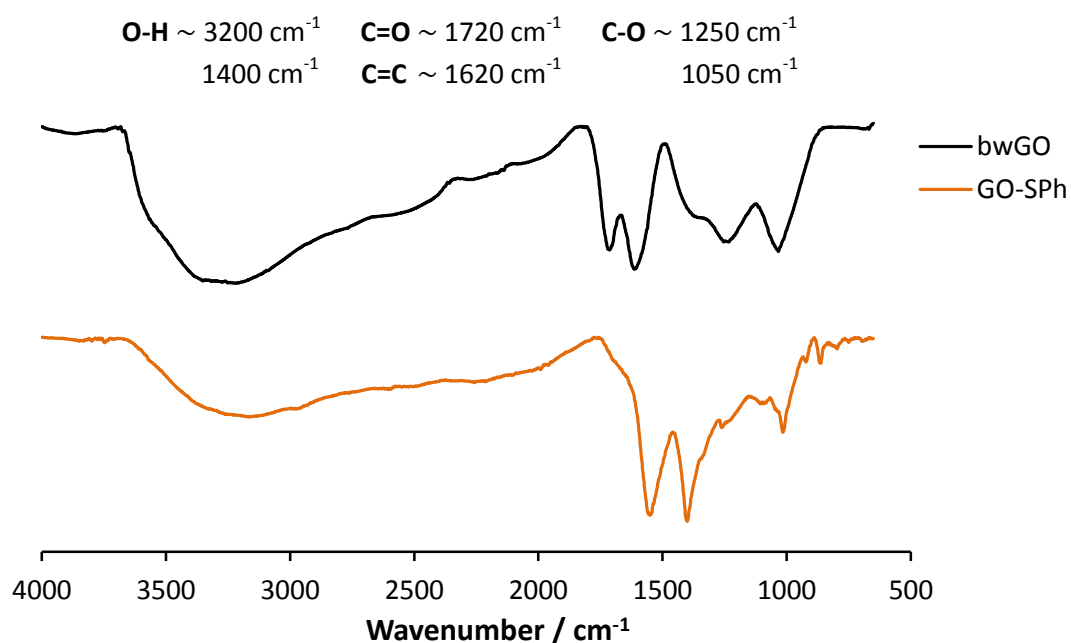
Fig. 4.14 ATR-FTIR spectra of bwGO (black) and GO-SPh (orange).

Similarly to the GO-SH material, in FTIR a decrease in the epoxy absorbance for GO-SPh relative to bwGO is seen (figure 4.14). The spectrum also shows a notable decrease in the amount of hydrogen-bonded OH; this is likely to be due to the desorption of surface water as the O-H bending signal around 1400 cm^{-1} remains strong. As with GO-CN, the absence of the C=O band for GO-SPh can be attributed to the presence of COO$^-$Li$^+$ salts.

C=C ~ 130 ppm   C-OH ~ 70 ppm   C-O-C ~ 60 ppm
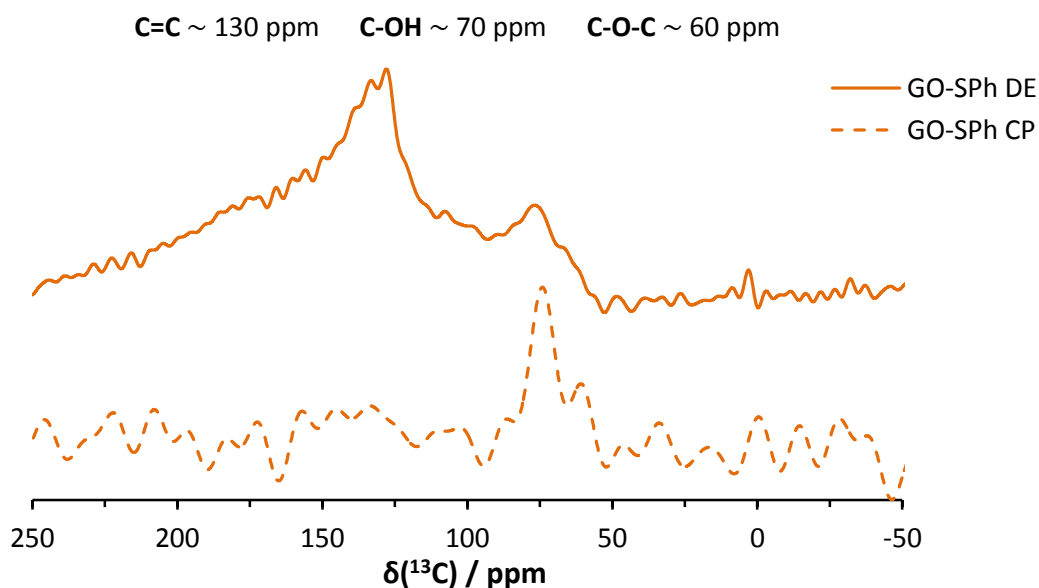
Fig. 4.15 ^{13}C MAS ssNMR spectra of GO-SPh, both the direct excitation (DE) spectrum (solid) and the cross polarised (CP) spectrum (dashed) are shown.

The ^{13}C MAS ssNMR spectra for GO-SPh (figure 4.15) has poor resolution due to line broadening and it is thus difficult to assign with confidence. Looking at the directly observed spectrum: the sp^2 carbon signal at 128 ppm is strong, but the hydroxyl carbon signal (78 ppm) is largely obscured. In addition, the peak for any remaining epoxy groups gets lost in noise (expected chemical shift, 62 ppm). The cross polarised spectrum shows an enhanced signal for the hydroxide carbons, as expected.
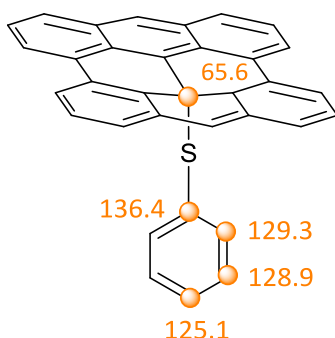
Fig. 4.16 ^{13}C ssNMR chemical shift predictions for the new signals in GO-SPh. The orange spheres indicate carbons of interest, with predicted chemical shifts as labelled.

As discussed in section 4.1, it is not possible to make accurate chemical shift predictions for GO-based materials. However as seen from figure 4.16, some peaks due to the thioether carbon and the sp^2 carbons of the phenyl ring are expected. There is a peak at 62 ppm in the

119

CP spectrum, which could be due to residual epoxy groups or thioether carbons. The aryl C–H carbons are lost within the broad peak at 129 ppm in the DE spectrum, and furthermore they are not possible to distinguish in the CP spectrum due to the level of noise. What is clear however is that the number of epoxy groups has decreased compared to bwGO. The ^{13}C ssNMR, in this case, does not provide compelling evidence, but is also not inconsistent with functionalisation.

EDX measurements confirm the incorporation of sulfur, without the reductive effects seen for the reaction with thioacetate: C 75 (2); O 23 (1); S 1.3 (0.8).

D band ~ 1340 cm^{-1} **G band** ~ 1600 cm^{-1} **G' band** ~ 2700 cm^{-1}

Raman Shift / cm^{-1}
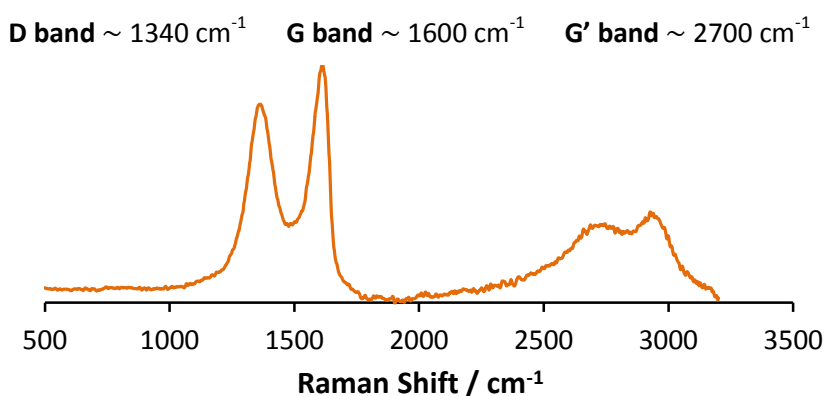
Fig. 4.17 Raman spectrum of GO-SPh; excitation wavelength 514 nm.

The Raman spectrum of GO-SPh is characteristic of a GO-based material, D/G ratio = 1.6. Thus the surface functionalisation has again resulted in an increased D/G ratio relative to bwGO.
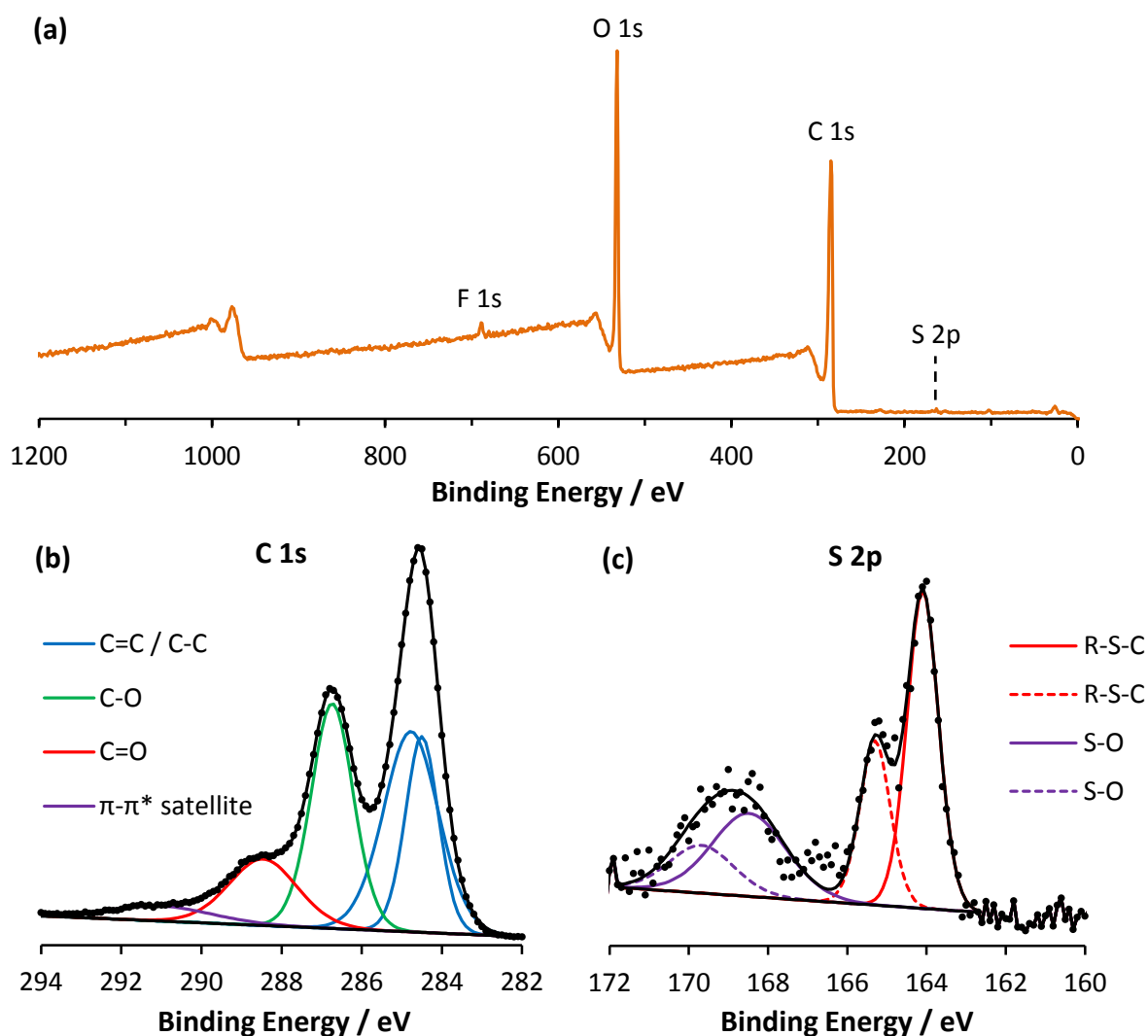
Fig. 4.18 XPS analysis of GO-SPh, complete with survey scan **(a)**, and core level spectra C 1s **(b)** and S 2p **(c)**. The experimental data is shown as points with the underlying lines showing the fitted peaks (assignments as labelled). Note that for **(c)** the $2p_{3/2}$ orbital assignments are represented by solid lines while the corresponding dashed lines refer to the $2p_{1/2}$ orbitals.

The XPS survey scan in figure 4.18 (a) shows an usually high proportion of oxygen, and the atomic percentages derivated from the same data are as follows: C 46.4; O 50.1; S 0.6; F 2.9. The abnormal oxygen percentage may be the result of surface contamination and thus the atomic composition is not to be relied on in this case. However the core level spectra of carbon and sulfur can be used to confirm the bonding environments within the CMG.

The C 1s core level spectrum, figure 4.18 (b), shows a typical profile for a GO-based material, showing major contributions from C-O, C=O, sp^2 and sp^3 C-C bonding environments. The S 2p spectrum in figure 4.19 (c) is more informative since the principal bonding environment can be assigned to a thioether: R-S-C.
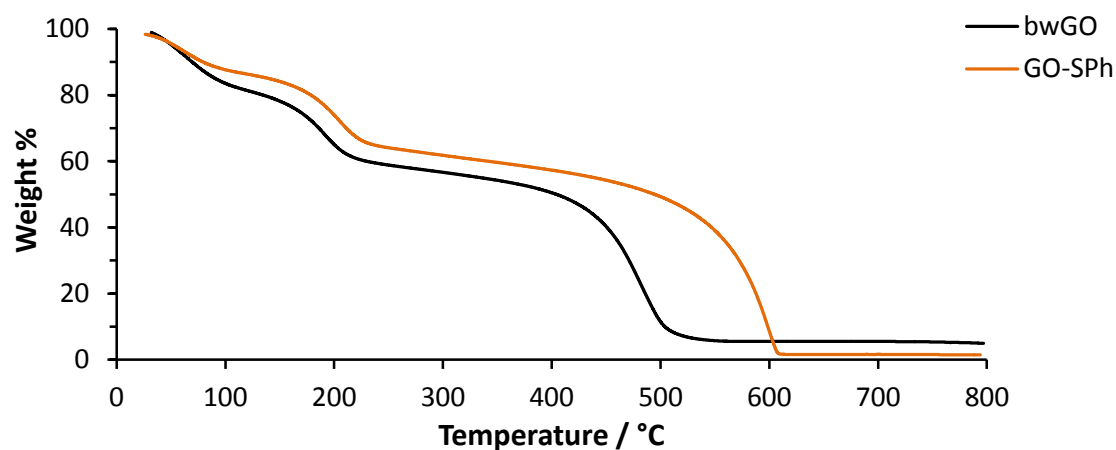
Fig. 4.19 TGA profile of bwGO (black) and GO-SPh (orange).

The TGA of the GO-SPh material is shown in figure 4.19. The overall thermal stability of the material has increased by 100 °C compared to bwGO. If the thiophenol was merely bound to bwGO via non-covalent interactions we would expect to see a lower temperature mass loss in the TGA, much like we do for the OD in aGO which is also expected to be bound via π-π stacking and hydrogen bonds. In the TGA of GO-SPh the mass loss at ~200 °C is proportionally less than that seen for bwGO, and the overall thermal stability of the material has increased. This result is significant and is not consistent with π- π stacking, instead it strongly suggests chemical modification of the GO sheets. Other research groups have also reported an increase in the thermal stability of CMGs.[20, 38-40] While justification remains speculative, it is thought that the attachment of different functional groups prevents the usual decomposition pathway via the production of CO, CO_2 and H_2O. See chapter 5 for more examples of thioether functionalised CMGs.

4.3   Reaction of bwGO with Long Chain Polymers

Graphene-polymer composites are currently of great interest, with researchers keen to combine to superlative physical properties of graphene-based materials with the tuneable properties of polymers. With this in mind, thiol terminated polymers were studied to see if they could be grafted to the GO surface in a similar manner.

A series of water-soluble poly(*N*-isopropylacrylamide), or p(NIPAM), polymers (figure 4.20) with differing chain lengths: 30, 200 and 440 repeat units, were used for reaction with bwGO.
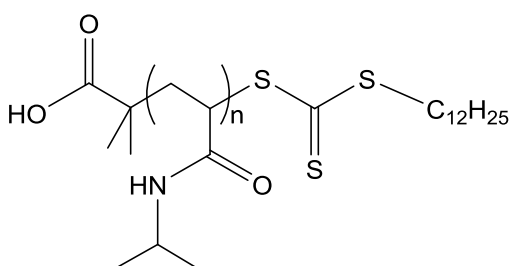
Fig. 4.20 poly(N-isopropylacrylamide); n = 30, 200 and 440.

The trithiocarbonate moiety at the ω-terminus of these RAFT-derived polymer chains was exploited for reaction with bwGO: the p(NIPAM) polymers were treated with methylamine to yield a thiolate terminated polymer (scheme 4.4). The primary amine attacks the polymer at the reactive double bond of the trithiocarbonate end group, breaking the weak S-C bond to form a dithiocarbonate and a sulfur anion.[41]
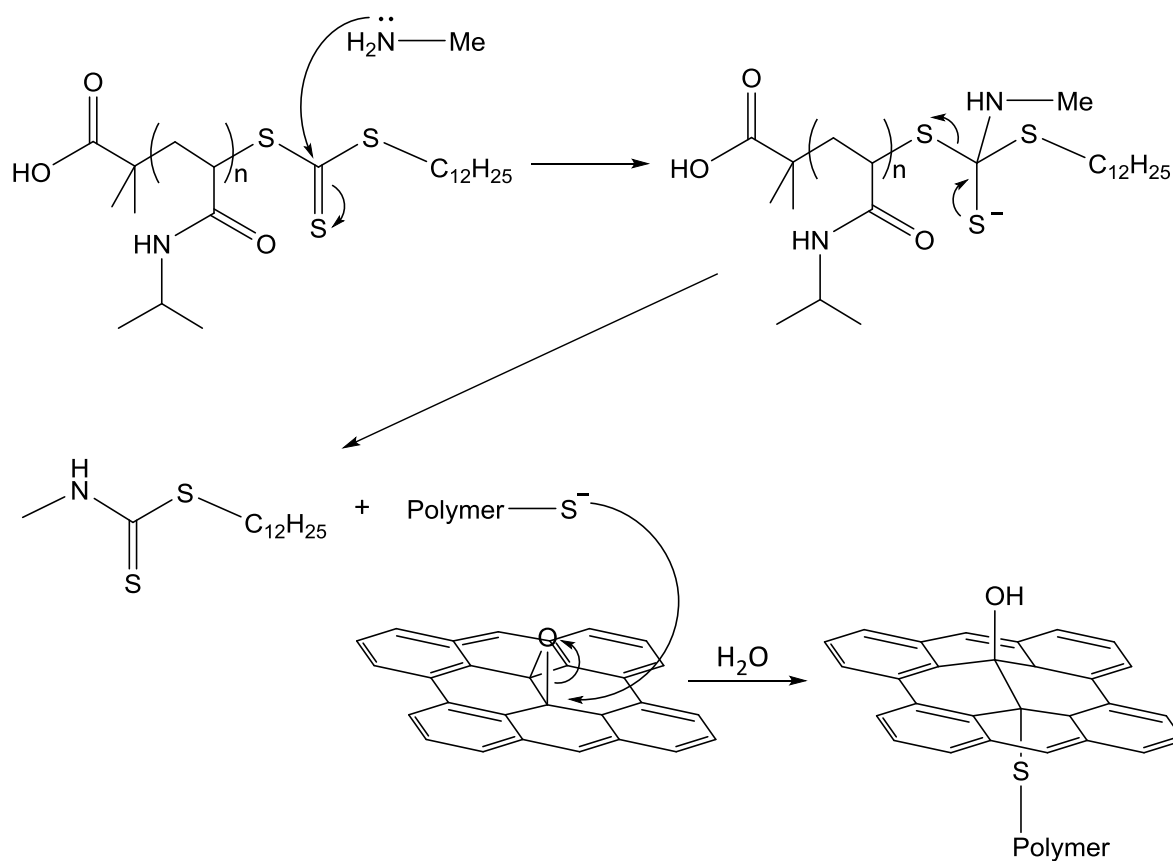
Scheme 4.4 Mechanism for the reaction of p(NIPAM) with the epoxide groups on the bwGO sheet surface.

All three polymers (30, 200 and 440 repeat unit chains) were reacted with bwGO to give the composite materials denoted GO-pNIPAM$_{30}$, GO-pNIPAM$_{200}$ and GO-pNIPAM$_{440}$ respectively.
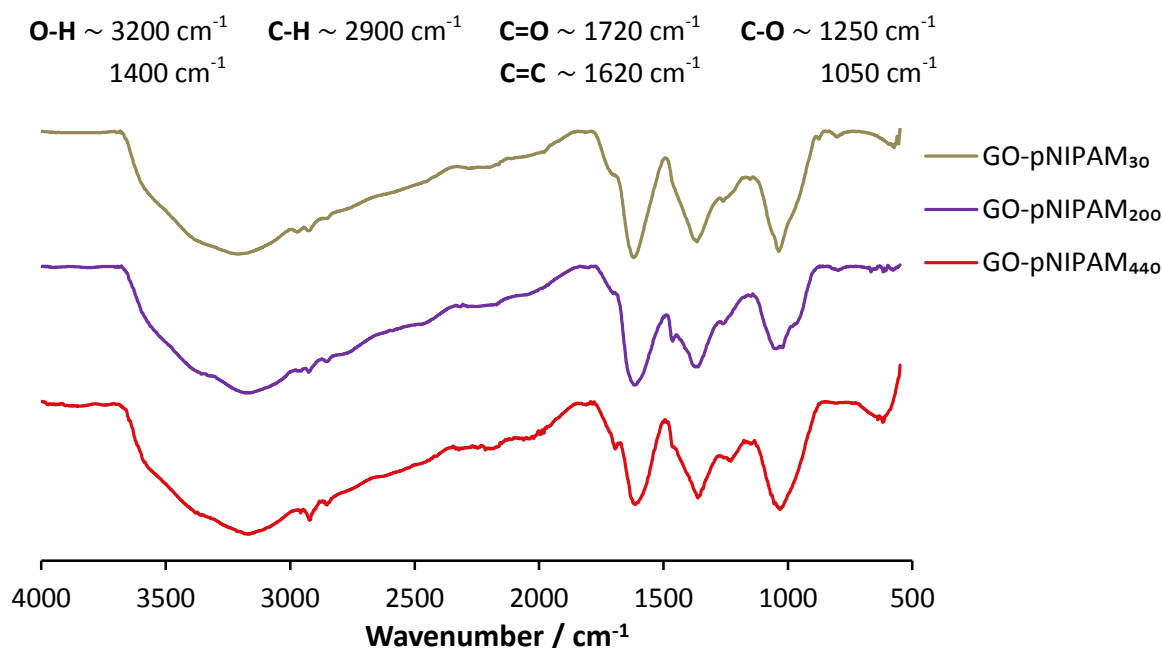
Fig. 4.21 ATR-FTIR spectra of the three p(NIPAM) functionalised GO materials.

The FTIR spectra of the GO-pNIPAM materials (figure 4.21) are very similar to bwGO, with the exception of: new alkyl peaks present at 2880 and 2900 cm^{-1}, due to C-H stretches from the repeat unit of the p(NIPAM) polymers; and a reduction in the intensity of epoxy groups at 1240 cm^{-1}. The C=O stretch of an amide would be expected to fall between 1630 and 1670 cm^{-1}, but in practice it was found that the amide absorbance could not be distinguished from the overlapping carboxyl C=O and C=C bands.

EDX was used to confirm the incorporation of nitrogen to the GO sheets. The atomic compositions measured for all three samples are shown in Table 4.2.

Sample	atomic % (standard deviation)			
	C	O	N	C/O
GO-pNIPAM$_{30}$	75 (1)	24 (1)	1.3 (0.8)	3:1
GO-pNIPAM$_{200}$	76 (1)	20 (1)	2.9 (0.2)	4:1
GO-pNIPAM$_{440}$	79 (2)	18 (2)	2.7 (0.4)	4:1

Table 4.2 EDX derived atomic % of the GO-pNIPAM materials with the standard deviation given in parentheses.

The FTIR and EDX data suggest that GO-polymer composites have been successfully prepared. However, characterisation was also sought from ^{13}C ssNMR, Raman, XPS and TGA. Since all three polymers have the same repeat unit structure, the data collected was very similar. For clarity only the results from the longest chain polymer composite (GO-pNIPAM$_{440}$) are presented here, but for completeness, it should be stressed that the results for all three cases led to the same conclusion.

CONH ~ 170 ppm   **C=C** ~ 130 ppm   **C-OH** ~ 70 ppm   **C-C** ~ 45 ppm
C-O-C ~ 60 ppm   **C-H** ~ 30 ppm

GO-pNIPAM$_{440}$ DE
GO-pNIPAM$_{440}$ CP
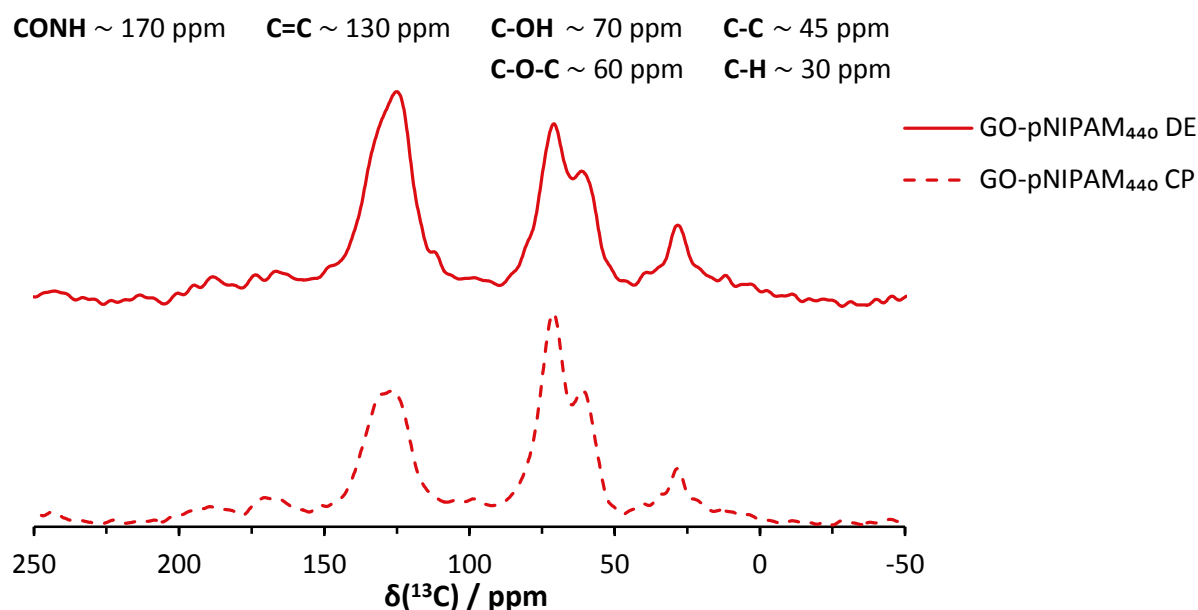
Fig. 4.22 ^{13}C MAS ssNMR spectra of GO-pNIPAM$_{440}$, both the direct excitation spectrum (solid) and the cross polarised spectrum (dashed) are shown.

New peaks are expected in the ^{13}C ssNMR from the repeat unit of the NIPAM polymer, these should correspond to the sp^3 alkyl carbons and the amide carbon. Amide carbons lie at a high chemical shift, around 170 ppm, and indeed a new peak can be seen in the DE spectrum (figure 4.22) at 169 ppm, which is enhanced in the CP spectrum. A broad signal at 30 ppm can also be seen which may be a combination of peaks with overlapping chemical shifts.
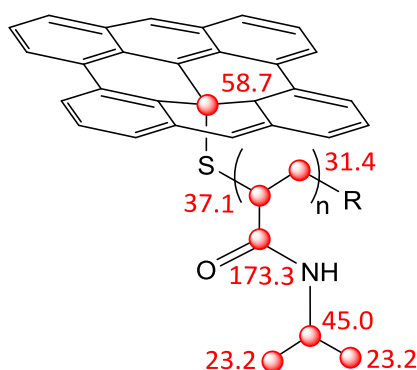
Fig. 4.23 ^{13}C ssNMR chemical shift predictions for the new signals in GO-pNIPAM. The red spheres indicate carbons of interest, with predicted chemical shifts as labelled.

Figure 4.23 shows a number of new sp^3 signals for the GO-pNIPAM materials with estimated chemical shifts ranging from 23 to 45 ppm, they are thus in agreement with the spectra in figure 4.22.
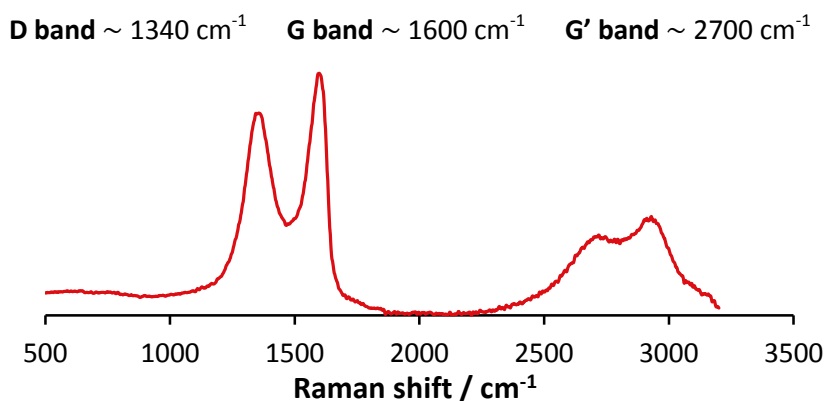
Fig. 4.24 Raman spectrum of GO-pNIPAM$_{440}$; excitation wavelength 514 nm.

The Raman spectrum of GO-pNIPAM$_{440}$ (figure 4.24) is as expected; showing strong D, G and G' bands. The D/G ratio is calculated to be 1.3, indicating that the addition of the polymer chain has caused no significant change (e.g. reduction) to the sheet structure of GO.

Meanwhile, the XPS survey scan of GO-pNIPAM$_{440}$, figure 4.25 (a), clearly shows the incorporation of nitrogen. Integration of the regions measures 4 ± 0.4 atomic % nitrogen, which is similar to the EDX measurements (2.7%; sd = 0.4). The C 1s core level spectrum, figure 4.25 (b), shows the environments expected for a GO-based material. The binding energy of an amide carbon is measured at 287.9–288.3 eV,[42] it is therefore not possible to distinguish it from the C-O and C=O (keto, carboxy) peaks of GO itself.

The N 1s core level spectrum shows nitrogen from two different chemical environments. The principal contribution has a measured binding energy of 400 eV, consistent with amide functionalities,[42] by area, this peak corresponds to 80% of the nitrogen present in GO-pNIPAM$_{440}$. The smaller peak at 401.5 eV can be assigned to residual DMF solvent in this particular sample.
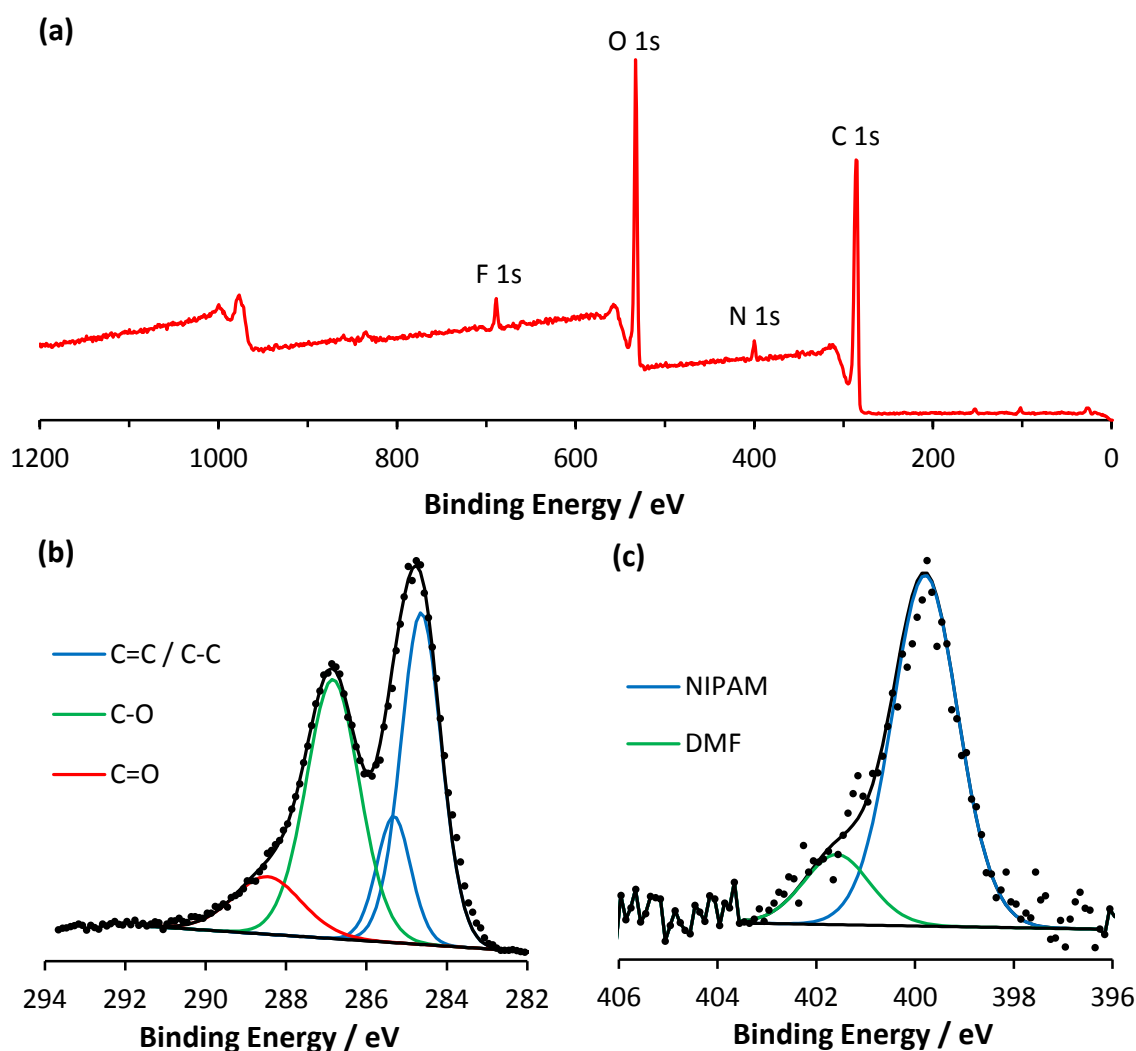
Fig. 4.25 XPS analysis of GO-pNIPAM$_{440}$, complete with survey scan **(a)**, and core level spectra C 1s **(b)** and N 1s **(c)**. The experimental data is shown as points with the underlying lines showing the fitted peaks (assignments as labelled).

Final structural characterisation came from TGA (figure 4.26). Some mass loss is seen below 200 °C, which is believed to be due to the residue DMF. However, the thermal stability of the GO sheets has increased to over 600 °C. This is the highest decomposition temperature seen for any of the CMGs prepared so far, and is presumably due to the presence of the

long polymer chains in place of hydroxide, epoxide, or thiol groups which might inititate decompostion.
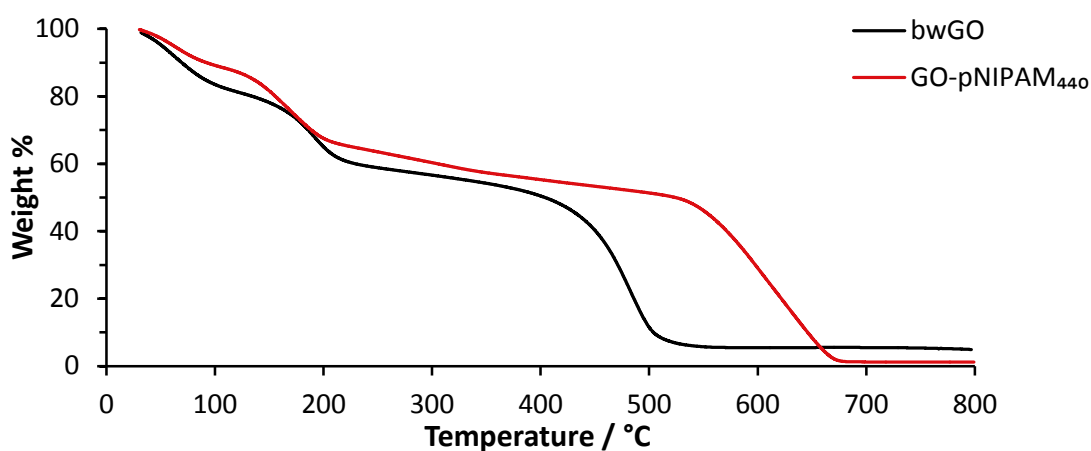
Fig. 4.26 TGA profile of GO-pNIPAM$_{440}$.

This increase in thermal stability does not come at the cost of reduced dispersibility, in fact the GO-polymer composites show smaller contact angles (34°) than bwGO, suggesting an increase in hydrophilicity (figure 4.27).
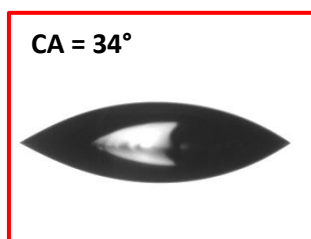
Fig. 4.27 Drop shape analysis of GO-pNIPAM$_{440}$.

4.4 Conclusions

Four different CMGs have been prepared from the clean bwGO material discussed in chapter 3 using a variety of different nucleophiles to selectively ring-open epoxy groups on the basal plane of GO. FTIR, EDX, ^{13}C ssNMR, Raman, XPS, TGA and contact angle measurements have been used to provide a complete picture of characterisation.

By expanding on the Swager study of carbon nucleophiles,[1] it has been demonstrated that GO-CN can be prepared without the presence of OD. The GO-CN material has a higher thermal stability compared to bwGO, presumably due to the replacement of labile C-O bonds with C-C bonds, and the nitrile group itself is amenable to further chemical modification via nucleophilic addition, hydrolysis, reduction and alkylation.

Next, novel reactions using sulfur nucleophiles were investigated. A novel GO-SH material with surface thiol groups which could be reacted with many different electrophiles was prepared, allowing for extensive functionalisation of the GO surface and a convenient route towards making CMGs with a wide variety of chemical and physical properties. The material shows similar thermal stability to bwGO; it is possible that the decomposition pathway of both materials is similar, initiated at the reactive SH centres of GO-SH and at the OH sites of bwGO. Capping the SH groups and preventing that decomposition pathway may lead to a higher thermal stability, and indeed this has been shown to be case for GO-SPh.

Finally, the GO-pNIPAM materials demonstrate that it is possible to directly graft a polymer to the surface of GO. Contact angle measurements show an increase in hydrophilicity compared to unfunctionalised bwGO, and TGA studies show a significant enhancement in the thermal stability of the material, compared to both bwGO and the isolated polymer which decomposes sharply at 400 °C. The increased thermal stability of GO-polymer composites has previously been attributed to the attractive interactions between the GO sheets and the polymer chains (e.g. hydrogen bonds).[43]

1. Collins, W. R.; Schmois, E.; Swager, T. M. *Chem. Commun.* **2011,** 47, (31), 8790-8792.
2. Dikin, D. A.; Stankovich, S.; Zimney, E. J.; Piner, R. D.; Dommett, G. H. B.; Evmenenko, G.; Nguyen, S. T.; Ruoff, R. S. *Nature* **2007,** 448, (7152), 457-460.
3. Medhekar, N. V.; Ramasubramaniam, A.; Ruoff, R. S.; Shenoy, V. B. *ACS Nano* **2010,** 4, (4), 2300-2306.
4. Compton, O. C.; Cranford, S. W.; Putz, K. W.; An, Z.; Brinson, L. C.; Buehler, M. J.; Nguyen, S. T. *ACS Nano* **2012,** 6, (3), 2008-2019.
5. Swager, T. M. *ACS Macro Lett.* **2012,** 1, (1), 3-5.
6. Park, N.; Park, K.; Jang, M.; Lee, S. *J. Org. Chem.* **2011,** 76, (11), 4371-4378.
7. Veca, L. M.; Lu, F.; Meziani, M. J.; Cao, L.; Zhang, P.; Qi, G.; Qu, L.; Shrestha, M.; Sun, Y.-P. *Chem. Commun.* **2009**, (18), 2565-2567.
8. Shen, J.; Shi, M.; Ma, H.; Yan, B.; Li, N.; Hu, Y.; Ye, M. *J. Colloid Interface Sci.* **2010,** 352, (2), 366-370.
9. Avinash, M. B.; Subrahmanyam, K. S.; Sundarayya, Y.; Govindaraju, T. *Nanoscale* **2010,** 2, (9), 1762-1766.
10. Hu, H.; Wang, X.; Wang, J.; Liu, F.; Zhang, M.; Xu, C. *Appl. Surf. Sci.* **2011,** 257, (7), 2637-2642.
11. Xu, C.; Wang, X.; Wang, J.; Hu, H.; Wan, L. *Chem. Phys. Lett.* **2010,** 498, (1–3), 162-167.
12. Collins, W. R.; Lewandowski, W.; Schmois, E.; Walish, J.; Swager, T. M. *Angew. Chem., Int. Ed.* **2011,** 50, (38), 8848-8852.
13. Chang, D. W.; Lee, E. K.; Park, E. Y.; Yu, H.; Choi, H.-J.; Jeon, I.-Y.; Sohn, G.-J.; Shin, D.; Park, N.; Oh, J. H.; Dai, L.; Baek, J.-B. *J. Am. Chem. Soc.* **2013,** 135, (24), 8981-8988.
14. Sun, Z.; Kohama, S.-i.; Zhang, Z.; Lomeda, J.; Tour, J. *Nano Res.* **2010,** 3, (2), 117-125.
15. Liu, Y.; Deng, R.; Wang, Z.; Liu, H. *J. Mater. Chem.* **2012,** 22, (27), 13619-13624.
16. Collins, W. R.; Lewandowski, W.; Schmois, E.; Walish, J.; Swager, T. M. *Angew. Chem.* **2011,** 123, (38), 9010-9014.
17. Sydlik, S. A.; Swager, T. M. *Adv. Funct. Mater.* **2013,** 23, (15), 1873-1882.
18. Pham, T. A.; Kumar, N. A.; Jeong, Y. T. *Synth. Met.* **2010,** 160, (17–18), 2028-2036.
19. Lin, Z.; Liu, Y.; Wong, C.-p. *Langmuir* **2010,** 26, (20), 16110-16114.
20. Yang, H.; Shan, C.; Li, F.; Han, D.; Zhang, Q.; Niu, L. *Chem. Commun.* **2009**, (26), 3880-3882.
21. Yang, H.; Li, F.; Shan, C.; Han, D.; Zhang, Q.; Niu, L.; Ivaska, A. *J. Mater. Chem.* **2009,** 19, (26), 4632-4638.
22. Bourlinos, A. B.; Gournis, D.; Petridis, D.; Szabó, T.; Szeri, A.; Dékány, I. *Langmuir* **2003,** 19, (15), 6050-6055.
23. Hsiao, M.-C.; Liao, S.-H.; Yen, M.-Y.; Liu, P.-I.; Pu, N.-W.; Wang, C.-A.; Ma, C.-C. M. *ACS Appl. Mater. Inter.* **2010,** 2, (11), 3092-3099.
24. Chua, C. K.; Pumera, M. *Chem. Eur. J.* **2014,** 20, (7), 1871-1877.
25. Magid, R. M. *Tetrahedron* **1980,** 36, (13), 1901-1930.
26. Hougefrydrych, C. S. V.; Marsh, A.; Pinto, I. L. *J. Chem. Soc., Chem. Commun.* **1989**, (17), 1258-1259.
27. Ibrahim, M.; Nada, A.; Kamal, D. E. *Indian J. Pure Appl. Phys.* **2005,** 43, 911-917.
28. Effenberger, F.; Gaupp, S. *Tetrahedron: Asymm.* **1999,** 10, (9), 1765-1775.
29. Rosen, T.; Lico, I. M.; Chu, D. T. W. *J. Org. Chem.* **1988,** 53, (7), 1580-1582.
30. Rakotomanomana, N.; Lacombe, J. M.; Pavia, A. A. *Carbohydr. Res.* **1990,** 197, 318-323.
31. Shangguan, N.; Katukojvala, S.; Greenburg, R.; Williams, L. J. *J. Am. Chem. Soc.* **2003,** 125, (26), 7754-7755.
32. Kim, S.; Zhou, S.; Hu, Y.; Acik, M.; Chabal, Y. J.; Berger, C.; de Heer, W.; Bongiorno, A.; Riedo, E. *Nat. Mater.* **2012,** 11, (6), 544-549.
33. Bug, T.; Mayr, H. *Journal of the American Chemical Society* **2003,** 125, (42), 12980-12986.
34. Bagiyan, G. A.; Koroleva, I. K.; Soroka, N. V.; Ufimtsev, A. V. *Russian Chemical Bulletin* **2003,** 52, (5), 1135-1141.
35. Park, N.; Hong, S.; Kim, G.; Jhi, S.-H. *J. Am. Chem. Soc.* **2007,** 129, (29), 8999-9003.

36.   Srinivas, G.; Zhu, Y.; Piner, R.; Skipper, N.; Ellerby, M.; Ruoff, R. *Carbon* **2010,** 48, (3), 630-635.

37.   Li, J.; Cheng, X.; Shashurin, A.; Keidar, M. *Graphene* **2012,** 1, (1), 1-13.

38.   Sandoval, S.; Kumar, N.; Sundaresan, A.; Rao, C. N. R.; Fuertes, A.; Tobias, G. *Chemistry – A European Journal* **2014,** 20, (38), 11999-12003.

39.   Lee, W.; Lee, J. U.; Jung, B. M.; Byun, J.-H.; Yi, J.-W.; Lee, S.-B.; Kim, B.-S. *Carbon* **2013,** 65, (0), 296-304.

40.   Yan, J.-l.; Chen, G.-j.; Cao, J.; Yang, W.; Xie, B.-h.; Yang, M.-b. *New Carbon Materials* **2012,** 27, (5), 370-376.

41.   Willcock, H.; O'Reilly, R. K. *Polym. Chem.* **2010,** 1, (2), 149-157.

42.   Jagst, E. Surface Functional Group Characterization Using Chemical Derivatization X-ray Photoelectron Spectroscopy (CD-XPS).

43.   Yuan, B.; Bao, C.; Song, L.; Hong, N.; Liew, K. M.; Hu, Y. *Chemical Engineering Journal* **2014,** 237, (0), 411-420.

Chapter 5

Functionalisation of GO-SH
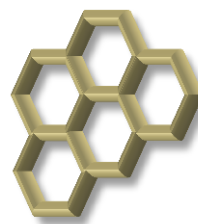
5.1 Reaction of GO-SH with Organic Molecules

In order to produce CMGs with tuneable properties, further functionalisation is needed. A variety of different electrophiles were used to modify the surface thiol groups of the GO-SH material from chapter 4 in order to explore its reactivity.

The increased thermal stability seen for the thioether functionalised GO materials in chapter 4 (GO-SPh and GO-pNIPAM) warranted further investigation. Thus, GO-SH was reacted with alkyl halides, methyl vinyl ketone and 1,3-propanesultone to give three different surface thioether functionalised GO materials. All three CMGs exhibited enhanced thermal stability in line with the results from chapter 4. In addition, functionalisation with 1,3-propanesultone was carried out without any loss in hydrophilicity.

Since thiol groups can act as good ligands to soft heavy metals, attempts were also made to prepare metallo-organic CMGs from GO-SH. The successful attachment of both Au(I) and Pd(II) to the surface of GO-SH is demonstrated in this chapter, as is the homogenous deposition of AuNPs. The metallo-organic complexes suggest that GO-SH could be used as an effective precursor to catalytic CMGs.

5.1.1 Reaction with Alkyl Halides

Being in the same group of the periodic table, sulfur and oxygen have similar electron configurations. Consequently there are many sulfur compounds which are analogous to oxygen compounds. However slight differences between sulfur and oxygen have a significant effect on their reactivity. Sulfur is much less electronegative than oxygen – on the Pauling scale of electronegativity, sulfur measures at 2.58 and oxygen at 3.44. Sulfur also has a much larger atomic radius (S 0.104 nm *vs* O 0.066 nm). The electron cloud of sulfur is thus more disperse and more easily polarisable. These two factors mean that the electrons

in an oxygen atom are more tightly bound and are thus less able to be shared in the formation of a new bond. Hence sulfur is comparatively more reactive than oxygen and acts as a better nucleophile.

Alkyl halides were used to functionalise GO-SH, with the expectation that the nucleophilic thiol groups would react to give a CMG with surface thioether groups. GO-SH was deprotonated using sodium hydride at room temperature under an inert atmosphere and was subsequently reacted with the alkyl halides bromobutane and bromodecane (scheme 5.1). The thioether functionalised GO materials are denoted, from now on, as GOS-C_4 and GOS-C_{10} respectively.
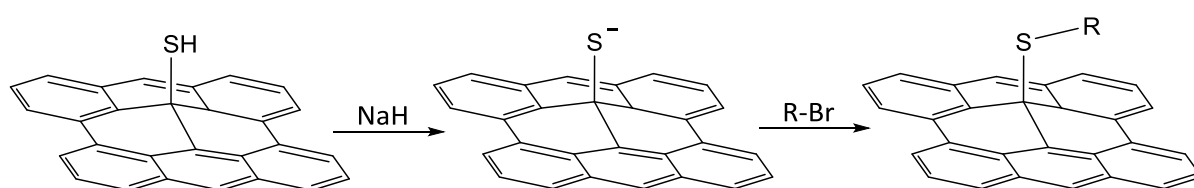
Scheme 5.1 Reaction of GO-SH with an alkyl bromide. R = C_4H_9 or $C_{10}H_{21}$.

As a control, the respective alkyl halides were reacted with bwGO under the same conditions giving GO-C_4 and GO-C_{10}. In this case, the NaH was expected to deprotonate the OH groups which would then react in much the same way as the SH groups of GO-SH to form surface ethers. Since sulfur is more nucleophilic than oxygen, thioethers are expected to form preferentially on GO-SH rather than ethers from any remaining OH groups. In order to determine whether functionalisation was taking place on GO-SH, and if so whether it was occuring from sulfur or oxygen points of attachment, FTIR, EDX, Raman, ^{13}C ssNMR, XPS, TGA, TEM and drop shape analysis were used to identify any differences between the reacted bwGO and GO-SH materials.

In this section characterisation results from the reactions with bromodecane – GO-C_{10} and GOS-C_{10} – are presented. Although it should be noted that reaction with bromobutane yielded the same results.

O-H ~ 3200 cm^{-1} C-H ~ 2900 cm^{-1} C=O ~ 1720 cm^{-1} C-O ~ 1250 cm^{-1}
1400 cm^{-1} C=C ~ 1620 cm^{-1} 1050 cm^{-1}
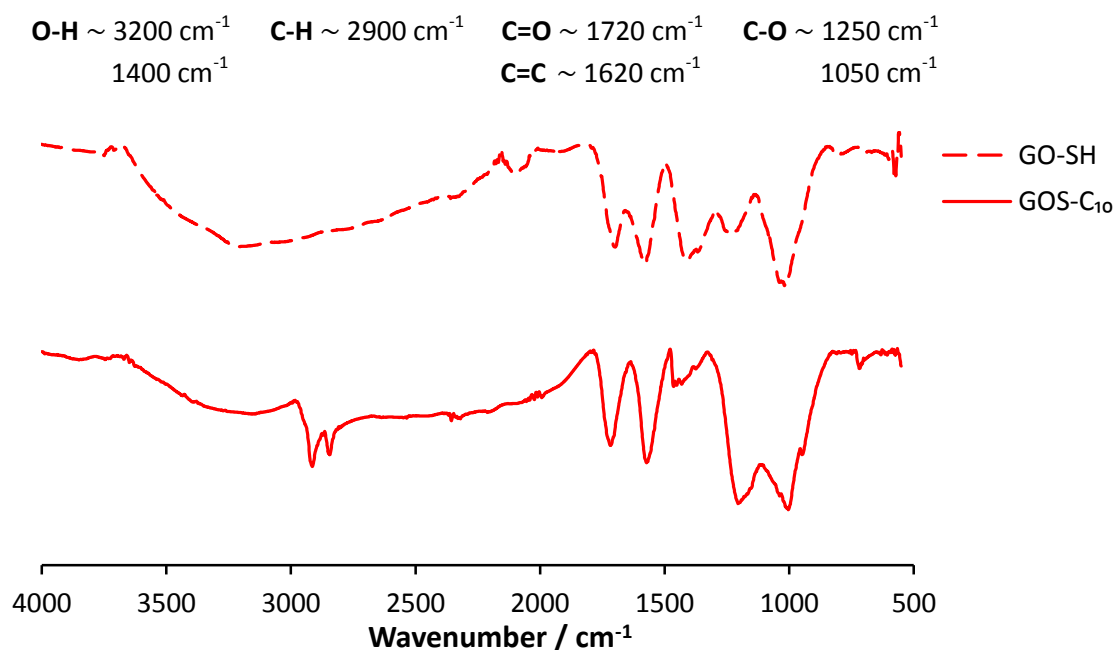
Fig. 5.1 ATR-FTIR spectra of GO-SH (dashed) and GOS-C$_{10}$ (solid).

The FTIR spectrum of GOS-C$_{10}$ (figure 5.1) shows strong absorbances at 2850 and 2920 cm^{-1} which can be attributed to C-H stretching from the new CH$_2$/CH$_3$ groups in the decyl chain. A reduction in the intensity of the hydroxyl bands can also be seen, alongside a new absorbance at 1220 cm^{-1} in the fingerprint region.

O-H ~ 3200 cm^{-1} C-H ~ 2900 cm^{-1} C=O ~ 1720 cm^{-1} CH$_2$ ~ 1350 cm^{-1} C-O ~ 1250 cm^{-1}
1400 cm^{-1} C=C ~ 1620 cm^{-1} 950 cm^{-1} 1050 cm^{-1}
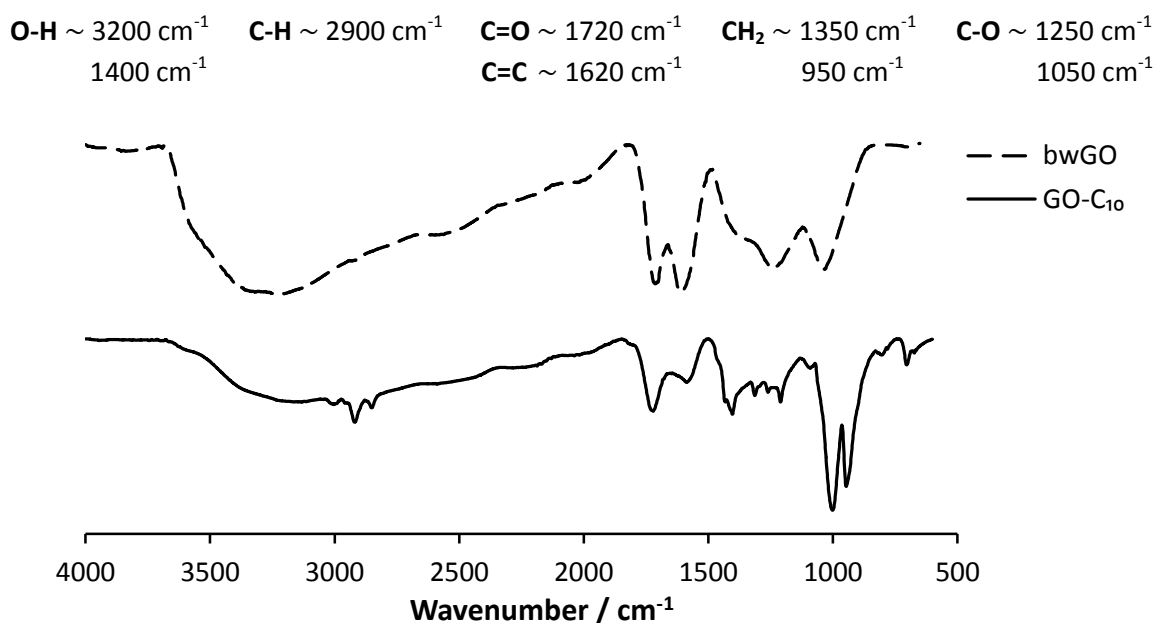
Fig. 5.2 ATR-FTIR spectra of bwGO (dashed) and GO-C$_{10}$ (solid).

Figure 5.2 shows the FTIR spectra of bwGO and GO-C$_{10}$. As with figure 5.1, reaction with bromodecance has introduced new alkyl absorbances between 2850 and 3000 cm^{-1},

although these bands appear less intense than those seen for GOS-C_{10}. Looking at GO-C_{10}, the intensity of the OH bands has decreased significantly compared to bwGO, and new C-H deformations and CH_2 rocking bands are seen at 1350 and 950 cm^{-1} respectively.
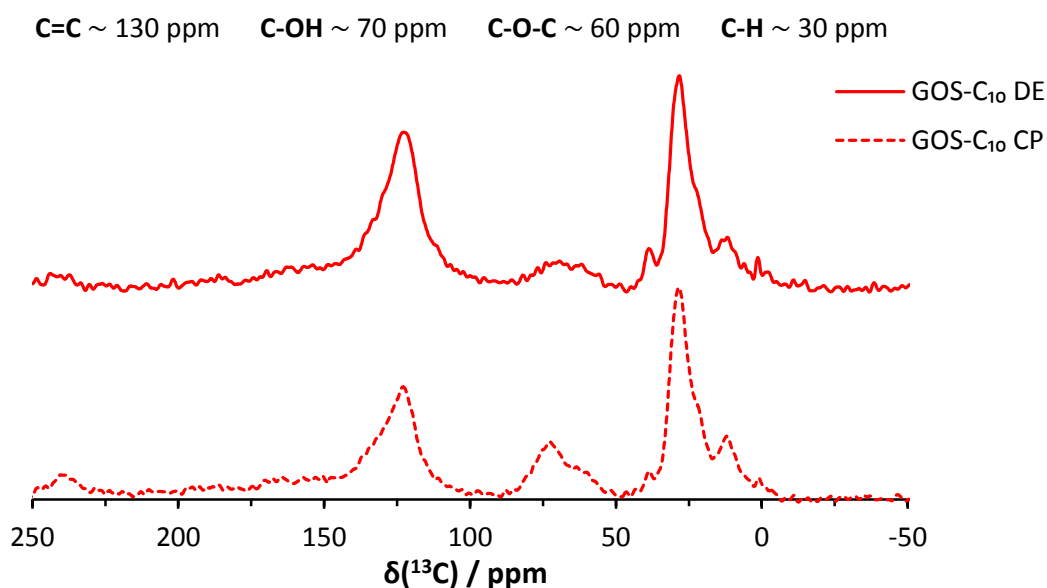
Fig. 5.3 ^{13}C MAS ssNMR of GOS-C_{10}, both the direct excitation (DE) spectrum (solid) and the cross polarised (CP) spectrum (dashed) are shown.

^{13}C MAS ssNMR of the GOS-C_{10} material (figure 5.3) shows a very strong peak at 29 ppm, which correlates nicely with the CH_2 groups of the decyl chain (see chemical shift estimations, figure 5.4). There is also a smaller peak at 14 ppm, which can be assigned to the CH_3 group at the end of the decyl chain. As with GO-SH, hardly any contribution from hydroxyl and epoxy groups is seen in the DE spectrum. The sp^2 carbon signal at 125 ppm remains strong for GOS-C_{10} indicating that the graphene-like backbone of the material remains intact.
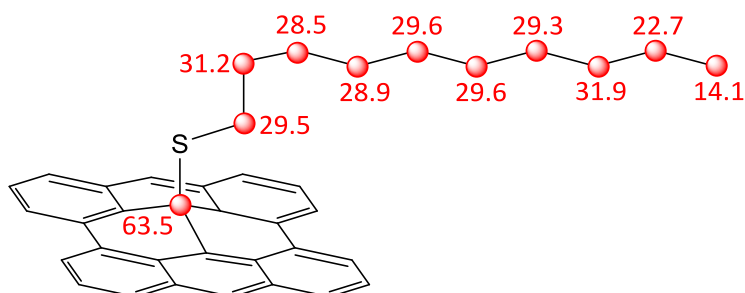
Fig. 5.4 ^{13}C ssNMR chemical shift predictions for the new signals in GOS-C_{10}. The red spheres indicate carbons of interest, with predicted chemical shifts as labelled.

C=C ~ 130 ppm   **C-OH** ~ 70 ppm   **C-O-C** ~ 60 ppm   **C-H** ~ 30 ppm
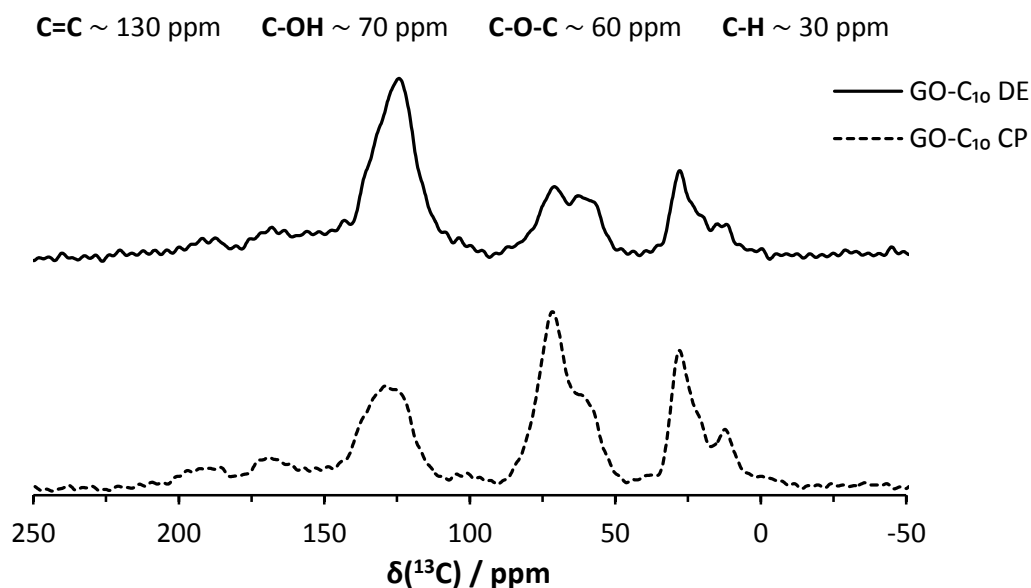
Fig. 5.5 ^{13}C MAS ssNMR of GO-C$_{10}$, both the direct excitation (DE) spectrum (solid) and the cross polarised (CP) spectrum (dashed) are shown.

The ^{13}C MAS ssNMR spectrum of GO-C$_{10}$ (figure 5.5) also shows new peaks (29 ppm and 15 ppm) consistent with a long chain alkyl. Looking at the DE spectrum, it can be seen that the epoxy signal of GO-C$_{10}$ (61 ppm) is similar in intensity, but broader, than the epoxy signal of bwGO. However the intensity of the hydroxyl signal (72 ppm) has significantly decreased for GO-C$_{10}$, which supports the expected formation of ether groups from OH groups.
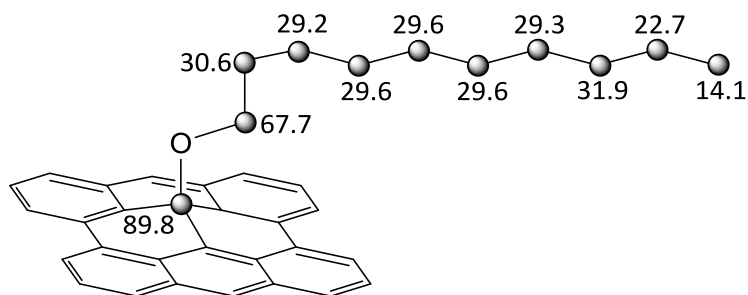
Fig. 5.6 ^{13}C ssNMR chemical shift predictions for the new signals in GO-C$_{10}$. The black spheres indicate carbons of interest, with predicted chemical shifts as labelled.

The only significant difference in the estimated chemical shifts of GO-C$_{10}$ (figure 5.6) and GOS-C$_{10}$ (figure 5.4) comes from the carbons directly attached to the heteroatoms (O or S). Unfortunately, the aliphatic region in the ssNMR of GO-C$_{10}$ and GOS-C$_{10}$ is dominated by the peak at 29 ppm from the central carbon atoms of the decyl chain, making the spectra hard

to interpret. The ssNMR spectra of GO-C$_4$ and GOS-C$_4$ are more conclusive: figure 5.7 shows the DE spectra of both butyl materials. GOS-C$_4$ shows new aliphatic resonances at 40, 29, 26 and 13 ppm, whereas GO-C$_4$ only has new peaks at 27, 19 and 13 ppm, with the first carbon in the butyl chain expected to resonance between 60 and 70 ppm (and so will be obscured by the peaks from residual C-OH and C-O-C groups). Significantly, there is no sign of any resonance between 60 and 70 ppm in the GOS-C$_4$ spectrum, suggesting that there are no notable levels of ether formation from the residue OH groups on GO-SH. This ssNMR data thus provides strong evidence that the alkyl chains on bwGO and on GO-SH are bonded at different points of attachment.

C=C ~ 130 ppm   **C-OH** ~ 70 ppm   **C-O-C** ~ 60 ppm   **C-H** ~ 30 ppm

GO-C$_4$
GOS-C$_4$

$\delta(^{13}C)$ / ppm
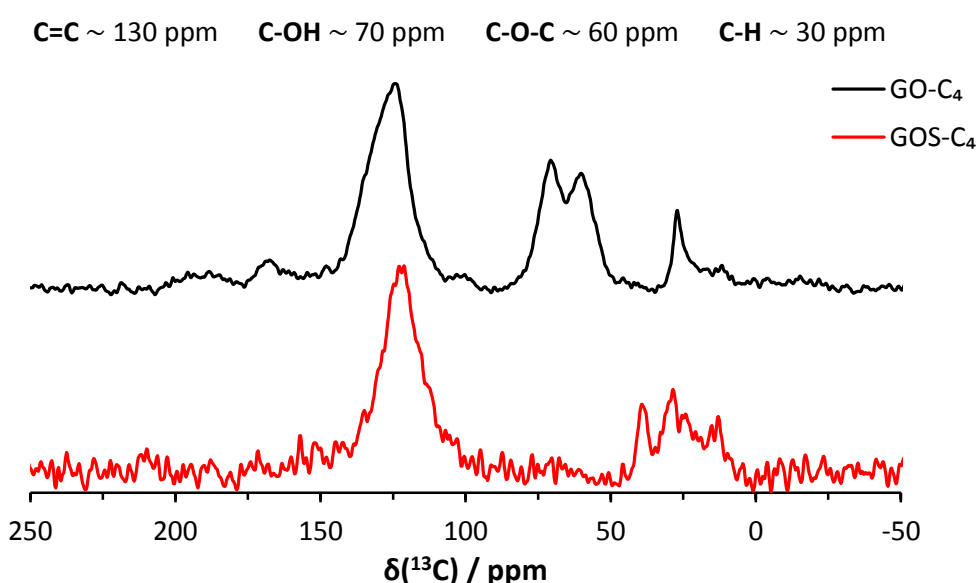
Fig. 5.7 Direct excitation ^{13}C MAS ssNMR of GO-C$_4$ (black) and GOS-C$_4$ (red).

A qualitative assessment on the degree of alkyation for GO-C$_{10}$ and GOS-C$_{10}$ can also be made: the ssNMR studies (figures 5.3 and 5.5), show that GOS-C$_{10}$ has a much stronger alkyl peak at 29 ppm (relative to the sp^2 carbon signal) than GO-C$_{10}$. From the ^{13}C ssNMR of GO-SH (which shows only small C-OH and C-O-C peaks, see chapter 4) it is clear that the number of OH groups on bwGO far exceeds the number of OH groups on GO-SH. Hence GO-SH cannot achieve a greater level of alkylation than bwGO (under the same reaction conditions) through ether formation alone, and indeed the ssNMR discussed above indicates that ether formation does not play a significant role in the reaction of alkyl halides with GO-SH. The OH groups on bwGO are also expected to outnumber the SH groups on GO-SH which suggests that the greater level of alkylation seen for GOS-C$_{10}$ compared to GO-C$_{10}$ is down to the

increased reactivity of the SH groups on GO-SH compared with the OH groups on bwGO. Since sulfur is more nucleophilic than oxygen,[1, 2] this is unsurprising.

The alkylation of GO-SH is also apparent from EDX, which shows a slightly increased C/O ratio of 8:1 for GOS-C$_{10}$, compared to 5:1 for GO-SH. In comparison, the proportion of carbon in the GO-C$_{10}$ material has not significantly increased, suggesting only low levels of functionalisation (both bwGO and GO-C$_{10}$ have a C/O ratio of 4:1). The atomic composition of the new CMGs, as measured by EDX (with the standard deviation given in parentheses), is given below:

GOS-C$_{10}$: C 86 (1); O 11 (1); S 1.9 (0.3).

GO-C$_{10}$: C 79 (2); O 20 (2).

Raman studies of GO-C$_{10}$ and GOS-C$_{10}$ confirm that both samples have a graphene-type structure. The D/G ratios of GOS-C$_{10}$ and GO-C$_{10}$ are calculated to be 1.8 and 1.6 respectively. This increase in the D band intensity for both samples is expected as a result of alkylation.

TEM was used to further confirm that the GO sheets remained intact after alkylation. Figure 5.8 (a) shows the bright field TEM image of GO-C$_{10}$ positioned over a hole in a lacey carbon grid. The diffraction pattern of GO-C$_{10}$, shown in figure 5.8 (b), was taken from within the red circle shown in (a). This diffraction pattern shows a single set of inner spots in a hexagonal array. These spots are more intense than the outer set, confirming that the material is both graphene-based and is fully exfoliated to a single layer material.
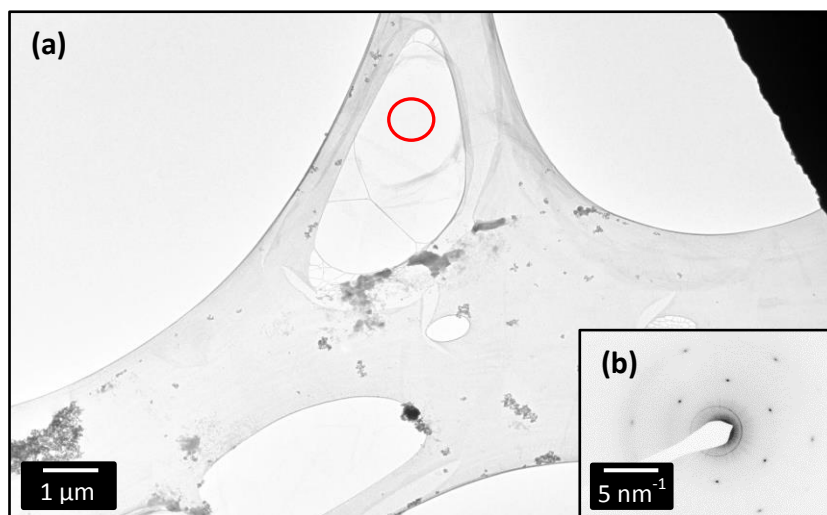
Fig. 5.8 (a) Bright field TEM image of GO-C$_{10}$ on a lacey carbon grid. The diffraction pattern **(b)** is taken from the area in the red circle.

XPS studies (figure 5.9) were carried out in order to investigate the bonding environments – ether *vs* thioether formation – in GOS-C$_{10}$.
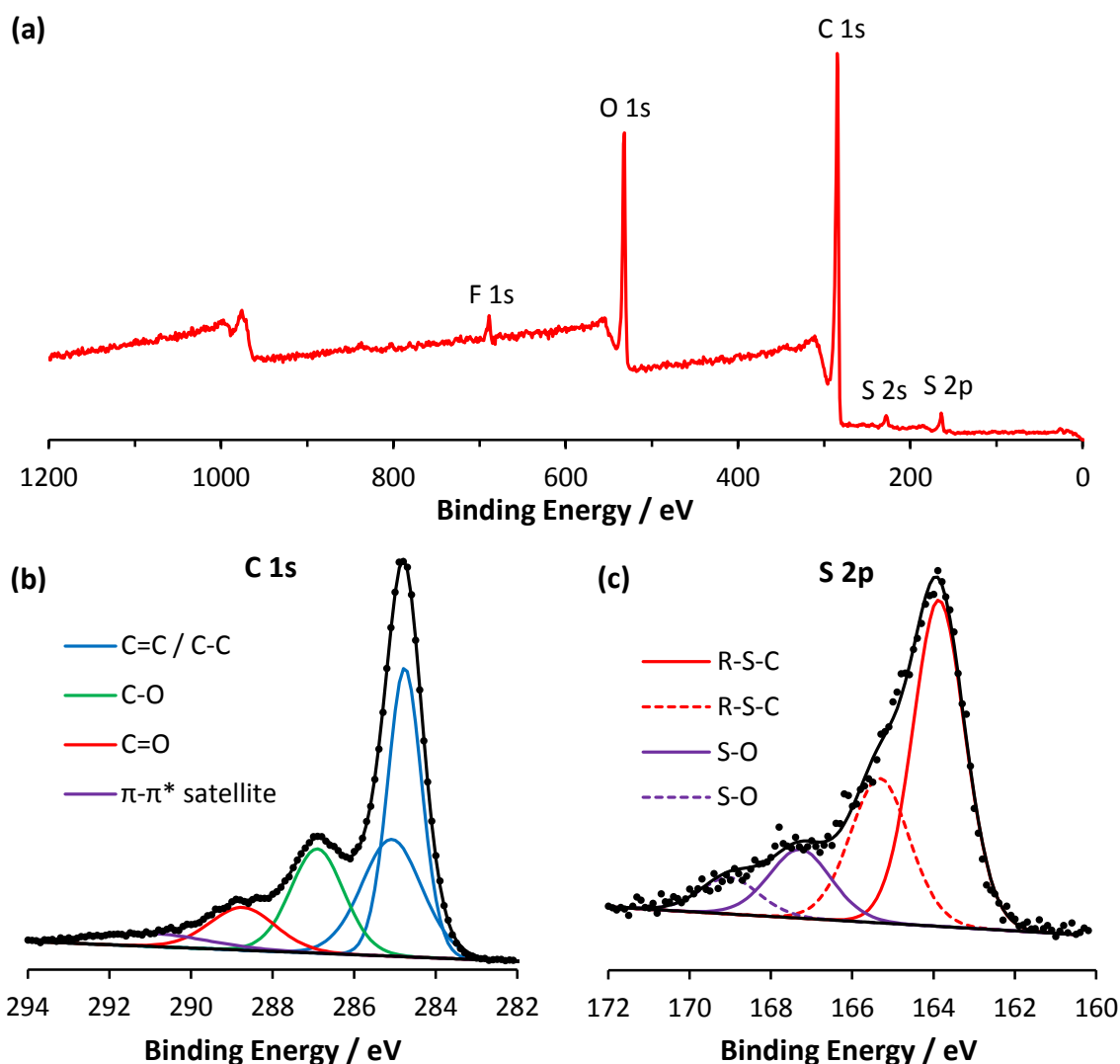
Fig. 5.9 XPS analysis of GOS-C$_{10}$, complete with survey scan **(a)**, and core level spectra C 1s **(b)** and S 2p **(c)**. The experimental data is shown as points with the underlying lines showing the fitted peaks (assignments as labelled). Note that for **(c)** the 2p$_{3/2}$ orbital assignments are represented by solid lines while the corresponding dashed lines refer to the 2p$_{1/2}$ orbitals.

Figure 5.9 (a) shows the XPS survey scan of GOS-C$_{10}$, which measures 2.3 atomic % S by peak area. Meanwhile, the C 1s core level spectrum of GOS-C$_{10}$ in figure 5.9 (b) shows the typical peaks expected from a GO-based material. The S 2p spectrum in figure 5.9 (c) shows that there are two different chemical environments for the sulfur in GOS-C$_{10}$. The dominant doublet which measures 164 eV for the 2p$_{3/2}$ orbital, represents 80% of the sulfur present, and can be assigned to thioether functionalities. The remaining 20% comes as a result of

oxidised sulfur impurities (e.g. sulfonic acid). This result is very similar to the thioether functionalised material previously studied in chapter 4: GO-SPh.

Figure 5.9 indicates that the percentage incorporation of sulfur has been reduced as a result of functionalisation. This is unsurprising since functionalising with a long alkyl chain will increase the proportion of carbon, and consequently decrease the proportion of other elements (O and S) in the material.
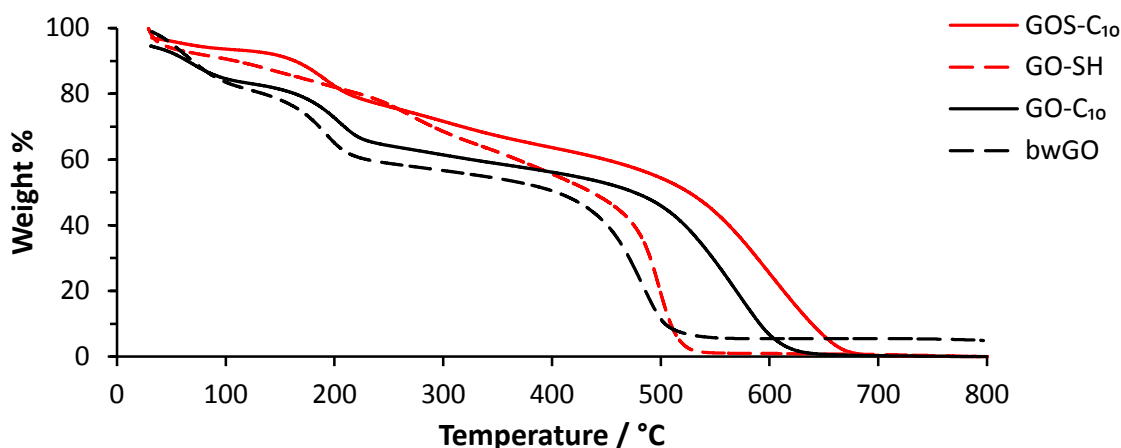
Fig. 5.10 TGA profile of bwGO (black dash), GO-SH (red dash), GO-C_{10} (black) and GOS-C_{10} (red).

Both the GO-C_{10} and GOS-C_{10} materials have increased thermal stability compared to bwGO and GO-SH, as measured by TGA (figure 5.10). This is presumably due to the decyl chains capping the OH and SH groups, preventing any decomposition pathway initiated at these reactive sites. In addition, GOS-C_{10} has a decomposition temperature roughly 50 °C higher than GO-C_{10}, which could indicate an inherently lower level of OH groups on GOS-C_{10}, or incomplete capping of the OH groups in GO-C_{10}.

Alkylation of the GO materials clearly affects the thermal stability, and the dispersibility of GOS-C_{10} was also found to be noticeably reduced in DMF and DMSO compared to GO-SH. Meanwhile, GO-C_{10} retained similar dispersibility to bwGO. The contact angle measurements shown in figure 5.11 reflect these findings: GOS-C_{10} has a contact angle of 62°, suggesting reduced hydrophilicity compared to GO-SH; GO-C_{10} has a contact angle of 45° which is very similar to bwGO.
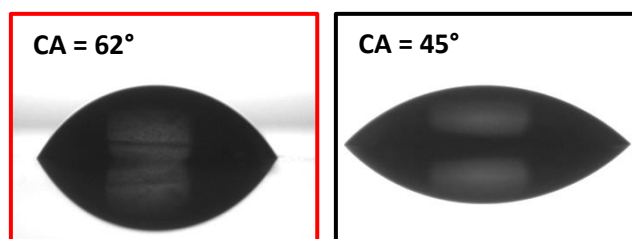
Fig. 5.11 Drop shape analysis of GOS-C$_{10}$ (red) and GO-C$_{10}$ (black).

From the characterisation gathered, it appears that both the bwGO and GO-SH sheets have been alkylated by the reaction with bromodecane (and bromobutane). However ssNMR, FTIR and TGA indicate that unreacted OH groups remain present in the GO-C$_{10}$ sample. The GOS-C$_{10}$ material shows a greater degree of functionalisation than GO-C$_{10}$, meaning that functionalisation must have occurred somewhere other than the remaining OH groups on GO-SH. From this, and the XPS data, it is clear that a GO material with surface thioethers has been prepared. Due to the lower reactivity of the OH groups compared to the SH groups, surface ethers are not expected on GOS-C$_{10}$ in large quantities (if at all).

5.1.2 Reaction with Methyl Vinyl Ketone

Click reactions – originally defined by Sharpless *et al*. – are modular, stereospecific, wide in scope, with high yields and only inoffensive side products.[3] Such reactions include the nucleophilic ring-opening of epoxides and aziridines.

The thiol-ene click reaction has become popular in polymer chemistry[4] as it is a convenient way of introducing a C-S bond using nucleophilic conjugate addition to α,β-unsaturated carbonyls (Michael-type addition, scheme 5.2).[5]
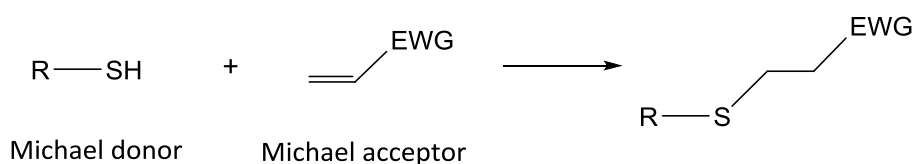
Scheme 5.2 Generic thiol-ene click reaction: nucleophilic conjugate addition of a thiol group to an alkene with an electron withdrawing group (EWG).

The SH groups on GO-SH are thus expected to be suitable for thiol-ene click reactions, providing a convenient route to further functionalisation.

Molecular iodine is known to act as a lewis acid, providing an effective and green catalyst for such thiol-Michael additions.[6, 7] The conjugate addition of the nucleophilic sulfur groups on GO-SH to methyl vinyl ketone was thus attempted, using molecular iodine to promote the reaction (Scheme 5.3). The end product is referred to as GOS-MVK.
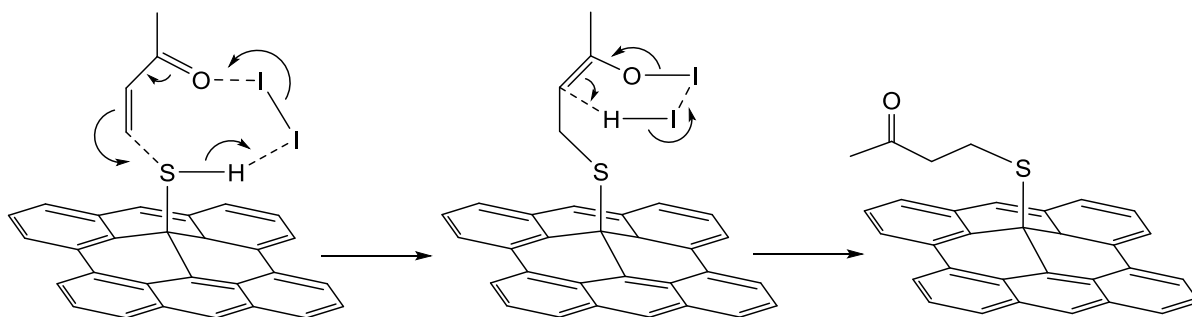
Scheme 5.3 Iodine catalysed thiol-ene click reaction of GO-SH and methyl vinyl ketone.

A control reaction was carried out under the same conditions using bwGO instead of GO-SH. The type of intermolecular oxa-Michael reaction which could occur on bwGO can be challenging due to the poor nucleophilicity of the alcohol groups and reaction reversibility,[8] however acid catalysts have been shown to sufficiently activate the Michael acceptor for reaction.[9-11] Some level of functionalisation is thus expected for both bwGO and GO-SH, but at different points of attachment. The control product is referred to as GO-MVK.

O-H ~ 3200 cm^{-1} C-H ~ 2900 cm^{-1} C=O ~ 1720 cm^{-1} CH$_2$ ~ 1350 cm^{-1} C-O ~ 1250 cm^{-1}
1400 cm^{-1} C=C ~ 1620 cm^{-1} 950 cm^{-1} 1050 cm^{-1}
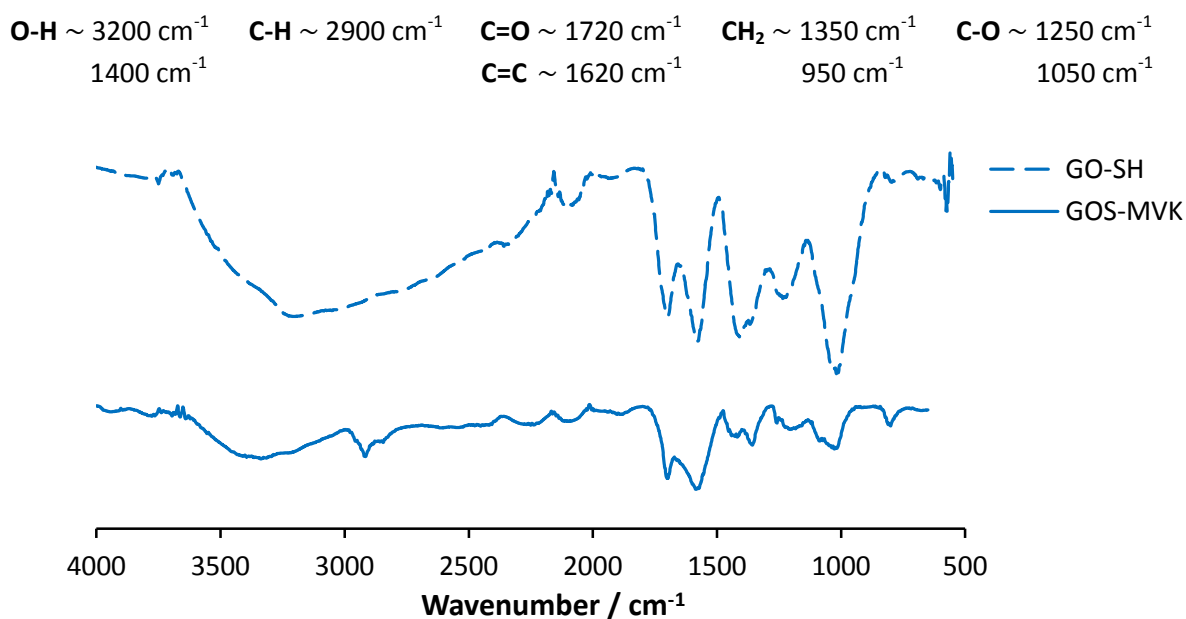
Fig. 5.12 ATR-FTIR spectra of GO-SH (dashed) and GOS-MVK (solid).

Figure 5.12 shows the FTIR spectra of GO-SH and GOS-MVK: reaction with MVK has introduced new CH$_2$/CH$_3$ stretching (2940 cm^{-1}) and CH$_2$ rocking (810 cm^{-1}) absorbances.

Similar changes are seen in the FTIR of the control reaction (figure 5.13): small bands resulting from CH$_2$ and CH$_3$ groups can be seen in the FTIR of GO-MVK, alongside a decrease in the intensity of the OH absorbances.

O-H ~ 3200 cm^{-1} C-H ~ 2900 cm^{-1} C=O ~ 1720 cm^{-1} CH$_2$ ~ 1350 cm^{-1} C-O ~ 1250 cm^{-1}
1400 cm^{-1} C=C ~ 1620 cm^{-1} 950 cm^{-1} 1050 cm^{-1}
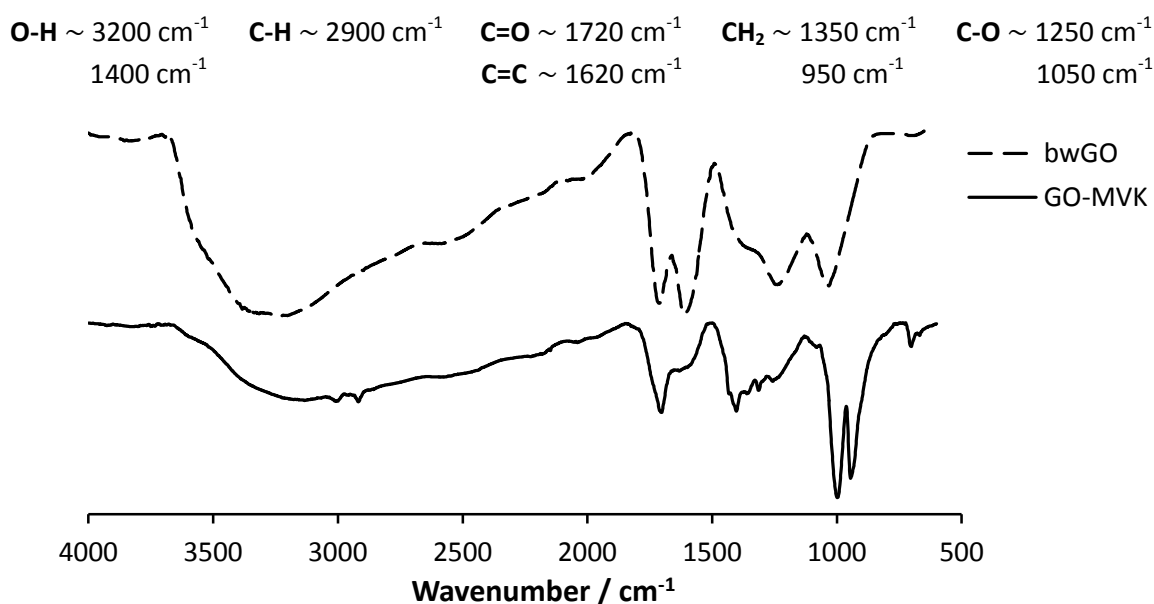
Fig. 5.13 ATR-FTIR spectra of bwGO (dashed) and GO-MVK (solid).

The EDX measurements of GOS-MVK indicate an increase in the C/S ratio: C 82 (1); O 13 (1); S 3.8 (0.5), equating to one sulfur for every 22 carbons. Compared with the one sulfur for every 19 carbons on GO-SH, this increase is consistent with the addition of C_4H_7O groups. However the EDX of GO-MVK: C 77 (1); O 23 (1) shows no change from bwGO. This is not inconsistent with functionalisation: attachment of MVK groups to the bwGO sheets should not alter the C/O ratio since the C/O ratio of both MVK and bwGO is 4:1.

The Raman spectra of GO-MVK and GOS-MVK confirm that both materials are still graphene-based with D/G ratios of 1.7 and 1.6 respectively.
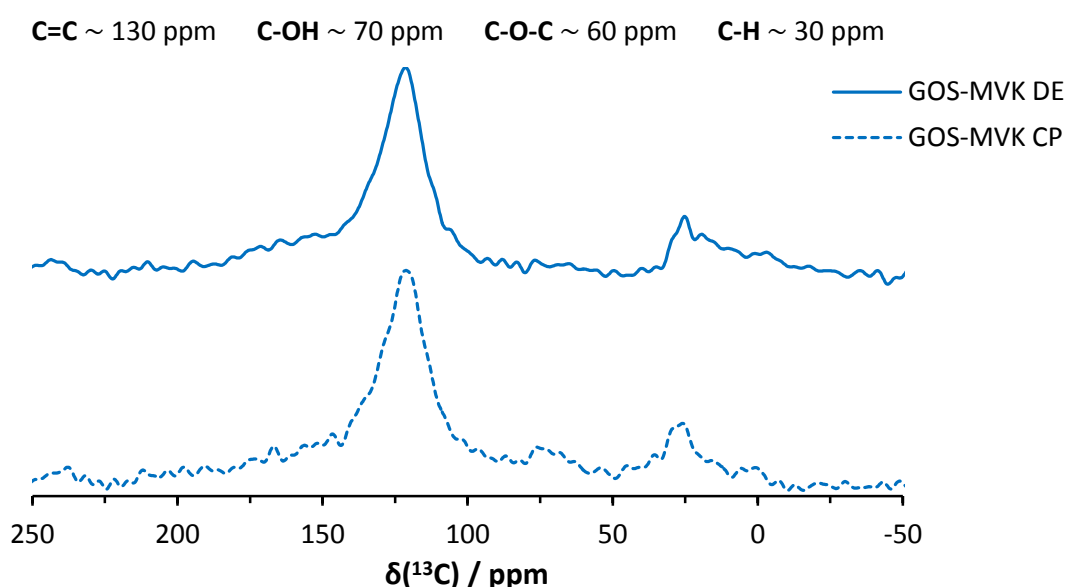
Fig. 5.14 ^{13}C MAS ssNMR spectra of GOS-MVK, both the direct excitation (DE) spectrum (solid) and the cross polarised (CP) spectrum (dashed) are shown.

The ^{13}C ssNMR spectra of GOS-MVK (figure 5.14) shows next to no signal for hydroxyl and epoxy functionalities in the DE spectrum, with only a small enhancement of intensity for the OH carbons in the CP spectrum. Some low chemical shift peaks can be seen between 20 and 40 ppm, which are consistent with the CH_3 and CH_2 carbons of the MVK group (see chemical shift estimations in figure 5.15). Unfortunately the thioether carbon on the GO sheet and the keto carbon of MVK cannot be clearly distguished in the DE spectrum due to the level of noise, and furthermore, there is no obvious enhancement of the intensity of either group in the CP spectrum as neither are directly attached to a proton.
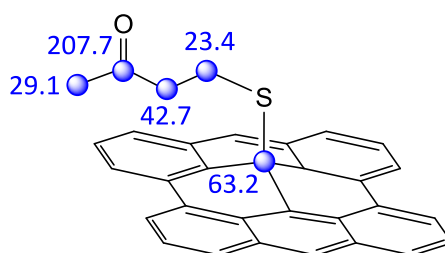
Fig. 5.15 ^{13}C ssNMR chemical shift predictions for the new signals in GOS-MVK. The blue spheres indicate carbons of interest, with predicted chemical shifts as labelled.

Fig. 5.16 ^{13}C MAS ssNMR spectra of GO-MVK, both the direct excitation (DE) spectrum (solid) and the cross polarised (CP) spectrum (dashed) are shown.

The DE ^{13}C ssNMR spectrum of GO-MVK (figure 5.16) shows two signals at 58 and 16 ppm, these two peaks are believed to be due to residue ethanol solvent in the NMR rotor. With this in mind, the remaining peaks around 30 ppm can be assigned to the CH_2 and CH_3 carbons of the MVK group (see chemical shift estimations in figure 5.17). The GO-MVK material still has significant levels of hydroxyl and epoxy groups as evidenced by the peaks at 71 and 62 ppm respectively. As with GOS-MVK, the keto carbon from the MVK group is hard to identify with confidence, however, a small peak at 204 ppm in the DE spectrum can be seen.

Fig. 5.17 ^{13}C ssNMR chemical shift predictions for the new signals in GO-MVK. The black spheres indicate carbons of interest, with predicted chemical shifts as labelled.

The XPS of GOS-MVK was used to study the bonding environment of the sulfur functionalities. Figure 5.18 (a) shows the survey scan where strong sulfur signals, measuring at 4.8 at.% incorporation, can be seen.

Looking at the C 1s core level spectrum of GOS-MVK in figure 5.18 (b), it can be seen that the contribution from C=O functionalities has marginally increased when compared to GO-SH. By area, the proportion of carbon involved in C=O bonding is 12% for GOS-MVK, and 9% for GO-SH, which is consistent with the introduction MVK groups.

Finally, the S 2p core level spectrum, figure 5.18 (c), shows that the dominant sulfur environment (87%) comes from R-S-C bonding: a thioether. As with GOS-C$_{10}$, the higher binding energy doublet can be assigned to oxidised thiol groups.
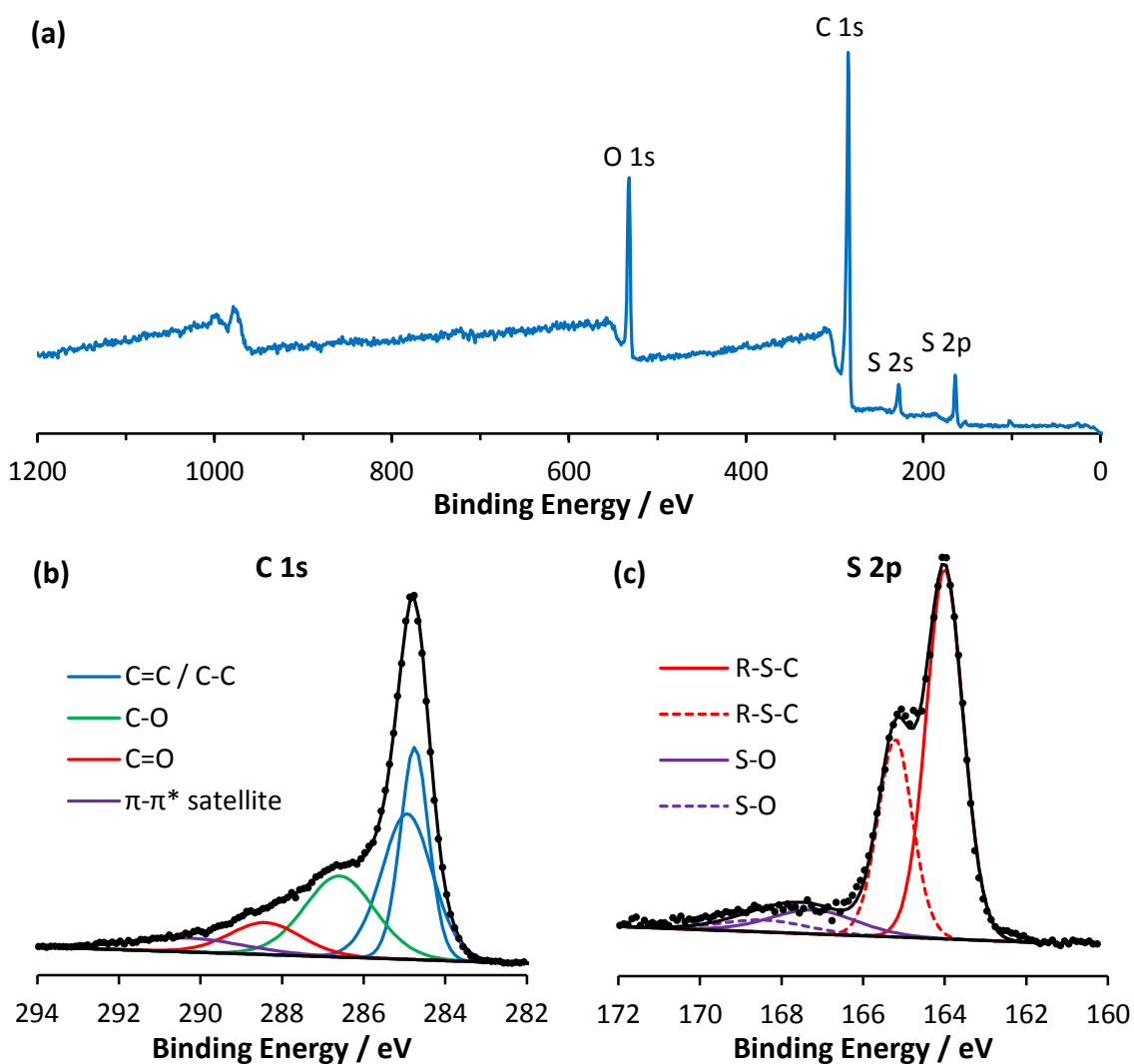
Fig. 5.18 XPS analysis of GOS-MVK, complete with survey scan **(a)**, and core level spectra C 1s **(b)** and S 2p **(c)**. The experimental data is shown as points with the underlying lines showing the fitted peaks (assignments as labelled). Note that for **(c)** the $2p_{3/2}$ orbital assignments are represented by solid lines while the corresponding dashed lines refer to the $2p_{1/2}$ orbitals.

The TGA profiles of the CMGs GOS-MVK and GO-MVK are shown in figure 5.19, both materials show a significant enhancement in thermal stability compared to GO-SH and bwGO.
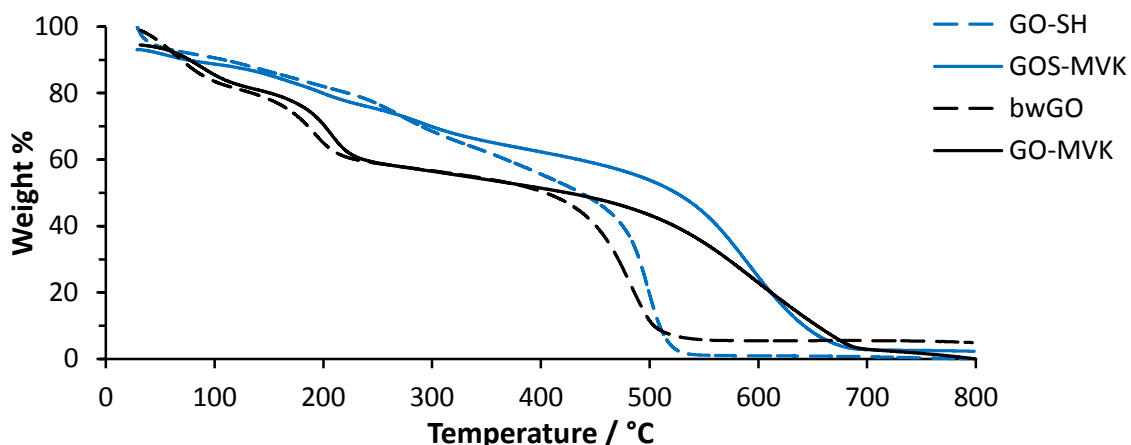
Fig. 5.19 TGA profiles of GO-SH (blue dash), GOS-MVK (blue), bwGO (black dash) and GO-MVK (black).

Both bwGO and GO-SH have a decomposition temperature of around 500 °C, which increases to over 600 °C for both GO-MVK and GOS-MVK. This is strong evidence for the successful reaction of methyl vinyl ketone with both bwGO and GO-SH: the reactive SH and OH groups are being capped, increasing the thermal stability of the materials.

The drop shape analysis, shown in figure 5.20 shows that functionalisation has significantly reduced the hydrophilicity of GOS-MVK compared to GO-SH: the contact angle has increased from 41° to 54°. In comparison, the contact angle of GO-MVK (41°) remains similar to bwGO (38°).
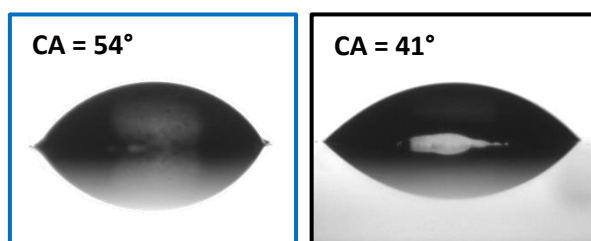
Fig. 5.20 Drop shape analysis of GOS-MVK (blue) and GO-MVK (black).

Due to the higher nucleophilicity of sulfur compared to oxygen, GO-SH is expected to preferentially undergo thiol-Michael additions with methyl vinyl ketone, and indeed the XPS confirms that thiol-Michael addition has taken place. However, due to the successful reaction of bwGO under the same conditions, it is possible that any remaining OH groups on GO-SH are also undergoing oxa-Michael additions.

5.1.3 Reaction with 1,3-propanesultone

A typical issue with producing graphene-like materials for particular applications is dispersibility which, as shown in sections 5.1.1 and 5.1.2, generally decreases as the surface gets more heavily functionalised – bwGO will form stable dispersions in H_2O, DMSO and DMF, the concentration of these dispersions was greatly reduced for the S-C$_{10}$ and S-MVK functionalised materials. However, by grafting certain groups to the surface it is possible to increase the dispersibility, as demonstrated with the NIPAM polymers in chapter 4. The third electrophile was chosen in an attempt to increase the water dispersibility of GO-SH by attaching sulfonate groups to the GO surface. NaH was used to deprotonate the reactive thiol groups of GO-SH, which were subsequently reacted with 1,3-propanesultone (scheme 5.4). The GO-based product is referred to as GOS-PrSO$_3$.
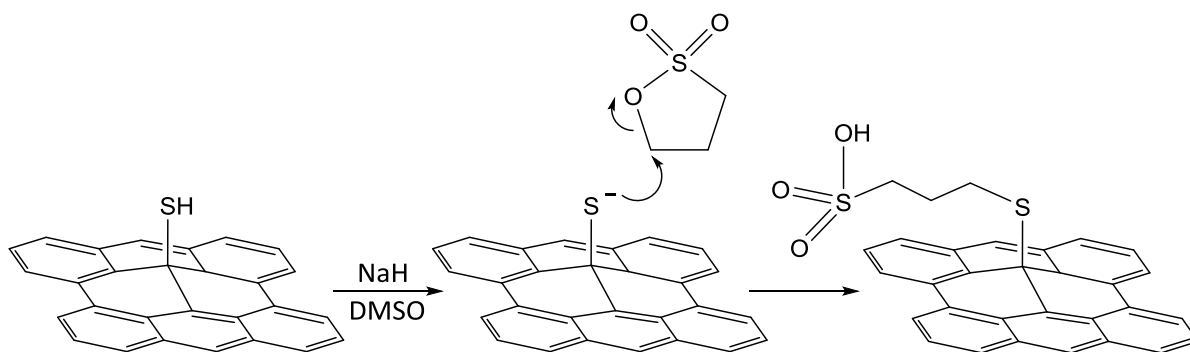
Scheme 5.4 Reaction of GO-SH with 1,3-propanesultone.

As a control, bwGO was also reacted with 1,3-propanesultone under the same conditions. Potentially both the edge carboxylic acids and the basal plane hydroxyls of bwGO could react with the sultone group in a similar manner to the SH groups of GO-SH. The control product is referred to as GO-PrSO$_3$.

EDX suggests that both bwGO and GO-SH have reacted with the sultone, as sulfur incorporation is seen for both cases:

GOS-PrSO$_3$: C 80 (0.5); O 15 (1); Na 1.5 (0.2); S 3.4 (0.5).

GO-PrSO$_3$: C 72 (2); O 20 (2); Na 6 (1); S 1.9 (0.6).

O-H ~ 3200 cm⁻¹   **C-H** ~ 2900 cm⁻¹   **C=O** ~ 1720 cm⁻¹   **C-O** ~ 1250 cm⁻¹   **SO₃⁻** ~ 1190 cm⁻¹
1400 cm⁻¹   **C=C** ~ 1620 cm⁻¹   1050 cm⁻¹
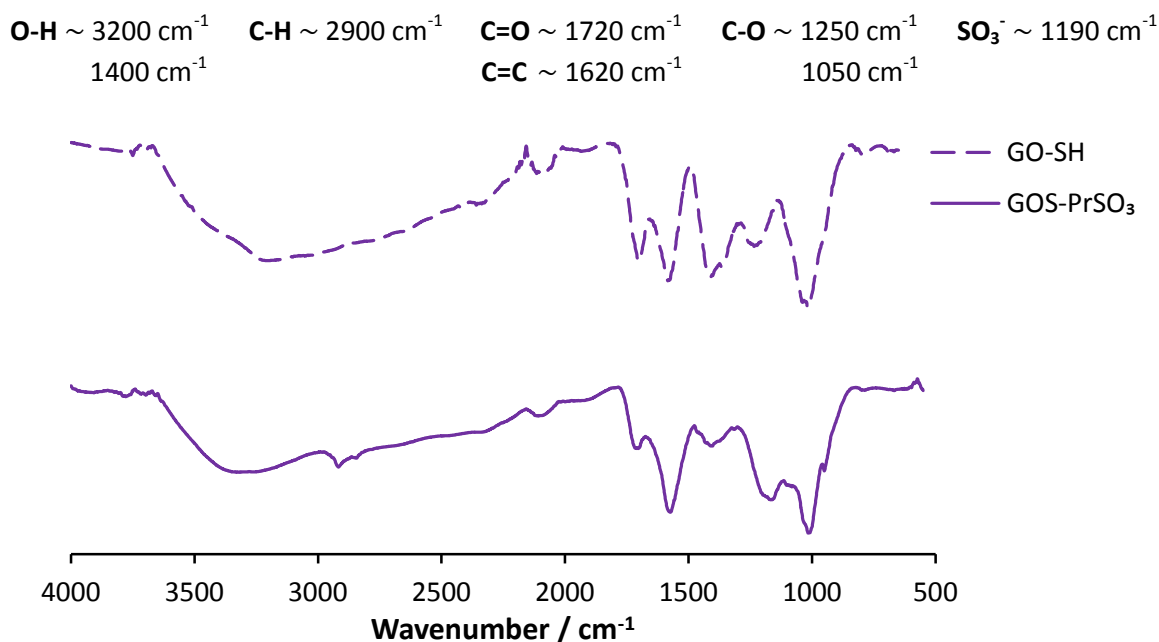
Fig. 5.21 ATR-FTIR spectra of GO-SH (dashed) and GOS-PrSO₃ (solid).

Compared to GO-SH, the FTIR spectrum of the GOS-PrSO₃ material (figure 5.21) shows a reduction in OH and carboxyl functionalities, new alkyl bands at 2960 cm⁻¹, and a new sulfonate anion band at 1190 cm⁻¹. A similar change is seen in the FTIR spectrum of GO-PrSO₃ compared to bwGO (figure 5.22): the COOH carboxyl signal has practically disappeared, a new band at 1195 cm⁻¹ (SO₃⁻) is apparent and a very small absorbance at 2960 cm⁻¹ can be seen.

O-H ~ 3200 cm⁻¹   **C-H** ~ 2900 cm⁻¹   **C=O** ~ 1720 cm⁻¹   **C-O** ~ 1250 cm⁻¹   **SO₃⁻** ~ 1190 cm⁻¹
1400 cm⁻¹   **C=C** ~ 1620 cm⁻¹   1050 cm⁻¹
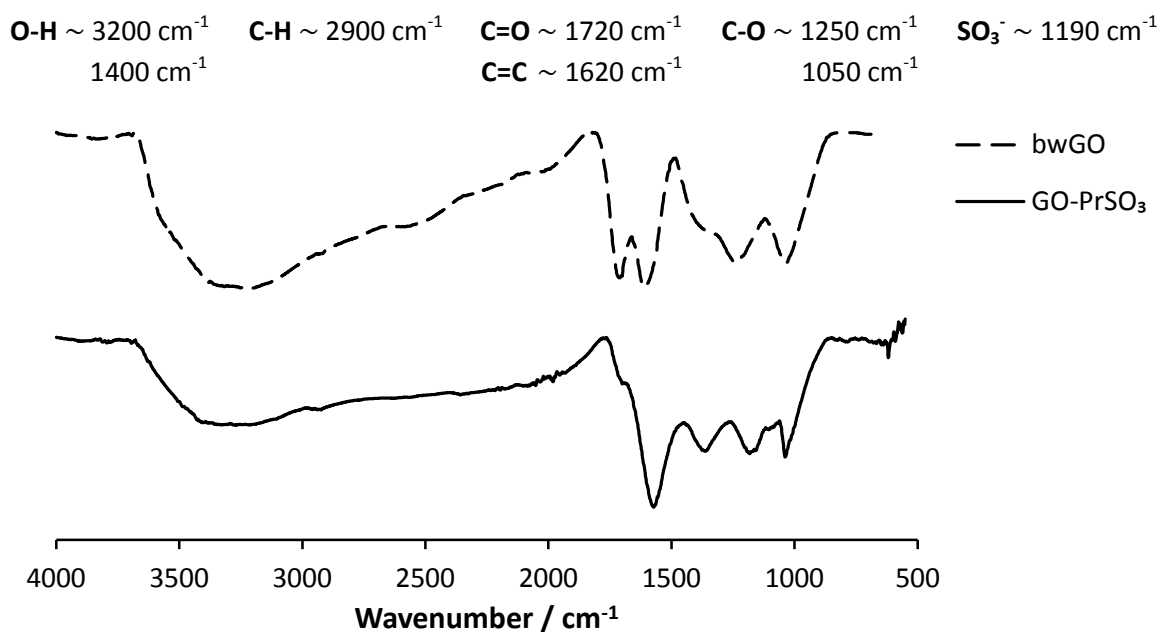
Fig. 5.22 ATR-FTIR spectra of bwGO (dashed) and GO-PrSO₃ (solid).

^{13}C ssNMR results provide further evidence for sultone functionalisation, with assignable spectra produced for both the GOS-PrSO$_3$ and GO-PrSO$_3$ materials.
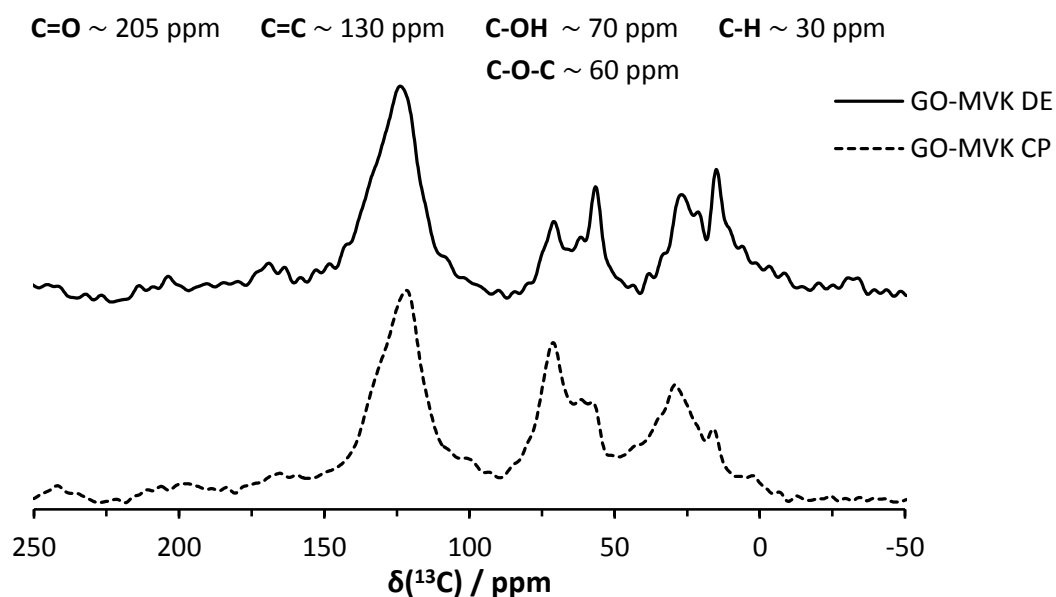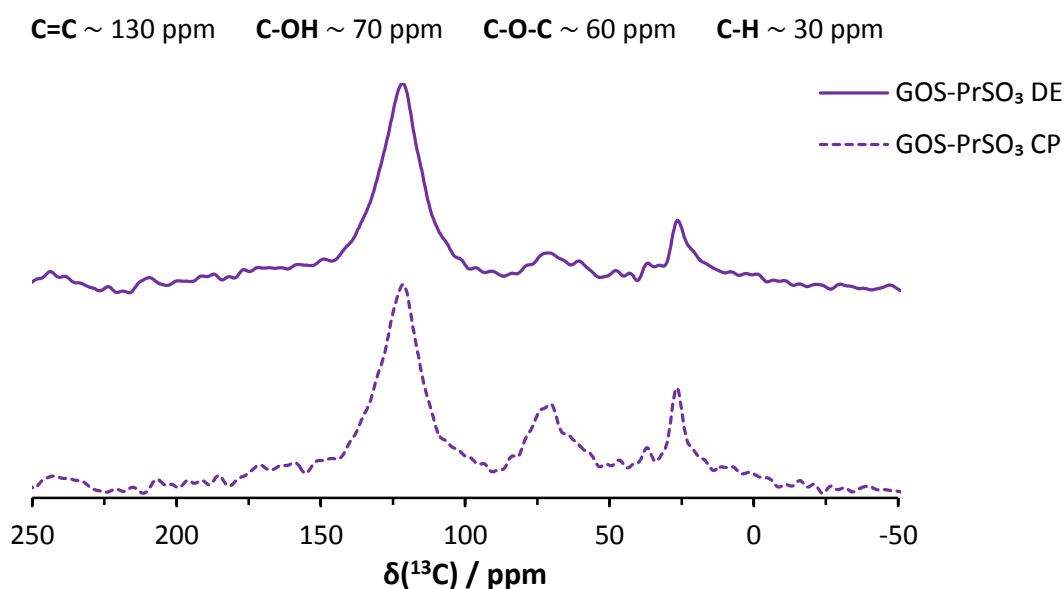

Fig. 5.23 ^{13}C MAS ssNMR spectra of GOS-PrSO$_3$, both the direct excitation (DE) spectrum (solid) and the cross polarised (CP) spectrum (dashed) are shown.

The ^{13}C ssNMR of GOS-PrSO$_3$ (figure 5.23) shows new alkyl peaks at around 27 ppm as well a broad signal for C-OH and C-O-C functionalities. Figure 5.24 shows the chemical shift estimations for the covently bonded sulfonate group on GO-SH – two of the carbons on the propane chain are expected to lie at 26 and 28 ppm, which is therefore consistent with the NMR spectra. The carbon atom directly attached to the sulfonate group should lie at a lower field ppm: approximately 57 ppm. Hence it is not possible to determine whether the signal at 60 ppm is due to residue epoxides, sulfonate groups, or a mixture of the two.
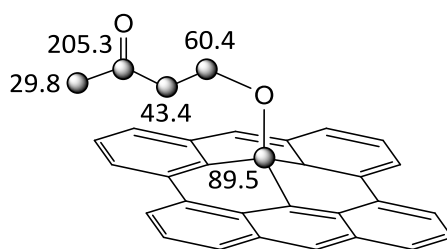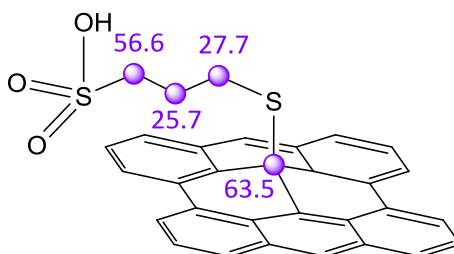

Fig. 5.24 ^{13}C ssNMR chemical shift predictions for the new signals in GOS-PrSO$_3$. The purple spheres indicate carbons of interest, with predicted chemical shifts as labelled.

C=C ~ 130 ppm   **C-OH** ~ 70 ppm   **C-O-C** ~ 60 ppm   **C-H** ~ 30 ppm
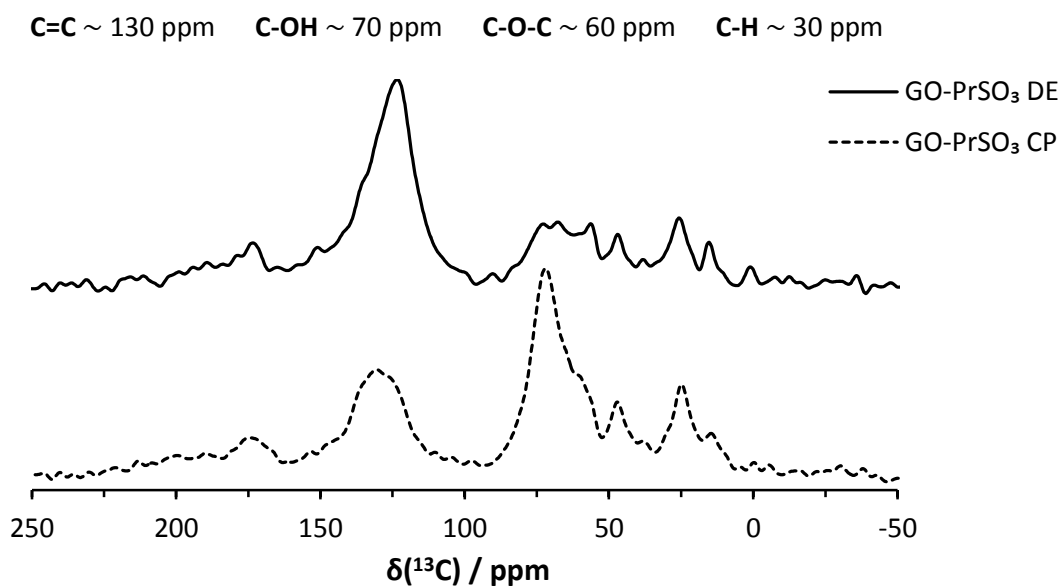
Fig. 5.25 ^{13}C MAS ssNMR spectra of GO-PrSO$_3$, both the direct excitation (DE) spectrum (solid) and the cross polarised (CP) spectrum (dash) are shown.

The ^{13}C ssNMR of the GO-PrSO$_3$ control sample (figure 5.25) shows similar functionalisation to GOS-PrSO$_3$. There are a mixture of peaks between 50 and 80 ppm which can be attributed to epoxides, hydroxides, sulfonates and ether carbons. A clear alkyl signal at 26 ppm, consistent with an alkyl carbon of the propane chain (see chemical shift estimations, figure 5.26), is also seen.
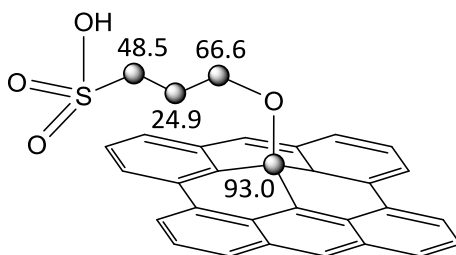

Fig. 5.26 ^{13}C ssNMR chemical shift predictions for the new signals in GO-PrSO$_3$. The black spheres indicate carbons of interest, with predicted chemical shifts as labelled.

The ^{13}C ssNMR spectra of both GOS-PrSO$_3$ and GO-PrSO$_3$ have strong sp^2 carbon signals, indicating that the graphene-type backbone remains intact after functionalisation. Raman studies also confirm this to be the case, with strong D, G and G' peaks seen for both materials. The D/G ratios are calculated to be 1.7 for both materials, consistent with this type of surface functionalisation.

Attention was then shifted to XPS, where the sulfur bonding environments were studied for both CMGs.
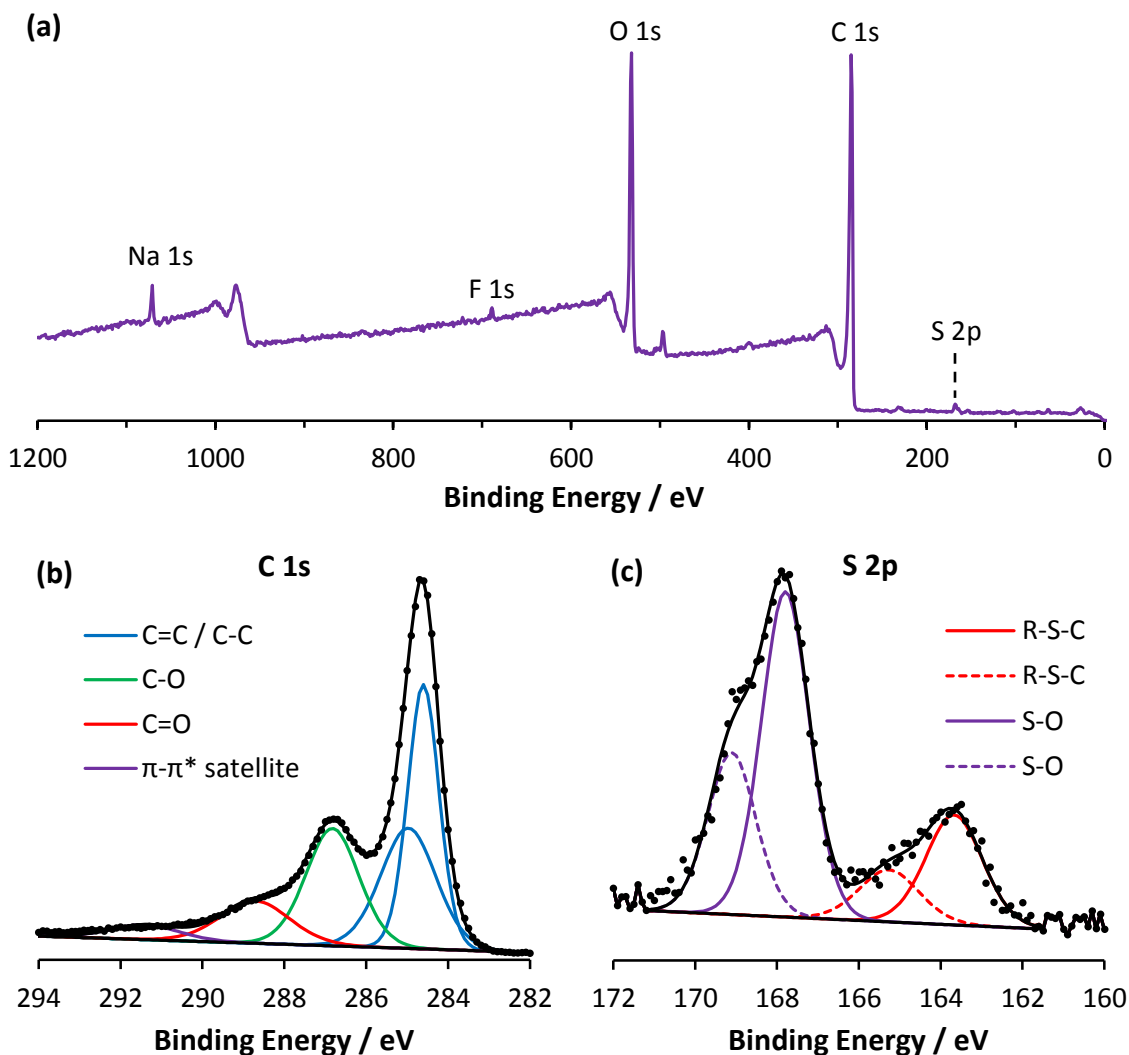
Fig. 5.27 XPS analysis of GOS-PrSO$_3$, complete with survey scan **(a)**, and core level spectra C 1s **(b)** and S 2p **(c)**. The experimental data is shown as points with the underlying lines showing the fitted peaks (assignments as labelled). Note that for **(c)** the 2p$_{3/2}$ orbital assignments are represented by solid lines while the corresponding dashed lines refer to the 2p$_{1/2}$ orbitals.

The XPS survey scan of GOS-PrSO$_3$ (figure 5.27) shows a high proportion of oxygen, consistent with the introduction of sulfonate groups. The core level spectra were studied to gather more information: the C 1s spectrum shows the characteristic peaks of a GO-based material, while the S 2p spectrum shows that there are two different chemical environments for the sulfur in GOS-PrSO$_3$. Some sulfur is attached to the basal plane of GO via C-S-C bonds, identified in the S 2p spectrum as the lower energy doublet. The remaining

sulfur in the GOS-PrSO$_3$ sample is present as sulfates, and is represented by the doublet around 168 eV. Clearly there is more sulfur present as SO$_3$ than as C-S-C, implying that both the SH and OH groups on GO-SH are reacting with 1,3-propanesultone.
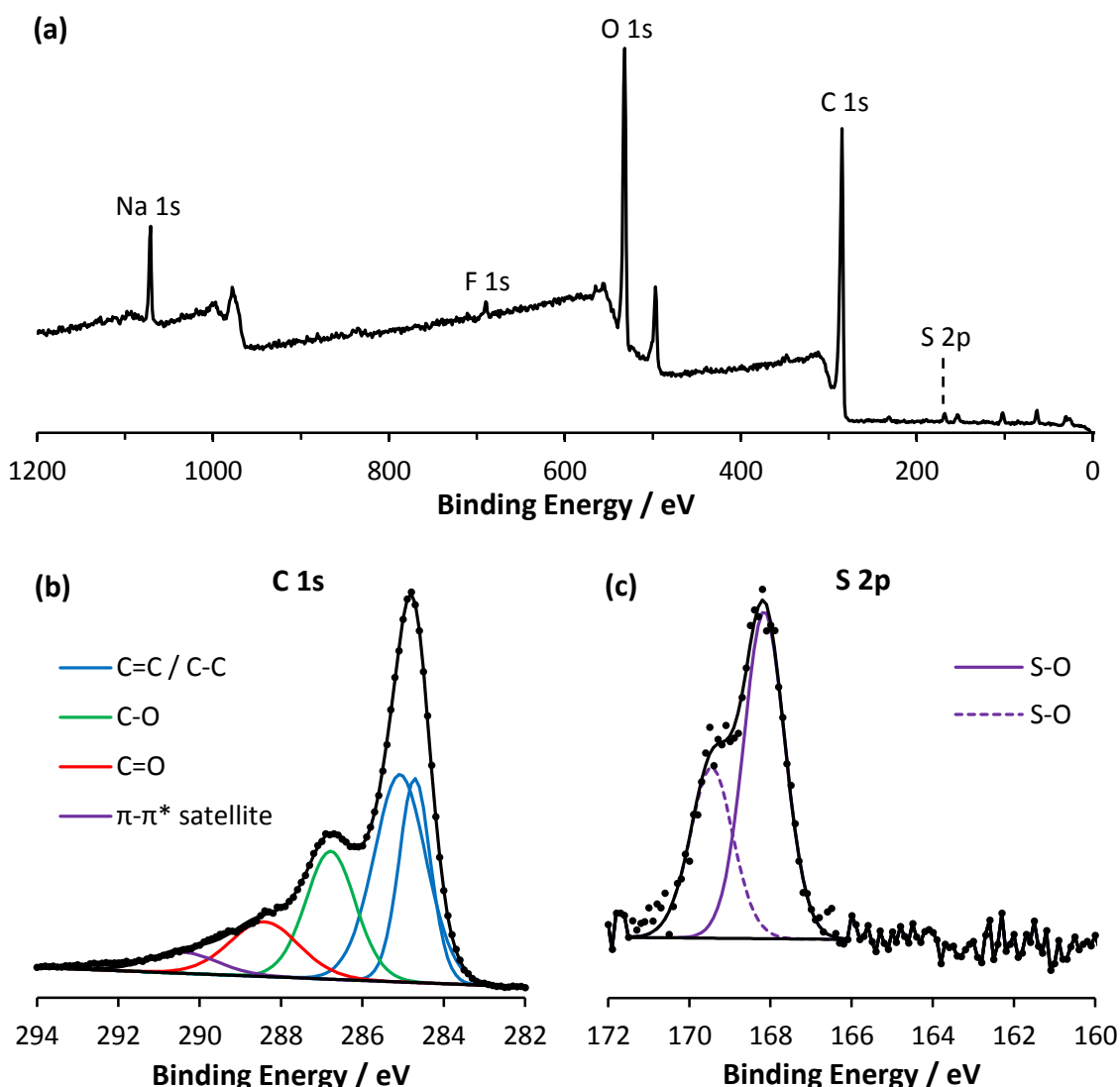
Fig. 5.28 XPS analysis of GO-PrSO$_3$, complete with survey scan **(a)**, and core level spectra C 1s **(b)** and S 2p **(c)**. The experimental data is shown as points with the underlying lines showing the fitted peaks (assignments as labelled). Note that for **(c)** the 2p$_{3/2}$ orbital assignments are represented by solid lines while the corresponding dashed lines refer to the 2p$_{1/2}$ orbitals.

Figure 5.28 shows the XPS survey scan of GO-PrSO$_3$, a small signal due to the incorporation of sulfur is seen, as is an increase in the proportion of oxygen when compared to bwGO. Note that the peak at 500 eV corresponds to Na Auger electrons, and that the smaller, lower binding energy peaks around 100 eV are due to Si 2s and Si 2p.

The C 1s and S 2p spectra of GO-PrSO$_3$ are very similar to GOS-PrSO$_3$, with the main difference being that the sulfur in GO-PrSO$_3$ is found in SO$_3$ bonding environments only. This is consistent with the sultone covalently binding to bwGO via the OH groups.
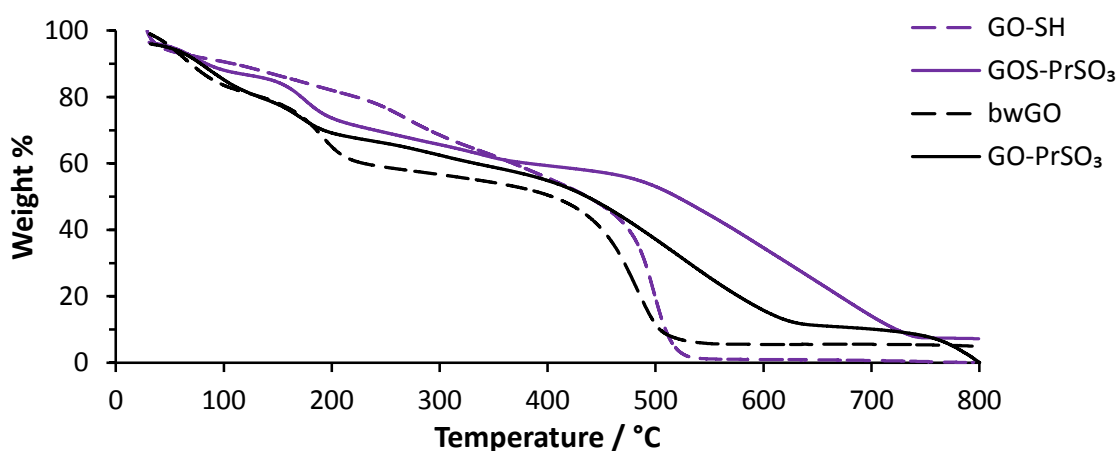
Fig. 5.29 TGA profile GO-SH (purple dash), GOS-PrSO$_3$ (purple), bwGO (black dash) and GO-PrSO$_3$ (black).

The GO-PrSO$_3$ and GOS-PrSO$_3$ materials both have better thermal stability than bwGO and GO-SH, as shown by the TGA profiles in figure 5.29. Furthermore, the decomposition temperature of the GOS-PrSO$_3$ material is 100 °C higher than GO-PrSO$_3$, indicating a better coverage of the OH and SH groups.

Drop shape analysis of these new CMG materials (figure 5.30) show that GO-PrSO$_3$ is significantly more hydrophilic than bwGO: a contact angle of 22° was measured for GO-PrSO$_3$ compared to 38° for bwGO. In addition, GOS-PrSO$_3$ retains a similar contact angle (40°) to GO-SH (41°), suggesting no loss in dispersibility despite high levels of functionalisation.
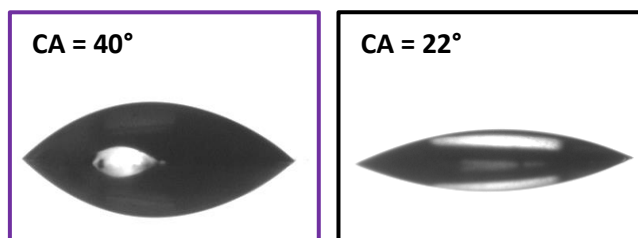
Fig. 5.30 Drop shape analysis of GOS-PrSO$_3$ (purple) and GO-PrSO$_3$ (black).

5.2   Reaction of GO-SH with Heavy Metals

Having successfully demonstrated the chemical modification of bwGO and GO-SH by attaching a variety of different functional groups, with a view to altering the dispersibility and thermal stability of the materials (see chapter 4 and section 5.1), focus was then shifted to functionalisation with heavy metals. Other researchers have previously demonstrated the deposition and coordination of heavy metals to CNTs[12, 13] and CMG[14-17] materials, and so carrying out similar procedures to the novel GO-SH material was a logical next step.

5.2.1 GO-Gold Complexes

The thiol groups on GO-SH could potentially act as ligands for heavy metal coordination: Au(I) ions are soft Lewis acids and are thus compatible with soft Lewis base ligands such as thiols and thioethers.[18]

GO-SH was reacted with $HAuCl_4$, with the expectation that two *trans* chloride ligands (due to steric considerations) would be substituted for two thiolate ligands from separate GO-SH sheets, accompanied by the release of HCl. In aqueous conditions, $HAuCl_4$ is slowly hydrolysed to $Au(OH)_3$, however the reaction with thiolate ligands is much quicker, and so only once the $HAu(SR)_2Cl_2$ complex has formed would ligand exchange with HO^- be expected. Since a S-Au bond is much stronger than a S-Cl bond, a remaining Cl ligand is displaced, again with the production of HCl. Once a hydroxyl ligand is present, *cis* to a thiolate ligand, reductive elimination can occur which reduces the Au(III) to Au(I) and oxidises the thiolate to a sulfoxide group. The resultant material is expected to have RSOH and [Au(SR)Cl]H groups on both sides of the GO type sheets[19] (scheme 5.5).

Scheme 5.5 Reaction of GO-SH and HAuCl$_4$ to give Au(I)-sulfur coordination on GO.

EDX of the resultant material, referred to as GOS-Au, suggests that some gold has been incorporated: C 79 (1); O 18 (2); Au 0.9 (0.5); S 1.0 (0.3), Cl 0.8 (0.3).

Furthermore, Raman studies (figure 5.31) confirm that the isolated material is still graphene-based, and with a D/G ratio of 1.6 it is safe to assume that GOS-Au has a similar structure to GO-SH.

D band ~ 1340 cm^{-1} **G band** ~ 1600 cm^{-1} **G' band** ~ 2700 cm^{-1}
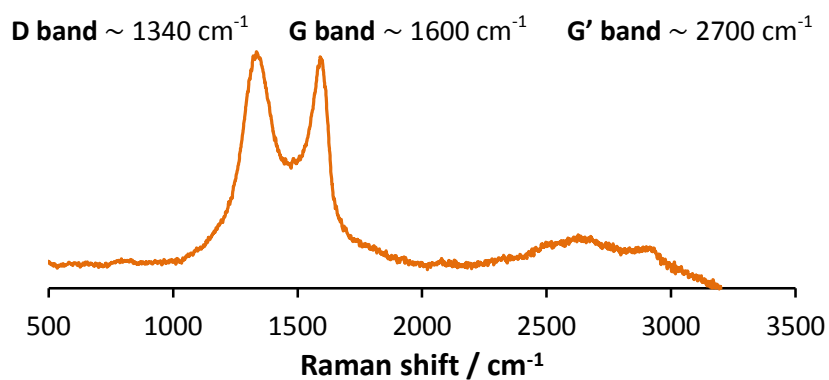
Fig. 5.31 Raman spectrum of GOS-Au; excitation wavelength 633 nm.

XPS is an important tool for monitoring reactions such as this, as it should be possible to identity whether the gold present is Au(III) (i.e. residual HAuCl$_4$) or whether it has been reduced to Au(I). The survey scan and core level spectra of GOS-Au are shown in figure 5.32.

(a)

O 1s

C 1s

Au 4d³

Au 4d⁵

Cl 2p

S 2p

Au 4f

(b) **C 1s**

C=C / C-C
C-O
C=O
π-π* satellite

(c) **S 2p**

S-Au
S-Au
R-S-H
R-S-H
S-O
S-O

(d)

Au 4f

Au(0)
Au(0)
Au(I)
Au(I)
Au(III)
Au(III)

Fig. 5.32 XPS analysis of GOS-Au, complete with survey scan **(a)**, and core level spectra C 1s **(b)**, S 2p **(c)**, and Au 4f **(d)**. The experimental data is shown as points with the underlying lines showing the fitted peaks (assignments as labelled). Note that for **(c)** and **(d)** the $2p_{3/2}$ and $4f_{7/2}$ orbitals are represented by solid lines while the corresponding dashed lines refer to the $2p_{1/2}$ and $4f_{5/2}$ orbitals.

The XPS survey scan of GOS-Au (figure 5.32) shows a clear signal for the Au 4f orbital as well as small signals from S 2p and Cl 2p. In addition, the core level spectra of C 1s, S 2p and Au 4f were studied. The C 1s core level spectrum of GOS-Au serves to prove that the material is still graphene-based with C=C, C-C, C-O and C=O functionalities. The S 2p spectrum is much more informative and shows that roughly one third (36%) of the sulfur on GO-SH has reacted with the HAuCl$_4$ to give S-O and S-Au groups. The majority of the sulfur present remains unreacted and still exists as SH. The Au 4f spectrum shows that the gold present on GO-SH is predominantly Au(I) as expected.

For the synthesis of GOS-Au, it was found that long reaction times (over 30 minutes) yielded an insoluble CMG. This material was unsuitable for TEM studies and so the reaction was limited to 30 minutes. From the XPS data it is clear that the 30 minute reaction had not gone to completion, however it represents a good compromise between dispersibility and gold incorporation. A possible explanation for the loss of dispersibility is the formation of aurophilic interactions;[20] with longer reaction times further Au functionalisation is expected, which might cause the GO sheets to crumple up, sacrificing dispersibility while stabilising thiol-Au(I) coordination.
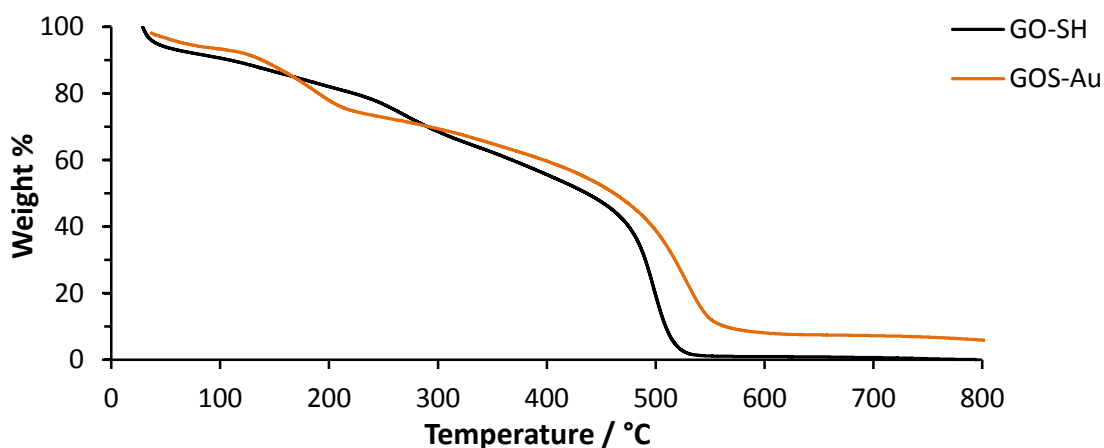
Fig. 5.33 TGA profiles of GO-SH (black) and GOS-Au (orange).

The TGA profile of GOS-Au (figure 5.33) shows increased thermal stability by approximately 30 °C compared to GO-SH. This moderate increase presumably results from only capping a third of the reactive SH groups on GO-SH. More importantly, it appears that not all of the GOS-Au material has decomposed by 800 °C: 7 wt.% remains. This remaining mass can be attributed to the gold on GOS-Au.

As discussed above, the short reaction time used to synthesise GOS-Au resulted in a GO-Au complex with acceptable dispersibility. Figure 5.34 shows the drop shape analysis image, which indicates that the hydrophilicity of GOS-Au is in line with GO-SH: the CA of GOS-Au has increased by only 2° compared to GO-SH.
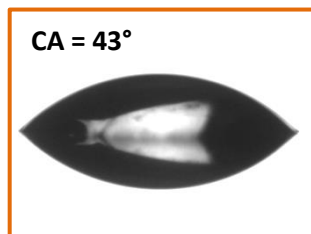
Fig. 5.34 Drop shape analysis of GOS-Au.

The final method of characterisation for GOS-Au was TEM. Figure 5.35 shows comparative HR-TEM images of GO-SH and GOS-Au. While GO-SH shows some dark contrast atoms (see chapter 4), GOS-Au shows appreciably more. In addition, while the dark contrast atoms of GO-SH seem to lie preferentially on amorphous regions and move easily under the electron beam, the dark contrast atoms of GOS-Au are more stable and can be seen on graphene-like areas of the GO sheets. While not definitive evidence, this suggests that some of the contrast atoms seen for GOS-Au are indeed due to coordinated Au(I).
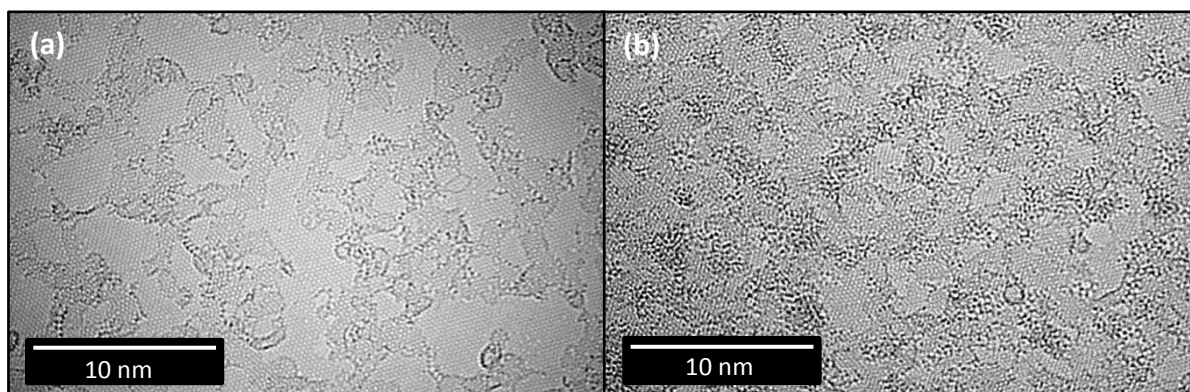
Fig. 5.35 HR-TEM images of **(a)** GO-SH and **(b)** GOS-Au.

This gold coordination is specific to thiolated GO: a control experiment using the same reaction conditions to coordinate gold to bwGO showed no evidence of Au incorporation via EDX, TGA or TEM.

The gold on GOS-Au is believed to be mostly mono-atomic. However, the Au 4f core level XPS spectrum in figure 5.32 (d) does show a small contribution from Au(0) species, and indeed using low resolution TEM, some gold nanoparticles were found on the surface of the

GOS-Au sheets. By comparison, bwGO sheets were found to be clean of gold clusters after reaction with HAuCl$_4$, confirming that any unreacted gold on GOS-Au would be washed away during the reaction workup. These TEM images are shown in figure 5.36.
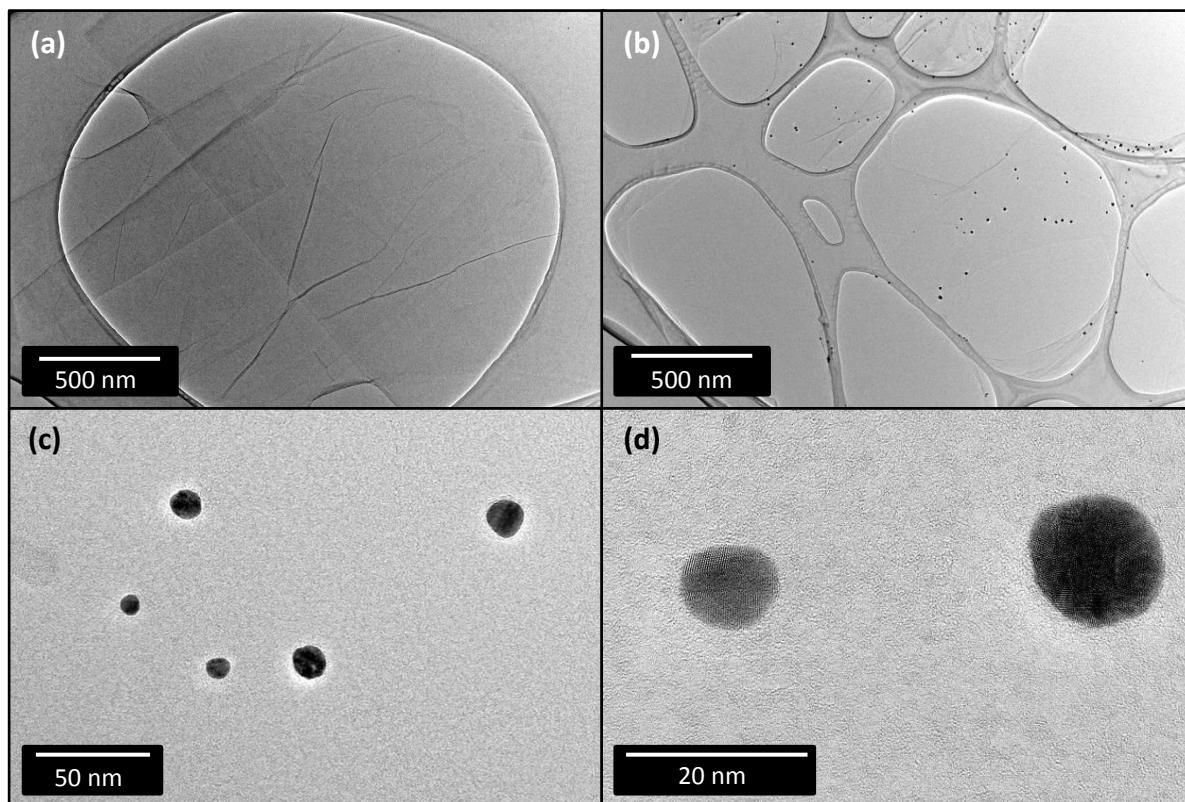
Fig. 5.36 Low resolution TEM images of **(a)** bwGO reacted with HAuCl$_4$ and **(b)** GOS-Au. **(c)** and **(d)** show progressively higher resolution images of the Au clusters on GOS-Au.

From the characterisation data gathered it seems that Au(I) has been successfully complexed to the surface of GO-SH through thiol ligands, while maintaining appreciable dispersibility in DMF.

5.2.2 GO-Palladium Complexes

After investigating GO-gold complexes through coordination via SH ligands, attention was shifted to other heavy metals: palladium should also coordinate to GO-SH via thiol linkages.

GO-SH was reacted with the Pd(II) complex bis(benzonitrile)palladium chloride, with the expectation that one of the hard chloride ligands would be replaced by a softer thiolate ligand from the SH groups on GO-SH (scheme 5.5). Any (PhCN)$_2$PdCl$_2$ not coordinated to the

GO-SH sheets after reaction was removed via acetone washes. The resultant Pd(II)-sulfur complex is referred to as GOS-Pd.
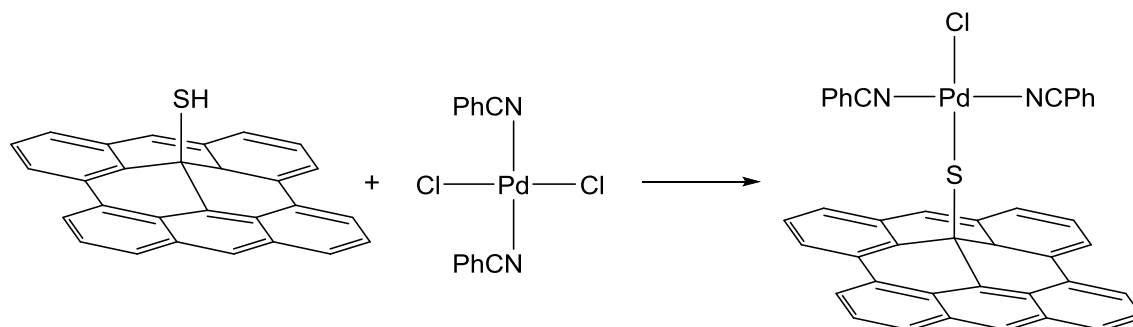
Scheme 5.6 Reaction of GO-SH and (PhCN)$_2$PdCl$_2$ to give Pd(II)-sulfur coordination on GO.

EDX analysis shows incorporation of Pd and Cl to GO-SH: C 83 (1); O 14 (1); S 1.0 (0.1); Cl 0.6 (0.1); Pd 0.6 (0.1), and Raman studies (figure 5.37) confirm that the graphene-like structure is intact (D/G = 1.7).

D band ~ 1340 cm^{-1} **G band** ~ 1600 cm^{-1} **G' band** ~ 2700 cm^{-1}
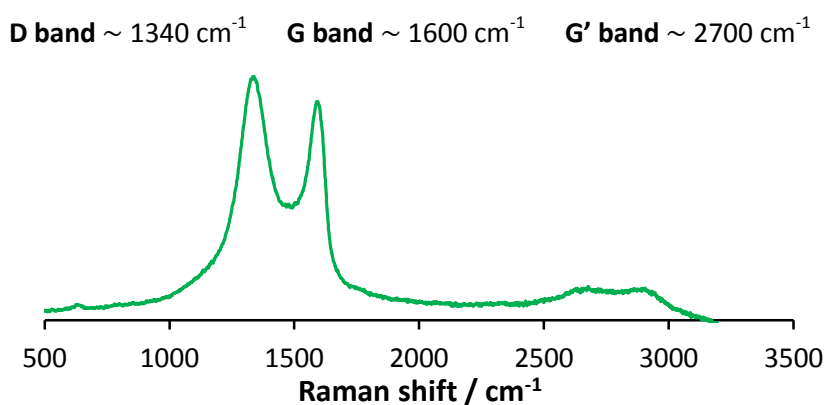
Fig. 5.37 Raman spectrum of GOS-Pd; excitation wavelength 633 nm.

The XPS survey scan shown in figure 5.38 (a) shows the elements expected for GO-SH alongside a strong Pd 3d signal.
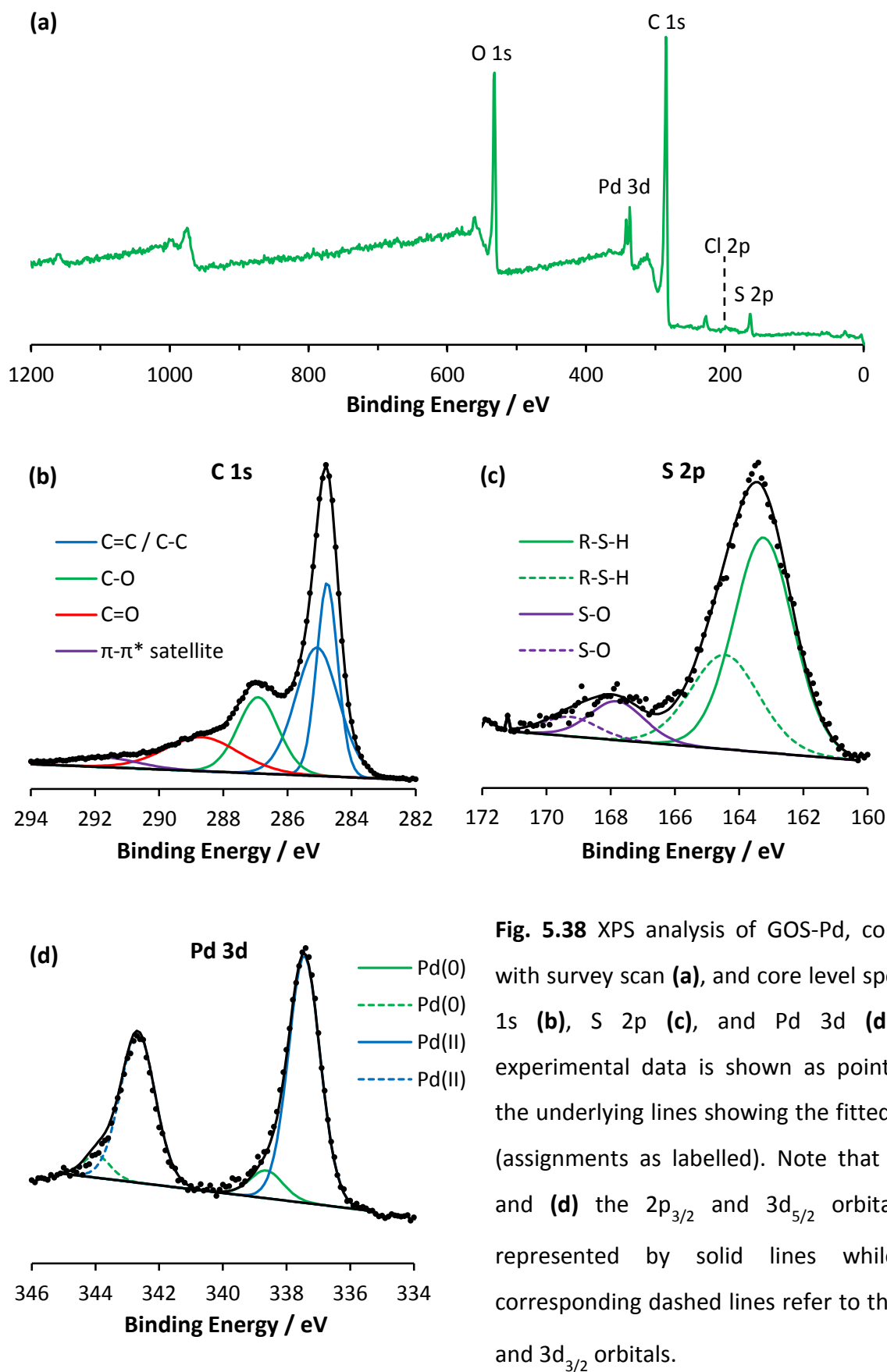
Fig. 5.38 XPS analysis of GOS-Pd, complete with survey scan **(a)**, and core level spectra C 1s **(b)**, S 2p **(c)**, and Pd 3d **(d)**. The experimental data is shown as points with the underlying lines showing the fitted peaks (assignments as labelled). Note that for **(c)** and **(d)** the $2p_{3/2}$ and $3d_{5/2}$ orbitals are represented by solid lines while the corresponding dashed lines refer to the $2p_{1/2}$ and $3d_{3/2}$ orbitals.

The XPS characterisation data is not inconsistent with Pd coordination, certainly Pd is present. The C 1s spectrum (figure 5.38) is as expected for a GO-based material. The only notable difference between the S 2p spectrum of GOS-Pd and GO-SH, is the broadness of the R-S-H doublet in GOS-Pd. Binding Pd to a thiol group will generally result in only a very slight shift in peak position.[21, 22] Hence it is not possible to separate contributions from R-S-H and R-S-Pd, but the increased line width of the R-S-H signal likely indicates a mixture of thiol groups and thiolate-Pd groups on the GO surface. The Pd 3d spectrum shows that 89% of the palladium is present is Pd(II). While both uncoordinated $(PhCN)_2PdCl_2$ and GOS-Pd contain Pd(II), it is reasonable to assume that no $(PhCN)_2PdCl_2$ is present due to the extensive washing of GOS-Pd during the work-up.

The TGA profile of GOS-Pd (figure 5.39) shows a more gradual decomposition of the GOS-Pd sheets compared to GO-SH resulting in a significant increase in the overall thermal stability of the material. Furthermore, as with GOS-Au, GOS-Pd is not fully decomposed at 800 °C – the remaining mass can be attributed to palladium.
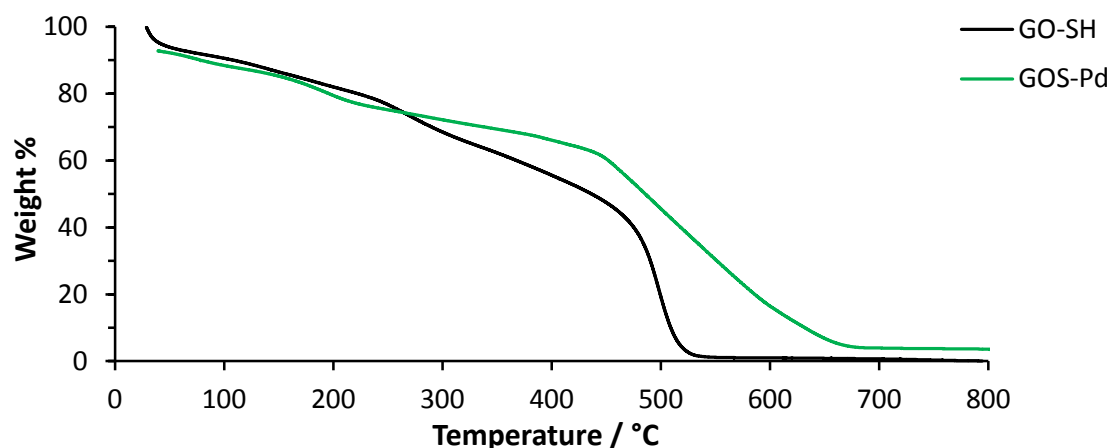
Fig. 5.39 TGA profile of GO-SH (black) and GOS-Pd (green).

The dispersibility of GOS-Pd is limited, although a stable suspension in DMF can still be prepared. Figure 5.40 shows the drop shape analysis image of GOS-Pd, with an increased contact angle of 61° indicating decreased hydrophilicity.
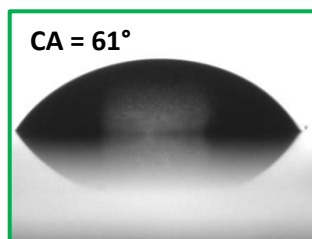
Fig. 5.40 Drop shape analysis of GOS-Pd.

These changes in the thermal properties and dispersibility of GOS-Pd indicate that the GO-SH sheets have been chemically modified on reaction with $(PhCN)_2PdCl_2$.

HR-TEM studies of GOS-Pd (figure 5.41) show dark contrast atoms consistent with heavy metals. GOS-Pd does not have noticeably more dark contrast atoms than GO-SH, however, for GOS-Pd (as previously seen for GOS-Au) the contrast atoms are seen to lie over the graphene-like regions of the sheets. For example, see those shown within the green circle in figure 5.41 (b). By comparison, the contrast atoms on GO-SH seem to lie preferentially on the amorphous regions.
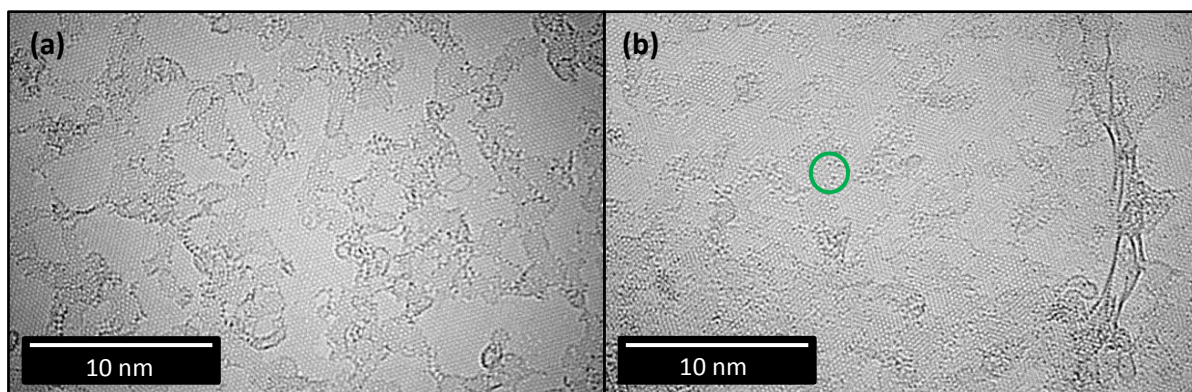
Fig. 5.41 HR-TEM images of **(a)** GO-SH and **(b)** GOS-Pd. Heavy contrast atoms which lie on top of a graphene-like area can be seen within the green circle.

This palladium coordination is also specific to thiolated GO: a control experiment using the same reaction conditions to coordinate palladium to bwGO showed no evidence of Pd incorporation via EDX, TGA or TEM.

XPS (figure 5.38) showed that the predominating palladium species in GOS-Pd is Pd(II), which is likely to be bound to the GO-SH surface via thiolate ligands. However, similar to GOS-Au, low resolution TEM (figure 5.42) reveals some palladium clusters on GOS-Pd. By

contrast, the control experiment shows no evidence of Pd nanoparticles: the bwGO surface appears to be clean after reaction with $(PhCN)_2PdCl_2$.
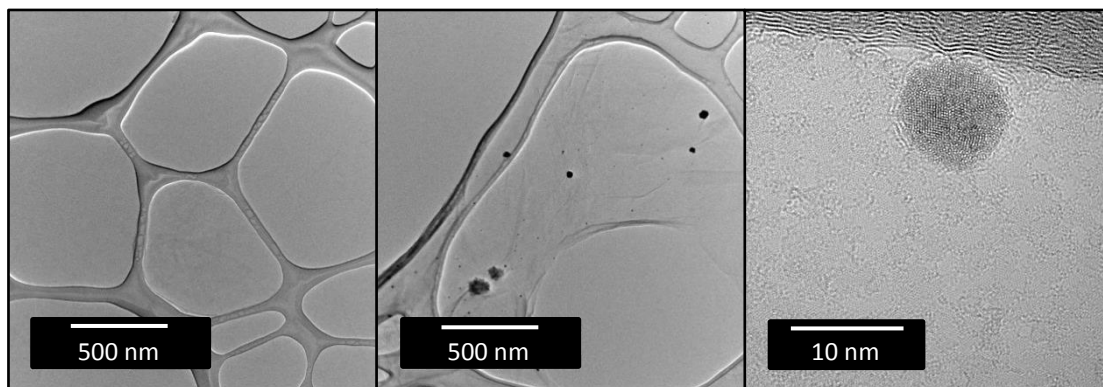
Fig. 5.42 Low resolution TEM images of **(a)** bwGO reacted with $(PhCN)_2PdCl_2$ and **(b)** GOS-Pd. **(c)** shows a higher resolution image of the Pd clusters on GOS-Pd.

The results outlined in this section indicate that the reaction of GO-SH with $(PhCN)_2PdCl_2$, has been successful, forming a Pd(II) functionalised GO-based material with increased thermal stability.

5.2.3 Deposition of Gold Nanoparticles

Having demonstrated that the thiol groups on the GO-SH material have an affinity for mono-atomic gold, it was interesting to see whether nanoparticles (NPs) could also be anchored to the surface. Thus, a solution of $HAuCl_4$ was prepared and treated with $NaBH_4$ to generate gold nanoparticles. This mixture was immediately added to a dispersion of GO-SH and was left for approximately one minute. The carbonaceous material was isolated via centrifugation and was washed with water and acetone. This product is referred to as GOS-AuNP.

Raman studies (figure 5.43) confirm that the isolated material is still graphene-based, showing strong D and G bands. The D/G ratio remains the same as GO-SH (1.7).

D band ~ 1340 cm^{-1} **G band** ~ 1600 cm^{-1} **G' band** ~ 2700 cm^{-1}
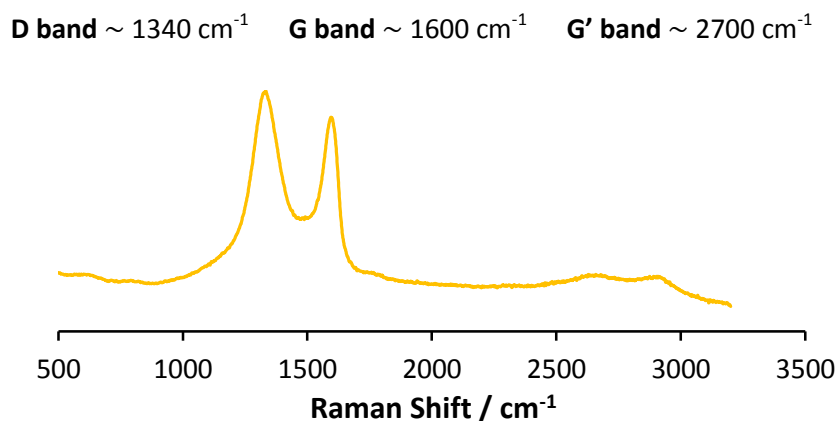
Fig. 5.43 Raman spectrum of GOS-AuNP; excitation wavelength 633 nm.

EDX studies confirm the presence of gold for GOS-AuNP: C 64 (2); O 6 (2); Au 28 (2); S 1.2 (0.5). A control experiment in which bwGO was treated with HAuCl$_4$ and NaBH$_4$ under the same conditions, showed no significant levels of gold after work-up.

The TGA profile of GOS-AuNP is shown in figure 5.44. Similar to other CMGs, the carbonaceous portion of GOS-AuNP has fully decomposed by 600 °C. However, unusually, 87 wt.% of the material still remains at 800 °C. This measurement is in good agreement with the EDX which measured 86 wt.% (calculated from 28 at.% Au). These results alone provide convincing evidence that the surface of the GO-SH material is now coated with AuNPs.
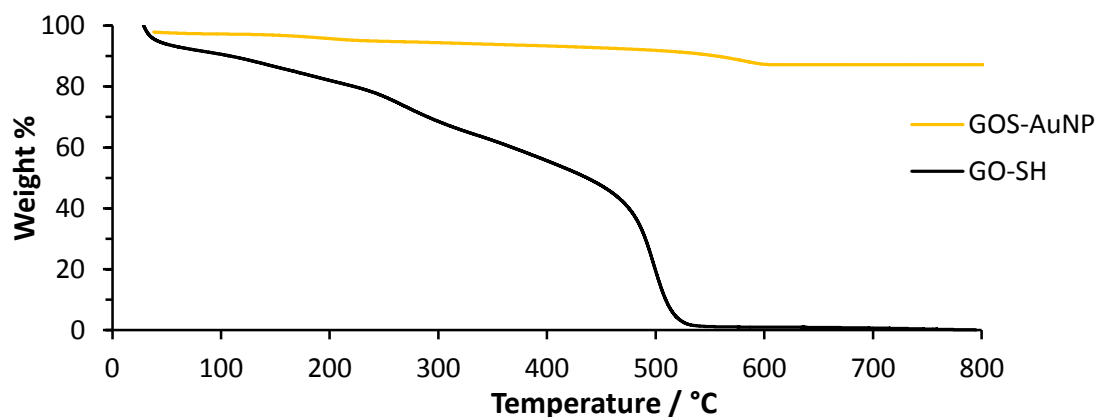
Fig. 5.44 TGA profile of GO-SH (black) and GOS-AuNP (yellow).

SEM imaging was used to further the investigation of GOS-AuNP, the results of which can be seen in figure 5.45.
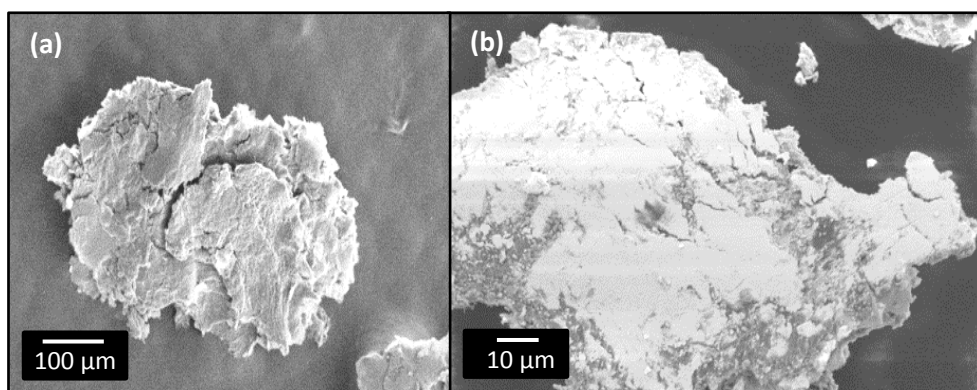
Fig. 5.45 SEM images of **(a)** GO-SH and **(b)** GOS-AuNP.

Figure 5.45 (a) shows the SEM image of a powdered GO-SH sample, it can be seen that the material has clumped together and as a result has a noticeably rough surface. By comparison, the GOS-AuNP flake in figure 5.45 (b) also appears to be clumped together, but the surface is much smoother. The lighter contrast shown for the GOS-AuNP surface is indicative of a heavy element, and is thus consistent with a gold coating.

In order to directly observe the Au nanoparticles via TEM a grid was prepared *in-situ*: GO-SH was drop cast onto a lacey carbon TEM support grid which was then placed in a solution of $HAuCl_4$. $NaBH_4$ was added to reduce the $HAuCl_4$ as before, and the grid was then rinsed with both water and acetone and was dried in air on filter paper.
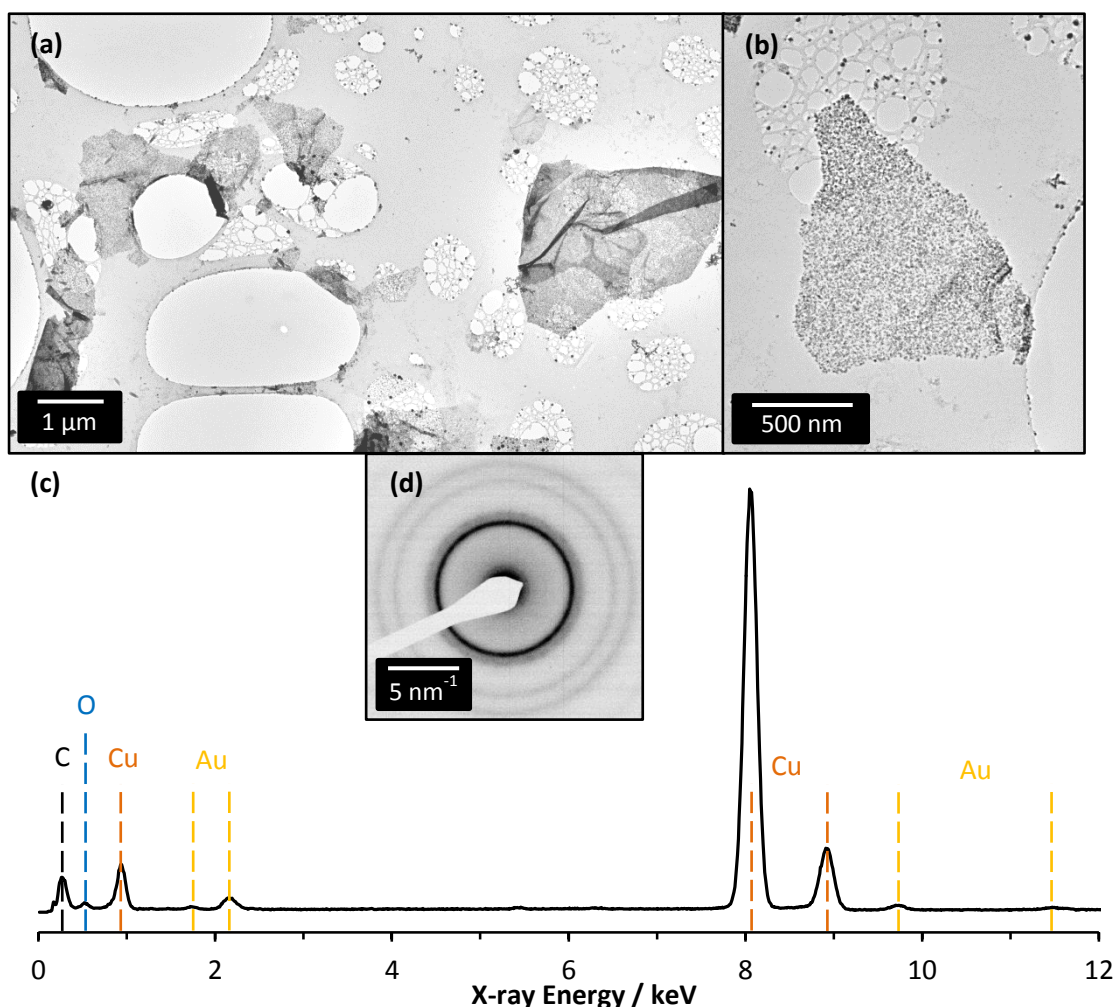
Fig. 5.46 (a) Low magnification bright field TEM image showing several GOS-AuNP sheets, each uniformly coated in nanoparticles. (b) Higher magnification bright field image of one GOS-AuNP sheet. (c) EDX analysis of GOS-AuNP. (d) GOS-AuNP SAED pattern.

Figures 5.46 and 5.47 show the TEM analysis of GOS-AuNP. The low magnification images (figures 5.46 (a), (b) and figure 5.47 (a)), show a homogeneous deposition of nanoparticles on the GO-SH sheets, whilst the background lacey carbon support is almost entirely uncoated. Figure 5.46 (c) shows the EDX analysis: the carbon and oxygen peaks are predominantly from the lacey carbon support films, and the copper is from the TEM grid. The SAED pattern of GOS-AuNP in figure 5.46 (d) shows diffraction rings: the spacing of these rings is consistent with Au, and the ring patterns indicate no preferential orientation between the AuNPs and GO-SH. Hence the nanoparticles seen in TEM can be confidently attributed to Au, as expected.
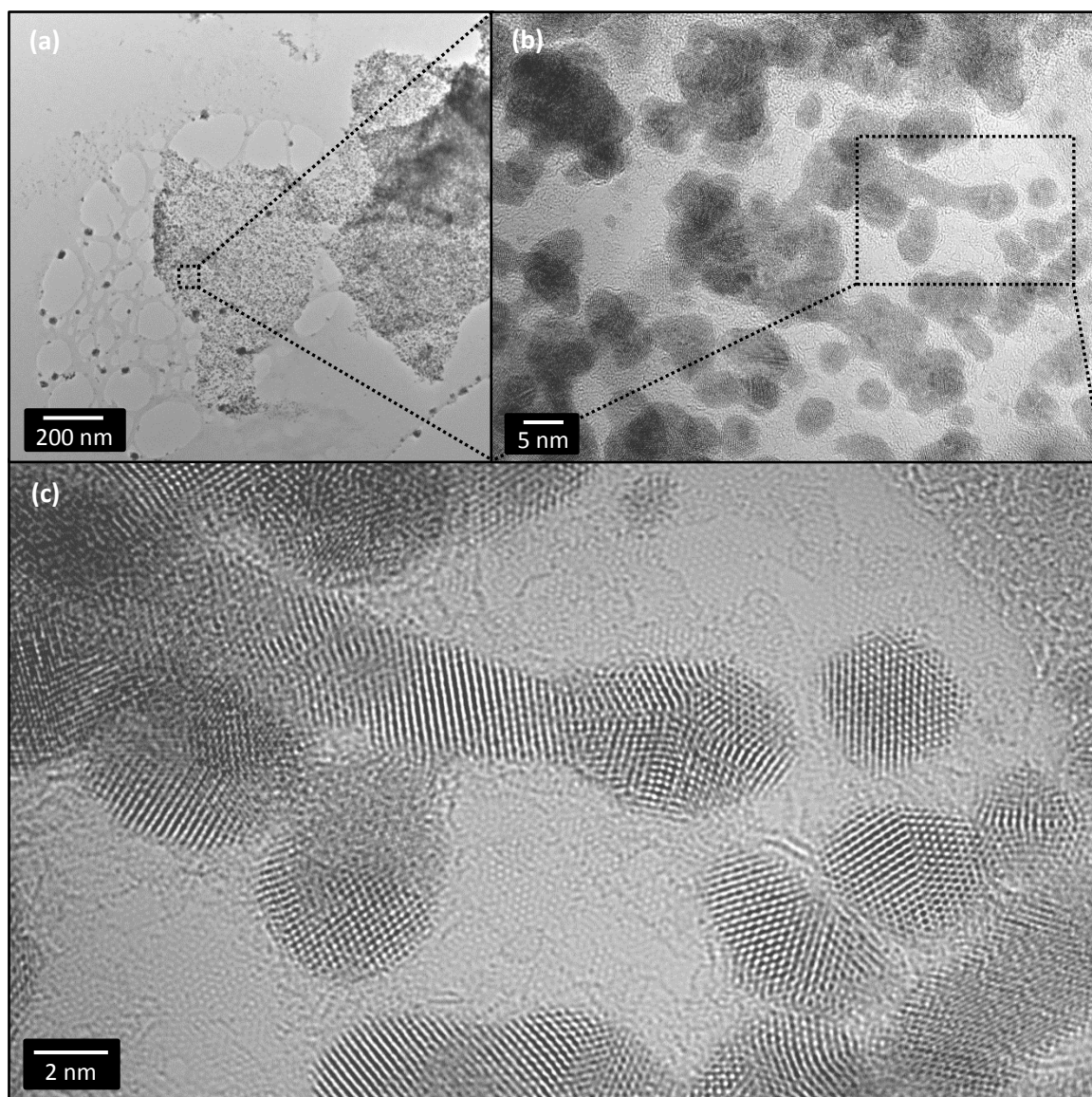
Fig. 5.47 (a) Low magnification bright field TEM image of GOS-AuNP sheets on a lacey carbon support. **(b)** and **(c)** show successively higher magnification images of the same region taken from within the dashed boxes.

The HR-TEM images in figure 5.47 show that a high density of small nanoparticles have formed. The nanoparticle sizes range from small clusters of Au atoms through to agglomerations of coalesced nanoparticles, but the typical size of the isolated nanoparticles is 5–10 nm. The nucleation density is very high, but is difficult to quantify due to the obvious coalescence of many smaller particles to form larger ones, however the spacing between the nanoparticles is typically in the order of a few nanometers. The high-resolution images resolve the crystalline lattice of the Au nanoparticles, but there is no evidence for any preferred orientation of the Au lattice relative to the underlying graphene-like lattice, which

can also be seen in the high resolution images. The morphology of the nanoparticle deposition is very different from what would be expected on graphene or graphene oxide: the interaction between gold and graphene is weak, such that gold nanoparticles normally form a droplet-like morphology.[23] Here, the nanoparticles are often elongated and branched, characteristic of a high density of nucleation, with the coalescence of clusters without subsequent rearrangement. This indicates a much stronger interaction between the gold and GO-SH, consistent with the presence of thiol groups on the GO surface.

This deposition of AuNPs is selective to GO-SH; some large particles are observed on the lacey carbon support film (figure 5.46), but these appear to have been formed in solution and deposited on the support film during drying. As a control a bwGO coated TEM grid was placed in a $HAuCl_4$ solution for *in situ* reduction with $NaBH_4$. There was no evidence for Au deposition on bwGO, (figure 5.48), and this was reproducible over several measurements. This is consistent with previously published results of gold deposition on CMGs.[24]
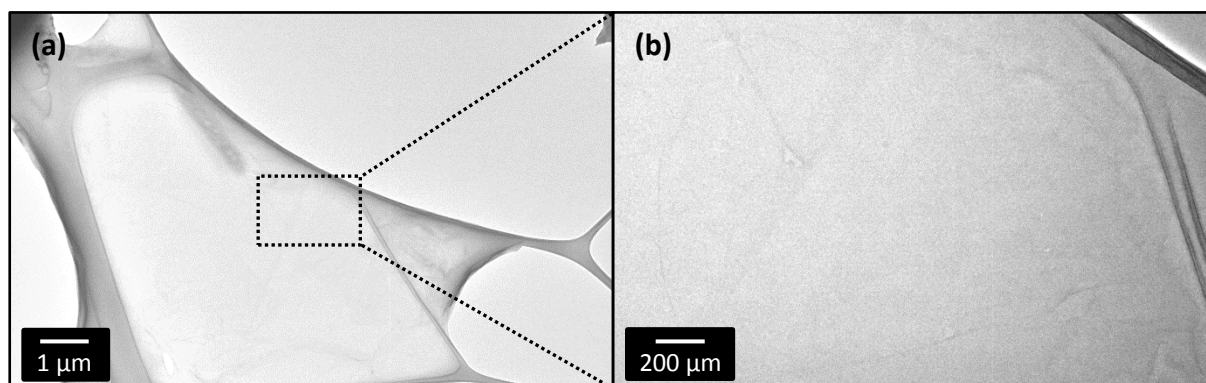
Fig. 5.48 TEM of bwGO after being subjected to the same conditions used to deposit Au on GOSH. **(a)** Low magnification bright field TEM image of several overlapping bwGO sheets supported on a lacey carbon support. **(b)** Higher magnification view of the area within the dotted box of **(a)**.

The deposition of AuNPs[25, 26] provides further evidence for the synthesis of thiol functionalised GO materials, and for the changes in the functional properties that this synthesis creates.[27] The uniformity of deposition and the high density of the nanoparticles indicate that the thiol groups must be homogeneously distributed across the sheets of GO-SH. The robust anchoring of gold nanoparticles also indicates the possibility of anchoring other metal nanoparticles to the GO surface, facilitating both catalytic and electrochemical reactions.

5.3   Conclusions

Through this chapter further functionalisation of the GO-SH material has been explored and three novel CMGs have been prepared using the surface thiols of GO-SH to anchor organic functional groups. In all three cases, the thermal stability of the CMGs has significantly increased, and the incorporation of sulfonate groups was found to prevent any further loss in dispersibility as a result of functionalisation.

The control experiments carried out show that the same functionalisation may occur through the OH groups on both bwGO and GO-SH. However, the data suggests that the SH groups on GO-SH are completely capped during the reactions, whereas the OH groups are only partially capped; it appears that the reaction with SH is favoured, particularly for the reactions with alkyl halides and MVK.

In addition Au(I) and Pd(II) GO complexes were prepared, where the heavy metals were grafted to the GO surface via thiolate ligands, and the selective deposition of AuNPs on GO-SH was demonstrated. These hybrid materials illustrate the significance of the novel GO-SH material, showing that it can be used as a platform for chemical modification with heavy metals. Since there is currently much interest in carbon materials with coordinated heavy metals for sensor[28, 29] and catalytic[30, 31] applications, it is plausible that metallo-organic derivatives of GO-SH could play a role in future research.

1. Pearson, R. G.; Sobel, H.; Songstad, J. *J. Am. Chem. Soc.* **1968,** 90, 319-326.
2. Phan, T. B.; Breugst, M.; Mayr, H. *Angew. Chem., Int. Ed.* **2006,** 45, (23), 3869-3874.
3. Kolb, H. C.; Finn, M. G.; Sharpless, K. B. *Angew. Chem., Int. Ed.* **2001,** 40, (11), 2004-2021.
4. Hoyle, C. E.; Bowman, C. N. *Angew. Chem., Int. Ed.* **2010,** 49, (9), 1540-1573.
5. Kumari, S.; Malvi, B.; Ganai, A. K.; Pillai, V. K.; Sen Gupta, S. *J. Phys. Chem. C* **2011,** 115, (36), 17774-17781.
6. Chu, C.-M.; Gao, S.; Sastry, M. N. V.; Yao, C.-F. *Tetrahedron Lett.* **2005,** 46, (30), 4971-4974.
7. Yerli, G.; Gezegen, H.; Ceylan, M. *Org. Commun.* **2012,** 5, (2), 70-76.
8. Nising, C. F.; Brase, S. *Chem. Soc. Rev.* **2012,** 41, (3), 988-999.
9. Wabnitz, T. C.; Yu, J.-Q.; Spencer, J. B. *Chem. Eur. J.* **2004,** 10, (2), 484-493.
10. Singh, R.; Goswami, T. *J. Phys. Org. Chem.* **2008,** 21, (3), 225-236.
11. Wabnitz, T. C.; Spencer, J. B. *Org. Lett.* **2003,** 5, (12), 2141-2144.
12. Zhu, J.; Hiltz, J.; Lennox, R. B.; Schirrmacher, R. *Chem. Commun.* **2013,** 49, (87), 10275-10277.
13. Zanella, R.; Basiuk, E. V.; Santiago, P.; Basiuk, V. A.; Mireles, E.; Puente-Lee, I.; Saniger, J. M. *J. Phys. Chem. B* **2005,** 109, (34), 16290-16295.
14. Mayavan, S.; Sim, J.-B.; Choi, S.-M. *J. Mater. Chem.* **2012,** 22, (14), 6953-6958.
15. Lu, X.; Qi, H.; Zhang, X.; Xue, Z.; Jin, J.; Zhou, X.; Liu, X. *Chem. Commun.* **2011,** 47, (46), 12494-12496.
16. Faria, A. F.; Martinez, D. S. T.; Moraes, A. C. M.; Maia da Costa, M. E. H.; Barros, E. B.; Souza Filho, A. G.; Paula, A. J.; Alves, O. L. *Chem. Mater.* **2012,** 24, (21), 4080-4087.
17. Sattayasamitsathit, S.; Gu, Y.; Kaufmann, K.; Jia, W.; Xiao, X.; Rodriguez, M.; Minteer, S.; Cha, J.; Burckel, D. B.; Wang, C.; Polsky, R.; Wang, J. *J. Mater. Chem. A* **2013,** 1, (5), 1639-1645.
18. Pearson, R. G. *J. Am. Chem. Soc.* **1963,** 85, (22), 3533-3539.
19. Awaleh, M. O.; Baril-Robert, F.; Reber, C.; Badia, A.; Brisse, F. *Inorg Chem.* **2008,** 47, (8), 2964-2974.
20. Schmidbaur, H.; Schier, A. *Chem. Soc. Rev.* **2012,** 41, (1), 370-412.
21. Xu, L.; Liao, J.; Huang, L.; Gu, N.; Zhang, H.; Liu, J. *Appl. Surf. Sci.* **2003,** 211, (1–4), 184-188.
22. Love, J. C.; Wolfe, D. B.; Haasch, R.; Chabinyc, M. L.; Paul, K. E.; Whitesides, G. M.; Nuzzo, R. G. *J. Am. Chem. Soc.* **2003,** 125, (9), 2597-2609.
23. Pandey, P. A.; Bell, G. R.; Rourke, J. P.; Sanchez, A. M.; Elkin, M. D.; Hickey, B. J.; Wilson, N. R. *Small* **2011,** 7, (22), 3202-10.
24. Bosch-Navarro, C.; Coronado, E.; Martí-Gastaldo, C. *Carbon* **2013,** 54, (0), 201-207.
25. Hermes, J. P.; Sander, F.; Peterle, T.; Urbani, R.; Pfohl, T.; Thompson, D.; Mayor, M. *Chem. Eur. J.* **2011,** 17, (48), 13473-13481.
26. Yarzhemsky, V. G.; Battocchio, C. *Russ. J. Inorg. Chem.* **2011,** 56, (14), 2147-2159.
27. Nakamura, T.; Ohana, T.; Hagiwara, Y.; Tsubota, T. *Phys. Chem. Chem. Phys.* **2009,** 11, (4), 730-734.
28. Kong, J.; Chapline, M. G.; Dai, H. *Adv. Mater.* **2001,** 13, (18), 1384-1386.
29. Kubesa, O.; Morrisey, K.; Mathews, S.; Proetta, J.; Li, C.; Skladal, P.; Hepel, M. *Mediterr. J. Chem.* **2014,** 3, (3), 916-928.
30. Giovanni, M.; Poh, H. L.; Ambrosi, A.; Zhao, G.; Sofer, Z.; Sanek, F.; Khezri, B.; Webster, R. D.; Pumera, M. *Nanoscale* **2012,** 4, (16), 5002-5008.
31. Movahed, S. K.; Dabiri, M.; Bazgir, A. *Appl. Catal. A-Gen.* **2014,** 488, (0), 265-274.

Chapter 6

Conclusions
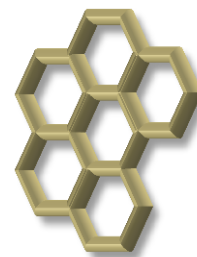
The aim of the work presented in this thesis was to resolve some of the ambiguity around the structure of graphene oxide by studying the chemical reactivity and properties of the material. Good supporting evidence was found for the two-component bwGO-OD model, and novel CMGs were prepared from the cleaned bwGO material, showing its potential as a future precursor material for graphene-like materials.

A thorough investigation into the structure of graphene oxide was undertaken, where a number of different characterisation techniques were utilised in order to gather as much information as possible on aGO and the constituent bwGO and OD materials. Topographical studies indicated no significant differences between Hummers aGO and bwGO: no difference in the layer spacing was seen by AFM, and no obvious structural differences were seen by TEM. Furthermore, the Raman spectrum of bwGO was consistent with a graphene-type material. EDX measured notably less oxygen for bwGO than for aGO, which is in agreement with the reduced hydroxyl and epoxy contributions seen by FTIR and ssNMR. Hence, from the characterisation data gathered, there is no evidence of any significant chemical changes on treating aGO with NaOH – except for a deoxygenation which can be explained by the loss of highly oxygenated OD. The removal of the OD thus yields a more graphene-like material.

An investigation was launched to identify any inconsistencies in GO research which might occur through the different synthetic routes to GO and thus aGO materials were prepared using the four most common synthetic protocols. FTIR, EDX, Raman, ssNMR and TGA studies showed that the aGO materials from all protocols were very similar. The four aGO materials were treated with aqueous NaOH to extract bwGO, and roughly ⅓ OD by mass was found for all four materials. No evidence of significant structural or chemical differences was found between the different aGO and bwGO materials, leading to the conclusion that the materials are independent of the synthetic protocol.

In addition aGO was washed with NH_3, extracting bwGO in the same manner as with a NaOH wash. No differences were found between the bwGO materials extracted via NaOH and via NH_3, suggesting that the synthesis of bwGO is independent of the base used. This process of treating aGO with NaOH or NH_3 is referred to as cleaning: the OD is washed away from the sheet surface, causing deoxygenation while unveiling the "true" GO sheets. By comparison, treatment with hydrazine both cleans aGO and genuinely reduces the GO sheets.

Studies on the OD material revealed that properties previously attributed to aGO, such as good dispersibility and photo-luminescence, actually originate from the presence of the OD. The results gathered in this thesis suggest that the OD consists of a range of low molecular weight, carbonaceous fragments, with many of the same oxidation functionalities as bwGO but without the extensive graphitic structure. The OD exhibits wavelength dependent fluorescence, and is potentially the source of the broad, non-dispersive emission of aGO. The OD also acts as a surfactant to stabilise bwGO sheets in solution, and the non-covalent interactions which bind OD to the sheet surface in aGO actually affect the electronic structure of the graphene-type sheets, rendering them insulating.

bwGO was functionalised using different nucleophiles to ring open epoxy groups on the graphene-type surface. The attachment of a malononitrile group was successfully demonstrated using the protocol originally outlined by Swager *et al*.[1] who used the reaction to functionalise aGO. The lower N incorporation from the reaction with bwGO suggests that Swager *et al*. were inadvertently functionalising the OD as well as the GO sheets. Moving onto sulfur nucleophiles, surface thiol groups were successfully introduced to the bwGO sheets via reaction with thioacetate to give GO-SH. The characterisation evidence on the reaction of bwGO with thiophenol was less conclusive, but the TGA in particular was suggestive of the successful formation of surface thioethers. Polymer chains were grafted directly onto bwGO using three different chain lengths of p(NIPAM), which resulted in a GO-polymer composite with increased thermal stability and increased hydrophilicity when compared to bwGO.

The novel GO-SH material was reacted further using organic and metal moieties to functionalise the reactive thiol groups. Alkylation of the SH groups on GO-SH, a thiol-ene click reaction with methyl vinyl ketone, and a reaction with water-soluble 1,3-

propanesultone were all successfully demonstrated. In all three cases, the further functionalisation resulted in enhanced thermal stability. The alkylation and thiol-ene click reactions also appeared selective towards the SH groups. Incorporation of the sulfonate groups to bwGO and GO-SH yielded CMGs with good dispersibility in H_2O, DMSO and DMF, and are thus examples of CMGs which are able to undergo further wet chemistry.

Gold deposition experiments were carried out on GO-SH, demonstrating that the thiol groups had a high affinity for gold: the selective and homogenous dispersion of AuNPs on GO-SH was directly observed via TEM. Gold clusters were seen to coalesce, forming branched nanoparticles, characteristic of a high nucleation density. The SH groups on GO-SH were also found to be good ligands for soft metals such as Au and Pd, readily reacting with Au(III) and Pd(II) complexes to form metallo-organic CMGs with appreciable dispersibility in DMSO.

There is still a lot to be explored in GO chemistry. For example, further investigation is still needed on the two-component model of aGO. ^{17}O labelling experiments would be a good avenue for future work – using ^{17}O labelled water or sulfuric acid in the synthesis of GO could provide mechanistic insight into the formation and position of the oxygenated groups on aGO via ^{17}O ssNMR studies.

In addition, having fabricated CMGs with potential uses in sensor and catalytic applications, and designed a number of composite materials with enhanced thermal stability, it would be prudent to test the practical usage of these materials. Future investigation should focus on tuning and optimising the catalytic performance, dispersibility and thermal stability of these CMGs for specific purposes.

The OD has been shown to affect certain properties of aGO e.g. dispersibility, conductivity and fluorescence, and it is not known how many other characteristics of aGO are truly a function of the OD. Consequently bwGO itself is a relatively unexplored material. The focus of this thesis has been the chemical reactivity of the bwGO via its epoxy groups, routes to selectively functionalisated bwGO materials via the other functional groups require further study.

1.   Collins, W. R.; Schmois, E.; Swager, T. M. *Chem. Commun.* **2011,** 47, (31), 8790-8792.

Chapter 7

Experimental
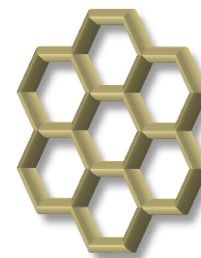
7.1   Safety and General Information

All reactions were carried out in a fume hood with full protective clothing. Particular care was taken when handling strong oxidising agents such as $KClO_3$ and $KMnO_4$ due to their explosive nature. Work with thiols was done on the smallest possible scale. Any gloves, paper towels and glasswear that came into contact with the thiol solutions were decontaminated with bleach before being removed from the fume cupboard.

All chemicals were purchased from standard suppliers, unless otherwise stated, and were used as received with purity ≥95%. The exceptions are as follows: the N-isopropylacrylamide polymers used in chapter 4 were obtained courtesy of Dan Phillips, University of Warwick; the lacey carbon supports used for TEM, and the oxidised silicon wafers (300 nm SiO_2 layer) used for AFM were both obtained courtesy of Dr Neil Wilson, University of Warwick.

All centrifuge cycles were operated at 12,500 rpm, and all samples were dried on a Schlenk line (vacuum 0.1 Torr or better) until there was no further mass loss (typically 2 hours).

Details of the chemicals and materials used in this thesis are given in Table 7.1

Material	Details and Supplier
1-bromobutane	99%, ReagentPlus, Sigma Aldrich
1-bromodecane	98%, Sigma Aldrich
1,3-propanesultone	98%, Sigma Aldrich
Ammonia solution	35%, Fisher Scientific
Bis(benzonitrile)palladium(II) chloride	>99%, Fisher Scientific
Gold(III) chloride hydrate HAuCl$_4$	~50% Au basis, Sigma Aldrich
Hydrazine monohydrate	64-65%, Sigma Aldrich
Hydrochloric acid	32%, Analytical Reagent, Fisher Scientific
Hydrogen peroxide	30 wt.%, ACS Reagent, Sigma Aldrich
Iodine	>99%, Sigma Aldrich
Lithium Hydroxide	>99%, Fisher Scientific
Malononitrile	99%, Sigma Aldrich
Methylamine	98%, Sigma Aldrich
Methyl vinyl ketone	90%, VWR International
Natural graphite powder	≥85%, Graphite Trading Company
Nitric acid (fuming)	>90%, Sigma Aldrich
Phosphoric acid	≥85%, ACS Reagent, Sigma Aldrich
poly(N-isopropylacrylamide)	Courtesy of Dan Phillips, University of Warwick.
Potassium chlorate	99%, ACS Reagent, Sigma Aldrich
Potassium nitrate	99%, ACS Reagent, Sigma Aldrich
Potassium permanganate	≥99%, ACS Reagent, Sigma Aldrich
Potassium thioacetate	98%, Sigma Aldrich
Silver nitrate	>99%, VWR International
Sodium borohydride	98%, Sigma Aldrich
Sodium hydride	95%, Sigma Aldrich

Sodium hydroxide pellets	98%, Sigma Aldrich
Sulfuric acid	>95-97%, ACS Reagent, Sigma Aldrich
Thiophenol	97%, Sigma Aldrich
40 – 60 °C Petroleum ether	Laboratory Reagent, Fisher Scientific
Acetone	99%, Sigma Aldrich
Acetonitrile	Laboratory Reagent, Fisher Scientific
Benzene	99.8%, Sigma Aldrich
Chloroform	99.8%, ReagentPlus, Sigma Aldrich
Deuterated water, D_2O	99.9 atom % D, Sigma Aldrich
Diethyl ether	99.8%, ACS reagent, Sigma Aldrich
Distilled Water	Milli-Q reagent water
DMF	Laboratory Reagent, Fisher Scientific
DMSO	AnalaR, VWR International
Ethanol	99.8%, Sigma Aldrich
Ethyl acetate	AnalaR, VWR International
Glacial acetic acid	Fisher Scientific laboratory reagent grade
IPA	99.6%, ACS reagent, Fisher Scientific
Methanol	Laboratory Reagent, Fisher Scientific
Octan-1-ol	≥98%, Fisher Scientific
Pyridine	99.8%, Sigma Aldrich
THF	99.9%, Sigma Aldrich
Toluene	99.7%, ACS Reagent, Sigma Aldrich
Oxidised silicon wafer (Si/SiO_2)	300 nm SiO_2 layer, courtesy of Neil Wilson, Warwick University
TEM grid	Lacey carbon support, courtesy of Neil Wilson, Warwick University
Nitrogen	BOC gases

Table 7.1 A listing of the chemicals and materials used in this thesis.

7.2   Instrumental Techniques

FTIR spectra were recorded on an Avatar 320 FTIR spectrometer as solids on a total internal reflectance device.

EDX readings were recorded on a Zeiss SUPRA 55-VP FEGSEM with an EDAX Genesis analytical system, the values given are averaged readings from four or more sample sites.

Raman spectra were recorded on a Renishaw 2000 spectrometer, under 514 nm excitation unless otherwise specified.

Solid-state MAS NMR data were measured at an external field B_0 of 9.4 T using a Bruker DSX-400 spectrometer (chapter 3) or a Varian VNMRS 400 spectrometer (chapters 4 and 5), operating at a ^{13}C Lamor frequency of 100.562 MHz. Both DE and CP, MAS spectra were recorded with a 1 s recycle time, and the CP spectra were recorded with a 1 ms contact time. All ^{13}C chemical shifts are calibrated against external tetramethylsilane (δ 0 ppm).

Solution phase NMR spectra were run on a Bruker Avance II 700 MHz NMR spectrometer; ^{1}H (direct observe) and ^{13}C (direct observe with gated decoupling); spectra were referenced to external tetramethylsilane.

ESI mass spectroscopy measurements were taken on a Bruker MaXis high resolution mass spectrometer: an aqueous solution of the OD material was injected into a reverse phase (C18) LC column and eluted into the mass spectrometer with water/methanol (ramping from 100% water to 100% MeOH over 15 minutes). The very first material that eluted from the column was discarded to remove the NaCl.

MALDI-TOF mass spectroscopy measurements were taken on a Bruker Ultraflex II MALDI TOF mass spectrometer using 2,5-dihydroxybenzoic acid and α-cyano-4-hydroxycinnamic acid + NaI matrices.

XPS data were collected at the Science City Photoemission Facility, University of Warwick. The samples were mounted on Omicron sample plates using electrically conducting carbon tape and loaded in to the vacuum chamber. XPS measurements were conducted in the main analysis chamber (base pressure 2 x 10^{-11} mbar), with the sample being illuminated using an

XM1000 monochromatic Al kα x-ray source (Omicron Nanotechnology). The measurements were conducted at room temperature and at a take-off angle of 90° with respect to the surface parallel. The photoelectrons were detected using a Sphera electron analyser (Omicron Nanotechnology), with the core levels recorded using a pass energy of 10 eV (resolution approx. 0.47 eV). The spectrometer work function and binding energy scale were calibrated using the Fermi edge and $3d_{5/2}$ peak recorded from a polycrystalline Ag sample immediately prior to the commencement of the experiments. The data were analysed using the CasaXPS package, using Shirley backgrounds, mixed Gaussian-Lorentzian (Voigt) lineshapes and asymmetry parameters for the sp^2 graphitic components.

AFM measurements were recorded on an Asylum Research MFP3D-SA. Samples were spin coated before analysis: a drop of the sample suspension was placed on an oxidised silicon substrate. The substrate was rotated at 3000 rpm for 45 s, with acceleration and deceleration times of 0.1 s.

TEM measurements were recorded at 200 kV on a Jeol 2000FX with Gatan Orius camera.

High-resolution TEM images were acquired on a Jeol ARM200F TEM/STEM with dual aberration correction, operated at 80 kV.

TGA spectra were recorded on a Mettler-Toledo TGA/DSC1 system at a heating rate of 10 °C min^{-1} from 25–800 °C under air.

Contact angle measurements were carried out on a DSA100 Contact Angle Measuring System with DAS3 software.

7.3   Syntheses

7.3.1 Hummers aGO:

Natural flake graphite (5.020 g) and KNO_3 (4.507 g) were suspended, with stirring, in concentrated sulfuric acid (169 ml). The mixture was cooled on ice and $KMnO_4$ (22.443 g) was added over 70 minutes. The mixture was then allowed to warm to room temperature with constant stirring. After 24 hours the green dispersion had become too thick to stir, it was left for a further 4 days over which time there was a colour change to purple. This mixture was slowly dispersed into 550 ml, 5 wt.% H_2SO_4 in water over the course of one hour and was left to stir for a further 3 hours. Hydrogen peroxide (45 ml, 30 vol) was then added to the brown mixture over 5 minutes, with considerable effervescence, leaving a glittery gold suspension which was left stirring for 2 hours. This suspension was then further diluted with 500 ml of 3 wt.% H_2SO_4/0.5 wt.% H_2O_2 in H_2O and was left stirring for 12 hours.

The mixture was centrifuged (20 minutes) and the separated solid was collected, re-dispersed into 500 ml of 3 wt.% H_2SO_4/0.5 wt.% H_2O_2 in H_2O and re-centrifuged. In total, 6 such acidic washes were done, followed by 8 washes with distilled water which gave a neutral pH. After 3 acidic washes the glittery flakes had all disappeared leaving a much thicker, darker mixture. The resultant brown dispersion was dried under vacuum to give a brown film-like solid (5.0955 g).

EDX atomic % (standard deviation): C 58 (1); O 40 (2)

7.3.2 Brodie aGO:

Natural flake graphite (1.052 g) and potassium chlorate (8.523 g) were mixed together and cooled on dry ice to -20 °C. Fuming nitric acid (20 ml) was added slowly over 40 minutes with constant stirring. The mixture was then allowed to warm to room temperature and was left stirring for 8 hours. This green suspension was then heated to 60 °C and was left stirring overnight, over which time there was a colour change to blue.

The suspension was centrifuged (20 minutes) and the solid was collected, washed with water and re-centrifuged. Drying under vacuum gave blue/silver flakes which were mixed

with potassium chlorate (8.517 g) and fuming nitric acid (20 ml) as before. After an overnight stir at 60 °C, the suspension was allowed to cool to room temperature at which point it was left for a further 2 days under constant stirring. The mixture was then dispersed into water (100 ml) via sonication (20 minutes). A cloudy, brown dispersion was formed.

A gold/brown flaky solid was extracted by centrifugation (20 minutes), washed with water and re-centrifuged. The collected solid was dried under vacuum to give a gold-coloured solid. Once again, this was mixed with potassium chlorate (8.523 g) and fuming nitric acid (60 ml). The mixture was stirred at room temperature for 12 hours, and was then heated to 60 °C for 36 hours followed by a further 2 days at room temperature. The mixture was then dispersed into water (100 ml) via sonication (20 minutes) to form a creamy brown dispersion.

A gold/brown flaky solid was collected by centrifugation (20 minutes), washed with water, and re-centrifuged. The solid was dried under vacuum to leave gold/brown flakes (1.043 g).

EDX atomic % (standard deviation): C 51 (2); O 45 (1); S 1.9 (1).

7.3.3 "Improved" Hummers aGO (Tour):

Natural flake graphite (2.9860 g) and $KMnO_4$ (17.994 g) were dispersed into a 9:1 mixture of concentrated sulfuric acid (360 ml) and concentrated phosphoric acid (40 ml). The green suspension was heated to 50 °C and was stirred for 15 hours, by which point a thick purple mixture had formed. Once cool, the mixture was dispersed gradually into an ice cold solution of water (400 ml) and H_2O_2 (3 ml, 30 vol).

The mixture was centrifuged (1 hour) and the filtrate was washed successively with water (×2), 30% HCl (×1) and ethanol (×6). After each washing the supernatant was discarded and as much unreacted graphite was removed as possible. The resultant brown dispersion was dried under vacuum to give a brown film-like solid (1.7023 g).

EDX atomic % (standard deviation): C 58 (2); O 38 (1); S 2.8 (0.5).

7.3.4 "Pristine" aGO (Quenched):

Natural flake graphite (3.056 g) was suspended in concentrated sulfuric acid (400 ml), and was left stirring for 10 minutes before $KMnO_4$ (3.072 g) was added. The green flaky mixture was left stirring at room temperature overnight, over which time there was a colour change to purple. More $KMnO_4$ (2.952 g) was added, turning the dispersion back to green within 5 minutes. After 6 hours, and a colour change back to purple, even more $KMnO_4$ (3.048 g) was added. One last portion of $KMnO_4$ (3.048 g) was added after the mixture had been left stirring overnight. This mixture was left to stir over the weekend, resulting in a thick, purple mixture.

90 ml of ice cold water was added slowly, followed by H_2O_2 (0.5 ml, 30 vol). The pink mixture was then centrifuged for 20 minutes and the yellow supernatant was discarded. The pink solid was washed with ethyl acetate and the centrifuge cycle was repeated 6 times, by which point the supernatant was clear. The extracted solid was dried under vacuum to give a pink solid (16.434 g).

Some of this "pristine" GO (0.2765 g) was dispersed in water via sonication. The resultant light brown dispersion was centrifuged (15 minutes) and the extracted brown filtrate was washed with water (×2) and acetone (×2) before being dried under vacuum leaving a dark brown solid (0.0436 g, 16%).

EDX atomic % (standard deviation): C 72 (1); O 27 (1).

7.3.5 NaOH Wash of aGO:

The same general method (as detailed below) was used for the GO prepared via all four synthetic routes:

Hummers GO: 140 mg of aGO was re-dispersed in H_2O (250 ml) via sonication to form a stable light brown dispersion. NaOH was added (0.140 g) under constant stirring to give a 0.014 M dispersion. There was an immediate darkening on dissolution of the NaOH. The dispersion was then heated to 70 °C for 1 hour.

The resultant dark brown dispersion was centrifuged (30 minutes) leaving a dark brown solid and colourless supernatant. This supernatant, and that of all subsequent centrifuge cycles, was collected. The dark brown solid was washed with water and re-centrifuged. The solid was re-protonated with dilute HCl (250 ml, 0.014 M) and was stirred for 1 hour at 70 °C. Once cool, the solid was collected as before and washed with water. The wet solid, bwGO, could then be dried under vacuum to give to a black solid (90.3 mg, 65%) or dispersed in a H_2O/CH_3CN solvent mixture via sonication.

EDX atomic % (standard deviation): C 76 (1); O 21 (1); Na 1.9 (0.4); Cl 1.0 (0.1).

Meanwhile, the collective supernatants were dried under vacuum to give an off-white powder (239.1 mg) of OD contaminated with NaCl (calculated to be 204.5 mg), i.e. 34.6 mg (25%) of OD.

Brodie GO: Treating aGO (154.2 mg) with NaOH (0.015 M) yielded a dark brown solid, bwGO (111.7 mg, 72%).

EDX atomic % (standard deviation): C 77 (1); O 22 (1); Cl 0.4 (0.2).

The collected supernatants gave an off-white powder (258.0 mg) of OD contaminated with NaCl (calculated to be 219.0 mg), i.e. 39.0 mg (25%) of OD.

Tour GO: Treating aGO (196.2 mg) with NaOH (0.015 M) yielded a dark brown solid, bwGO (120.6 mg, 61%).

EDX atomic % (standard deviation): C 76 (1); O 22 (1); Na 0.7 (0.3); Cl 0.4 (0.1).

The collected supernatants gave an off-white powder (281.8 mg) of OD contaminated with NaCl (calculated to be 219.0 mg), i.e. 62.8 mg (32%) of OD.

Quenched GO: Treating aGO (107.2 mg) with NaOH (0.014 M) yielded a dark brown solid, bwGO (61.3 mg, 57%).

EDX atomic % (standard deviation): C 77 (2); O 18 (1); Na 1.1 (0.2); Cl 1.2 (0.4).

The collected supernatants gave an off-white powder (234.6 mg) of OD contaminated with NaCl (calculated to be 204.5 mg), i.e. 30.1 mg (28%) of OD.

7.3.6 Ammonia Wash of aGO:

The same general method (as detailed below) was used for the GO prepared via different synthetic routes:

Hummers GO: 154 mg of aGO was re-dispersed in H_2O (200 ml) to give a brown dispersion. The dispersion was stirred at room temperature and excess aqueous ammonia (5 ml, 18.1 M) was added. The mixture was bought to reflux for 30 minutes, causing it to darken appreciably, but not coagulate.

Once cool, the mixture was centrifuged (3 hours) to give separation into a black solid and pale yellow supernatant. The black solid was refluxed for 30 min with HCl (50 ml, 1 M) and was washed with water (×3). The wet solid could then be dried under vacuum to give to a black solid (113.9 mg, 74%) or dispersed in a H_2O/CH_3CN solvent mixture via sonication.

EDX atomic % (standard deviation): C 83 (0.1); O 17 (0.1).

Meanwhile, the pale yellow supernatant was collected and re-centrifuged for 40 minutes. This left a small amount of brown residue and a colourless supernatant. The colourless liquid was dried under vacuum to give a pale yellow powder, OD (34.3 mg, 23%).

Brodie GO: Treating aGO (100 mg) with NH_3 (5 ml, 18.1 M) yielded a black solid, bwGO (69 mg, 69%).

EDX atomic % (standard deviation): C 79 (0.5); O 21 (1).

The collected supernatants gave a pale yellow powder, OD (21 mg, 21%).

7.3.7 Chemical Reduction of Hummers aGO:

Hummers aGO (148 mg) was re-dispersed in water (100 ml) and was stirred at room temperature. A solution of hydrazine monohydrate (5 ml, 12.8 mol dm^{-3}) was added. The mixture was stirred at room temperature for 3 hours, during which time it darkened appreciably.

The mixture was centrifuged (20 minutes) leaving a dark brown solid and colourless supernatant (which was discarded). The dark brown solid was collected, washed with water and re-centrifuged (30 minutes). Drying under vacuum yielded a black/silver flaky solid, raGO (102.1 mg).

EDX atomic % (standard deviation): C 70 (1); O 30 (1).

7.3.8 Chemical Reduction of Brodie aGO:

Brodie aGO (101 mg) was re-dispersed in water (100 ml) and stirred at room temperature. A solution of hydrazine monohydrate (5 ml, 12.8 mol dm^{-3}) was added. The mixture was heated at 70 °C for 1 hour, during which time it darkened appreciably.

The mixture was centrifuged (30 minutes) leaving a dark brown solid and colourless supernatant (which was discarded). The dark brown solid was extracted, washed with water and re-centrifuged (30 minutes). Drying under vacuum yielded a black/silver flaky solid (89.3 mg).

EDX atomic % (standard deviation): C 80 (1); O 18 (1).

7.3.9 Chemical Reduction of Hummers bwGO:

A solution of hydrazine monohydrate (5 ml, 12.8 M) was added to a dispersion of Hummers bwGO (112 mg) in CH_3CN (150 ml). The mixture was stirred at room temperature for 3 hours.

The black mixture was centrifuged (30 minutes) leaving a black solid and colourless supernatant (which was discarded). The black solid was collected, washed with water and re-centrifuged (30 minutes). Drying under vacuum yielded a flaky black solid (96.4 mg).

EDX atomic % (standard deviation): C 71 (1); O 27(2).

A number of different reaction times and temperatures were carried out:

80 °C, 1 hour. EDX atomic % (standard deviation): C 77 (1); O 23 (1).

80 °C, 24 hours. EDX atomic % (standard deviation): C 85 (0.4); O 15 (0.4).

80 °C, 48 hours. EDX atomic % (standard deviation): C 91 (2); O 8 (2).

7.3.10 Preparation of GO-CN:

A solution of sodium hydride (82 mg, 3.41 mmol) in acetonitrile (30 ml) was prepared and placed under nitrogen before being cooled to 0 °C in an ice bath. The malononitrile (220 mg, 3.33 mmol) was then added in one portion. This mixture was stirred for 10 minutes. A fine suspension of bwGO in CH_3CN (40 mg, 200 ml) was prepared and the malononitrile mixture was added dropwise. The combined reaction mixture was then brought to 60 °C in an oil bath for 24 hours, under N_2.

The suspension was centrifuged for 20 minutes to obtain a black solid and red supernatant. Sonicative dispersion, with subsequent centrifugation was repeated with water (×3), methanol (×2) and acetone (×2). By the end of these repetitive washes, the discarded supernatant was colourless.

The resultant black solid was dried under vacuum to give a flaky black solid: GO-CN (35 mg).

EDX atomic % (standard deviation): C 75 (2); N 1.5 (0.5); O 19 (2); Na 5 (2).

7.3.11 Preparation of GO-SH:

Hummers bwGO (100 mg) was dispersed in DMSO (50 ml) via sonication. The black dispersion was stirred in a Schlenk tube and placed under nitrogen. Meanwhile a solution of potassium thioacetate (10 mg) in DMSO (5 ml) was prepared, and was added to the bwGO dispersion. The mixture was heated to 50 °C and was left stirring overnight, under N_2.

The black suspension was then allowed to cool before HCl (5 ml, 1 M) was added. The mixture was stirred for a further 5 minutes before being centrifuged (20 minutes). The pale yellow supernatant was discarded and the black solid was further washed with water (×5) and acetone (×2). Drying under vacuum yielded a black flaky solid: GO-SH (73.2 mg).

EDX atomic % (standard deviation): C 78 (1); O 19 (2); S 3 (1).

7.3.12 Preparation of GO-SPh:

A dispersion of bwGO in CH_3CN (300 ml, 0.3 mg ml^{-1}) was cooled on ice for 15 minutes. LiOH (10 mg) and 5 drops of thiophenol solution were added, after which the mixture was allowed to warm to room temperature and was left stirring for 6 hours.

The dark brown dispersion was extracted with CH_2Cl_2, washed with water and dried under vacuum to give a black solid (82 mg).

EDX atomic % (standard deviation): C 75 (2); O 23 (1); S 1.3 (0.8)

7.3.13 Preparation of GO-pNIPAM$_{30}$:

Three schlenk tubes separately containing: bwGO (60 mg) dispersed in DMF (120 ml); methylamine (3 ml); and pNIPAM$_{30}$ (20 mg) dispersed in DMF (3 ml) with a catalytic amount of glacial acetic acid, were placed under nitrogen. A syringe thrice flushed with N_2 was used to add the methylamine to the pNIPAM$_{30}$ solution, generating effervescence. This mixture was then immediately transferred to the bwGO dispersion. The GO-pNIPAM$_{30}$ mixture was heated to 50 °C for one hour before being allowed to cool to room temperature, and left to stir under N_2 overnight.

The product was extracted via centrifugation, and was washed with acetone (20 minutes, ×2), methanol (30 minutes, ×2) and water (1 hour, ×5) before being dried under vacuum to give a black solid, GO-pNIPAM$_{30}$ (85.5 mg).

EDX atomic % (standard deviation): C 75 (1); O 24 (1); N 1.3 (0.8).

Using the same general procedure, and different polymer chain lengths, two other GO-pNIPAM samples were prepared:

GO-pNIPAM$_{200}$ – EDX atomic % (standard deviation): C 76 (1); O 20 (1); N 2.9 (0.2).

GO-pNIPAM$_{440}$ – EDX atomic % (standard deviation): C 79 (2); O 18 (2); N 2.7 (0.4).

7.3.14 Preparation of GOS-C$_4$ and GOS-C$_{10}$:

GO-SH (100 mg) was re-dispersed in DMSO (50 ml) via sonication (1 hr). The dispersion was placed under nitrogen and was stirred at room temperature before an excess of sodium hydride (10 mg) was added. After 5 minutes, 1-bromobutane (3 ml) was also added and the mixture was heated to 100 °C (2 hours), allowed to cool to room temperature, and was left stirring for a further 16 hours. The mixture was centrifuged and the solid collected was washed with acetone (30 minutes, ×3), diethyl ether (10 minutes, ×2), and distilled water (3 hours, ×3). The black solid was collected and dispersed in ethanol (15 ml) before being dried under vacuum at room temperature to leave a flaky grey/black powder, GOS-C$_4$ (62.1 mg).

EDX atomic % (standard deviation): C 85 (1); O 12 (1); S 2.7 (0.8).

Using the same general procedure, but substituting 1-bromobutane for 1-bromodecance:

GOS-C$_{10}$ – EDX atomic % (standard deviation): C 86 (1); O 11 (1); S 1.9 (0.3).

7.3.15 Preparation of GO-C$_4$ and GO-C$_{10}$:

bwGO (100 mg) was re-dispersed in DMSO (50 ml) via sonication (1 hour). The dispersion was placed under nitrogen and was stirred at room temperature before an excess of sodium hydride (10 mg) was added. After 5 minutes, 1-bromobutane (3 ml) was also added and the mixture was heated to 100 °C (2 hours), allowed to cool to room temperature, and was left stirring for a further 16 hours.

The mixture was centrifuged and the collected solid was washed with acetone (30 minutes, ×3), petroleum ether (10 minutes, ×2), and distilled water (3 hours, ×3). The black solid was collected and dispersed in ethanol (15 ml) before being dried under vacuum at room temperature to leave a flaky grey/black powder, GO-C$_4$ (65.2 mg).

EDX atomic % (standard deviation): C 78 (1); O 21 (1).

Using the same general procedure, but substituting 1-bromobutane for 1-bromodecance:

GO-C$_{10}$ – EDX atomic % (standard deviation): C 79 (2); O 20 (2).

7.3.16 Preparation of GOS-MVK:

GO-SH (80 mg) was dispersed into DMSO (150 ml) and was placed under nitrogen. Meanwhile 50 mg of iodine was dissolved in methyl vinyl ketone (2 ml) resulting in a colour change from pale orange to dark red with the evolution of heat. The MVK and I_2 catalyst mixture was added to the GO-SH dispersion which was then left stirring overnight, under N_2 at room temperature.

The mixture was centrifuged and was then washed with H_2O (×2), acetone (×2) and petroleum ether (×1) before being dried under vacuum (73.0 mg).

EDX atomic % (standard deviation): C 82 (1); O 13 (1); S 3.8 (0.5).

7.3.17 Preparation of GO-MVK:

bwGO (80 mg) was dispersed into DMSO (150 ml) and the dispersion was placed under nitrogen. Meanwhile 50 mg of iodine was dissolved in methyl vinyl ketone (2 ml), resulting in a colour change from pale orange to dark red with the evolution of heat. The MVK and I_2 catalyst mixture was added to the bwGO dispersion which was left stirring overnight, under N_2 at room temperature.

The mixture was centrifuged and was then washed with H_2O (×2), acetone (×2) and petroleum ether (×1) before being dried under vacuum (75.2 mg).

EDX atomic % (standard deviation): GO-MVK: C 77 (1); O 23 (1).

7.3.18 Preparation of GOS-PrSO$_3$:

GO-SH (80 mg) was dispersed in DMSO (150 ml) and was placed under nitrogen. NaH (5 mg) was then mixed with DMSO and immediately added to the GO-SH dispersion. This mixture was left stirring for 5 minutes before a colourless solution of 1,3-propanesultone (10 mg) in DMSO was then added. The mixture was heated to 50 °C and was left overnight under N_2.

The mixture was centrifuged and was then washed with H_2O (×2), acetone (×2), petroleum ether (×1) and was dried under vacuum (67.4 mg).

EDX atomic % (standard deviation): GOS-PrSO$_3$: C 80 (0.5); O 15 (1); Na 1.5 (0.2); S 3.4 (0.5).

7.3.19 Preparation of GO-PrSO$_3$:

bwGO (80 mg) was dispersed in DMSO (150 ml) and was placed under nitrogen. NaH (5 mg) was then mixed was DMSO and immediately added to the bwGO dispersion. The mixture was left stirring for 5 minutes before a colourless solution of 1,3-propanesultone (10 mg) in DMSO was then added. The mixture was heated to 50 °C and was left overnight under N$_2$.

The mixture was centrifuged and was then washed with H$_2$O (×2), acetone (×2), petroleum ether (×1) and was dried under vacuum (71.8 mg).

EDX atomic % (standard deviation): GO-PrSO$_3$: C 72 (2); O 20 (2); Na 6 (1); S 1.9 (0.6).

7.3.20 Preparation of GOS-Au:

A fine suspension of GO-SH (10 mg) in DMF (5 ml) was prepared and added to a solution of HAuCl$_4$ (100 mg) in H$_2$O (5 ml). The mixture was left stirring at room temperature for 30 minutes before being centrifuged (5 minutes). The brown/gold solid was extracted and washed with water (×2) and acetone (×2) before being dried under vacuum (10 mg).

EDX atomic % (standard deviation): C 79 (1); O 18 (2); Au 0.9 (0.5); S 1.0 (0.3), Cl 0.8 (0.3).

7.3.21 Control Reaction: bwGO and HAuCl$_4$:

A dispersion of bwGO (10 mg) in DMF (5 ml) was prepared and added to a solution of HAuCl$_4$ (100 mg) in H$_2$O (5 ml). The mixture was left stirring at room temperature overnight before being centrifuged (5 minutes); the brown solid was extracted and washed with water (×2) before being dried under vacuum (9 mg).

EDX atomic % (standard deviation): C 74 (1); O 26 (2); Cl 0.3 (0.2).

7.3.22 Preparation of GOS-Pd:

A fine suspension of GO-SH (10 mg) in DMF (5 ml) was prepared and added to a solution of $(PhCN)_2PdCl_2$ (50 mg) in DMF (5 ml). The mixture was heated to 50 °C and was left stirring overnight. The solid was extracted via centrifugation and was washed with acetone (×2), diethyl ether (×2), and was dried under vacuum (8 mg).

EDX atomic % (standard deviation): C 81 (2); O 15 (2); S 0.7 (0.2); Cl 1.1 (0.5); Pd 0.6 (0.1).

7.3.23 Control Reaction: bwGO and bis(benzonitrile)palladium chloride:

A fine suspension of bwGO (10 mg) in DMF (5 ml) was prepared and added to a solution of $(PhCN)_2PdCl_2$ (50 mg) in DMF (5 ml). The mixture was heated to 50 °C and was left stirring overnight. The solid was extracted via centrifugation and was washed with acetone (×2), diethyl ether (×2), and was dried under vacuum (9 mg).

EDX atomic % (standard deviation): C 77 (2); O 22 (2).

7.3.24 Preparation of GOS-AuNPs:

GO-SH (2 mg) was dispersed in DMSO (10 ml) via sonication to form a light brown dispersion. Meanwhile a solution of $HAuCl_4$ (5 mg) in H_2O (1 ml) was prepared. $NaBH_4$ (2 mg) was added to the $HAuCl_4$ solution which was then immediately mixed with the GO-SH dispersion. Instantaneous darkening of the dispersion and effervescence was observed. After 5 minutes a precipitate had formed leaving a colourless supernatant.

The precipitate was collected via centrifugation and washed with distilled water (5 minutes, ×2) and acetone (5 minutes, ×2) before being dried under vacuum leaving a black powder (4 mg).

EDX atomic % (standard deviation): C 64 (2); O 6 (2); Au 28 (2); S 1.2 (0.5).

7.3.25 Control Reaction: bwGO and AuNPs:

bwGO (2 mg) was dispersed in DMSO (10 ml) via sonication to form a light brown dispersion. Meanwhile a solution of $HAuCl_4$ (5 mg) in H_2O (1 ml) was prepared. $NaBH_4$ (2 mg) was added to the $HAuCl_4$ solution which was then immediately mixed with the bwGO dispersion. Instantaneous darkening of the dispersion and effervescence was observed. After 5 minutes a precipitate had formed leaving a light brown supernatant.

The precipitate was collected via centrifugation and washed with distilled water (5 minutes, ×2) and acetone (5 minutes, ×2) before being dried under vacuum leaving a brown powder (2 mg).

EDX atomic % (standard deviation): C 74 (2); O 25 (2); Au 0.5 (0.6).

7.3.26 Preparation of Ag Coated SERS Substrate:

Procedure adapted from Ariga *et al.*[1]: Excess silver nitrate was dispersed in octan-1-ol via sonication (1 hour) to form a saturated solution. The excess silver nitrate was removed by gravity filtration. An oxidised silicon substrate was submerged in the solution, and the vessel was left wrapped in foil for 4 days.

The substrate was rinsed with acetone and water before being left in dry in air on filter paper. NH_3 washed OD was dissolved in a 50:50 water-acetone mixture. The solution was drop cast onto the Si-Ag substrate and was left to dry before being used to record Raman spectra.

1.   Shrestha, L. K.; Wi, J. S.; Williams, J.; Akada, M.; Ariga, K. *J. Nanosci. Nanotechno.* **2014,** 14, (3), 2245-2251.